University of Parma

Department of Civil and Environmental Engineering and Architecture - DICATEA

Doctoral Thesis in Civil Engineering

Mechanical Modelling of Short-Fibre-Reinforced Materials under Static or Cyclic Loading

Author:
Eng. Daniela Scorza
(XXVI Ciclo)

Tutor:
Prof. Roberto Brighenti

Head of Doctorate School:
Prof. Gianfranco Forlani

Co-tutors:
Prof. Andrea Carpinteri
Prof. Sabrina Vantadori

January 2015

ABSTRACT

Fibre-Reinforced Composite (FRC) materials typically consist of two or more constituents combined at a macroscopic level. Due to their high mechanical properties (such as good tensile strength, fracture resistance, durability, corrosion resistance, enhanced wear and fatigue strength), composites are commonly used in advanced engineering applications. The mechanical properties of such multiphase materials depend on those of their constituents, i.e. the bulk material (matrix) and the reinforcing phase (such as fibres), as well as on their reciprocal interface bonding. The strength and durability design of composite structural elements must consider the typical damage phenomena occurring in such materials under in-service loading. Such degrading effects, usually responsible for a significant decrease of the structural mechanical performances, can be mainly related to the fibre-matrix delamination (also identified as debonding), fibre breaking, fibre buckling, matrix plastic deformation or cracking. The proper evaluation of the safety factor of composite materials during the service life and also at their limit state, is a crucial task in the design and durability assessment of structural components made by such materials.

The present Ph.D. Thesis deals with the development of a micro-mechanical-based approach for the assessment of the mechanical behaviour of short fibre reinforced composites under static and cyclic loading, by taking into account the principal damage failure modes. A homogenisation approach, based on an energetic formulation, has been generalised in order to take into account the spatial arrangement and distribution of the fibre reinforcing phase. Fibres effectiveness is considered by means of a proper parameter, the sliding function s, that quantifies the stress transfer capability of the fibre-matrix interface bond. Such a parameter has been determined through the fracture mechanics based approach proposed in this Ph.D. Thesis, in alternative to the classical "Shear Lag" model. A correlation between the present model and the shear lag one has been proposed in order to allow the quantification of the static critical interface parameters (such as fracture toughness and fracture energy), necessary to identified the condition of incipient detachment propagation. The progressive debonding due to the action of cyclic

loads is quantified through a fatigue power law.

In order to consider all the micro-mechanical phenomena involved in static and fatigue problems, the mechanical behaviour of the single constituents of the composite are also analysed. The matrix is assumed to be characterised by a linear elastic, elastic-plastic or brittle mechanical behaviour in case of static loads, whereas an approach based on the experimental Wöhler diagrams (S-N curves) is adopted to simulate fatigue effects. The fibre-reinforcing phase is assumed to present a linear elastic behaviour until reaching a suitable condition of failure at which the fibre breaks into two parts. Fibre-fibre reciprocal interaction is also considered, whereas the effect of the cycle loading on the fibre material has been neglected.

Finally, the formulation proposed has been implemented in a non-linear 2-D FE code and used for the simulation of simple structural elements under static and cyclic loads. Some of the obtained results have been reported, discussed and compared with literature available data.

Acknowledgements

This Ph.D.Thesis is the result of many years of work and I am using this opportunity to express my gratitude to everyone who supported me throughout the course of this experience. I would like to express my special appreciation and thanks to my tutor Professor Roberto Brighenti for his important supervision and for encouraging my research.

I would also like to thank my Co-tutors Professor Andrea Carpinteri and Professor Sabrina Vantadori for their advices on both research as well as on my career that have been priceless, and for allowing me to grow in my competences.

I would also like to thank Professor Andrea Spagnoli with which I have had the pleasure to collaborate. I also want to thank my colleagues of Doctorate Eng. Camilla Ronchei and Eng. Nicholas Corbari, and the laboratory technicians Mr Vittorio Leporati, Mr Giovanni Mingardi and Mr Eustacchio Guatteri, because it has been a pleasure to work with all of them.

I would like to gratefully acknowledge my parents, Lidia and Sergio, for all of the sacrifices, support and love in this years of study from the bachelor's degree till today and my husband Alan for his understanding, endless patience and encouragement when it was most required.

Finally, my greater heartily thankful goes to my daughter Arianna, from her I have understood what is really important in my life.

Thank to you all.

Daniela

Contents

List of Figures

List of Tables

NOMENCLATURE

Latin Symbols

Symbol	Definition
A_f, A_m	Cross-section area of the fibre and matrix cross-section area related to a single fibre, respectively.
A, B	Wöhler's fatigue constants of the matrix material.
$\boldsymbol{B}$	Compatibility matrix.
$\boldsymbol{C}_{eq}$, $\boldsymbol{C}'_{eq}$	Homogenised elastic tensor and tangent homogenised elastic tensor of the composite, respectively.
$\boldsymbol{C}_f$, $\boldsymbol{C}_m$	Elastic tensor of the fibre phase and of the matrix material, respectively.
$\boldsymbol{C}'_f$, $\boldsymbol{C}'_m$	Tangent elastic tensor of the fibre phase and of the matrix material, respectively.
C_i, m_i	Paris constants of the fibre-matrix interface.
d, D	Characteristic microscopic and macroscopic length of the composite, respectively.
D_1, D_2	Eingenequations of the λ_1 and λ_2 eingenvalues.
$D_c(\sigma^*, R^*, N)$	Damage parameter after N loading cycles with stress amplitude σ^* and stress ratio R^*.
D_i	Debonding-related damage parameter, $D_i \approx 1-s(\overline{\varepsilon_f^m})$.
$E_f = E_1$, $E_m = E_2$	Young's modulus of the fibre phase (material 1) and of the matrix (material 2), respectively.
E'_f, E'_m	Post-yielding stress-strain slope of the fibre phase and of the matrix material, respectively.
E_i	Young's modulus of the fibre-matrix interface.
$E_f = E_1$, $E_m = E_2$	Young's modulus of the fibre phase (material 1) and of the matrix (material 2), respectively.
E_{m0}, $E_m(N)$	Young's modulus for the undamaged matrix material and corresponding reduced value after N cycles, respectively.

$\mathcal{F}$	yielding function for the matrix material.
$\boldsymbol{F} = \boldsymbol{k} \otimes \boldsymbol{k}$	Second-order tensor related to the fibre lying along the $\boldsymbol{k}$ direction, respectively.
f_t	Matrix material tensile strength.
$f_{t,f}$	Fibre tensile strength.
$G_f = G_1$, $G_m = G_2$	Shear modulus of the fibre phase (material 1) and of the matrix (material 2), respectively.
G_i	Shear modulus of the fibre-matrix interface.
$\mathcal{G}_f$	Matrix material fracture energy.
$\mathcal{G}_{ic}$	Fibre-matrix interface fracture energy.
H	Hardening parameter.
$H(\boldsymbol{x})$	Heaviside jump function across the crack line.
$\boldsymbol{i}$, $\boldsymbol{j}$	versors identifying the normal and tangential directions to the discontinuity at a generic point C.
I_1,I_2, I_3	Stress tensor invariants.
J_1,J_2, J_3	Deviatoric stress tensor invariants.
$\boldsymbol{k}$	Unit vector parallel to the generic fibre axis.
$\overline{k}$	Stiffness of the fibre-matrix interface.
$K_{1x} = K_1(\sigma_x^\infty)$	Mode I SIF due to the remote stress σ_x^∞.
$K_{2x} = K_2(\sigma_x^\infty)$	Mode II SIF due to the remote stress σ_x^∞.
$K_{3x} = K_3(\sigma_x^\infty)$	Mode III SIF due to the remote stress σ_x^∞.
$K_{1z} = K_1(\sigma_z^\infty)$	Mode I SIF due to the remote stress σ_z^∞.
$K_{2z} = K_2(\sigma_z^\infty)$	Mode II SIF due to the remote stress σ_z^∞.
K_i	Equivalent interface I SIF in the case of mixed mode of fracture.
K_{ic}	Fibre-matrix interface fracture toughness.
$K_{I,w}$, $K_{II,w}$	Mode I and II SIFs at the corner of the wedge.
$K_{Ieq,w}$	Equivalent SIF at the corner of the wedge.
$K_{Mw}(\theta)$	Mode M SIF ($M = I, II, III$) at the point along the crack front (identified by the angle θ) due to the remote stress $\sigma_w^\infty (w = x, y, z)$.
$K_{Mw}^*(\theta)$	Dimensionless SIF related to $K_{Mw}(\theta)$.
$\overline{\boldsymbol{K}}$	Condensed incremental tangent stiffness matrix of the cracked finite element.

$2L_{ad}$	Length of the non-debonded portion of the fibre.
$2L_f$	Length of the fibre.
$l = L_f - 2L_{ad}$	Debonded lengthof the fibre at each extremities.
N^*	Number of loading cycles to failure under stress amplitude $\sigma^* \leq \sigma_0$.
$\boldsymbol{N}(\boldsymbol{x})$	Shape function matrix.
p	Perimeter of the fibre.
$p(\varphi, \vartheta) = p_\varphi(\varphi) \cdot p_\vartheta(\vartheta)$	Probability density functions of the fibre orientation angles.
$\boldsymbol{Q}$	Nodal discontinuity matrix.
R^*.	Fatigue load Ratio.
$R.V.E.$	Representative Volume Element.
$s(\varepsilon_f^m)$, $s(\overline{\varepsilon_f^m})$	Sliding function such that $[[\varepsilon_{f-m}]] = \varepsilon_f^m \cdot \left[1 - s(\varepsilon_f^m)\right]$ and its mean value along a single fibre, respectively.
u, v, w	Displacements measured along the $x-y$ and z axis, respectively.
u_c, v_c	Relative crack opening and sliding displacement, respectively.
V, V_m, V_F	Volume of the composite, volume of the matrix phase and volume of the fibre fraction present in the R.V.E., respectively.
v_{cg}	Crack growth velocity measured with respect to the number of cycles.
$\boldsymbol{w_c} = u_c\boldsymbol{i} + v_c\boldsymbol{j}$	Relative displacement vector across the crack.
W, $\overline{W}$	Effective fibre energy density evaluated by using the stress values and the fibre strain and the mean fibre energy density evaluated by using the mean stress values and the mean fibre strain, respectively.
$\boldsymbol{x}$	Generic position vector.

Greek Symbols

Symbol	Definition
α_D, β_D	Dunders' composite constants.
$\gamma = E_f/E_m$	Young modulus ratio.
$\boldsymbol{\delta}(\boldsymbol{x})$	Total displacement field vector.
$\overline{\boldsymbol{\delta}}(\boldsymbol{x})$, $\boldsymbol{\delta}_d(\boldsymbol{x}) = H(\boldsymbol{x})[[\boldsymbol{\delta}(\boldsymbol{x})]]$	Continuous part and discontinuous one of the displacement field, respectively.
$[[\boldsymbol{\delta}(\boldsymbol{x})]]$	Displacement jump vector across the crack line.
δ_s	Dirac delta function.
ΔK_i	Equivalent stress intensity factor range.
ΔK_{th}	Threshold stress intensity factor range.
$\boldsymbol{\varepsilon}^b(\boldsymbol{x})$, $\boldsymbol{\varepsilon}^u(\boldsymbol{x})$	Bounded and unbounded parts of the strain vector along the discontinuity line, respectively.
$\boldsymbol{\varepsilon}$, $\dot{\boldsymbol{\varepsilon}}$	Strain and strain rate tensors, respectively.
$[[\varepsilon_{f-m}]]$	Strain jump between the fibre and the matrix (parallel to the fibre axis) in the case of an imperfect bond.
ε_f, $\dot{\varepsilon}_f$, $\varepsilon_{m,i}$	Uniaxial fibre strain, uniaxial fibre strain rate and matrix strain in the direction $i (i = x, y, z)$, respectively.
ε_f^m	Uniaxial matrix strain measured at the location and in the fibre direction.
$\overline{\varepsilon_f^m}$	Mean matrix strain evaluated in the fibre direction.
$\eta = 2L_f/\varphi_f$	Fibre geometrical aspect ratio.
ζ, κ_j	bi-material mechanical coefficients.
θ	Angular co-ordinate of the cylindrical crack front.
$\overline{\varepsilon_f^m}$	Mean matrix strain evaluated in the fibre direction.
$\kappa(\boldsymbol{x})$	Point function denoting the presence of the matrix at the location $\boldsymbol{x}$.
λ_1, λ_2	Parameters affecting the stress singularities at the corner inclusion.
$\dot{\lambda}$	plastic multiplier.
$\mu_m = V_m/V$	R.V.E. matrix volume fraction.
$\mu_f = V_f/V$	R.V.E. fibre volume fraction of the fibre phase.
μ_f^*	R.V.E. effective fibre volume fraction of the fibre phase.

ν_i	Poisson's ratio of the fibre-matrix interface.
$\nu_f = \nu_1$, $\nu_m = \nu_2$	Poisson's ratio of the fibre phase (material 1) and of the matrix (material 2), respectively.
$\xi = l/L_f$	Relative fibre debonded length.
$\boldsymbol{\sigma}$, $\dot{\boldsymbol{\sigma}}$, $\dot{\boldsymbol{\sigma}}_f$, $\dot{\boldsymbol{\sigma}}_{eq}$	Stress tensor, stress rate tensor, stress rate tensor at the location of the generic fibre and in the equivalent material, respectively.
σ_c, τ_c	Normal and tangential bridging stresses, respectively.
σ_f, $\sigma_{m,i}$	Axial stress in a fibre and stress in the matrix in the fibre direction, respectively.
$\sigma_{red}(w_c)$	Reduced stress tensor of a cracked finite element.
σ_x^∞, σ_y^∞, σ_z^∞	Remote stress acting along the x and y direction (normal to the fibre) and z direction (parallel to the fibre), respectively.
σ_r^∞	Uniform remote radial stress acting normal the fibre.
$\sigma_{z,c}^\infty$	Remote uniaxial critical stress.
σ^*, σ_0^*	Generic stress amplitude, and conventional fatigue limit of the matrix material, respectively.
τ_i	Fibre-matrix interface shear stress.
τ_{au}, τ_{fu}	Maximum fibre-matrix interface shear stress and friction fibre-matrix interface shear stress, respectively.
τ_{xy}^∞	Remote tangential stress acting in the $x-y$ plane.
φ, ϑ	Angles to identify the fibre orientation in the three-dimensional (3D) space.
$\overline{\varphi}$, $\overline{\vartheta}$, δ_φ, δ_ϑ	Mean values and standard deviations of the probability distribution functions of the fibre orientation angles, respectively.
ϕ_f	Fibre diameter.
$\chi(\boldsymbol{x})$	Point function denoting the presence of reinforcing phase at the location $\boldsymbol{x}$.

To my daughter Arianna

Chapter 1

Introduction

1.1 Overview

Fibre-Reinforced Composite (FRC) materials typically consist of two or more constituents combined at a macroscopic level. Due to their high mechanical properties quality (such as good tensile strength, fracture resistance, durability, corrosion resistance, enhanced wear and fatigue strength), composites are commonly used in advanced engineering applications where traditional materials cannot be conveniently used [1–3]. The mechanical properties of such multiphase materials depend on those of their constituents, i.e. the bulk material (matrix) and the reinforcing phase (such as fibres), as well as on their reciprocal interface bonding.

The assumption of the composite as an assembly of many Representative Elementary Volumes (REVs) has been widely used in the literature. The composite macroscopic behaviour is finally obtained by extending to the whole material volume, the mechanical quantities computed for the REV.

Moreover the reinforcing arrangement inside the bulk material (such as the fibre orientation) must be carefully taken into account since it is responsible for the final anisotropic behaviour of the multiphase material, which is also of primary importance in the evaluation of the damage occurring during the service life. Both the microscopic scale (with the order of the size and spacing distribution of the reinforcement) and macroscopic level (with the dimension of the characteristic length of the composite structure) must be properly considered in order to describe the composite material behaviour through a physically-based mechanical model.

The individual characteristics of the various constituents of the composite (such as the matrix material, the reinforcing fibres, the matrix-fibre interface etc.) are studied at the microscopic scale, whereas the composite material is treated as a single entity at the macroscopic level. In fact, the mechanical and geometrical characteristics of the reinforcing phases in the composite and its interaction with the matrix must be taken into account from both a local and global point of view. Since the global formulation of the composite macroscopic mechanical behaviour reflects the mechanical aspects at a microscopic scale, the analytical solution of this problem is very complex and represents a difficult task in the framework of material science mathematical modelling.

The strength and durability design of composite structural elements must consider the typical damage phenomena occurring in such materials under in-service loading. Such degrading effects, typically responsible for a significant decrease of the structure mechanical performances, can be mainly related to the fibre-matrix delamination (also identified as debonding), fibre breaking, fibre buckling, matrix plastic deformation or cracking.

The proper evaluation of the safety factor of composite materials during the service life and also at their limit state, is a crucial task in the design and the durability assessment of structural components made by such materials. During the last decades, several theoretical [4–13], phenomenological or approximate [14–16] and computational approaches [17–19] have been developed for the above purpose. The safety assessment must take into account various damaging phenomena occurring in such multiphase materials: matrix material damage (such as cracking, plasticization, ect), fibre debonding, fibre breaking.

In short fibre-reinforced materials (i.e. with fibres shorter than a critical length, depending on the geometry, fibre tensile strength and matrix-fibre limit shear stress) damage, associated with fibre pull out, is generally predominant with respect to fibre breaking and must carefully be evaluated in order to quantify the loss of load bearing capacity of the structural element.

Typical damaging phenomena in composites are also associated to repeated loading (fatigue), responsible for a progressive fibre-matrix detachment and matrix degradation leading to a loss of the main mechanical characteristics of these materials [20–23].

1.2 Objectives and content of the Thesis

The present Ph.D. Thesis deals with the development of a micro-mechanical-based approach for the assessment of the mechanical behaviour of short fibre reinforced composites under static and cyclic loading, by taking into account for the principal damage failure modes.

One of the main objectives of this work is to develop a comprehensive computational model capable to represent the complex mechanical damaging phenomena occurring at the micro-scale level and to provide a macroscopic response suitable to simulate the behaviour of real structural components.

Particular attention has been focused on the fibre-matrix reciprocal interaction that is responsible of the composite mechanical properties. Finally, the proposed computational approach has been implemented in a non-linear 2-D FE code enabling to predict the mechanical behaviour of FRC materials subjected to plastic, fracture and/or fatigue phenomenon.

Since the main objective of this work was to propose and implement a useful computational model to quantitative describe the mechanical properties of Short Fibre Reinforced materials, Chapter 2 contains a literature review on the subject. It includes the classical homogenization approaches used to study heterogeneous materials and the most common techniques employed to model the damage phenomena in fibre-reinforced materials, both in case of static and cyclic loadings.

The homogenization approach based on an energetic formulation [15] and developed in the present Ph.D. Thesis, is explained in Chapter 3, together with the Gaussian formulae used to take into account for the effect of fibre arrangement on composite elastic parameters. This Chapter also contains a description of the "Shear Lag" model [24] initially adopted to determine the effectiveness of the fibre-matrix interfacial bond through a scalar parameter called sliding function. The last paragraphs of Chapter 3 are devoted to explain how the fibre breaking and fibre-fibre reciprocal interaction are represented.

The mechanical behaviour of the matrix material under static and cyclic loads is described in Chapter 4. In the present Thesis, both brittle and ductile behaviour are considered for the matrix material by adopting a fracture approach based on the cohesive crack model and an elastic-plastic constitutive formulation, respectively. The Wöhler curves are adopted to describe the fatigue damaging effects on the bulk material. A final paragraph is entirely devoted to explain the algorithm

implemented in the computational code.

The fracture mechanics-based approach proposed in the present Thesis to model the fibre-matrix debonding phenomenon (in alternative to the classical "Shear Lag" model) is described in Chapter 5. Since the detachment between fibre and matrix is assumed to be represented by means of a three-dimensional cylindrical crack, both in the case of static and cyclic loading, the analytical formulation for the equivalent Interface Stress Intensity Factor (SIF) is reported. In order to obtain the SIF values necessary to model the fibre-matrix debonding as a propagating crack, an extensive parametric campaign of numerical simulations has been carried out; some of the obtained SIFs are reported in Chapter 5, while the remaining values are reported in Appendix. A correlation between the proposed debonding approach and the classical "Shear Lag" model is also determined and discussed in a paragraph of Chapter 5. Such a correlation is aimed to determine the interface critical parameters necessary to assess the condition of incipient crack propagation from standard material's mechanical ones.

A summary of the computational algorithm developed in this Ph.D. Thesis is explained in the first part of Chapter 6. In the second one, some numerical examples , are reported both for static and cyclic loads and, where possible, a comparison with numerical and experimental results found in literature is made. Finally, some conclusions and remarks, based on the obtained results, are presented together with some prospective issues related to such a problem.

Chapter 2

State of Art on Fibre Reinforced Materials

2.1 Introduction

Composite materials offer numerous advantages compared to conventional homogeneous media; the concept of composite structures was adopted very early in human history in order to create tools, mainly weapons, with enhanced properties. For example the Mongolian horn bow arcs were made by mixing different materials: the compressed parts were made of corn and the stressed ones of wood and cow tendons, glued together to obtained extraordinary strength. structure, with translucent aerogel-filled GFRP sandwich walls being placed between the GFRP frames.

Reference to highly interesting structures exhibiting elements of almost modern technology can also be found in Homeric epics. The shields of Achilles and Ajax Telemonius are presented as laminated structures consisting of successive layers of different metals and metal and leather layers, respectively, and are characteristic examples of the advanced knowledge of the science and technology of materials and structures possessed by the Mycenaen Greeks [25]. Metals used in this respect were hard bronze, tin and pure gold (shield of Achilles) and hard bronze and calf's leather (shield of Ajax). The impressive impact properties of this structure are also praised in the Iliad, for describing of the duel between Ajax and Hector. These

Figure 2.1: The Eyecatcher building in Basel Switzerland (a) and the Pontresina footbridge (b).

unique detailed descriptions, which also include the weapon's battle behaviour, constitute the first known applications of laminated structures in human history.

Composite structures were made based on the idea of mixing soft matrices with strong reinforcements, a concept copied from nature, with wood and bone being possibly the most common and easily comprehensible examples of natural composites. Wood consists of cellulose fibres, which give it the ability to bend without breaking, embedded in a compound called lignin, which provides the stiffening property. Bone is a combination of a soft form of protein known as collagen and a strong but brittle material called apatite. This concept has been adopted by humans for building applications (e.g., mixing mud and straw to make bricks) since very early times, or even for contemporary reinforced concrete, but it is only over the last century that composite materials have been used for advanced engineering structures in all fields of applications ranging from aerospace (where the need for composites was determined by operational conditions) to automotive, civil and mechanical engineering in order to optimize existing designs and create novel more effective (light and durable) products.

Fibre-Reinforced Materials (FRMs) are used today instead of such homogeneous isotropic materials as steel, concrete and even the anisotropic wood that has long been employed in numerous applications.

A typical example of the use of FRMs for structural elements in order to achieve lightweight and easily assembled structures, is shown in Figure 2.1a. The Eyecatcher building in Basel, Switzerland is a 15m tall, five-story, mobile, lightweight building,

Figure 2.2: Wind turbines with composite structural elements.

the tallest multi-story Glass Fibre-Reinforced Polymer (GFRP) building in the world. The building concept was based on a single-layer load-bearing GFRP envelope integrating structural, building physical and architectural functions. Three GFRP frames composed of adhesively-bonded assembled sections were used as the main load-bearing The Pontresina bridge (Fig. 2.1b) is a temporary lightweight pedestrian bridge, installed each year in the autumn and removed in the spring. It is made by two $12.5m$ truss girder spans, with adhesively-bonded joints in one span (fully load-bearing) and bolted joints in the other span.

Composites were introduced in the aerospace sector, long before any other engineering domain, since they offer multiple advantages such as high strength and stiffness at light weight, an asset directly connected to cost reduction or higher transferring capacity, and impressive thermal stability, needed when structures operate in extremely aggressive environments as in space. Numerous applications of "advanced" composite materials in the aerospace industry can be found [26].

It is thanks to the free formability concept and the superior specific mechanical properties offered by fibre-reinforced composites that the wind industry grew so rapidly during the last quarter of the twentieth century and is still growing (Fig. 2.2).

Multifunctional structural elements can also be constructed using composite materials. According to [26] multifunctional composite materials (MFCMs) are defined as the structural composite materials that are designed to perform more than one other non-structural function. Some of the multiple subsystem functions include thermal management, damping, electrical energy generation and storage,

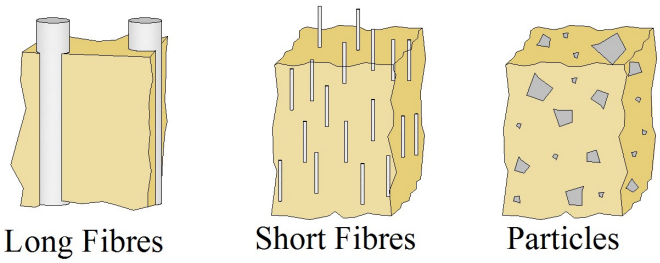

Figure 2.3: Different types of reinforcements for a composite materials.

sensing radiation shielding and health monitoring.

The technical production guarantees a high-quality fabricated composite structural element and quality control of fabrication since it can be performed in well-controlled laboratory conditions, and results in reduced construction times compared to conventional building procedures.

2.2 Generality

Composite material are a combination of two or more components that contribute mutually to provide mechanical and physical properties generally better than those of its individual constituents. A composite material is made by:

1. the matrix that, by bonding the fibres, transfers to them the external load and protects them from environmental factors and from mechanical degradation actions such as cutting;

2. the reinforcing material that is added in the form of long fibres, short fibres or particles (Fig. 2.3);

3. the interface between the reinforcing material and the matrix.

In the case of the fibres arranged parallel to each other inside the matrix, the material is called unidirectional oriented composites and the mechanical properties of such a material are strongly anisotropic: this peculiar characteristic offers the possibility to design and build a material according to the structural requirements. Materials with desired mechanical properties can in fact be constructed by forming layers each one made by parallel fibres and by superimposing the layers with fibres

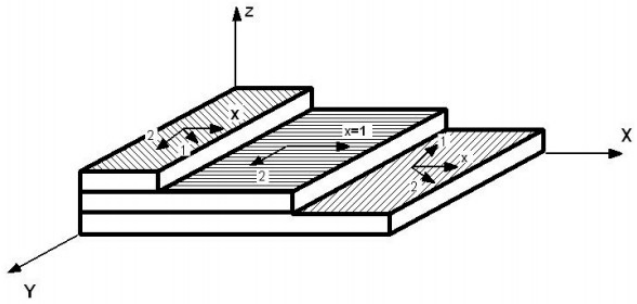

Figure 2.4: Example of laminate constituted by many plies.

arranged in different orientations. In this case the individual layers are defined plies, and the set of plies, laminate (Fig. 2.4).

The properties of composite materials are closely related to the ones of individual components, to their shape, size, concentration, distribution, orientation, as well as their mutual interaction. The strength and stiffness of the composite materials depend widely on the reinforcing phase and, in the particular case of long or short fibres, on their orientation with respect to the applied loads directions. In fact, the mechanical behaviour does not depend exclusively on the reinforcement material, but also on the synergy between the reinforcement and the matrix. For example, when a bundle of fibres without matrix is stretched, the breaking of one of them, entails that the stress is transferred to the remaining fibres, with a consequent reduction of the overall strength of the bundle. On the other hand, if the fibres are embedded in a matrix, the break of one of them does not compromise its mechanical strength by virtue of the presence of the interface and of the deformability of the matrix which allow the load redistribution. In fact, the elastic deformation or the plastic flow of the matrix transfers the shear stress that is gradually shared by the fractured fibre parts.

2.2.1 Classification

The two common classifications of composite materials are function of:

- Mechanism of resistance, depending on the shape and orientation of the reinforcement: "fibre reinforced composites" and "composites reinforced with particles";

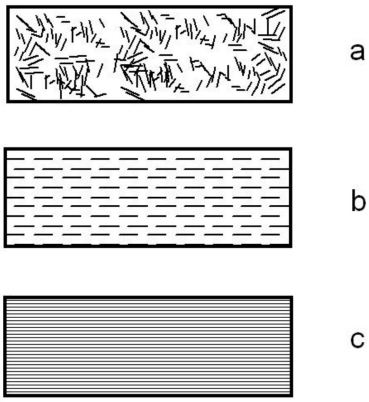

Figure 2.5: Discontinuous fibers randomly arranged (a) and arranged unidirectionally (b); continuous fibers(c).

- Type of matrix: plastic, metallic or ceramic.

Classification based on the resistant mechanism

The reinforcements, both in the case of fibres that of particles, may be oriented random or according to a preferential direction. The fibres, which may be long or short, can be arranged so as to constitute a single lamina or a laminate (superposition of laminae, Fig. 2.4). In addition, if the fibre is long it is called continuous fibre laminate, otherwise discontinuous fibre laminate (Fig. 2.5).

The *particles* typically has the purpose of improving the composite resistance to wear, the surface hardness, workability, resistance to high temperatures and thermal expansion. However, in general, the presence of particles, although very resistant, does not contribute significantly to improve the mechanical properties of the composite, unlike what occurs, instead, in the fibrous composite, in which almost all of the load is supported by the fibres. In fact, the presence of hard particles in a brittle matrix can generate phenomena of local stress concentration, by undermining the mechanical strength of the composite. It was also found that, in the case of fractures, the presence of resistant and hard particles do not prevents effectively the propagation of any cracks or defects. Examples of composite particles are those obtained by combining various metal materials such as lead particles used in a matrix of copper alloys or steel in order to improve the workability or the

lubrication in anti-friction alloys. In materials obtained by reinforcing a polymer matrix with inorganic substances, such as silica, or with metals, such as silver, significant improvements in heat resistance and abrasion have been noted.

The *fibrous composite* are the most widely used in mechanical engineering. Their success is closely linked to the high strength / weight ratio (specific resistance) and the high rigidity / weight ratio (specific form), together with the possibility to act on the concentration and orientation of the fibres in order to vary the degree of anisotropy. The high specific resistance of the fibrous composite is essentially linked to the high fibre strength and low weight of fibre and matrix. Experimentally it has been observed that the resistance of a given material increases significantly when it is produced in thin fibres, in fact, the fibre strength increases with decreasing size of the cross section because of the reduced probability to have defects in the material at smaller sizes of the element.

Classification based on the nature of the matrix

- The *plastic composite*, whose matrix consists of a plastic material, are undoubtedly the most common and popular both for their simplicity of realization and economy. They have supplanted other materials in a wide range of applications.

  The matrix can be classified into two types:

  - Thermosetting resins;
  - Thermoplastic resins.

  The term "thermosetting" indicates plastic materials characterized by the property to become infusible and insoluble after being brought to melting and then cooled. This characteristic is derived from the formation, after the first melting and at a molecular level, of a three-dimensional lattice bonded by strong covalent bonds which make the process irreversible. A classification of such resins can be made according to the temperature range to which the matrices must work. For temperatures lower than 250°C, the epoxy resins are the most used, since they have better mechanical properties than other polymers, excellent adhesion to the fibres, good chemical resistance, low shrinkage and therefore low value of residual stresses, associated with

a remarkable thermal stability. In general, epoxy resins are mainly used in aerospace and aeronautical applications. The polyester resins are used in combination to the glass fibres (GRP), and they are characterized by a low cost and good mechanical characteristics. They are used in railway, marine, chemical and electrical applications.

For temperatures above 250°C, the phenolic resins ensure the same properties of epoxy resins even at high temperatures. The main disadvantages are due to the high pressure needed during the polymerization process, to the high content of voids and to the characteristic black color. Phenolic resins are used in transport applications, where it is required a certain resistance to fire. The vinyl resins have the same characteristics of polyester resins but with a fibre-matrix bond stronger, while the polyamide polymers maintain good mechanical properties despite the high operating temperatures.

Thermoplastic polymer matrices are resins with linear molecular structure that during the hot stamping do not suffer any chemical modification. The heat causes the fusion and the solidification occurs during the cooling. The cycle can be repeated for a limited number of times since too many heatings can degrade the resins. There are two classes of polymers: those wholly amorphous and those semi-crystalline. Amorphous polymers are composed of chains randomly arranged and they are characterized by a transition (vitreous transition temperatures) during which they change between a brittle behaviour and a behaviour similar to that of rubbers. For this kind of polymers, the melting of the material does not occur at a given temperature; the material passes gradually from the solid state, through the viscous one and finally the fluid one. The useful range for the processing is limited to a few degrees centigrade, since below the melting point of the material it is still solid while it is not prudent to significantly exceed the melting temperature since it may trigger the phenomenon of thermal degradation.

- The *metal matrices* are not widely used for reasons inherent to the introduction of the fibres inside the matrix, which of course, must be in the liquid state, but also at a temperature that does not damage the fibres themselves. Another problem is to obtain a uniform distribution of fibres in the matrix, in addition to the difficulty to get their perfect alignment. The wettability is one of requirements more difficult to obtain, since often the metal matrix

does not wet completely the fibres. To improve the wettability, for example of carbon fibres, it is necessary that the metallic materials of the matrix, such as titanium, zirconium, niobium, tungsten, etc., contribute to the formation of carbides. These carbides, in a thin layer, improve the wettability but can damage the surface of the fibre remarkably. The main danger, however, resides in the temperature at which the matrix comes to wet the fibre, that creates the possibility of forming intermediate deposits that can damage the fibres. Despite these difficulties, the aerospace industry has interest in the development of metal matrix composites because they possess the characteristics of low thickness and high specific resistance (matrices of aluminium, magnesium and titanium) required in this sector.

- The reinforcement increases the toughness and the resistance of the brittle matrix, by reducing the crack propagation. In the case of polymer matrix, composites are trying to maximize the balance between mechanical strength and density and between the elastic modulus and density. In metal matrix the use of composites attempts to increase the elastic modulus, whereas in the case of ceramic matrix the purpose of composites is the toughness improvement. The covalent or ionic partially covalent bonds, that bind together the atoms of these materials, are extremely strong, consequently, they generally have a high refractoriness and chemical inertness, a high elastic modulus and considerable toughness, and maintain these properties even at temperatures above 1000°C. The ceramics break with a typical mechanism of brittle materials; i.e. through the appearance of fracture that propagates at high speed in the artefact, while the reinforcement phase has the aim to improve this behaviour, together with material tensile strength.

The reinforcement phase

The fibres are more resistant than monolithic materials essentially for two reasons: first, the size effect, that is to say that in elements of small volume the probability of finding defects is lower, and second the good molecular orientation induced during the fibre production. So, generally, the reinforcing phases in composites, may be viewed as inclusions that operate as a reinforcement for the matrix. The reinforcements can be classified according to their morphology into:

- Fibres;

- Particles.

The individual fibres (whose length is indicated by $2L_f$), generally, having diameters (ϕ_f) ranging between 7 and 30 μm, can be short if the aspect ratio ($\eta = 2L_f/\phi_f$) is lower than 1000 and long fibres if the aspect ratio ranges between 1000 and infinite. Such fibres are usually commercialized in the form of threads which contain thousands of mono-filaments. The shape of the fibre, dependent on their production process, is fundamental in defining the fibres properties. Important is also the fineness of the fibres, i.e. the mass in function of the length (with measurement unit in $g/9000m$). The most important feature for the fibres used for structural reinforcement, is the high tensile strength or stiffness / weight ratio. The existing fibres can be of different nature:

- Natural;
- Artificial;
- Synthetic.
- The *glass fibres* are widely used as a reinforcement for thermosetting or thermoplastic matrix. These have some advantages, such as high toughness, high strength and good performance/cost ratio, whereas the relatively low modulus, low abrasion resistance, low adherence to the matrices, moisture sensitivity and density relatively high are some of the most common drawbacks.
- The *carbon fibres* have high mechanical properties that derive from the particular graphite crystal structure. The raw materials used to obtain the carbon fibres are: PAN, Rayon, bitumen. This type of fibre also has disadvantages mainly represented by easy flammability and high electrolytic potential.
- The *aramid fibres* are fibres formed by long chains of synthetic polyamide. The advantages are low density, high elastic modulus, high tensile strength and not catastrophic failure, whereas the drawbacks are low values of compression strength, low resistance to Temperature (max 160°C) and high moisture sensitivity. Commercial names of aramid fibers are Kevlar, Nomex, etc..
- The *steel fibres* are widely used to reinforce ceramic material such as concrete matrices and they can be shaped in order to optimize the mechanical performance of the composite. They can be of different types:

- fibre with low carbon content (less than $0,20\%$);
- fibre with high carbon content (more than $0,20\%$);
- stainless steel fibre.

The stainless steel fibres coated with zinc represent the solutions for particular exposure to corrosive agents, but they are expensive (from 3 to 10 times more than the common carbon fibres). The use of fibres to reinforce concrete matrices involves the reduction of the matrix microcracks. The advantages to employ steel fibres are numerous: increasing control of plastic shrinkage of concrete, improvement of ductility, wear resistance and impact resistance, improvement of the characteristics of the material during post-crack phase.

2.3 Micro-Mechanics of Composite Materials

Micro-mechanics based models of heterogeneous materials have a fundamental role in the development of new material systems by enabling (i) identification and selection of suitable materials for given applications, (ii) development of engineered materials with desired thermo-mechanical and physical properties and (iii) design/optimization of composite structural components in a multi-scale analysis setting. At the very fundamental level, micro-mechanical analysis facilitates understanding of how the local properties of constituent phases and their arrangement influence the macroscopic material and structural behaviour.

In order to successfully achieve these goals, the used of micro-mechanics technique should be accurate at the macroscopic as well as the microscopic levels in order to yield information not just on the average deformation characteristics in a structural analysis setting, but also on potential failure modes. As discussed by Pindera and Bansal [27], an ideal micro-mechanics model that satisfies the above objectives would also possess the following features: multiphase material modelling capability with complex micro-structures (including the ability to admit multi-inclusion regular or random arrays), arbitrary elastic/inelastic constitutive model capability at individual phase level and closed-form constitutive equations for combined thermo-mechanical multi-axial loading.

Micro-mechanics aided formulation of such mechanism-based constitutive equations requires, particularly if the chosen technique is incorporated into an opti-

mization algorithm, to identify optimal constitutive parameters within the chosen framework.

Much work in the area of micro-mechanics of heterogeneous materials has been conducted during the past 50 years, starting with the simplest assumptions on the stress and strain sharing among the constituent phases and development of detailed geometric models that require more demanding analytical and numerical treatment. The various approaches have been summarized in reports and monographs by Hashin [28], Achenbach [29], Bensoussan et al. [30], Christensen [31], Sanchez-Palencia [32], Suquet [33], Aboudi [34], Kalamkarov and Kolpakov [35], Nemat-Nasser and Hori [36], Markov and Preziosi [37], Buryachenko [38], among others. The development of these approaches had occurred along different paths, leading to interchangeable use of terminology in describing methods based on fundamentally different geometric models of material micro-structure. While the early models based on simplified micro-structural representations of heterogeneous materials were amenable to analytical treatment, the need to consider more complex micro-structures in greater detail has led to the widespread use of purely numerical or semi-analytical approaches.

Rapid progress in the development of computational technology, such as the finite-element, finite difference or finite-volume methods, has also stimulated a renewed interest in analytical techniques. Elasticity problems involving heterogeneities are also reducible to systems of algebraic equations involving coefficients in the field variable representations which satisfy the local equations exactly. To realize this goal, however, fundamental difficulties related to the manner of applying boundary conditions to a sub-volume whose response is representative of the material-at-large, must be resolved.

Pindera et al. [39] separate the approaches into three different categories: micro-structural detail-free approaches; approaches based on statistically homogeneous micro-structures and the associated Representative Volume Element (RVE) concept; approaches based on periodic micro-structures and the associated Repeating Unit Cell (RUC) concept.

2.3.1 Fundamental Micro-mechanics Problem

The fundamental problem in the micro-mechanics of heterogeneous materials is the determination of strain concentration tensor $\mathbb{A}^{(k)}$ that relate the average strain

in the $k-th$ phase of a spatially uniform heterogeneous material to the applied average or macroscopic strain [6]. It is a fourth-order tensor and depends on the concentration and phase mechanical properties and generally it is unsymmetric. In the presence of thermo-inelastic effects represented by the fourth-order tensor $\mathbb{D}^{(k)}$, the so-called localization relation has the form

$$\overline{\boldsymbol{\varepsilon}}^{(k)} = \mathbb{A}^{(k)}\overline{\boldsymbol{\varepsilon}} + \mathbb{D}^{(k)} \tag{2.1}$$

Taking the volume average of the stress fields over all phases of the heterogeneous material, the following expression ban be obtained:

$$\overline{\boldsymbol{\sigma}} = \frac{1}{V}\int_V \boldsymbol{\sigma}(x)dV = \frac{1}{V}\sum_{k=1}^{N}\int_{V_k}\boldsymbol{\sigma}^{(k)}(x)dV_k = \sum_{k=1}^{N}\mu_k\overline{\boldsymbol{\sigma}}^{(k)} \tag{2.2}$$

where $\mu_k = V_k/V$ is the volume fraction of the $k-th$ phase. Assuming a general form of the stress-strain equations for the $k-th$ phase in presence of thermal and inelastic effects

$$\boldsymbol{\sigma}^{(k)} = \boldsymbol{C}^{(k)}(\boldsymbol{\varepsilon}^{(k)} - \boldsymbol{\alpha}^{(k)}\Delta T) - 2G^{(k)}\varepsilon^{pl(k)} \tag{2.3}$$

where the inelastic response is assumed to be isotropic, and substituting the above volume-averaged into Eq. 2.2, the homogenized macroscopic equation reads

$$\overline{\boldsymbol{\sigma}} = \boldsymbol{C}^*\overline{\boldsymbol{\varepsilon}} - (\overline{\boldsymbol{\sigma}}^{th} + \overline{\boldsymbol{\sigma}}^{pl}) \tag{2.4}$$

where the homogenized stiffness matrix $\boldsymbol{C}^*$ and the corresponding thermal and plastic terms are given in terms of the sub-volume geometry, material properties and Hill's concentration matrices

$$\boldsymbol{C}^* = \sum_{k=1}^{N}\mu_k\boldsymbol{C}^{(k)}\mathbb{A}^{(k)}, \quad (\overline{\boldsymbol{\sigma}}^{th}+\overline{\boldsymbol{\sigma}}^{pl}) = -\sum_{k=1}^{N}\mu_k\left[\boldsymbol{C}^{(k)}\mathbb{D}^{(k)}-\boldsymbol{\Gamma}^{(k)}\Delta T-\overline{\boldsymbol{\sigma}}^{pl(k)}\right] \tag{2.5}$$

A completely analogous description is given based on the compliance formulation using the phase strain-stress relations and stress concentration tensors. For a two-phase composite made of fibres embedded in the matrix phase (denoted by the superscripts f and m, respectively) the expression for the macroscopic elastic

stiffness matrix simplifies to

$$\boldsymbol{C}^* = \boldsymbol{C}^m + \mu_f \big[\boldsymbol{C}^f - \boldsymbol{C}^m\big] \mathbb{A}^{(f)} \tag{2.6}$$

with the macroscopic elastic compliance matrix $\boldsymbol{S}^*$ given by

$$\boldsymbol{S}^* = \boldsymbol{S}^m + \mu_f \big[\boldsymbol{S}^f - \boldsymbol{S}^m\big] \mathbb{B}^{(f)} \tag{2.7}$$

where $\mathbb{B}^{(f)}$ is the stress concentration matrix for the fibre or inclusion phase that relates the average fibre and composite stresses in a manner analogous to $\mathbb{A}^{(f)}$.

The structure of the stiffness matrix $\boldsymbol{C}^*$ for a composite material depends both on the elastic moduli of the individual phases and on their arrangement, which dictate the number of planes of material symmetry. Isotropic composites are characterized by an infinite number of such planes, which lead to only two independent elastic constants.

Transversely isotropic composites are characterized by five independent material constants, defined with respect to the principal material coordinate system formed by the intersections of the planes of material symmetry; whereas orthotropic composites are characterized by nine, monoclinic composites by 13 and fully anisotropic composites by 21 constants. An orthotropic composite material is herein considered and its homogenized stiffness matrix has the structure

$$\boldsymbol{C}^* = \begin{bmatrix} C^*_{11} & C^*_{12} & C^*_{13} & 0 & 0 & 0 \\ C^*_{21} & C^*_{22} & C^*_{23} & 0 & 0 & 0 \\ C^*_{31} & C^*_{32} & C^*_{33} & 0 & 0 & 0 \\ 0 & 0 & 0 & C^*_{44} & 0 & 0 \\ 0 & 0 & 0 & 0 & C^*_{55} & 0 \\ 0 & 0 & 0 & 0 & 0 & C^*_{66} \end{bmatrix} \tag{2.8}$$

Transverse isotropy in the 2-3 plane, a behaviour that is exhibited by unidirectional composites reinforced along the 1 axis, is obtained by setting $C^*_{12} = C^*_{13}$, $C^*_{22} = C^*_{33}$, $C^*_{44} = 1/2 \cdot (C^*_{22} - C^*_{23})$ and $C^*_{55} = C^*_{66}$. Further reduction to isotropy results upon setting $C^*_{11} = C^*_{22} = C^*_{33}$, $C^*_{12} = C^*_{13} = C^*_{23}$ and $C^*_{44} = C^*_{55} = C^*_{66} = 1/2 \cdot (C^*_{11} - C^*_{12})$.

Transversely isotropic or orthotropic materials in coordinate systems other than the principal material coordinate system, exhibit apparent anisotropy which may

be of the monoclinic or fully anisotropic type, depending on the coordinate system orientation.

The elements of the macroscopic stiffness matrix C^*_{ij} can be also expressed in terms of the engineering moduli, which are generated by applying one non-zero average stress component at a time and measuring the resulting deformations. The nine independent engineering moduli for an orthotropic composite consist of three Young's moduli E^*_{11}, E^*_{22}, E^*_{33}, three Poisson's ratios ν^*_{12}, ν^*_{13}, ν^*_{23} and three shear moduli G^*_{12}, G^*_{13}, G^*_{23}. The elements C^*_{ij} are complicated functions of these moduli.

For transversely isotropic composites having the 2-3 plane of isotropy, the elements C^*_{ij} become simple functions of five independent engineering moduli upon use of the plane strain bulk modulus $k^*_{23} = \overline{\sigma}_{22}/2\overline{\varepsilon}_{22}$, defined for the loading $\overline{\sigma}_{22} = \overline{\sigma}_{33}$ subject to the constraint $\overline{\varepsilon}_{11} = 0$,

$$\begin{aligned} C^*_{11} &= E^*_{11} + 4k^*_{23}(\nu^*_{12})^2 \\ C^*_{12} &= 2k^*_{23}\nu^*_{12} \\ C^*_{22} &= k_{23} + G^*_{23} \\ C^*_{23} &= k_{23} - G^*_{23} \\ C^*_{66} &= G^*_{12} \end{aligned} \tag{2.9}$$

The internal structure of a transversely isotropic unidirectional composite reinforced along the 1 axis imposes the constraint $\overline{\varepsilon}_{11} = \overline{\varepsilon}^m_{11} = \overline{\varepsilon}^f_{11}$, which leads to the following two relations originally derived by Hill [6],

$$\begin{aligned} E^*_{11} &= \mu_m E_m + \mu_f E_f + \frac{4(\nu_m - \nu_f)^2}{(1/k_m - 1/k_f)^2}\Big[\Big(\frac{\mu_f}{k_f} + \frac{\mu_m}{k_m}\Big) - \frac{1}{k^*_{23}}\Big] \\ \nu^*_{12} &= \mu_m \nu_m + \mu_f \nu_f + \frac{(\nu_m - \nu_f)}{(1/k_m - 1/k_f)}\Big[\frac{1}{k^*_{23}} - \Big(\frac{\mu_f}{k_f} + \frac{\mu_m}{k_m}\Big)\Big] \end{aligned} \tag{2.10}$$

thereby reducing the number of engineering moduli that need to be calculated to completely define the material. Once the macroscopic plane strain bulk modulus k^*_{23} is determined, the axial Young's modulus E^*_{11} and the Poisson's ratio ν^*_{12} of an unidirectionally-reinforced, transversely isotropic composite are calculated from the constituent moduli and the respective volume fractions. The two remaining moduli that need to be determined are the axial and transverse shear moduli G^*_{12} and G^*_{23}.

In the case of isotropic composites, such as those produced by uniform dis-

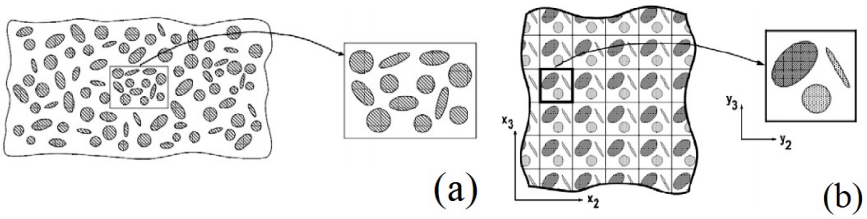

Figure 2.6: Two geometric representations of a material micro-structure: statistically homogeneous micro-structure characterized by a RVE (a) and periodic micro-structure characterized by a RUC (b) (taken from [41]).

persions of spherical particles or voids, the constitutive equations are typically decomposed into deviatoric and dilatational parts, leading to the description of the elastic behaviour in terms of the homogenized shear and bulk moduli, G^* and k^*, respectively.

2.3.2 Statistical homogeneity and periodicity

Micro-mechanical analyses of spatially uniform heterogeneous media, which explicitly account for the actual micro-structural details at the local level, may be grouped into two broad categories, each based on a different geometric representation of material micro-structure. These representations involve the concepts of statistical homogeneity and periodicity based on the concepts of Representative Volume Element (RVE) and Repeating Unit Cell (RUC), as discussed by Drago and Pindera [40] and illustrated in Figure 2.6.

Definition of Statistically homogeneous materials

Analysis of statistically homogeneous materials is based on the RVE concept. The RVE is the smallest sub-volume of the statistically homogeneous micro-structure which contains the same phase volume fractions and statistical distributions as the material-at-large; this small volume element responds in a manner identical to that of the entire assemblage under either homogeneous displacement or homogeneous traction boundary conditions

$$u_i(S) = \varepsilon^0_{ij} \cdot x_j \qquad \text{or} \qquad t_i(S) = \sigma^0_{ij} \cdot n_j \tag{2.11}$$

where $x_j \in S$ and S is the boundary of the sub-domain. These homogeneous displacements and traction boundary conditions produce uniform strains and stresses, respectively, when applied to an equivalent homogenized material, which are the same as the corresponding volume averages in the macroscopically uniform heterogeneous material. This is verified upon use of the average strain theorem

$$\begin{aligned} \overline{\varepsilon}_{ij} &= \frac{1}{V}\int_V \varepsilon_{ij} dV = \\ &= \frac{1}{V}\int_V (u_{i,j} + u_{j,i}) dV = \\ &= \frac{1}{2V}\int_S (u_i \cdot n_j + u_j \cdot n_i) dS = \varepsilon^0_{ij} \end{aligned} \tag{2.12}$$

and average stress theorem

$$\begin{aligned} \overline{\sigma}_{ij} &= \frac{1}{V}\int_V \sigma_{ij} dV = \\ &= \frac{1}{2V}\int_S (t_i \cdot x_j + t_j \cdot x_i) dS = \sigma^0_{ij} \end{aligned} \tag{2.13}$$

For a sub-volume of material as an RVE, the application of homogeneous displacement boundary conditions must produce homogeneous traction boundary conditions, and vice versa. If this boundary condition equivalence $u_i(S) = \varepsilon^0_{ij} x_j \Leftrightarrow t_i(S) = \sigma^0_{ij} n_j$ holds, then

$$\frac{1}{2}\int_V \sigma_{ij}\varepsilon_{ij} dV = \frac{1}{2}\overline{\sigma}_{ij}\overline{\varepsilon}_{ij} = \frac{1}{2}\sigma^0_{ij}\varepsilon^0_{ij} \tag{2.14}$$

and the invertibility of the homogenized stiffness and compliance tensors, $\boldsymbol{C}^* = [\boldsymbol{S}^*]^{-1}$, can be established, rendering the strain energy of the RVE independent of which set of homogeneous boundary conditions is applied. This requirement follows naturally from the definition of linearly hyperelastic homogeneous materials.

However, homogeneous traction boundary conditions applied to any sub-domain of a heterogeneous material with statistically homogeneous micro-structure do not yield homogeneous displacement boundary conditions, and vice versa. The exception is a very special micro-structure discussed in Ref [7].

To avoid this problem for a general statistically homogeneous micro-structure,

Hill [6] proposed an energetic definition for the RVE based on the equivalence of strain energies induced by homogeneous traction or displacement boundary conditions. This implies that the RVE must contain sufficiently large number of inclusions or fibres for the strain energy densities induced by either of these boundary conditions to be essentially the same

$$\frac{1}{2}\overline{\sigma}_{ij}\overline{\varepsilon}_{ij} = \frac{1}{2}\overline{\sigma}_{ij}\overline{\varepsilon}_{ij}^{\sigma^0} = \frac{1}{2}\overline{\sigma}_{ij}^{\varepsilon^0}\overline{\varepsilon}_{ij} \tag{2.15}$$

where $\overline{\varepsilon}_{ij}^{\sigma^0}$ are the average strains in a candidate material sub-volume due to homogeneous surface tractions $t_i = \sigma_{ij}^0 n_j$ applied on the boundary of this sub-volume, and $\overline{\sigma}_{ij}^{\varepsilon^0}$ are the average stresses due to the homogeneous displacements $u_i(S) = \varepsilon_{ij}^0 x_j$, where the constant components ε_{ij}^0 are adjusted such that $\varepsilon_{ij}^0 = \overline{\varepsilon}_{ij}^{\sigma^0}$. In such a case, the relations between average stresses and strains are the same for both types of boundary conditions, with the effective moduli connecting the two sets of quantities through the common strain energy density such that the invertibility condition $\boldsymbol{C}^* = [\boldsymbol{S}^*]^{-1}$ holds.

Periodic materials

In contrast, analysis of periodic materials is based on the RUC concept. The RUC is the smallest element of a periodic micro-structure which serves as the basic building block for the material through replication regardless of its content. Thus, the response of the entire array under macroscopically uniform loading is identical to that of an arbitrary RUC subjected to the same loading. This loading is specified by periodic boundary conditions related to the surface displacements and tractions,

$$u_i(x_0 + d) = u_i(x_0) + \overline{\varepsilon}_{ij} d_j \qquad \text{and} \qquad t_i(x_0 + d) + t_i(x_0) = 0 \tag{2.16}$$

where $x_0 \in S$, S is the boundary of the domain and d is the characteristic length scale of the micro-structure. Thus, the RUC's boundary deformation is not dictated by equivalent homogeneity considerations, but by the actual micro-structural content.

2.3.3 Principal Differences between RUC and RVE

The concepts of RVE and RUC had been often confused in literature, and the corresponding terminology had been used interchangeably, which continues even nowadays. Possible reasons are rooted in the popular approximations of unidirectional composites in the early 1970s by periodic arrays of circular fibres arranged in square or hexagonal arrays, which could be represented by a single RUC amenable to analysis by the finite-element method. It has only been recently that periodic boundary conditions became available in commercial finite-element codes. The RVE and RUC concepts have been re-examined in greater detail during the past 15 years. This was motivated by the work of Huet [42] aimed at the fundamental problem of characterizing macroscopic moduli of materials, such as concrete, with micro-structures large enough to make the testing of specimens, representative of a material's micro-structure, difficult or impossible. To deal with such specimens or materials, Huet introduced the concept of apparent moduli obtained from repeated micro-mechanical analyses of multiple material sub-volume realizations smaller that a RVE under different types of boundary conditions, including homogeneous displacement, traction and periodic boundary conditions. Accordingly, energetic bounds were established for such apparent moduli, which were extended by Hazanov and Huet [43] and by Hazanov and Amieur [44], for mixed boundary conditions which simulate experiments. Subsequent investigations addressed the differences in the analysis of statistically uniform and periodic materials, the effect of different boundary conditions, and the question of the number of inclusions contained in an heterogeneous sub-volume so that it responds like an RVE under appropriate boundary conditions. Hollister and Kikuch [45] appear to be the first to quantitatively address this question in the context of heterogeneous materials containing aligned cylindrical porosities arranged in a square array, and subjected to homogeneous traction, displacement and periodic boundary conditions. Convergence of selected effective stiffness matrix elements of sub-volumes, subjected to homogeneous boundary conditions, to the corresponding elements obtained under periodic boundary conditions, was demonstrated with large number of unit cells contained within the sub-volume. Subsequently Pecullan et al. [46] investigated the periodic unidirectional composites with different inclusion/matrix stiffness moduli ratios. Homogeneous displacement boundary conditions produced apparent moduli closer to the corresponding moduli under periodic boundary conditions for materials

with high inclusion/matrix stiffness moduli ratios, whereas homogeneous traction boundary conditions produced better moduli estimates for low inclusion/matrix stiffness moduli ratio. Povirk [47] determined the size of a periodic unit cell with a micro-structure statistically similar to a more complex, random two-phase micro-structure, showing that as many as 12 inclusions were required to obtain a comparable effective transverse Young's modulus.

An extensive finite-element study involving periodic composites with hexagonal cylindrical inclusion/porosity arrays in a state of plane strain was subsequently conducted by Jiang et al. [48]. A comprehensive investigation of the convergence of the complete set of elastic moduli of unidirectional composites to the periodic values with the number of fibres contained within a candidate sub-volume was conducted by Drago and Pindera [40]. Information on the deformation of investigated sub-volumes resulting from different boundary conditions was also provided, which is important in plastic strain localization and bifurcation problems [49].

2.3.4 Classical approaches for material homogenization

The classical approaches include models that contain either no direct information on the actual distribution of phases, or explicitly account for their interaction. Such approaches can be called micro-structural detail-free estimates [39]. These approaches are analytical and lead to closed-form expressions for the stress or strain concentration tensors (which may be explicit or implicit). Included in the category of classical approaches is the only analytical RVE-based model, which has been the mainstay of the micro-mechanics community since it was first proposed in the 1960s by Hashin [5, 7], that is the composite sphere assemblage model for isotropic composites, or its composite cylinder counterpart for unidirectionally-reinforced transversely isotropic composites. Even though this model reduces to the determination of the stress field in a single composite sphere or cylinder subjected to homogeneous tractions or displacements, its basis is a certain geometric representation of the material micro-structure which renders a single composite cylinder or sphere an RVE under certain loading conditions.

Micro-structural detail-free estimates Micro-structural detail-free estimates typically lead to homogenized isotropic or transversely isotropic moduli. Isotropic composites include uniform dispersions of spherical inclusions or voids, while

unidirectionally-reinforced composites with statistically uniform reinforcement distribution in the plane transverse to the reinforcement, exhibit transversely isotropic behaviour.

Reuss and Voigt estimates For a uniform dispersion of isotropic phases, Voigt [50] and Reuss [51] proposed to estimate the resulting isotropic homogenized moduli by assuming the following strain and stress partitioning. For Voigt [50], the strain concentration tensors for the matrix and inclusion phases are taken as unity. This assumption yields the following expressions for the homogenized bulk and shear moduli

$$k_V^* = \mu_i k_i + \mu_m k_m \qquad \text{and} \qquad G_V^* = \mu_i G_i + \mu_m G_m \tag{2.17}$$

According to Reuss [51], the stress concentration tensors for both phases are taken as unity. This yields the following homogenized bulk and shear moduli

$$\frac{1}{k_R^*} = \frac{\mu_i}{k_i} + \frac{\mu_m}{k_m} \qquad \text{and} \qquad \frac{1}{G_R^*} = \frac{\mu_i}{G_i} + \frac{\mu_m}{G_m} \tag{2.18}$$

The differences between Voigt and Reuss estimates are large when the phase moduli differ by a factor greater than two, producing poor estimates in the case of modern particulate composites. In the case of single metallic grains with relatively weak material orthotropy in the principal material coordinate system, the orientational variation of single grain moduli is not large, enabling reasonable estimates of the homogenized moduli for polycrystalline metals. In addition to applications involving predictions of homogenized moduli of metals, the Reuss and Voigt estimates have been employed recently to calculate bounds on micro-mechanics based damage evolution parameters in cracked solids [52]. Selective application of the Reuss and Voigt strain and stress partitioning assumptions to unidirectional composites, produces the so-called rule-of-mixtures formulas and their derivatives. While an accurate estimate of Young's modulus along the fibre direction is obtained in light of the correct kinematic constraint, the remaining moduli are generally quite inaccurate when the fibre/matrix modulus mismatch is large for realistic fibre volume fractions. When applied to lamellar materials, however, these assumptions produce exact expressions for the effective elastic moduli [53].

Self-consistent and generalized self-consistent schemes More accurate estimates of homogenized moduli of two-phase particulate or unidirectionally-reinforced materials are obtained from the self-consistent scheme, originally developed for estimating macroscopic moduli of polycrystalline metals by Hershey [54] and Kroner [55]. The self-consistent scheme is a device used to calculate strain or stress concentration tensors for the inclusion phase(s).

In the self-consistent scheme's original adaptation to polycrystalline metals, the concentration tensor elements are determined by embedding a single ellipsoidal or cylindrical inclusion, representative of a grain with a specific crystallographic orientation, in the equivalent homogenized polycrystal loaded at infinity by a uniform (macroscopic or average) strain. The solution to this problem has been obtained by Eshelby [4] who showed that the strain or stress field within the ellipsoidal inclusion is uniform. Averaging over all possible orientations of a single ellipsoidal grain, representative of the orientations of all grains, produces the self-consistent expression for the macroscopic moduli of a polycrystalline metal.

Hill [56] adapted the self-consistent scheme to unidirectional composites by taking the average strain in a single ellipsoidal inclusion obtained from the solution to the Eshelby problem as the average strain over all the inclusions. As discussed extensively by Christensen [31], this assumption leads to incompatible geometric representations of the same material, producing erroneous results in certain cases. Nonetheless, the self-consistent scheme continues to be used for estimating homogenized moduli of heterogeneous materials, including functionally graded materials.

In the case of a uniform dispersion of spheres, calculation of the stress concentration matrix elements under dilatational and pure shear loading produces coupled equations for the macroscopic bulk and shear moduli of the form [56]

$$\begin{aligned} \frac{1}{k^*} &= \frac{1}{k_m} + \left(1 - \frac{k_i}{k_m}\right) \frac{\mu_i}{\left[k^* + \alpha(k_i - k^*)\right]} \quad \text{and} \\ \frac{1}{G^*} &= \frac{1}{G_m} + \left(1 - \frac{G_i}{G_m}\right) \frac{\mu_i}{\left[G^* + \beta(G_i - G^*)\right]} \end{aligned} \tag{2.19}$$

where

$$\alpha = \frac{1 + \nu^*}{3(1 - \nu^*)} \qquad \text{and} \qquad \beta = \frac{6}{5}\left(\frac{k^* + 2G^*}{3k^* + 4G^*}\right)$$

In the case of unidirectionally-reinforced transversely isotropic composites,

the plane strain bulk and transverse shear moduli are also coupled through the concentration factors, yielding two coupled equations in k_{23}^* and G_{23}^*. In contrast, the axial shear modulus is calculated directly from the knowledge of the constituent shear moduli, of the fibre volume fraction and of the concentration factor for axial shear loading that involves only the homogenized axial shear modulus G_{12}^*. The expressions for the axial Young's modulus and the Poisson's ratio then follow from Hill's relations (Eq. 2.10).

The self-consistent scheme does not account explicitly for the presence of the matrix phase, precluding straightforward estimation of the elastic-plastic response of metal matrix composites. The above limitations lead to well-known anomalies of the estimates. For instance, in the case of uniform dispersions of spheres in an incompressible matrix, the expressions for the homogenized shear and bulk moduli reduce as follows in the case of spherical porosities

$$G_i = k_i = 0, \qquad , \qquad G^* = \frac{3(1-2\mu_i)}{3-\mu_i} G_m$$
$$k^* = \frac{4(1-\mu_i)(1-\mu_i)}{(3-\mu_i)\mu_i} G_m$$

which are not valid in the range $0.5 \leq \mu_i \leq 1$. Similarly, for rigid inclusions, i.e. with $G_i = k_i = \infty$, the two homogenized moduli reduce to

$$G^* = \frac{G_m}{1-(5/2)\mu_i} \quad \text{for} \quad 0 \leq \mu_i \leq 2/5 \quad \text{and}$$
$$k^* = \infty \quad \text{for all} \quad \mu_i = \infty \quad \text{for} \quad 2/5 \leq \mu_i \leq 1$$

which clearly is physically inadmissible.

Two approaches have been proposed to address this problem, namely the Mori-Tanaka scheme and the three-phase model discussed below.

Mori-Tanaka scheme Mori and Tanaka [57] provided a different interpretation of the embedding approach based on the average stress in the matrix phase determined from the solution of an auxiliary Eshelby-type problem for a two-phase composite with isotropic or transversely isotropic macroscopic moduli. In this approach, the strain concentration tensor $\mathbb{A}^{(f)}$ in Eq. 2.1 is calculated by first embedding a single inclusion/fibre in the matrix phase, and then by applying far-field conditions that correspond to the macroscopic average matrix strain for

an infinite homogeneous body. This intermediate step produces the concentration tensor $\mathbb{A}^{(f)}_{m\infty}$ which relates the average inclusion/fibre strain to the average matrix strain, i.e. $\overline{\boldsymbol{\varepsilon}}_f = \mathbb{A}^{(f)}_{m\infty}\overline{\boldsymbol{\varepsilon}}_m$. Since for a two-phase composite

$$\overline{\boldsymbol{\varepsilon}} = \mu_f\overline{\boldsymbol{\varepsilon}}_f + \mu_m\overline{\boldsymbol{\varepsilon}}_m \Rightarrow \overline{\boldsymbol{\varepsilon}} = [\mu_f\mathbb{A}^{(f)}_{m\infty} + \mu_m\mathbb{I}]\overline{\boldsymbol{\varepsilon}}_m \tag{2.20}$$

the strain concentration tensor for the inclusion/fibre phase becomes

$$\mathbb{A}^{(f)} = \mathbb{A}^{(f)}_{m\infty}[\mu_f\mathbb{A}^{(f)}_{m\infty} + \mu_m\mathbb{I}]^{-1} \tag{2.21}$$

leading to the macroscopic elastic stiffness matrix

$$\boldsymbol{C}^* = \boldsymbol{C}^{(m)} + \mu_f(\boldsymbol{C}^{(f)} - \boldsymbol{C}^{(m)})\mathbb{A}^{(f)}_{m\infty}[\mu_f\mathbb{A}^{(f)}_{m\infty} + \mu_m\mathbb{I}]^{-1} \tag{2.22}$$

Thus, the presence of the matrix phase is explicitly taken into account, but only in an average sense. Therefore in the presence of matrix plasticity, initial yielding is overestimated. In the case of a transversely isotropic, unidirectionally-reinforced composite containing a von Mises matrix, this direction is given by Pindera and Aboudi [58], with

$$\overline{\boldsymbol{\sigma}} = [1\,\lambda\,\lambda\,0\,0\,0]\sigma_0 \qquad \text{with} \qquad \lambda = \frac{B^m_{21} - B^m_{11}}{2B^m_{12} - (B^m_{22} + B^m_{23})} \tag{2.23}$$

where B^m_{ij} are the elements of the stress concentration tensor $\mathbb{B}^m_{ij}$ for the matrix phase. A consequence of the above result is that the subsequent elastic-plastic response, whose extent depends on the proximity of the loading path to the above loading direction, is also overestimated. In the extreme case of applied load aligned with the above direction, no yielding occurs and the response remains elastic regardless of the applied stress magnitude.

An additional problem with the Mori-Tanaka scheme is the loss of symmetry of homogenized stiffness matrix under certain circumstances, as discussed by Ferrari [59]. This problem has been addressed through the effective field method approach, recently summarized by Kanaun and Jeulin [60], which employs the constant strain in the inclusion assumption within a statistical framework for randomly distributed families of inclusions.

Despite the above limitations, the Mori-Tanaka scheme continues to be employed by a number of researchers due to the simplicity of the calculation of the elastic

response of different classes of heterogeneous materials. These materials include unidirectional as well as particulate composites reinforced by inclusions that may be approximated by cylinders of elliptical or circular cross-sections, or ellipsoidal inclusions. Aligned, biased or random arrangements of particulate and continuous reinforcement can be modelled approximately through appropriate orientational averaging. In addition, the analysis of local stress fields based on the assumption of average matrix stress, facilitates incorporation of inelastic effects in order to enable modelling of metal and polymeric matrix composites, as well as ceramic matrix composites at elevated temperatures, where creep or visco-plastic effects become important. The contributions of Weng and coworkers in extending the Mori-Tanaka scheme to the inelastic analysis of different classes of composites have paved the way for the continuing work in this area, [61–65]. Extensions of this mean-field approach have evolved leading to the capability to deal with visco-elastic, elastic-plastic and visco-plastic applications; in this context Doghri and Tinel [66] and Mercier and Molinari [67] studied metal matrix composites, while Shu and Huang [68] determined the dynamic moduli of advanced asphalt/concrete mixtures and Bohm and Nogales [69] considered the thermal conductivity of composites reinforced with different particle sizes.

A general theoretical framework based on uniform phase plastic strain fields was proposed by Dvork [70]. The capabilities and limitations of this simplification have been discussed recently by Chaboche et al. [71].

Three-phase model Alternatively, Christensen and Lo [10] proposed a different interpretation of the generalized self-consistent scheme limited to elastic phases, called the three-phase model. In this model an energy approach was used to derive expressions for the effective moduli of a composite fibre/matrix inclusion embedded in the equivalent homogenized medium by solving the related elasticity problem. The homogenization was achieved through the use of Eshelby formula for strain energy in a medium with a homogeneous material with an embedded inclusion. Under homogeneous traction boundary conditions $t_i^0 = \sigma_{ij}^0 n_j$ at infinity, the strain energy can be written as:

$$U = U_0 + \frac{1}{2}\int_{S_i}(t_i u_i^0 - t_i^0 u_i)dS \tag{2.24}$$

where U_0 is the strain energy induced by t_i^0 in a homogeneous matrix material, S_i is the surface of the inclusion, u_i^0 are the resulting displacement components, and t_i and u_i are the corresponding traction and displacement components in the presence of the inclusion. Setting $U = U_0$ provides the homogenization condition which allows to relate the internal stress and displacement fields within the composite inclusion embedded in a homogenous matrix (i.e., surrounding homogenized composite) to the far-field homogeneous tractions. A similar homogenization condition is obtained in presence of homogeneous displacement boundary conditions. Under axisymmetric loading, the homogenized moduli obtained from the three-phase model are the same as those of a single composite cylinder or sphere. The remaining shear modulus is obtained by solving a boundary-value problem based on the three-phase model geometry wherein application of the Eshelby formula results in a quadratic equation for the unknown modulus.

Multiparticle models The classical self-consistent scheme and its derivatives produce homogenized elastic moduli of isotropic or transversely isotropic composites in the absence of detailed geometrical information on the actual distribution of the inclusion phase wherein local phase interaction is explicitly taken into account. Approximate schemes for incorporating local fibre interactions include the poly-inclusion, multi-inclusion or mean-field methods, [59, 60, 72–74].

Statistically homogeneous materials

Composite spherical/cylindrical assemblage model The composite spherical assemblage (CSA) and composite cylinder assemblage (CCA) models, proposed by Hashin [5] and Hashin and Rosen [7], are the earliest geometric RVE-based models that provide closed-form expressions for one of the two, and four of the five, effective moduli required to characterize the elastic response of isotropic and unidirectionally-reinforced composites, respectively. Within the models' framework, the composite is viewed as an assemblage of inclusion/matrix spheres or fibre/matrix cylinders of various sizes but fixed radii ratios.

This allows the entire space to be completely filled by such composite inclusions while maintaining a fixed inclusion volume content. For axisymmetric and axial shear loading, the response of the entire assemblage under homogeneous traction or displacement boundary conditions is equivalent to the response of a single

composite sphere or cylinder which acts as the RVE. Specifically for this loading type, homogeneous displacement boundary conditions produce homogeneous traction distributions, and vice versa. Thus exact expressions are obtained for the homogenized bulk modulus, k_{23}^*, of an isotropic dispersion of spheres, and its plane strain counterpart for unidirectionally-reinforced composites, given by

$$k_{23}^* =_m + \frac{G_m}{3} + \frac{\mu_f}{1/[k_f - k_m + (G_f - G_m)/3] + \mu_m/(k_m + 4/3G_m)} \tag{2.25}$$

which leads to the axial Young's modulus and Poisson's ratio upon use of the above expression in Hill's universal relations (Eq. 2.10). Similarly, the homogenized shear modulus due to shearing along the fibre direction is obtained in the form

$$G_{12}^* = G_m + \frac{(1+\mu_f)G_f + \mu_m \cdot G_m}{\mu_m \cdot G_f + (1+\mu_f)G_m} \tag{2.26}$$

Under transverse normal and shear loading, however, the homogeneous boundary condition equivalence no longer holds, and a single sphere and cylinder composite region does not represent the RVE leading to energetic bounds only on the corresponding homogenized moduli. In particular, the upper and lower bounds on the transverse shear modulus G_{23}^* are

$$\begin{aligned} G_{23}^{*(+)} &= G_m + \frac{\mu_f(1+\beta_m)\cdot G_m}{\rho - \mu_f[1 + 3\beta_m^2\mu_m^2/(1+\alpha\mu_f^2)]} \\ G_{23}^{*(-)} &= G_m + \frac{\mu_f}{1/(G_f - G_m) + \mu_m(k_m + 2G_m)/[2G_m(k_m + G_m)]} \end{aligned} \tag{2.27}$$

where

$$\alpha = \frac{\beta_m - \beta_f(\frac{G_f}{G_m})}{1 + \beta_f(\frac{G_f}{G_m})}, \quad \rho = \frac{\beta_m + (\frac{G_f}{G_m})}{\frac{G_f}{G_m} - 1}, \quad \beta_m = \frac{1}{3 - 4\nu_m} \quad \text{and} \quad \beta_f = \frac{k_f}{k_f + 2G_f}$$

Unfortunately, there are no other simple geometric models readily amenable to analytical treatment that satisfy the homogeneous boundary condition equivalence under all loading conditions.

In addition in order to prove reasonably accurate estimates of elastic moduli for different types of isotropic and transversely isotropic composites, the single non-interacting composite cylinder/sphere models proved efficient solutions for several technologically important problems involving metal matrix composites.

The fibre volume fraction in this class of composites is generally not too high, and the fibre/matrix modulus mismatch ratio does not exceed six, rendering the assumption of non-interacting fibres reasonable. Mulhern et al. [75] were perhaps the first to develop an analytical solution for an elastic cylinder coated by a non-hardening Tresca-type matrix subjected to axial deformation in order to simulate the response of a unidirectional composite loaded in the fibre direction. Chu and Hashin [76] subsequently developed a solution for a composite sphere with a vonMises non-hardening matrix loaded by external pressure.

Multiple concentric cylinder model Pindera and coworkers generalized the analytical solution for a single composite cylinder to arbitrarily layered composite cylinders subjected to axisymmetric loading by a combination of a uniform temperature change, axial deformation and externally applied transverse pressure, in the presence of elastic-plastic, strain-hardening matrix layers [77, 78]. The displacement-based solution was obtained in closed form in cylindrical coordinates for isotropic, transversely isotropic and orthotropic elastic fibres, and isotropic elastic-plastic matrix layers. For an orthotropic fibre shell, the radial displacement is obtained in the form [79],

$$u_r = A_1 r^{\lambda} + A_2 r^{-\lambda} + \frac{C_{\theta x} - C_{rx}}{C_{rr} - C_{\theta\theta}} r\varepsilon^0_{11} + \sum_{i=x,\theta,r} \frac{C_{ri} - C_{\theta i}}{C_{rr} - C_{\theta\theta}} r\alpha_i (T - T_0) \tag{2.28}$$

where $\lambda = \sqrt{C_{\theta\theta}/C_{rr}}$, while for an isotropic, elastic-plastic matrix shell the corresponding radial displacement is

$$\begin{aligned} u_r = {} & A_1 r + A_2 r^{-1} + \frac{1}{2}\int_{r_{k-1}}^{r} \sum_{i=x,\theta,r} \frac{C_{ri} + C_{\theta i}}{C_{rr}} \varepsilon^p_{ii}(r') r' dr' + \\ & + \frac{r}{2}\int_{r_{k-1}}^{r} \sum_{i=x,\theta,r} \frac{C_{ri} - C_{\theta i}}{C_{rr}} \varepsilon^p_{ii}(r') \frac{dr'}{r'} + \\ & + \frac{1}{2} \sum_{i=x,\theta,r} \frac{C_{ri}}{C_{rr}} \varepsilon^p_{ii}(r_{k-1}) \Big(\frac{r^2_{k-1}}{r^2} - 1 \Big) \end{aligned} \tag{2.29}$$

where $r_{k-1} \le r \le r_k$, with the remaining displacement components given by u_θ, $u_z = \varepsilon^0_{zz} z$.

The solution for the unknown coefficients A^k_1, A^k_2 is obtained by constructing a local stiffness matrix for the $k-th$ shell that relates the radial tractions $-\sigma^-_{rr}$ and

σ_{rr}^{+} at the shell's inner and outer radii to the corresponding radial displacement components u_r^- and u_r^+,

$$\begin{bmatrix} -\sigma_{rr}^{-} \\ \sigma_{rr}^{+} \end{bmatrix}^k = \begin{bmatrix} k_{11} & k_{12} \\ k_{21} & k_{22} \end{bmatrix}^k \begin{bmatrix} u_r^- \\ u_r^+ \end{bmatrix} + \begin{bmatrix} k_{13} \\ k_{23} \end{bmatrix}^k \varepsilon_{zz}^0 + \begin{bmatrix} f_1 \\ f_2 \end{bmatrix}^k (T - T_0) + \begin{bmatrix} g_1 \\ g_2 \end{bmatrix}^k \tag{2.30}$$

where explicit expressions for the elements of the mechanical, thermal and inelastic matrix elements have been provided in closed form. Systematic fulfilment of the interfacial traction and displacement continuity conditions at each interface, together with the boundary conditions, produces the global system of equations for the common interfacial displacements $u_r^-|_{k-1} = u_r^+|_k = u_k^*$

$$\boldsymbol{K}\boldsymbol{U}^* = \Delta\boldsymbol{k}\varepsilon_{zz}^0 + \boldsymbol{f}(T - T_0) + \boldsymbol{g} \tag{2.31}$$

Solution of these equations establishes the localizations relations (Eq. 2.1) required to generate the macroscopic response under uniform axial extension, external pressure in the plane transverse to the fibre direction, and a uniform temperature change. Extension of the above solution approach to an arbitrarily layered concentric sphere subjected to axisymmetric loading is straightforward.

Extension of the solution methodology to axial shear was provided by Williams and Pindera [80], where numerical evidence indicated that under this type of loading a single composite cylinder responded in nearly identical manner in the elastic-plastic domain under homogeneous displacement and traction boundary conditions.

2.3.5 Periodic materials

The intrinsic difficulty of simultaneously satisfy homogeneous displacement and traction boundary conditions, necessary in fulfilling the RVE requirement for sub-volumes with arbitrary statistically homogeneous micro-structures, has contributed with great emphasis on the development of methods for the analysis of periodic materials during the past 20 years. The early work on periodic materials conducted in the 1960s and 1970s was focused on the analysis of simple unit cells (RUC) containing single circular fibres arranged in square (or rectangular) and hexagonal arrays by using elasticity-based analytical and numerical techniques. This work was motivated by the lack of RVE-based approaches for detailed modelling of

realistic micro-structures with fibre interactions explicitly taken into account. The analyses were restricted to specific loading directions intended to generate specific elastic moduli and subsequent inelastic response, under simplified boundary conditions which often reflected the unit cell's material symmetry, but not necessarily periodicity.

In response to these limitations, approximate semi-analytical techniques were developed based on the explicit use of periodic boundary conditions, which provided the capability to simulate the elastic and inelastic response of periodic heterogeneous materials with arbitrary micro-structures under combined loading. The generalized method of cells developed by Paley and Aboudi [81] is perhaps the best known model in this category. The availability of closed-form expressions, for the determination of Hill's concentration matrices in both the elastic and inelastic domains, rendered this model well suited for use in structural analysis problems within an emerging multi-scale framework. Subsequent reformulation by Pindera and Bednarcyk [41] has increased its efficiency by an order of magnitude.

A systematic approach to the calculation of macroscopic elastic moduli and subsequent inelastic response of periodic materials was provided by the mathematical homogenization theory, which had emerged as a powerful tool in the analysis of this class of materials [33, 76]. Nonetheless, the kernel of the technique involves solution of the unit cell boundary-value problem which is typically tackled using the finite-element approach. As an alternative to the variational-based solution approaches for periodic unit cell problems, approximate semi-analytical and analytical techniques were developed based on elements of the homogenization theory. One of such techniques is the so-called higher-order theory for periodic multiphase materials, developed by Aboudi et al. [82]. The recent generalization of this theory through the incorporation of quadrilateral sub-volume discretization capability by Gattu [83] and Khatam and Pindera [84] has rendered this technique competitive with the finite-element based analyses of unit cells with complex micro-structures. Another recently developed technique is the locally-exact homogenization theory, [40], which is based on an exact elasticity solution of the inclusion or interior problem, and an approximate solution of the unit cell or exterior problem. The exterior problem involves fulfilment of the periodic boundary conditions using a new variational approach which leads to very fast convergence of the its commonly used series solution.

Homogenization theory

By considering a linearly elastic body, B, which consists of heterogeneous materials, let D and d be the macro- and micro-length scale; D is regarded as the dimension of a sample of the heterogeneous material while d is the size of typical micro constituents of this sample. The length scale of B is orders of magnitude greater than that of macro-length scale. A relative length scale parameter, $\epsilon = d/D \ll 1$, can be defined.

Let $\boldsymbol{C}^\epsilon = \boldsymbol{C}^\epsilon(\boldsymbol{X})$ be the variable elasticity tensor of B, where $\boldsymbol{X}$ denotes a continuum point in B. The superscript, ϵ emphasizes that the variation of this elasticity tensor is measured at the relative scale of ϵ. Displacement, strain and stress fields of B are denoted by $\boldsymbol{u}^\epsilon = \boldsymbol{u}^\epsilon(\boldsymbol{X})$, $\boldsymbol{\varepsilon}^\epsilon = \boldsymbol{\varepsilon}^\epsilon(\boldsymbol{X})$ and $\boldsymbol{\sigma}^\epsilon = \boldsymbol{\sigma}^\epsilon(\boldsymbol{X})$, respectively. These fields satisfy

$$\begin{aligned} \boldsymbol{\varepsilon}^\epsilon(\boldsymbol{X}) &= sym\{\nabla \otimes \boldsymbol{u}^\epsilon(\boldsymbol{X})\} \\ \nabla \cdot \boldsymbol{\sigma}^\epsilon(\boldsymbol{X}) &= 0 \\ \boldsymbol{\sigma}^\epsilon(\boldsymbol{X}) &= \boldsymbol{C}^\epsilon(\boldsymbol{X}) : \boldsymbol{\varepsilon}^\epsilon(\boldsymbol{X}) \end{aligned} \tag{2.32}$$

where sym stands for the symmetric part, i.e. $sym\{(\cdot)_{ij}\} = ((\cdot)_{ij} + (\cdot)_{ji})/2$. When B is subjected to surface displacements, $\boldsymbol{u} = \boldsymbol{u}^0$ on ∂B, these three sets of the field equations yield the following boundary-value problem for $\boldsymbol{u}^\epsilon$:

$$\begin{aligned} &\nabla \cdot (\boldsymbol{C}^\epsilon(\boldsymbol{X}) : (\nabla \otimes \boldsymbol{u}^\epsilon(\boldsymbol{X}))) = 0 \qquad \text{in } B, \\ &\boldsymbol{u}^\epsilon(\boldsymbol{X}) = \boldsymbol{u}^0(\boldsymbol{X}) \qquad \text{on } \partial B \end{aligned} \tag{2.33}$$

The homogenization theory considers the governing equations in Eq. 2.33 for $\boldsymbol{u}^\epsilon$, and in order to express the changes in $\boldsymbol{C}^\epsilon$ within a micro-length scale, it replaces this elasticity tensor field $\boldsymbol{C}^\epsilon$ by

$$\boldsymbol{C}^\epsilon(\boldsymbol{X}) \approx \boldsymbol{C}(\boldsymbol{x}) \tag{2.34}$$

with $\boldsymbol{x} = \epsilon^{-1}\boldsymbol{X}$, while ϵ is the ratio between the macro- and micro-length scales. Usually, it is assumed that $\boldsymbol{C}(\boldsymbol{x})$ is spatially periodic, and a periodic structure is used as a model of the micro-structure (Fig. 2.7). The dimensions of the unit cell, U, of the periodic structure are of the same order as the macro-length scale, D.

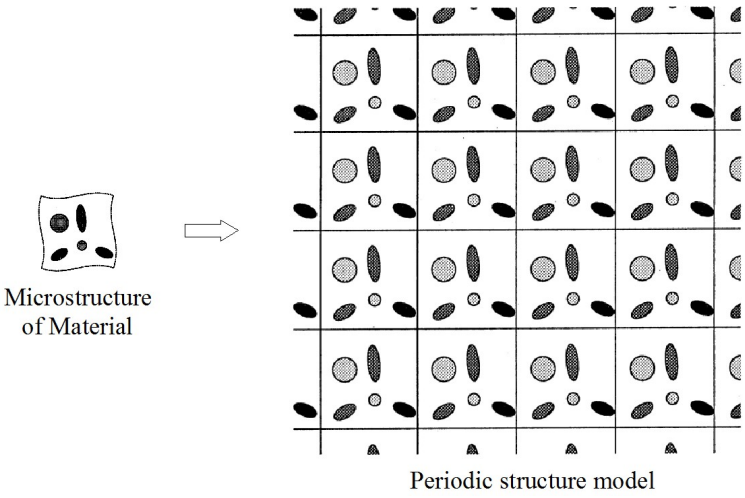

Figure 2.7: Periodic structure as model of material with micro-structure [85].

2.3.6 Singular perturbation applied to the homogenization theory

For a periodic $\boldsymbol{C}$, the homogenization theory considers the following multi-scale or singular perturbation representation of $\boldsymbol{u}^\epsilon$:

$$\boldsymbol{u}^\epsilon(\boldsymbol{X}) \approx \sum_{n=0} \epsilon^n \boldsymbol{u}^n(\boldsymbol{X}, \boldsymbol{x}) \tag{2.35}$$

where each $\boldsymbol{u}^n$ has the same periodicity as $\boldsymbol{C}$ with respect to $\boldsymbol{x}$. Since ∇ is now replaced by $\nabla_{\boldsymbol{X}} + \epsilon^{-1}\nabla_{\boldsymbol{x}}$, the substitution of Eq. 2.35 into the governing equations 2.33 yields

$$\begin{aligned}
&\epsilon^{-2}\big\{\nabla_{\boldsymbol{x}} \cdot \big[\boldsymbol{C}(\boldsymbol{x}) : (\nabla_{\boldsymbol{x}} \otimes \boldsymbol{u}^0(\boldsymbol{X}, \boldsymbol{x}))\big]\big\} + \\
&\quad + \epsilon^{-1}\big\{\nabla_{\boldsymbol{X}} \cdot \big[\boldsymbol{C}(\boldsymbol{x}) : (\nabla_{\boldsymbol{x}} \otimes \boldsymbol{u}^0(\boldsymbol{X}, \boldsymbol{x}))\big] + \\
&\quad + \nabla_{\boldsymbol{X}} \cdot \boldsymbol{C}(\boldsymbol{x}) : (\nabla_{\boldsymbol{X}} \otimes \boldsymbol{u}^0(\boldsymbol{X}, \boldsymbol{x}) + \nabla_{\boldsymbol{X}} \otimes \boldsymbol{u}^1(\boldsymbol{X}, \boldsymbol{x}))\big\} + \\
&\quad + \sum_{n=0} + \epsilon^n\big\{\nabla_{\boldsymbol{X}} \cdot \big[\boldsymbol{C}(\boldsymbol{x}) : (\nabla_{\boldsymbol{X}} \otimes \boldsymbol{u}^n(\boldsymbol{X}, \boldsymbol{x}) + \\
&\quad + \nabla_{\boldsymbol{x}} \otimes \boldsymbol{u}^{n+1}(\boldsymbol{X}, \boldsymbol{x}))\big] + \\
&\quad + \nabla_{\boldsymbol{X}} \cdot \boldsymbol{C}(\boldsymbol{x}) : (\nabla_{\boldsymbol{X}} \otimes \boldsymbol{u}^{n+1}(\boldsymbol{X}, \boldsymbol{x}) + \nabla_{\boldsymbol{x}} \otimes \boldsymbol{u}^{n+2}(\boldsymbol{X}, \boldsymbol{x}))\big\} = 0
\end{aligned} \tag{2.36}$$

To solve Eq. 2.36 up to $O(\epsilon^0)$, the homogenization theory first assumes that $\boldsymbol{u}^0$ is a function of $\boldsymbol{X}$ only and that $\boldsymbol{u}^1$ admits the representation $\boldsymbol{u}^1(\boldsymbol{X},\boldsymbol{x}) = \boldsymbol{\chi}^1(\boldsymbol{x}) : (\nabla_{\boldsymbol{X}} \otimes \boldsymbol{u}^0(\boldsymbol{X}))$, where a third-order tensor $\boldsymbol{\chi}^1$ is periodic with respect to $\boldsymbol{x}$. Then, terms of $O(\epsilon^1)$ vanish, and terms of $O(\epsilon^{-2})$ become $\big\{\nabla_{\boldsymbol{x}} \cdot \big[\boldsymbol{C}(\boldsymbol{x}) : (\nabla_{\boldsymbol{x}} \otimes \boldsymbol{\chi}^1(\boldsymbol{x}) + \mathcal{I})\big]\big\} : (\nabla_{\boldsymbol{x}} \otimes \boldsymbol{u}^0(\boldsymbol{X}))$ where $\mathcal{I}$ is the symmetric fourth-order identity tensor. In order for these terms to vanish identically for both $\boldsymbol{X}$ and $\boldsymbol{x}$, $\boldsymbol{\chi}^1$ must satisfy the following governing equation with the periodic boundary conditions

$$\nabla_{\boldsymbol{x}} \cdot \big[\boldsymbol{C}(\boldsymbol{x}) : (\nabla_{\boldsymbol{x}} \otimes \boldsymbol{\chi}^1(\boldsymbol{x}) + \mathcal{I})\big] = 0 \tag{2.37}$$

It is seen that $\boldsymbol{\chi}^1 : \nabla_{\boldsymbol{x}} \otimes \boldsymbol{u}^0$ is a microscopic displacement field in the presence of the stress field, $\boldsymbol{C} : (\nabla_{\boldsymbol{X}} \otimes \boldsymbol{u}^0)$. Since this stress field does not satisfy equilibrium, oscillating micro-strains and associated stresses are produced. In other words, $\boldsymbol{\chi}^1$ corresponds to the micro-scale response which accommodates the strain field $sym\{\nabla_{\boldsymbol{X}} \otimes \boldsymbol{u}^0\}$ which produces non-equilibrating stresses. Note that $\boldsymbol{\chi}^1$ satisfies the symmetry, $\chi^1_{ikl} = \chi^1_{ilk}$.

Once $\boldsymbol{\chi}^1$ is determined, terms of $O(\epsilon^0)$ in Eq. 2.36 become

$$\begin{aligned} \nabla_{\boldsymbol{x}} \cdot \big\{\boldsymbol{C}(\boldsymbol{x}) : \big[(\nabla_{\boldsymbol{x}} \otimes \boldsymbol{\chi}^1(\boldsymbol{x}) + \mathcal{I}) : (\nabla_{\boldsymbol{X}} \otimes \boldsymbol{u}^0(\boldsymbol{X}))\big]\big\} + \\ + \nabla_{\boldsymbol{x}} \cdot \big\{\boldsymbol{C}(\boldsymbol{x}) : \big[(\nabla_{\boldsymbol{X}} \otimes \boldsymbol{u}^1(\boldsymbol{X},\boldsymbol{x}) + \nabla_{\boldsymbol{x}} \otimes \boldsymbol{u}^2(\boldsymbol{X},\boldsymbol{x}))\big]\big\} \end{aligned} \tag{2.38}$$

If the volume average over the unit cell is considered, the terms varying with $\boldsymbol{x}$ drop out, and the governing equation for $\boldsymbol{u}^0$ is obtained as

$$\nabla_{\boldsymbol{X}} \cdot (\overline{\boldsymbol{C}}^0 : (\nabla_{\boldsymbol{X}} \otimes \boldsymbol{u}^0(\boldsymbol{X}))) = 0 \quad \text{in } B \tag{2.39}$$

with

$$\overline{\boldsymbol{C}}^0 = \frac{1}{U} \int_U \boldsymbol{C}(\boldsymbol{x}) : (\nabla \otimes \boldsymbol{\chi}^1(\boldsymbol{x}) + \mathcal{I}) dV \tag{2.40}$$

Therefore, a boundary-value problem for $\boldsymbol{u}^0$ is obtained if $\boldsymbol{u}^0 \approx \boldsymbol{u}^\epsilon$ is assumed and $\boldsymbol{u}^1 = \boldsymbol{u}^0$ is prescribed as the boundary conditions on ∂B.

Since the leading term of the perturbation expansion, $\boldsymbol{u}^0$, is a function of only $\boldsymbol{X}$, it corresponds to the macro-displacement in the average-field theory. The next term, $\epsilon \boldsymbol{u}^1$, contributes little, as it is of the order of $O(\epsilon^1)$. Indeed, the volume average of $\boldsymbol{u}^1 = \boldsymbol{\chi}^1 : (\nabla_{\boldsymbol{X}} \otimes \boldsymbol{u}^0)$ taken over U vanishes since $\boldsymbol{\chi}^1$ is periodic.

A singular perturbation expansion similar to Eq. 2.35 is applicable to the strain and stress fields, i.e., $\{\boldsymbol{\varepsilon}^\epsilon, \boldsymbol{\sigma}^\epsilon\} = \sum_{n=0} \varepsilon^n \{\boldsymbol{\varepsilon}^n, \boldsymbol{\sigma}^n\}$. The first terms of these expansions are expressed in terms of $\boldsymbol{u}^0$ and $\boldsymbol{\chi}^1$ as

$$\begin{aligned} \boldsymbol{\varepsilon}^0(\boldsymbol{X}, \boldsymbol{x}) =& sym\{\nabla_{\boldsymbol{X}} \otimes \boldsymbol{u}^0(\boldsymbol{X})\} + sym\{\nabla_{\boldsymbol{x}} \otimes \boldsymbol{\chi}^1(\boldsymbol{x})\} : (\nabla_{\boldsymbol{X}} \otimes \boldsymbol{u}^0(\boldsymbol{X})) \\ \boldsymbol{\sigma}^0(\boldsymbol{X}, \boldsymbol{x}) =& \boldsymbol{C}(\boldsymbol{x}) : (\nabla_{\boldsymbol{x}} \otimes \boldsymbol{\chi}^1(\boldsymbol{x}) + \mathcal{I}) : (\nabla_{\boldsymbol{X}} \otimes \boldsymbol{u}^0(\boldsymbol{X})) \end{aligned} \tag{2.41}$$

where $sym\{\nabla_{\boldsymbol{x}} \otimes \boldsymbol{\chi}^1\}$ stands for $(\partial \chi^1_{ikl}/\partial x_j + \partial \chi^1_{jkl}/\partial x_i)/2$. Since $\boldsymbol{\chi}^1$ is periodic, the volume averages of $\boldsymbol{\varepsilon}^0$ and $\boldsymbol{\sigma}^0$ taken over U become

$$\begin{aligned} \langle \boldsymbol{\varepsilon}^0 \rangle_U(\boldsymbol{X}) &= sym\{\nabla_{\boldsymbol{X}} \otimes \boldsymbol{u}^0(\boldsymbol{X})\} \\ \langle \boldsymbol{\sigma}^0 \rangle_U(\boldsymbol{X}) &= \overline{\boldsymbol{C}}^0 : \langle \varepsilon^0 \rangle_U(\boldsymbol{X}) \end{aligned} \tag{2.42}$$

where $\overline{\boldsymbol{C}}^0$ is defined by Eq. 2.40 and $\langle \bullet \rangle_U$ stands for the volume average taken over U. These volume averages correspond to the macro-strain and macro-stress of the average-field theory. That is, if the strain and stress of $O(\epsilon^0)$ are regarded as the micro-fields, the homogenization theory defines the macro-fields as their volume averages, as does the average-field theory. Note that $\boldsymbol{\varepsilon}^0$ and $\boldsymbol{\sigma}^0$ are expressed in terms of $\langle \boldsymbol{\varepsilon}^0 \rangle_U$ and $\langle \boldsymbol{\sigma}^0 \rangle_U$ as

$$\begin{aligned} \boldsymbol{\varepsilon}^0(\boldsymbol{X}, \boldsymbol{x}) =& \langle \boldsymbol{\varepsilon}^0 \rangle(\boldsymbol{X}) + sym\{\nabla_{\boldsymbol{x}} \otimes \boldsymbol{\chi}^1(\boldsymbol{x})\} : \langle \boldsymbol{\varepsilon}^0 \rangle(\boldsymbol{X}) \\ \boldsymbol{\sigma}^0(\boldsymbol{X}, \boldsymbol{x}) =& \langle \boldsymbol{\sigma}^0 \rangle(\boldsymbol{X}) + (\boldsymbol{C}(\boldsymbol{X}) : (sym\{\nabla_{\boldsymbol{x}} \otimes \boldsymbol{\chi}^1(\boldsymbol{x}) - \mathcal{I}) - \overline{\boldsymbol{C}}^0) : \langle \boldsymbol{\sigma}^0 \rangle(\boldsymbol{X}) \end{aligned} \tag{2.43}$$

2.3.7 Nemat-Nasser and Hori micro-mechanics theory

While the homogenization theory is based on the singular perturbation of the micro-fields, the resulting fields of $O(\epsilon^0)$ and their averages taken over U correspond to the micro-fields and the macro-fields of the average-field theory. There are, however, two major differences between these two theories. The first difference is the modelling of the micro-structure: the homogenization theory uses an unit cell of the periodic structure, while the average-field theory considers a representative volume element of a statistically homogeneous body. The second difference is that the homogenization theory is able to treat the macro/micro-relations more rigorously, allowing higher-order terms in the singular perturbation expansion. These differences are not essential, i.e., the homogenization theory can be applied to materials with a non-periodic micro-structure and higher order terms can be still

computed with the aid of suitable micro-structure models using the average-field theory. The micro-mechanics theory proposed by Nemat-Nasser and Hori [85] is a hybrid approach between the homogenization and average-field theories.

An elasticity tensor field $\boldsymbol{C} = \boldsymbol{C}(\boldsymbol{x})$ not necessarily periodic is considered. The singular perturbation of $\boldsymbol{u}^\epsilon$, Eq. 2.35, is still applicable and the assumptions $u_i^0 = \chi_{im}^0 u_m^0(\boldsymbol{X})$ and $u_i^1 = \chi_{imp}^1(\boldsymbol{x})(D_p u_m^0(\boldsymbol{X}))$ make terms of $O(\epsilon^{-2})$ and $O(\epsilon^{-1})$ to vanish, if $\chi_{ij}^0 = \delta_{ij}$ and χ_{ij}^0 satisfies Eq. 2.37. Furthermore, assuming that $\boldsymbol{u}^2$ is given by $u_i^2 = \chi_{impq}^2(\boldsymbol{x})(D_p D_q u_m^0)$, where $\boldsymbol{\chi}^2$ is a fourth-order tensor depending only on $\boldsymbol{x}$, the terms of $O(\epsilon^0)$ in Eq. 2.36 can be rewritten as $\overline{C'}^0_{ijkl} D_i D_l \boldsymbol{u}_k^0(\boldsymbol{X}) + R_j^0(\boldsymbol{X}, \boldsymbol{x})$, where R^0 is defined as

$$\begin{aligned} R_j^0(\boldsymbol{X}, \boldsymbol{x}) = & \Big(d_i \big(C_{ijkl}(\boldsymbol{x}) (d_l \chi_{kmpq}^2(\boldsymbol{x}) + \chi_{kmq}^1(\boldsymbol{x}) \delta_{lp}) \big) + \\ & + C_{pjkl}(\boldsymbol{x}) (d_l \chi_{kmq}^1(\boldsymbol{x}) + \chi_{km}^0(\boldsymbol{x}) \delta_{lq}) - \overline{C'}^0_{pjmq} \Big) \times \\ & \times \big(D_p D_q \boldsymbol{u}_m^0(\boldsymbol{X}) \big) \end{aligned} \tag{2.44}$$

where $d_i \equiv \partial / \partial x_i$ replaces $\nabla_{\boldsymbol{x}}$. The term $\overline{C'}^0_{ijkl} D_i D_l \boldsymbol{u}_k^0(\boldsymbol{X})$ yields a governing equation for $\boldsymbol{u}^0$ and the term, R_j^0, is a residual of this governing equation.

It is possible to enforce $R^0 = 0$ and to satisfy Eq. 2.35 up to $O(\epsilon^0)$ for any arbitrary $\overline{\boldsymbol{C'}}^0$, since $\boldsymbol{\chi}^2$ can be determined such that $\boldsymbol{R}^0$ vanishes. According to the average-field theory, however, the most suitable $\overline{\boldsymbol{C'}}$ is probably given by taking the volume average of $C_{ijpq}(d_q \chi_{pkl}^1 + \chi_{pk}^0 \delta_{lq})$, over a domain in which $\boldsymbol{\chi}^1$ is defined.

By supposing that V, not necessarily an unit cell of a periodic structure, is a domain in which $\boldsymbol{\chi}^1$ is defined, $\boldsymbol{\chi}^1$ or $\overline{\boldsymbol{C'}}^0$ that relates the average strain to the average strain energy as well as the average stress, independently of the boundary conditions prescribed on ∂V, can be determined. By remembering the universal inequalities [36]

$$\langle \boldsymbol{\varepsilon}^\Sigma : \boldsymbol{C} : \varepsilon^\Sigma \rangle_V \leq \langle \boldsymbol{\varepsilon}^G : \boldsymbol{C} : \varepsilon^G \rangle_V \leq \langle \boldsymbol{\varepsilon}^E : \boldsymbol{C} : \varepsilon^E \rangle_V \tag{2.45}$$

the following two inequalities hold

$$\int_V \boldsymbol{\varepsilon}^{0\Sigma} : \boldsymbol{C} : \boldsymbol{\varepsilon}^{0\Sigma} dV_x \leq \int_V \boldsymbol{\varepsilon}^{0G} : \boldsymbol{C} : \boldsymbol{\varepsilon}^{0G} dV_x \leq \int_V \boldsymbol{\varepsilon}^{0E} : \boldsymbol{C} : \boldsymbol{\varepsilon}^{0E} dV_x \tag{2.46}$$

where $\boldsymbol{\varepsilon}^E$, $\boldsymbol{\varepsilon}^G$ and $\boldsymbol{\varepsilon}^\Sigma$ are the strain field of $O(\epsilon^0)$ with a common volume average, when homogeneous strain, general and homogeneous stress boundary conditions are prescribed on ∂V in such a manner that they produce the same average strain. These $\boldsymbol{\chi}^{1E}$, $\boldsymbol{\chi}^{1G}$ and $\boldsymbol{\chi}^{1\Sigma}$ must satisfy the following relation:

$$\boldsymbol{\varepsilon}^{0(.)}(\boldsymbol{X},\boldsymbol{x}) = sym\{(\nabla_{\boldsymbol{x}} \otimes \boldsymbol{\chi}^{1(.)}(\boldsymbol{x}) + \mathcal{I}) : (\nabla_{\boldsymbol{X}} \otimes \boldsymbol{u}^0(\boldsymbol{X}))\} \tag{2.47}$$

and give the microscopic strain whose volume average coincides with $sym\{\nabla_{\boldsymbol{X}} \otimes \boldsymbol{u}^0(\boldsymbol{X})\}$, i.e.,

$$\langle sym\{(\nabla_{\boldsymbol{x}} \otimes \boldsymbol{\chi}^{1(.)} + \mathcal{I}) : (\nabla_{\boldsymbol{X}} \otimes \boldsymbol{u}^0)\}\rangle_V(\boldsymbol{X}) = sym\{\nabla_{\boldsymbol{X}} \otimes \boldsymbol{u}^0(\boldsymbol{X})\} \tag{2.48}$$

Hence, the average response of V does not depend on the prescribed boundary conditions, if value of average strain energy of V under the homogeneous strain boundary conditions, $\langle e^E\rangle_V$, is close to the value of the average strain energy under the homogeneous stress boundary conditions, $\langle e^\Sigma\rangle_V$, i.e.,

$$\frac{\langle e^E\rangle_V - \langle e^\Sigma\rangle_V}{\langle e^E\rangle_V} \ll 1 \tag{2.49}$$

where

$$\langle e^{\cdot}\rangle_V = \left\langle \frac{1}{2}\varepsilon^{0(.)} : \boldsymbol{C} : \varepsilon^{0(.)} \right\rangle_V \tag{2.50}$$

The effective elasticity tensor, $\overline{\boldsymbol{C}}'^0$, can now be uniquely determined as

$$\begin{aligned} \overline{\boldsymbol{C}}'^0 \approx & \langle \boldsymbol{C} : (\nabla_{\boldsymbol{x}} \otimes \boldsymbol{\chi}^{1(E)} + \mathcal{I})\rangle_V \\ \text{or} \quad & \langle \boldsymbol{C} : (\nabla_{\boldsymbol{x}} \otimes \boldsymbol{\chi}^{1(\Sigma)} + \mathcal{I})\rangle_V \end{aligned} \tag{2.51}$$

The effective elasticity tensor, $\overline{\boldsymbol{C}}'^0$, which is given by Eq. 2.40, corresponds to a case when periodic boundary conditions are prescribed on the boundary of a parallelepiped $V = U$ (Fig. 2.8). This effective elasticity tensor is bounded by two effective elasticity tensors, $\langle \boldsymbol{C} : (\nabla_{\boldsymbol{x}} \otimes \boldsymbol{\chi}^{1(E)} + \mathcal{I})\rangle_V$ and $\langle \boldsymbol{C} : (\nabla_{\boldsymbol{x}} \otimes \boldsymbol{\chi}^{1(\Sigma)} + \mathcal{I})\rangle_V$, which are determined when homogeneous strain and stress boundary conditions are prescribed on the parallelepiped U.

For a given (constant) average strain, $\langle \boldsymbol{\varepsilon}^0\rangle_V = sym\{\nabla_{\boldsymbol{X}} \otimes \boldsymbol{u}^0\}$, the boundary conditions for $\boldsymbol{\chi}^{1(E)}$ is prescribed as $\boldsymbol{\chi}^{1(E)} = 0$ on ∂V. Boundary conditions for $\boldsymbol{\chi}^{1(\Sigma)}$, however, are not easily defined; zero traction boundary conditions, $\boldsymbol{\nu} \cdot (\boldsymbol{C} :$

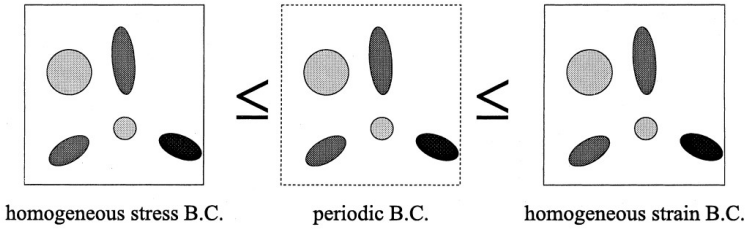

Figure 2.8: Unit cell used in hybrid micro-mechanics theory [85].

$(\nabla_{\boldsymbol{x}} \otimes \boldsymbol{\chi}^{1(\Sigma)})) = 0$, are not suitable since the resulting $\boldsymbol{\chi}^{1(\Sigma)}$ does not satisfy Eq. 2.48. Taking advantage of the linearity, however, $\boldsymbol{\chi}^{1(\Sigma)}$ can be determined by using the solution for the homogeneous stress boundary conditions. Indeed, $\boldsymbol{u}^{\Sigma} = \boldsymbol{u}^{\Sigma}(\boldsymbol{x}; \boldsymbol{\Sigma})$ is the displacement field when V is subjected to $\boldsymbol{t} = \boldsymbol{\nu} \cdot \boldsymbol{\Sigma}$ on ∂V, where $\boldsymbol{\Sigma}$ is constant. The volume average of the associated strain, $\langle \boldsymbol{\varepsilon}^{\Sigma} \rangle_V = sym\{\nabla_{\boldsymbol{X}} \otimes \boldsymbol{u}^{\Sigma}\}$, is linearly related to the prescribed stress, $\boldsymbol{\Sigma}$, which is the same as the average stress. Hence, the inverse of a fourth-order tensor which relates $\boldsymbol{\Sigma}$ to $\langle \boldsymbol{\varepsilon}^{\Sigma} \rangle_V$ is the effective elasticity tensor, and $\boldsymbol{\chi}^{1(\Sigma)}$ is given by

$$\boldsymbol{\chi}^{1(\Sigma)}(\boldsymbol{x}) : \langle \boldsymbol{\varepsilon}^{\Sigma} \rangle_V = \boldsymbol{u}^{\Sigma}(\boldsymbol{x}; \boldsymbol{\Sigma}) - \boldsymbol{x} \cdot \langle \boldsymbol{\varepsilon}^{\Sigma} \rangle_V \tag{2.52}$$

This $\boldsymbol{\chi}^{1(\Sigma)}$ satisfies Eq. 2.48, if $\boldsymbol{\Sigma}$ is chosen such that $\langle \boldsymbol{\varepsilon}^{\Sigma} \rangle_V = \langle \boldsymbol{\varepsilon}^{0} \rangle_V$ or $sym\{\nabla_{\boldsymbol{X}} \otimes \boldsymbol{u}^{0}\}$.

2.3.8 Kalamkarov and Liu mesomechanics model

Kalamkarov and Liu [15] consider the fibre-reinforced composite material consisting of a matrix and a vast number of microfibres and long fibres. The microfibres are heterogeneously distributed and randomly oriented in the matrix and the long fibres are usually oriented in some special directions. Since microfibres are randomly oriented and distributed in the matrix, they can be considered to be homogeneously distributed and oriented in the matrix in the statistical sense. Generally speaking, the bulk mechanical response of the fibre-reinforced composite material is the average result of interactions between the matrix and a great number of microfibres and/or long fibres. However, due to the different orientations of fibres in the matrix, the composite material can hardly be considered as a homogeneously isotropic continuous medium. Thus it is necessary to introduce some micro-structure in the

composite material model which can reflect the micro behaviour of the materials.

A representative volume of the composite material V includes the matrix and a large number of microfibres. Consider a bundle of long fibres of length l_l and volume V_l in the direction $\boldsymbol{l}$. The work rate of the bundle of fibres is defined as:

$$\Delta w_l = \frac{\sum_\alpha (f_\alpha \cdot \dot{l}_\alpha)}{V} = \frac{\sum_\alpha (\sigma_\alpha \cdot A_\alpha \cdot l_l \frac{\dot{l}_l}{l_l})}{V} \tag{2.53}$$

where f_l and $\dot{l}_l$ are the force-response function and the extension rate of the bundle of fibres in the direction $\boldsymbol{l}$. Since the fibres are of the same type, the above equation can be written as:

$$\Delta w_l = \frac{V_l}{V}\sigma_l \dot{\varepsilon}_l = c_l \sigma_l \dot{\varepsilon}_l \qquad V_l = \sum_\alpha A_\alpha \cdot l_l \tag{2.54}$$

where A_α is the cross-section area of each fibre, $c_l = V_l/V$ is the volume fraction of fibres in the direction $\boldsymbol{l}$, σ_l and $\dot{\varepsilon}_l$ are the stress and strain rates of fibres, respectively. By the equivalent principle of power rates, the bundle of fibres can be replaced by an equivalent fibre whose contribution to the unit element volume is equal to its power rate times its volume fraction.

Consider the microfibres homogeneously distributed in a volume element. The work rate contributed by the microfibres in the direction $\boldsymbol{l}$ is

$$\Delta w_l = \frac{\sum_\alpha (f_\alpha \cdot \dot{l}_\alpha)}{V} = \frac{\sum_\alpha (\sigma_\alpha \cdot A_\alpha \cdot h_\alpha \frac{\dot{l}_\alpha}{h_\alpha})}{V} = \frac{\sum_\alpha (\sigma_\alpha \cdot \dot{\varepsilon}_\alpha \Delta_\alpha)}{V} = \frac{\int_V \sigma \dot{\varepsilon} dV_l}{V} \tag{2.55}$$

where σ is the stress carried by the microfibre, $\dot{\varepsilon}$ is the extension rate of the microfibre of unit length, dV_l is a volume element in the direction $\boldsymbol{l}$. For the volume integral of all fibres in direction $\boldsymbol{l}$, Kalamakarov and Liu [15] define an average stress and strain rate, for which the work rate done by them is equal to the total stored or dissipated work rate of all fibres in direction $\boldsymbol{l}$:

$$\frac{\int_V \sigma \dot{\varepsilon} dV_l}{V} = c_h \overline{\sigma}\overline{\dot{\varepsilon}} \tag{2.56}$$

where c_h is the volume fraction of fibres homogeneously distributed in the matrix. Since the deformation of fibres must be compatible with that of the matrix, the extension rate of the fibre $\overline{\dot{\varepsilon}}$ generally depends on the macro strain rate $\boldsymbol{D}$. So the

average stress carried by fibres in direction $\boldsymbol{l}$ is defined as:

$$\overline{\sigma} = \frac{1}{V_h}\int_{\Omega} \sigma \frac{\dot{\varepsilon}}{\dot{\overline{\varepsilon}}} dV_l \qquad c_h = \frac{V_h}{V} \tag{2.57}$$

where V_h is the volume of fibres homogeneously distributed in the matrix. The average stress is equal to the weighted average of stresses carried by the microfibres in the direction $\boldsymbol{l}$. Thus, an equivalent fibre phase is defined by a pair of work conjugate variables $\overline{\sigma}$ and $\overline{\dot{\varepsilon}}$ which replaces the real microfibres in the matrix. The work rate in direction $\boldsymbol{l}$ is defined as:

$$\Delta w_l = c_h \overline{\sigma}\overline{\dot{\varepsilon}} \tag{2.58}$$

Due to the random distribution of microfibres in 3D space, the equivalent fibres are considered to be homogeneously distributed in the statistical average. The unit direction vectors of all equivalent fibres form a hemispherical surface in 3D space. By using the sum of the work rates of fibres in all directions, the total work rate contributed by the microfibres in the unit volume element is obtained as an integral on the hemispherical surface

$$\dot{w}_f = c_h \int_{\Omega} \overline{\sigma}\overline{\dot{\varepsilon}} d\Omega \tag{2.59}$$

In spherical coordinates

$$x = \cos\varphi \qquad y = \sin\varphi\cos\vartheta \qquad z = \sin\varphi\sin\vartheta \tag{2.60}$$

the orientation integral can be expressed as

$$\dot{w}_f = c_h \int_{\Omega} \overline{\sigma}\overline{\dot{\varepsilon}} d\Omega = \frac{1}{2\pi}\int_0^{2\pi}\int_0^{\pi/2} \overline{\sigma}\overline{\dot{\varepsilon}} \sin\varphi d\varphi d\vartheta \tag{2.61}$$

If there exist different kinds of microfibres and long fibres in the matrix, the equivalent fibre components are defined respectively by using each kind of fibre. Then the fibres in the composite material are replaced by different kinds of the equivalent fibres. It is not necessary to distinguish the variables $\overline{\sigma}$ and $\overline{\varepsilon}$ by the upper dash, so it will be omitted in the sequel. For the different equivalent fibre components and the matrix, Kalamkarov and Liu [15] assume the following:

1. In the same direction $\boldsymbol{l}$, different equivalent fibres are considered to be parallel; that is
$$\dot{\sigma}_l = \sum_\alpha c_\alpha \dot{\sigma}_{l\alpha} = \sum_\alpha c_\alpha \left(\frac{\partial \sigma_{l\alpha}}{\partial \varepsilon} \dot{\varepsilon}_{l\alpha} \right) \tag{2.62}$$

2. The extension rate of each equivalent fibre in direction $\boldsymbol{l}$ is equal to the macro extension rate along the same direction; that is
$$\dot{\varepsilon} = \boldsymbol{l} \otimes \boldsymbol{l} : \boldsymbol{D} = \boldsymbol{Q} : \boldsymbol{D} \quad \text{where} \quad \boldsymbol{Q} = \boldsymbol{l} \otimes \boldsymbol{l} \tag{2.63}$$
where $\boldsymbol{l}$ is a unit vector of the orientation of the fibre.

3. The matrix in the composite material forms a homogeneously isotropic continuous medium and its deformation is compatible with one of equivalent fibres.

In the framework of continuum mechanics, the constitutive equation may be stated as follows:
$$\dot{\boldsymbol{T}}_m = \boldsymbol{K}_m : \boldsymbol{D} \tag{2.64}$$
where $\dot{\boldsymbol{T}}_m$ is the stress rate tensor carried by the matrix, $\boldsymbol{D}$ is the strain rate tensor of the composite material, and $\boldsymbol{K}_m$ is the stiffness tensor of the matrix.

Using the above basic assumptions and definition of equivalent fibres, Kalamkarov and Liu [15] construct the model of the multiphase fibre-matrix composite material that is composed of the matrix and different kinds of equivalent fibres. Although the equivalent fibre component is one dimensional, the fibre, distinguished by its properties and orientation, is embedded into the matrix. Thus, the material model includes some micro-structure between the micro-scale and the macroscale: a mesostructure.

In the case that the equivalent fibres are homogeneously distributed and oriented in the matrix and the properties of the equivalent fibres in all directions are the same, the composite material is macroscopically isotropic. If the equivalent fibres are heterogeneously distributed in the matrix or their properties are heterogeneous along different directions, the composite material is macroscopically anisotropic. If the mesostructure and property of the equivalent fibres are axisymmetric, the composite material is macroscopically transversely isotropic. Hence, the property of the composite material depends on the properties of the matrix and equivalent

fibres as well as on the mesostructure defined by the orientations and distribution of the equivalent fibres in the matrix.

Meso-constitutive equation

The composite material is composed of the matrix, p kinds of equivalent fibres homogeneously distributed in the matrix, and q kinds of equivalent fibres with preferred orientations in q directions. Let us consider a unit volume element of the composite material. The total work rate in the unit volume, $\dot{w}$, is equal to the sum of the power rates of the matrix and the equivalent fibres:

$$\begin{aligned}\dot{w} &= \boldsymbol{T} : \boldsymbol{D} = \\ &= \frac{V_m}{V}\boldsymbol{T}_m : \boldsymbol{D} + \sum_{\alpha}^{p}\Big(c^{\alpha}\int_{\Omega}\sigma^{\alpha}\dot{\varepsilon}^{\alpha}d\Omega\Big) + \sum_{\beta}^{q}\Big(c^{\beta}\sigma^{\beta}\dot{\varepsilon}^{\beta}\Big) = \\ &= c_m\boldsymbol{T}_m : \boldsymbol{D} + + \sum_{\alpha}^{p}\Big(c^{\alpha}\int_{\Omega}\sigma^{\alpha}\boldsymbol{Q}^{\alpha}d\Omega : \boldsymbol{D}\Big) + \sum_{\beta}^{q}\Big(c^{\beta}\sigma^{\beta}\boldsymbol{Q}^{\beta} : \boldsymbol{D}\Big)\end{aligned} \tag{2.65}$$

where Ω is the hemispheric angle, c_m is the volume fraction of the matrix, c^{α} and c^{β} are the volume fractions of different fibres. Then the stress tensor in the fibre-matrix composite material is obtained as:

$$\boldsymbol{T} = c_m\boldsymbol{T}_m + \sum_{\alpha}^{p}\big(c^{\alpha}\boldsymbol{T}_f^{\alpha}\big) + \sum_{\beta}^{q}\Big(c^{\beta}\sigma^{\beta}\boldsymbol{Q}^{\beta}\Big) \tag{2.66}$$

where

$$\boldsymbol{T}_f^{\alpha} = \int_{\Omega}\sigma^{\alpha}\boldsymbol{Q}^{\alpha}d\Omega$$

is the stress tensor carried by the fibres homogeneously distributed in the matrix. Furthermore, the stress rate tensor $\dot{\boldsymbol{T}}_f^{\alpha}$ carried by the fibres homogeneously distributed in the matrix can be derived as follows:

$$\dot{\boldsymbol{T}}_f^{\alpha} = \int_{\Omega}\frac{\partial\sigma}{\partial\varepsilon}\boldsymbol{Q}\otimes\boldsymbol{Q}d\Omega : \boldsymbol{D} \tag{2.67}$$

The stress rate tensor $\dot{\boldsymbol{T}}_f^{\beta}$ carried by the fibres with preferred orientation is

$$\dot{\boldsymbol{T}}_f^{\beta} = \frac{\partial\sigma}{\partial\varepsilon}\boldsymbol{Q}\otimes\boldsymbol{Q} : \boldsymbol{D} \tag{2.68}$$

By using the above equation, the incremental meso-constitutive equation can be obtained as follows:

$$\dot{\boldsymbol{T}} = \boldsymbol{K} : \boldsymbol{D} \tag{2.69}$$

where the stiffness tensor is

$$\boldsymbol{K} = c_m \boldsymbol{K}_m + \sum_{\alpha}^{p} \Big(c^{\alpha} \int_{\Omega} \frac{\partial \sigma}{\partial \varepsilon} \boldsymbol{Q}^{\alpha} \otimes \boldsymbol{Q}^{\alpha} d\Omega \Big) + \sum_{\beta}^{q} \Big(c^{\beta} \frac{\partial \sigma}{\partial \varepsilon} \boldsymbol{Q}^{\beta} \otimes \boldsymbol{Q}^{\beta} \Big) \tag{2.70}$$

The above equation is the meso-constitutive equation for the multiphase fibre-matrix composite material. The material constants and volume fractions of different phases and mesostructures formed by all fibres in different orientations are reflected in the constitutive equation. In the derivation, Kalamkarov and Liu have not used any specific properties of each phase material, so it is a general form. The properties of the matrix and various fibres depend on $\boldsymbol{K}_m$ and $\frac{\partial \sigma}{\partial \varepsilon}$ respectively. The expression of the volume fractions of the matrix and different fibres is:

$$c_m + \sum_{\alpha}^{p} c^{\alpha} + \sum_{\beta}^{q} c^{\beta} = 1$$

Therefore the volume fraction of all fibres is

$$c = \sum_{\alpha}^{p} c^{\alpha} + \sum_{\beta}^{q} c^{\beta} = 1$$

then,

$$c_m = 1 - c \tag{2.71}$$

Thus, if there is only one kind of fibre distributed in the matrix, $c_f = c$ and $c_m = 1 - c$.

2.4 Damage and Fracture of Fibre-Reinforced Materials

Composite materials display a wide variety of failure mechanisms as a result of their complex structure and manufacturing processes, which include fibre failure, matrix cracking, buckling and delamination. Based on these failure mechanisms it

can be more appropriate to consider the composite as a structure rather than as a material.

- Fibre failure is one of the simplest failure mechanisms to identify and quantify, and occurs when the loads applied to a composite structure cause breaking in the fibres;

- Matrix cracks are an intralaminar form of damage and involve cracks or voids formation between fibres within a single composite layer or lamina;

- Buckling is a structural phenomenon that occurs in compression or shear, not necessary resulting in failure; however large deformations, bending and loss of structural capacity typically, involved promotes other types of damage and leads to structural collapse;

- Delaminations are separations between internal layers of a composite laminate caused by high through-the-thickness stresses, cause significant structural damage, particularly in compression.

When a fibre-reinforced materials fails, fracture energies are absorbed by matrix cracking, fibre fracture, fibre-matrix interface debonding, frictional work following debonding and fibre pull-out [86]. Two approaches to the fibre-matrix debonding phenomenon are available: one is based upon a maximum shear stress criterion such that it is equal to the shear strength of the fibre-matrix interface for debonding, and the other is based upon the fracture mechanics treating debonding as a particular fracture propagation problem. The first approach is typified by the work of Cox [24], Lawrence [87], Greszcuk [88], Takaku and Arridge [89] using the simple shear lag models, whereas representative works of the fracture mechanics approach include those of Gurney and Hunt [90], Outwater and Murphy [91], Bowling and Groves [92], Atkinson et al. [93], and Stang and Shah [94]. When a fibre is partially debonded, compressive stresses, due to matrix shrinkage and difference in thermal expansion coefficient of fibre and matrix, act on the fibre giving rise to friction in the debonded zone [95]. The influence of friction on fibre debonding is very important, and with the exception of Lawrence [87] and Bowling and Groves [92] work, friction is seldom included in the analysis.

2.4.1 Analytical modelling

The *shear lag model* developed by Cox [24] is one of the most often used approaches in the analysis of strength and damage of fibre reinforced composites. This model is often employed to analyse the load redistribution in fibre reinforced composites, resulting from failure of one or several fibres. This redistribution is described in the framework of various load sharing models. According to the global load sharing schema (GLS) (used for instance, in the fibre bundle model developed by Daniels [96]), the unsupported load, that results by a broken fibre, is equally re-distributed over all the remaining intact fibres in the cross-section of the composite. As noted by Zhou and Wagner [97], the GLS model is applicable only to a loose fibre bundle, with no matrix between the fibres. In the case of fibres which are bound together by the matrix, other models of the load sharing should be used.

Harlow and Phoenix [98] proposed the *local load sharing* (LLS) model, in which the extra-load, related with the failed fibre(s), is transferred to two nearest neighbors of the fibre(s). For the qualitative description of the load redistribution after the fibre failure, Stress Concentration Factor (SCF) is introduced. The stress concentration factor is defined as a ratio between the local stress in an intact fibre (equal to the load originally carried by the broken fibre plus the applied remote stress) and the applied remote stress [97].

Hedgepeth [99] applied the shear lag model to model the multi-fibre system. He studied the stress distribution around broken fibres in 2D unidirectional composites with infinite array of fibres. Hedgepeth and van Dyke [100] generalized the elastic model by Hedgepeth to the three-dimensional case and included the elastic-plastic matrix into the model.

Wagner and Eitan [101] used the shear lag model to study the redistribution of stress from a failed fibre to its neighbors. They determined SCF for the case of load redistribution after one single fibre failure in a 2D unidirectional composite, and demonstrated that the "local effect of a fibre break on the nearest neighbors is much milder than previously calculated, both as a function of the inter-fibre distance and of the number of adjacent broken fibres".

Zhou and Wagner [97] proposed a model of stress redistribution after the fibre failure, which incorporated the effects of fibre/matrix debonding and fibre/matrix interfacial friction. The interfacial friction in the debonding region was calculated

as proportional to the far-field longitudinal stress in the fibre. It was observed that SCF decreases with increasing inter fibre distance.

Curtin [102] noted that the problem of independent and successive fibre fractures under GLS condition is reduced to the problem of failure of single fibre in the matrix. Considering the cumulative number of defects in fibres from the Weibull distribution of fibre strengths, he estimated the ultimate strength of the composite as a function of the sliding resistance, and parameters of the Weibull distribution of the fibre strength.

Landis et al. [103] developed a three-dimensional shear lag model, in which matrix displacements was interpolated from the fibre displacements, and analysed the stress distributions around a single fibre break in square or hexagonal fibre arrays. The finite element equations were transformed into differential equations and solved using Fourier transform and the influence function technique. Further, Landis et al. [104] combined this approach with the Weibull fibre statistics and the influence superposition technique, and applied it to analyse the effect of statistical strength distribution and size effects on the strength of composites.

2.4.2 Fibre bundle model

A group of models of damage and failure of fibre reinforced composites has been developed on the fibre bundle model (FBM). This model was proposed initially by Daniels [96], and then expanded, modified and generalized by many authors.

Daniels considered a bundle of N fibres with identical elastic properties under uniform tensile stress. When a fibre breaks, the load from the broken fibre is distributed equally over all the remaining fibres (global load sharing). The strength of the fibres is a random value, which is described most often by the Weibull probability distribution.

Gücer and Gurland [105] developed a model for "dispersed fracture" as a chain of elements, each of them is considered as a fibre bundle. The strength of the bundles was analysed using the Daniels' theory, while the failure of the chain was studied using the weakest-link theory. The theoretical predictions of strength of composites, made through this theory, are generally higher than the corresponding experimental values.

The model by Gücer and Gurland was developed further by Rosen [106, 107], who studied the damage in composite as a failure of chains of bundles with

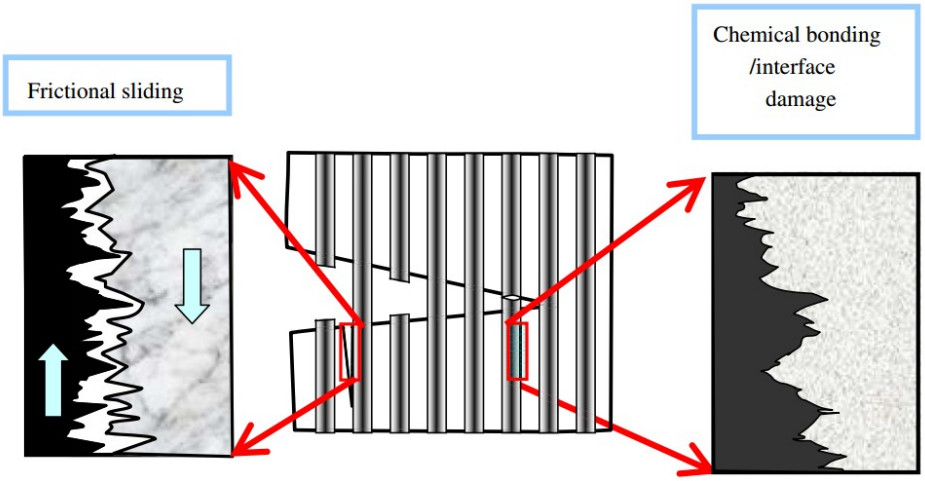

Figure 2.9: Mechanisms of the interface bonding in fibre bridged composites (interface sliding and chemical/physical bonding) [115].

fibres of limited (critical) length. Zweben [108] studied the influence of the stress concentration from a broken fibre on its closest neighbors, and demonstrated that failure of even a few fibres can lead to the failure of whole specimen.

Recently, a number of Finite Difference Methods (FDM)-based models were developed, which take into account the roles of the matrix and interfaces, non-linear behaviour of fibres and matrix, and the real micro-mechanisms of composite failure [109–114].

2.4.3 Fracture mechanics based models and crack bridging

In connection with the development of ceramic and other brittle matrix composites, the problem of the material toughening by crack bridging fibres gained in importance. In the cracked composite with bridging fibres, the fibre/matrix bonding (frictional bonding or chemical bonding) determine the fracture resistance of the composite. Figure 2.9 shows the schema of frictional and chemical bonding of bridging fibres in the composite.

The classical fracture mechanics based model of matrix cracking was developed by Aveston et al. [116] (the model is often referred to as ACK). Assuming that the fibres are held in the matrix only by frictional stresses, Aveston and colleagues carried out an analysis of the energy changes in a ceramic composite due to the

matrix cracking. On the basis of the energy analysis, they obtained the condition of matrix cracking in composites.

Marshall et al. [117] and Marshall and Cox [118] used the stress intensity approach to determine the matrix cracking stress in composites. The bridging fibres were represented by the traction forces connecting the fibres through the crack. It was supposed that the fibres are held in the matrix by frictional bonding. The matrix cracking stress was determined by equating the composite stress intensity factor, defined through the distribution of closure pressure on the crack surface, to the critical matrix stress intensity factor. Further, Marshall and Cox studied the conditions of the transitions between failure mechanisms (matrix and fibre failure) and the catastrophic failure, and determined the fracture toughness of composites as functions of the normalized fibre strength.

Budiansky et al. [119] considered the propagation of steady-state matrix cracks in composites, and generalized some results of the Aveston-Cooper-Kelly theory, including the results for the initial matrix stresses. Considering the energy balance and taking into account the frictional energy and potential energy changes due to the crack extension, Budiansky and colleagues determined the matrix cracking stress for composites with unbonded (frictionally constrained and slipping) and initially bonded, debonding fibres.

Hutchinson and Jensen [120] used an axisymmetric cylinder model to analyse the fibre debonding accompanied by the frictional sliding (both constant and Coulomb friction) on the debonded surface (Fig. 2.10). Considering the debonding as mode II interface fracture, Hutchinson and Jensen determined the debonding stress and the energy release rate for a steady-state debonding crack.

In several works, continuum models of a bridged matrix crack are used. In these models, the effect of fibres on the crack faces is smoothed over the crack length and modelled by continuous distribution of tractions, acting on the crack faces. The schema of the continuum model of a bridged crack is shown in Figure 2.11. The relationships between the crack bridging stresses and the crack opening displacement (bridging laws) are used to describe the effect of fibres on the crack propagation. For the case of the constant interface sliding stress τ, the crack opening displacement w can be determined as a function of the bridging stress σ [116, 121]

$$w = \lambda\sigma^2$$

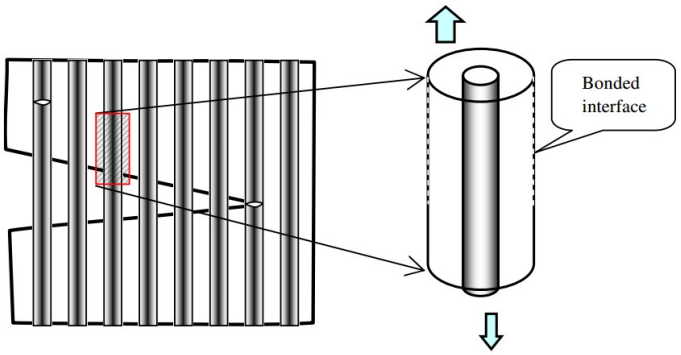

Figure 2.10: Two cylinder model of debonding and pull-out of a fibre. The dashed lines represent bonded interfaces [115].

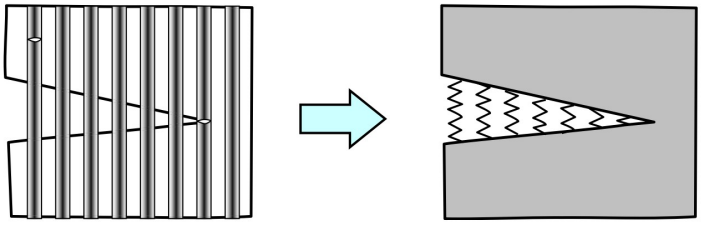

Figure 2.11: Spring bridging model: the crack bridging by fibres is represented by continuously distributed non-linear springs [115].

where $\lambda = (2r(1-\nu_f)^2 E_m^2)/(4\nu_f \tau E_f E^2)$, E is the composite Young's modulus, r is the fibre radius, the indices f and m relate to the fibres and matrix, respectively.

McCartney [122] used the continuum model of a bridged matrix crack, in order to derive the ACK-type matrix cracking criterion on the basis of the crack theory analysis. McCartney considered the energy balance for continuum and discrete crack models, and demonstrated that the Griffith fracture criterion is valid for the matrix cracking in the composites. He determined further the effective traction distribution on the crack faces resulting from the effect of fibres, and the stress intensity factor for the matrix crack.

Slaughter [123] developed a self-similar model for calculating the equivalent spring constant (i.e., the proportionality coefficient between the far-field stress and the part of the axial displacement related with the crack opening, [124]) in the crack bridging problem. His approach is based on the load transfer model by Slaughter and Sanders [125], in which the effect of an embedded fibre on matrix

is approximated by a distribution of axial forces and dilatations along the fibre axis. Using the shear lag model and the continuously distributed non-linear springs model, Budiansky et al. [126] determined the stresses in the matrix bridged by intact and debonded fibres, and derived an equivalent crack bridging law, which included the effect of debonding toughness and frictional sliding.

Gonzalez-Chi and Young [127] applied the partial-debonding theory by Piggott [128] to analyse the crack bridging. In the framework of this theory (based on the shear lag model and developed for the analysis of the fibre pull-out tests), the fibre/matrix interface is assumed to consist of a debonded area (where the stress changes linearly along the fibre length) and the fully bonded, elastically deformed area [128]. Considering each fibre and the surrounding matrix as a single pull-out test, Gonzalez-Chi and Young determined the stresses in the fibre and on the interface.

2.4.4 Continuum damage mechanics based models

The growth of micro-cracks, fibre breaking and interface debonding in composites can be described in the framework of continuum damage mechanics (CDM) as long as the problem size can be assumed to be sufficiently larger than the defect/micro-crack size. The advantages of the CDM approach for the modelling of fibre reinforced composites include rather simple definitions of damage variables in the unidirectional materials, and, consequently, the straightforwardness of its application.

A greater number of models of failure behaviour of fibre reinforced composites are based on the methods of continuum damage mechanics with internal variables, formulated in the framework of the thermodynamics of irreversible processes. This approach includes the introduction of corresponding internal state variables (ISV) to characterize damage modes (e.g., fiber cracking, void growth or micro-cracking in matrix, or interfacial micro-cracks), and derivation of the damage growth laws on the basis of thermodynamical analysis of the system.

Hild et al. [129, 130] and Burr et al. [131] introduced the internal state variables, describing the matrix cracking and interface debonding and sliding and employed this model to analyse the fibre and matrix breakage in ceramic matrix fibre reinforced composites. From the formula expressing the total free energy density, Hild and colleagues derived equations for the overall stress, energy release rate

density, and other parameters.

Matzenmiller et al. [132] developed a constitutive model, relating the effective elastic properties and damage of the material. The authors introduced a set of phenomenological internal (damage) variables, and a potential function, and derived the kinetic equations for these variables. The rate equation for damage variables was presented as a sum of local damage parameters multiplied by scalar growth functions, given as power functions of the state variables. The authors considered the damage evolution under uniaxial tension in fibre direction, and analysed the dependencies of the stress-strain diagrams on the material parameters.

Voyiadjis and Kattan [133] developed a continuum damage model of fibre reinforced metal matrix composite, in which two local damage tensors allow for nucleation and growth of voids in the ductile matrix, and for the fracture of fibres, respectively. The authors suggested to represent the debonding and delamination problems in terms of the combination of these two tensors.

Raghavan and Ghosh [16] developed a CDM model for composites with damageable interfaces. The interface debonding was simulated by using the cohesive zone models and the macroscopic damage variables and the damage evolution laws were determined on the basis of the micro-mechanical analysis of representative volume elements with subsequent asymptotic homogenization of microscopic variables. The micro-mechanical analysis was carried out with the Voronoi cell finite element method. In these models, micro-mechanical (unit cell) models of composites are used to determine parameters of the damage growth law. Often, continuum damage mechanics (CDM) based models for matrix are combined with either CDM or probabilistic models for fibre failure.

2.4.5 Continuum mechanical models of damage and fracture

In order to take into account both the non-linear behaviour of material components, and the interaction between phases and phases with emerging defects, discretised (e.g., finite element) continuum mechanical models are used. Differently by the phenomenological models (like shear lag, fibre bundle models, and continuum damage mechanics), the continuum mechanical models are most strictly justified, and have potentially no limitations in incorporating all the complex phenomena of damage evolution in composites. However, at the current stage of the development of modelling techniques, the incorporation of real or generic micro-structures of

composites into discrete models (especially, in 3D case) and including the emerging discontinuities still present challenges [134–136].

In the case of fibre reinforced composites under *transverse loading*, the problem can be conveniently reduced to a 2D formulation. The 2D unit cell models can be easily generalized from the case of one or two fibres to the case of many randomly arranged fibres.

Brockenborough et al. [137] used unit cell models for different (square edge-packing, diagonal-packing and triangle-packing) periodic fibre arrangements to study the effect of the fibre distribution and cross-sectional geometry on the deformation (stress-strain response and stress distribution) in Al alloy reinforced with boron fibres. Considering the random, triangle and square edge and square diagonal-packing of fibres and different fibre shapes, they demonstrated that the fibre arrangement influences the constitutive response of composites much more than the fibre shape.

Chen and Papathanasiou [138] employed the boundary element method to analyse the effect of the fibre arrangement on the interface stresses in transversely loaded elastic composites. They considered multi-fibre unit cells, generated with the use of the Monte-Carlo perturbation method, with varied volume fractions and minimum inter-fibre distances. Chen and Papathanasiou demonstrated that the distribution of maximum interface stresses on each fibre follows the Weibull-like probability distribution.

Trias et al. [139] simulated the transverse matrix cracking in FRCs. Real micro-structures of carbon fibre reinforced polymers were determined with the use of the digital image analysis, introduced into FE models and simulated in the framework of the embedded cell approach. In doing so, they used the results from Trias et al. [140], who determined the critical size of a statistical RVE for carbon fibre reinforced polymers, taking into account both mechanical and statistical (point pattern) criteria. Trias et al. obtained probability density functions of the stress, strain components and the dilatational energy density in the loaded composites.

Vejen and Pyrz [141] modelled the transverse crack growth in long fibre composites. The criteria of pure matrix cracking (strain density energy), fibre/matrix interface crack growth (bi-material model) and crack kinking out of a fibre/matrix interface were implemented into the automated crack propagation module of a finite element package. As a result, Vejen and Pyrz numerically obtained the crack paths for different fibre distributions.

In the analysis of the composite failure under tensile loading acting along the fibre direction, axisymmetric models are widely used. Differently by the 2D plain strain models, they cannot be simply generalized from 1 fibre to many fibres models. In this case, truly three dimensional models are required.

Walter [142] used axisymmetric unit cells with cohesive interface elements (perpendicular to fibre and along the interface) and elastic elements, to analyse the initiation and growth of damage in ceramic matrix composites. Independent cohesive laws for shear and normal displacements were used. The author carried out parametric studies of the interface and matrix toughness, and demonstrated that the interface strength "has a limited effect on the propagation of the matrix crack", but has a strong effect on the fibre failure: strong interfaces lead to high strength concentration in fibres, with the possibility to cause catastrophic brittle failure of the composite.

Zhang et al. [143] studied toughening mechanisms of FRCs using a micro-mechanical model ("embedded reinforcement approach"), taking into account both fibre bridging and matrix cracking. They defined the cohesive law for the matrix cracking as a linearly decreasing function of the separation. Bilinear traction-separation laws were taken for fiber-matrix debonding and the following interfacial friction. For different traction-separation laws of interfaces, R-curves were obtained. Zhang and colleagues demonstrated that the strong interfaces can lead to the lower toughness of the composites.

Zhang et al. [144] simulated unidirectional fibre reinforced polymers under off-axis loading, using 3D unit cell with non-linear viscoelastic matrix and elastic fibres. In order to model the matrix cracking, smeared crack approach was used. The matrix damage growth in the form of two "narrow bands" near the interface and along the fibre direction were observed in the numerical experiments.

It can be seen that the problems of modelling the fibre cracking and interface debonding have been differently tackled by various authors. The interface debonding and damage has been modelled by introducing cohesive interface elements, contact surface elements (debonded surfaces) and rigid beams connecting nodes in fibres and the matrix, and as the damage growth in interphase layers. The failure of components was described using Weibull probability model of strength (fibres), von Mises yield criterion and dilatational energy density criterion of cavitation-induced fracture (polymer matrix), strain invariant failure theory, strain density energy (matrix), cohesive crack models (with constant and random laws) and smeared

crack approach (matrix).

2.5 Fatigue Damage Modelling of Fibre-Reinforced Materials

The use of composite materials in a wide range of applications obliged researchers to consider fatigue when investigating a composite material and engineers to realize that fatigue is an important parameter that must be considered in calculations during design processes, even for structures where fatigue was not traditionally considered an issue.

The already developed and validated methods for the fatigue life modelling and prediction of "conventional" materials normally cannot be directly applied to composite materials. Moreover, the large number of different material configurations resulting from the multitude of fibres, matrices, manufacturing methods, lamination stacking sequences, etc. makes the development of a commonly accepted method, to cover all these variances, difficult.

2.5.1 Laminates

In general fatigue of fibre-reinforced composite materials is a quite complex phenomenon. Composite materials are inhomogeneous and anisotropic and their behaviour is more complicated than that of homogeneous and isotropic materials such as metals.

Among the parameters that influence the fatigue performance of composites, the most significant are:

- fibre type,
- matrix type,
- kind of reinforcement structure (unidirectional, fabric, braiding,...),
- laminate stacking sequence,
- environmental conditions (mainly temperature and moisture absorption),
- loading conditions (stress ratio R, cycling frequency,...) and boundary conditions.

In a fibre-reinforced composite damage starts very early and the extent of the damage zones grows steadily, while the damage type in these zones can change (e.g. small matrix cracks leading to large size delaminations). The gradual deterioration of a fibre-reinforced composite, with a loss of stiffness in the damaged zones, leads to a continuous redistribution of stress and a reduction of stress concentrations inside a structural component. As a consequence an appraisal of the actual state or a prediction of the final state (when and where final failure is to be expected) requires the simulation of the complete path of successive damage states.

According to Fong [145], there are two technical reasons why fatigue damage modelling in general is so difficult and expensive. The first reason are the several scales where damage mechanisms occur: from atomic level, through the subgrain, grain and specimen levels, to the component and structural levels. The second reason is the impossibility of producing "identical" specimens with well-characterized micro-structural features.

A rigorous classification is difficult, but a suitable classification can be based on that proposed by Sendeckyj [146]. According to Sendeckyj, fatigue criteria can be classified in to four major categories: the macroscopic strength fatigue criteria, criteria based on residual strength, criteria based on residual stiffness, and criteria based on the actual damage mechanisms.

Instead, Degrieck and Paepegem [147] classify the large number of existing fatigue models for composite laminates in three major categories: fatigue life models, phenomenological models for residual stiffness/strength and progressive damage models.

The *fatigue life models* use the information from S-N curves or Goodman-type diagrams and introduce a fatigue failure criterion which determines the fatigue life of the composite specimen. Regarding the characterization of the S-N behaviour of composite materials, Sendeckyj [148] advises to take into account three assumptions:

- the S-N behaviour can be described by a deterministic equation,
- the static strengths are uniquely related to the fatigue lives and residual strengths at runout,
- the static strength data can be described by a two-parameter Weibull distribution.

This approach requires extensive experimental work and does not take into account

the actual damage mechanisms, such as matrix cracks and fibre fracture.

The *phenomenological models* for residual stiffness and strength are based on an evolution law which describes the (gradual) deterioration of the stiffness or strength of the composite specimen in terms of macroscopically observable properties. Residual strength models have in fact an inherent "natural failure criterion": failure occurs when the applied stress equals the residual strength [149, 150]. In the residual stiffness approach, fatigue failure is assumed to occur when the modulus has degraded to a critical level which has been defined by many investigators. Hahn and Kim [151] and O'Brien and Reifsnider [152] state that fatigue failure occurs when the fatigue secant modulus degrades to the secant modulus at the moment of failure in a static test. According to Hwang and Han [153], fatigue failure occurs when the fatigue resultant strain reaches the static ultimate strain.

In the *progressive damage models*, the evolution law is proposed in direct relation with specific damage.

Damage accumulation models and life time prediction methodologies are very often inherently related, since the fatigue life can be predicted by establishing a fatigue failure criterion which is imposed to the damage accumulation model. For specific damage types, the failure value of the damage variable(s) can be determined experimentally.

Fatigue Life Models

The *fatigue life models* extract information from the S-N curves or Goodman-type diagrams and on its basis develop a fatigue failure criterion. They do not take into account damage accumulation, but predict the number of cycles at which fatigue failure occurs under fixed loading conditions.

One of the first fatigue failure criteria was proposed by Hashin and Rotem [154]. They distinguished a fibre failure and a matrix-failure mode:

$$\begin{aligned} &\sigma_A = \sigma_A^u \\ &\left(\frac{\sigma_T}{\sigma_T^u}\right) + \left(\frac{\tau}{\tau^u}\right) = 1 \end{aligned} \tag{2.72}$$

where σ_A and σ_T are the stresses along and transverse to the fibres, respectively, τ is the shear stress and σ_A^u, σ_T^u and τ^u are the ultimate tensile, the transverse tensile and the shear stress, respectively. Since the ultimate strengths are function

of fatigue stress level, the stress ratio and the number of cycles, the criterion is expressed in terms of three S-N curves which must be determined experimentally from testing off-axis unidirectional specimens under uniaxial load. This criterion is, in fact, valid only for laminates with unidirectional plies.

Ellyin and El-Kadi [155] demonstrated that the strain energy density can be used in a fatigue failure criterion for fibre-reinforced materials. The fatigue life N_f has been related to the total energy input ΔW^t through a power law type relation of the form:

$$\Delta W^t = \kappa N_f^{\alpha} \tag{2.73}$$

where κ and α are functions of the fibre orientation angle. The strain energy density is calculated under an elastic plane stress hypothesis. To include interlaminar shear and through-the-thickness stress distribution, another expression for the strain energy density should be derived.

Lawrence Wu [156] used a macroscopic failure criterion, based on the Tsai-Hill failure criterion. The criterion was expressed as:

$$\begin{aligned} &\frac{3}{2(F+G+H)}\big[F(\sigma_y-\sigma_z)^2+G(\sigma_z-\sigma_x)^2+ \\ &+H(\sigma_x-\sigma_y)^2+2L\sigma_{yz}^2+2M\sigma_{zx}^2+2N\sigma_{xy}^2\big]=\sigma^2 \end{aligned} \tag{2.74}$$

where F, G, H, L, M and N are functions of the lamina normal peak stresses X, Y, Z (acting in the x, y and z directions) and of Q, R and S, which are the lamina shear peak stresses corresponding to the shear stress components σ_{yz}, σ_{zx} and σ_{xy}, respectively. σ^2 is an equivalent stress in terms of X, Y and Z. The peak stresses X, Y, Z, Q, R and S are all functions of fatigue life N_f, while the corresponding S-N curves must be determined in advance.

Philippidis and Vassilopoulos [157] proposed a multiaxial fatigue failure criterion, which was very similar to the well known Tsai-Wu quadratic failure criterion for static loading:

$$F_{ij}\sigma_i\sigma_j + F_i\sigma_i - 1 \leq 0 \qquad i,j = 1,2,6 \tag{2.75}$$

where F_{ij} and F_i are functions of the number of cycles N, the stress ratio R and the frequency of loading. The values of the static failure stresses X_t, X_c, Y_t, Y_c and S for the calculation of the tensor components F_{ij} and F_i have further been replaced by the S-N curve values of the material along the same directions and under the

same conditions. Although, from the five S-N curves are required, the number was reduced to three, by assuming that $X_t = X_c$ and $Y_t = Y_c$. The researchers prefer to use the laminate properties instead of the lamina properties to predict the laminate behaviour, as they state that this enhances the applicability of the criterion to any stacking sequence of any type of composite, because the S-N curves for the laminate account for the different damage types occurring in these various types of composite materials. Under multiaxial loading the model by Philippidis and Vassilopoulos can produce acceptable fatigue failure predictions, but their choice of a multiaxial fatigue strength criterion based on the laminate properties, implies that for each laminate stacking sequence a new series of experiments is required.

Phenomenological models

Residual stiffness models Residual stiffness models describe the degradation of the elastic properties during fatigue loading. To describe stiffness loss, the scalar variable D is often used, which in the one-dimensional case is defined through the well-known relation $D = 1 - E/E_0$, where E_0 is the undamaged Young's modulus. Although D is often referred to as a damage variable, the models are classified as phenomenological models and not as progressive damage models, when the damage growth rate dD/dN is expressed in terms of macroscopically observable properties, and is not based on the actual damage mechanisms.

Hwang and Han [153, 158] introduced the concept of the "fatigue modulus", which was defined as the slope of applied stress and resultant strain at a specific cycle. The fatigue modulus degradation rate was assumed to follow a power function of the number of fatigue cycles, n:

$$\frac{dF}{dn} = -A \cdot c \cdot n^{c-1} \tag{2.76}$$

where A and c are material constants. Further they assumed that applied stress σ_a varied linearly with resultant strain in any arbitrary loading cycle, so that:

$$\sigma_a = F(n_i) \cdot \varepsilon(n_i) \tag{2.77}$$

where $F(n_i)$ and $\varepsilon(n_i)$ are the fatigue modulus and strain at loading cycle n_i, respectively. After integration and introducing the strain failure criterion, the

fatigue life N can be calculated as:

$$N = \left[B(1-r)\right]^{\frac{1}{c}} \tag{2.78}$$

where $r = \sigma_a/\sigma_u$ is the ratio of the applied cyclic stress to the ultimate static stress, while B and c are material constants. Hwang and Han proposed three cumulative damage models based on the fatigue modulus $F(n)$ and the resultant strain. Accordingly with it, the parameter D can be written as:

$$D = \frac{r}{1-r} \cdot \left[\frac{F_0}{F(n)} - 1\right] \tag{2.79}$$

Failure occurs when:

$$D = \sum_{i=1}^{m} \Delta D_i = 1 \tag{2.80}$$

where ΔD_i is the amount of damage accumulation during fatigue at stress level r_i and m is the number of load sequences until final failure.

Sidoroff and Subagio [159] proposed the following model for the damage growth rate:

$$\frac{dD}{dN} = \begin{cases} \dfrac{A \cdot (\Delta\varepsilon)^c}{(1-D)^b} & \text{in tension} \\ 0 & \text{in compression} \end{cases} \tag{2.81}$$

where the parameter $D = 1 - E/E_0$; A, b and c are three material constants to be identified from experiments and $\Delta\varepsilon$ is the applied strain amplitude. The model was applied to the results from three-point bending tests on glass-epoxy unidirectional composites under fixed load amplitudes.

Residual strength models Two types of residual strength models can be distinguished: the *sudden death* model and the *wearout* model. When composite specimens are subjected to a high level state of stress (low-cycle fatigue), the residual strength as a function of number of cycles is initially nearly constant and decreases drastically when the number of cycles to failure is being reached. The sudden death model is a suitable technique to describe this behaviour and is especially suitable for high-strength unidirectional composites [160, 161]. However at lower stress states level, the residual strength of the laminate, as a function of number of cycles, degrades more gradually. This behaviour is described by

degradation models which are often referred to as wearout models. In this model, initially presented by Halpin et al. [162], it is assumed that the residual strength $R(n)$ is a monotonically decreasing function of the number of cycles n, and that the change of the residual strength can be approximated by a power-law growth equation in the form:

$$\frac{dR(n)}{dn} = \frac{-A(\sigma)}{n[R(n)]^{m-1}} \tag{2.82}$$

where $A(\sigma)$ is a function of the maximum cyclic stress σ, and m is a constant.

Progressive damage models

Progressive damage models differ from the above mentioned models since they introduce one or more properly chosen damage variables which describe the deterioration of the composite component. These models are based on a physically sound modelling of the underlying damage mechanisms, which lead to the macroscopically observable degradation of the mechanical properties. The models have been subdivided into two classes: the damage models that predict the damage growth (by meaning the number of transverse matrix cracks per unit length and size of the delaminated area), and the models that correlate the damage growth with the residual mechanical properties (such as stiffness/strength).

Progressive damage models predicting damage growth Bergmann and Prinz [163] and Prinz [164] proposed a specific model for delamination growth:

$$\frac{dA}{dN} = c \cdot f(\mathcal{G}_{it})^n \tag{2.83}$$

where A is the delaminated area, $\mathcal{G}_{it}$ is the maximum variation of the energy release rate and c and n are experimentally determined values.

Feng et al. [165] developed a model for predicting fatigue damage growth in carbon fibre-reinforced specimens due to matrix cracking. From experimental observations, it was concluded that the mode I crack growth could be described by a modified Paris law:

$$\frac{dA}{dN} = D\mathcal{G}_{max}^n \tag{2.84}$$

where A is the damage area due to matrix cracking, N is the number of fatigue cycles, $\mathcal{G}_{max}$ is the maximum strain-energy release rate in a fatigue cycle, and D

and n are material constants.

Hénaff-Gardin et al. [166, 167] had studied progressive matrix cracking in cross-ply laminates. The propagation law under fatigue was established as:

$$\frac{dS}{dN} = A\Big(\frac{\mathcal{G}_I}{\mathcal{G}_{max}}\Big)^n \tag{2.85}$$

where S is the crack surface, $\mathcal{G}_I$ is the strain energy release rate for the current crack density, $\mathcal{G}_{max}$ is the value of the strain energy release rate when the first matrix crack initiates, and A and n are constants, which are determined from experimental measurements of crack density. When $\mathcal{G}_{max}$ is lower than $\mathcal{G}_{Ic}$, the initiation of the first matrix crack requires a micro-damage accumulation during the first fatigue cycles. In that case, a phenomenological law was used to predict the number of cycle, necessary for transverse cracking initiation.

Progressive damage models predicting residual mechanical properties This category of progressive damage models relates the damage variable(s) with the residual mechanical properties (stiffness/strength) of the laminate. The damage growth rate equations are often based on damage mechanics, thermodynamics, micro-mechanical failure criteria or specific damage characteristics (such as crack spacing, delamination area,...).

One of the first methods to calculate stiffness reduction due to matrix cracking is the shear-lag model, established by Highsmith and Reifsnider [168].

Reifsnider [169] further proposed the approach based on "representative volume concept", which has been further divided into critical and sub-critical elements. In the sub-critical elements, damage initiation and propagation was modelled on a micro-mechanical level and the local stress fields were calculated. The other details which are not important for the determination of the local stress field associated with the final failure event are grouped into continuum representations of the critical elements in the representative volume. In this approach the reduction in strength can be calculated using the integral formulation:

$$\frac{S_L^r(\tau_1)}{S_{Lu}^i} = \left[\frac{(F_e/F_L)^i}{(F_e(\tau)/F_L(\tau))}\right]_{rv} \cdot \left[1 - \int_0^{\tau_1} (1 - F_e(\tau))k(t)^{k-1}d\tau\right] \tag{2.86}$$

The quantity on the left hand side is the residual strength, normalized by the initial ultimate strength for that failure mode. The first factor on the right hand side is

the ratio of the initial stress concentration to the current stress concentration in a representative volume (subscript "rv"), where F is a generalized failure function. The subscript e indicates that the value of that failure function F is evaluated in the critical element, and the subscript L indicates the value of F in the laminate at some position remote from the location of the failure event. All quantities in the integral are evaluated in the critical element. The failure function is written as a function of time since the stress state in a critical element changes as damage develops in the sub-critical elements around it.

Ogin et al. [170] showed that the stiffness reduction for a $(0/90)_s$ glass fibre-reinforced laminate can be expressed by the very simple relation:

$$E = E_0(1 - cD) \tag{2.87}$$

where $D = 1/2s$ is the average crack density ($2s$ is the average crack spacing) and c is a constant. Further it was postulated that the crack growth rate is expressed as a power function of the stored elastic energy between two neighbouring cracks in the transverse ply. By using Eq. 2.87, the stiffness degradation rate due to transverse matrix cracking is then obtained as:

$$-\frac{1}{E_0}\frac{dE}{dN} = A\left[\frac{\sigma_{max}^2}{E_0^2(1 - E/E_0)}\right]^n \tag{2.88}$$

where σ_{max} is the maximum fatigue stress level, A and n are constants.

Carswell [171] introduced a model for laminates with unidirectional plies. The damage variable D was related to the length of the matrix cracks in the laminate and the following damage growth rate has been proposed:

$$\frac{dD}{dN} = p\sigma_c\frac{D^2}{N} \tag{2.89}$$

where p is a parameter, c is the cyclic stress amplitude and D is related to the stiffness by Eq. 2.87 determined previously by Ogin et al [170].

2.5.2 Short-Fibre-Reinforced Materials

The fatigue failure mechanism for short fibre-reinforced materials has been investigated intensively by various researchers. In the literature, the mechanism in

fatigue is often considered to consist of the following four stages [172]:

1. Initiation of local damage due to cyclic deformation, generally at the locations of highest stress intensity, i.e. the fibre end [173];
2. Initiation of crack;
3. Crack growth due to cyclic loading. Local modes of crack extension depend on local fibre orientation, matrix ductility and the degree of interfacial adhesion [174]. The mechanisms during breakdown of the composite are: fibre matrix separation along the interfaces of the fibre oriented parallel to the crack; deformation and fracture of the matrix between fibres; fibre pull-out; fracture of transverse (to the crack direction) fibres [175];
4. Fast (unstable) crack growth in the last load cycle, which is comparable to failure in a tensile test.

By experimental evidences on Glass Fibre-Reinforced Polyamide 6 (GFPA), Horst et al. [176] propose a different subdivision of the failure mechanism in the following stages (Fig. 2.12):

1. initiation of damage at the fibre ends;
2. growth of this damage into voids, accompanied by debonding;
3. the voids grow into micro-cracks which may remain bridged by either drawn matrix material or unbroken fibres;
4. the debonding relieves the constraint to which the matrix was subjected, which can therefore deform much more easily, forming bridges between the crack walls;
5. the bridged crack grows, until a critical size is reached, and the specimen fails.

A similar size-like behaviour in fatigue is reported by Dibenedetto and Salee [177] for compact tension specimens of graphite fibre-reinforced PA 66.

Li and Matsumoto [178] presented an analytic model for fatigue crack life prediction in fibre reinforced concrete (FRC). The model elucidates fatigue crack

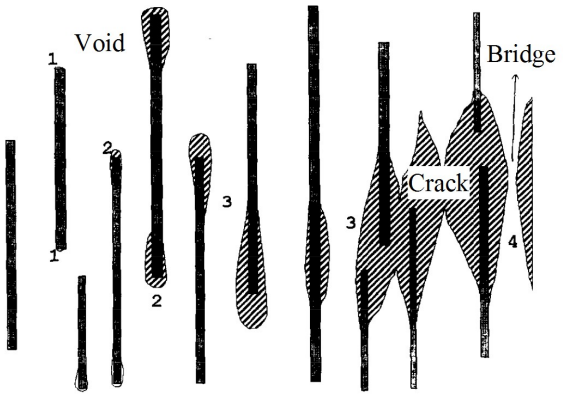

Figure 2.12: Failure mechanism in fatigue: development of damage from left to right.

growth in cementitious matrix material under the influence of external cyclic load and fibre and aggregate bridging. The theoretical model is based on the micro-mechanics of fibre bridging in short fibre reinforced brittle matrix composites and predicts fatigue crack growth, which is responsible for fatigue life of FRCs. The effects of micro-structural parameters (for example, fibre length, fibre diameter, fibre modulus, fibre volume fraction, and interfacial bond strength) on fatigue crack growth are examined.

According to Li and Matsumoto [178], the fatigue crack growth for short fibre composites is simulated with the following three factors. First, fatigue crack growth in the matrix is related to crack-tip-stress intensity factor amplitude with the Paris law. Second, the contribution of crack bridging to the crack-tip-stress intensity factor amplitude is examined using a cyclic constitutive law for the relation between crack bridging stress amplitude and crack opening displacement amplitude. Finally, the influence of frictional bond degradation at the fibre-matrix interface during repeated load cycles is introduced. This influence is assumed to be governed by accumulated crack opening displacement change.

Progressive fatigue damage on material constituents is responsible for fatigue life of a material. Among a number of microscopic changes during fatigue loading, fatigue crack growth can be considered the first responsible for fatigue life damage of FRCs and, therefore, must be focused on. FRCs fail under fatigue when a fracture propagates unstably subsequent to stable crack growth under fatigue loading.

Fatigue crack growth in FRCs is affected by three main factors: matrix fatigue crack growth law specific for matrix, fibre crack bridging, and fatigue damage in the fibre-matrix interface and/or bridging fibres.

Matrix fatigue crack growth has been observed to obey a Paris law type equation for metals, ceramics, and concrete [179–181]. The Paris law gives the relation between the crack growth rate and the crack-tip-stress intensity factor amplitude, namely

$$\frac{da}{dN} = c(\Delta K_{tip})^n \tag{2.90}$$

where a is the crack length, N is the number of load cycles, C and n are Paris constants and ΔK_{tip} is the crack-tip- stress intensity factor amplitude. Hence the fatigue life N_f, can be computed if ΔK_{tip} is known:

$$N_f = \int_{a_i}^{a_f} \frac{1}{C(\Delta K_{tip})^n} da \tag{2.91}$$

where a_i is the initial crack length and a_f is the final crack length. The crack-tip-stress intensity factor amplitude of fibre composites, that depends on N, is attributed to external applied loading and crack bridging, so ΔK_{tip}, can be divided into two terms [178]:

$$\Delta K_{tip} = \Delta K_a + \Delta K_b \tag{2.92}$$

where ΔK_a is the stress intensity factor amplitude due to external applied loading and ΔK_b is the reduction of the stress intensity factor amplitude due to crack bridging (Fig. 2.13).

Interfacial degradation under cyclic loading is suggested by experimental observations in fibre reinforced ceramics and fibre reinforced concrete (Stang and Jun [182]). Interfacial frictional bond degradation seems more reasonable for a composite with pull-out (frictional bond-controlled interface) of (shorter) fibres, whereas fatigue fracture of fibres is more reasonable for a composite with rupture (chemical bond-controlled interface) of (longer) fibres or with high stress amplitude conditions. Following Matsumoto and Li [183] a bilinear function for interfacial frictional bond strength, τ, is assumed:

$$\tau = \max \text{ of } \begin{cases} \tau_i + D \sum_{i=1}^{N} \Delta\delta_i \\ \\ \tau_f \end{cases} \tag{2.93}$$

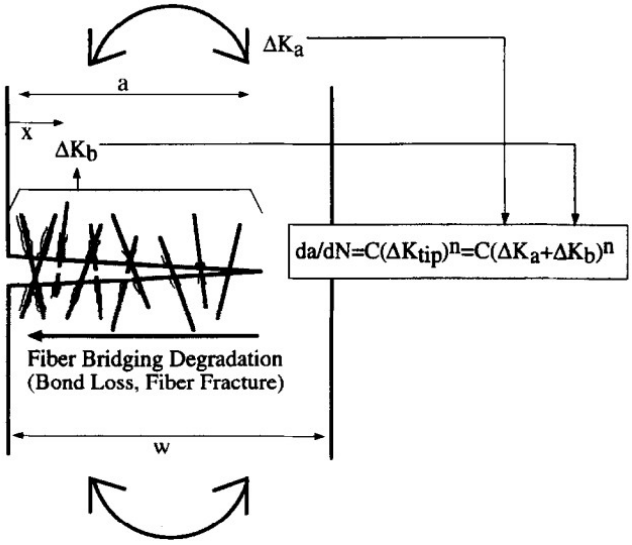

Figure 2.13: Fatigue damage on material constituents [178].

where τ_i is the initial bond strength, D is the degradation coefficient (negative for degradation), N is the number of load cycles, $\Delta\delta_i$ is the crack opening displacement change in the $i-th$ cycle, and τ_f is the final or steady state bond strength. The interfacial bond degradation is measured as

$$\sum_{i=1}^{N} \Delta\delta_i(x) = \text{accumulated crack opening displacement change}$$

where the non-uniform crack opening displacement in a generic case requires that the accumulated crack opening displacement change is a function of the position on the crack surface.

The bond strength degrades more significantly close to the crack mouth, since fibres are subjected to a greater stress amplitude cycles and crack opening displacement changes, whereas the undegraded bond strength is exerted in the newly created crack surface near the crack tip.

Kabir et al. [184] proposed a fatigue model based on a statistical microscopic damage law. Fatigue failure in fibre reinforced composites occurs as a result

of damage accumulation. In micro-mechanical approaches fibre breaking and fibre/matrix interface debonding are studied as principal damage mechanisms which depend on the loading direction. The authors assume that if the composite is loaded normal to the fibre direction, the fibre/matrix debonding, due to a relatively weak interface is the main failure mechanism, whereas in the case of loading parallel to the fibre axis (for example push-pull direction) mainly fibre breaking is observed. The statistical analysis of fibre breaking and fibre/matrix interfacial debonding can be predicted through Weibull's law [185, 186]. This law expresses the longitudinal (in fibre direction) tensile strength of the fibre reinforced composite in terms of parameters of the statistical distribution of the fibre strengths. It is based on the assumption that the composite fails as a result of accumulation of statistically distributed fibre flaws.

Kabir et al. [184] expressed the equation of Weibull's damage law for a reinforcing material particle failure:

$$P(\sigma_p) = 1 - exp\Big[-\Big(\frac{\sigma_p}{\sigma_0}\Big)^m\Big] \tag{2.94}$$

where $P(\sigma_p)$ is the fracture probability of a particle, σ_0 is the characteristic stress corresponding to the scatter of the particle failure in the composite, σ_p is the maximum principal stress along the particle and m is the Weibull parameter (shape parameter of particle strength distribution). This particle failure can be supplemented by fibre breaking, e.g. perpendicular to the fibre direction and fibre/matrix interfacial debonding. Weibull's law can directly relate the tensile strength of the material with damage in the material. The two Weibull parameters are related to the fibre or the fibre/matrix interface strength which determines the composite damage.

According to Kabir et al. [184], a principal source of damage is the failure of the fibre/matrix interface. This failure is governed by a local criterion that is dominated by interfacial normal stress. Since the interfacial damage is distributed statistically as a function of the spatial distribution of the micro-structure, the local interface failure criterion must be written in a statistical form following Weibull's law:

$$P^{deb}(\overline{\sigma}_L) = 1 - exp\left[-\left(\sqrt{\Big(\frac{\overline{\sigma}_L^U}{\overline{\sigma}_{0L}}\Big)^2 + \Big(\frac{\overline{\tau}_L^U}{\overline{\tau}_{0L}}\Big)^2}\right)^{m_L}\right] \tag{2.95}$$

where $P^{deb}(\overline{\sigma}_L)$ denotes the fibre/matrix interfacial debonding probability relative to a given interfacial state $\overline{\sigma}_L^U$ which is a function of the microscopic stress $\overline{\sigma}_L$, $\overline{\sigma}_{0L}$ denotes the interfacial stress and m_L is the statistical parameter. The parameter $\overline{\tau}_L^U$ denotes the interfacial shear stress and $\overline{\tau}_{0L}$ is the characteristic shear stress. If the fibre is perpendicular to the loading direction (90°), there is no significant influence of shear stresses and the equation can be written as follows:

$$P^{deb}(\overline{\sigma}_L) = 1 - exp\Big[-\Big(\frac{\overline{\sigma}_L^U}{\overline{\sigma}_{0L}}\Big)^{m_L}\Big] \tag{2.96}$$

The stress state of a cell can be predicted by the mixing rule [187] in which undebonding stresses and debonding stresses are taken into account:

$$\overline{\sigma}(\overline{\varepsilon}) = \big[1 - P^{deb}(\overline{\sigma}_L)\big]\overline{\sigma}_{ud}(\overline{\varepsilon}) + P^{deb}(\overline{\sigma}_L)\overline{\sigma}_{db}(\overline{\varepsilon}) \tag{2.97}$$

where $\overline{\sigma}_{ud}(\overline{\varepsilon})$ is the stress in an undamaged unit cell and $\overline{\sigma}_{db}(\overline{\varepsilon})$ is the stress in a damaged unit cell due to fibre/matrix interfacial debonding. In this equation $\overline{\sigma}(\overline{\varepsilon})$ is the stress behaviour of a composite cell with fibre perpendicular to the loading direction that includes the debonding damage behaviour. The first term on the right hand side indicates the stress-strain relation of the undamaged interface and the second term indicates the stress behaviour of damaged interface in a composite. Thus, the arithmetic sum in Eq. 2.97 expresses the stress behaviour of a composite cell in presence of debonding failure.

When loading is oriented parallel to the fibre axis, Kabir et al. [184] found that fibre failure is the principle source of damage in the composite. The fracture probability of each fibre is a function of its volume and of the maximum principal stress $\overline{\sigma}_F^U$ in the fibre.

Therefore, Weibull's law in Eq. 2.94 can be written in terms of fibre failure as follows:

$$P^{brk}(\overline{\sigma}_F) = 1 - exp\Big[-\Big(\frac{\overline{\sigma}_F^U}{\overline{\sigma}_{0F}}\Big)^{m_F}\Big] \tag{2.98}$$

In this equation $P^{brk}(\overline{\sigma}_F)$ is the failure probability of fibre fracture and m_F is the shape parameter of Weibull's law which corresponds to the scatter of the fibre breaking in the composite. $\overline{\sigma}_{0F}$ is a scale parameter, equivalent to the mean value of the fibre strength which gives a cumulative breaking probability of 63%, i.e. corresponds to 63% of broken fibres for a given fibre reinforced composite. This

parameter is strongly related to the reinforcement material. From experimental data, Kabir et al. [184] note that, in case of parallel loading, there is a combined effect of fibre breaking and debonding on the composite failure. Both these effects can be combined in a composite unit cell using the mixing rule:

$$\begin{aligned}\overline{\sigma}(\overline{\varepsilon}) =&\left[1 - P^{deb}(\overline{\sigma}_L) - P^{brk}(\overline{\sigma}_F)\right]\overline{\sigma}_{ud}(\overline{\varepsilon})+\\ &+P^{deb}(\overline{\sigma}_L)\overline{\sigma}_{db}(\overline{\varepsilon}) + P^{brk}(\overline{\sigma}_F)\overline{\sigma}_{brk}(\overline{\varepsilon})\end{aligned} \tag{2.99}$$

where $\overline{\sigma}_{brk}(\overline{\varepsilon})$ is the stress in a damaged unit cell due to the broken fibre.

The two Weibull parameters for interface failure and fibre failure are numerically identified by using the data from micro-mechanical models and the calculated finite element results to fit the experimental curves obtained from tensile tests.

Chapter 3

Homogenization Model for Short Fibre Reinforced Composite

3.1 Introduction

Whereas in the previous Chapter, a general description of the homogenization models present in literature has been given, in this Chapter the homogenization approach adopted to describe the macroscopic mechanical behaviour of short fibre-reinforced composites is shown. In the present Ph.D. Thesis, such an approach, based on the formulation proposed by Kalamkarov and Li [15], is modify by taking into account the generic fibre orientation by means of suitable probability functions [20], and by introducing a parameter (sliding function) that allows to quantify the fibre-matrix bond effectiveness. The basic assumptions of the proposed model are:

1. The fibres and the matrix are linearly elastic, the matrix is isotropic, and the fibres have uniaxial mechanical behaviour;
2. The fibres are cylindrical and identical in shape and size;
3. The fibres and matrix are well bonded at their interface, and remain that way during deformation (the debonding phenomenon is taken into account

by a further model explained in the present Chapter and in Chapter 5).

In Section 3.4 the effects of fibre orientation on the mechanical parameters of the composite material are analysed and a suitable formulation has been proposed. In Section 3.5 the debonding phenomenon at fibre-matrix interface is described through the classical "Shear Lag" model proposed by Cox [24] whereas a sliding function parameter has been introduced to account for the fibre matrix-detachment.

Finally, in Section 3.6 the fibre failure and their reciprocal interaction are taken into account by means of appropriate approaches proposed by the Author.

3.2 Equilibrium problem in a composite material

As is well-known, the equilibrium of a continuous body occupying a volume B can be mathematically stated as follows:

$$div\boldsymbol{\sigma} + \boldsymbol{b} = 0 \qquad \text{in } B \tag{3.1a}$$

$$\boldsymbol{\sigma} \cdot \boldsymbol{n} = \boldsymbol{t} \qquad \text{on } \Gamma_t \tag{3.1b}$$

$$\boldsymbol{u} = \boldsymbol{u}_0 \qquad \text{on } \Gamma_u \tag{3.1c}$$

where $\boldsymbol{u}, \boldsymbol{\sigma}, \boldsymbol{b}$ and $\boldsymbol{n}$ are the displacement field, the stress tensor, the body forces and the unit outward normal to the boundary, respectively; $\boldsymbol{t}$ and $\boldsymbol{u}_0$ represent the prescribed traction and displacement on the portion Γ_t and Γ_u of the boundary (Fig. 3.1) where traction and displacement are prescribed. The linearised strain-displacement equation is given by the relationship:

$$\boldsymbol{\varepsilon} = sym(grad\,\boldsymbol{u}) = sym\big[\nabla \otimes \boldsymbol{u}\big] = \frac{1}{2}\Big[(grad\,\boldsymbol{u}) + (grad\,\boldsymbol{u})^t\Big] \tag{3.2}$$

where $\boldsymbol{\varepsilon}$ is the strain tensor and the symbols "∇" and "$\otimes$" stand for gradient and tensor operator product, respectively. The incremental elastic constitutive relation, written in a specific point of the material, can be expressed as:

$$\dot{\boldsymbol{\sigma}}(\boldsymbol{x}) = \boldsymbol{C}' : \dot{\boldsymbol{\varepsilon}}(\boldsymbol{x}) = \boldsymbol{C}' : \big[sym(grad\dot{\boldsymbol{u}})\big] = \boldsymbol{C}' : sym\big[sym(\nabla \otimes \boldsymbol{u})\big] \tag{3.3}$$

where the dot applied to the stress tensor and to the displacement field denotes an increment, $\boldsymbol{C}'(\boldsymbol{x})$ is the fourth order tangent elastic tensor and $\boldsymbol{x}$ is the position vector that identifies the location of the point inside the body.

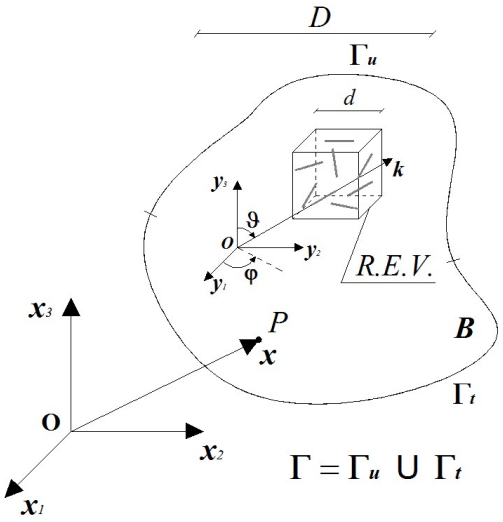

Figure 3.1: Body made of a fibre-reinforced composite material

The heterogeneous (composite) material is supposed to be composed by one matrix phase, denoted by the subscript m, and by q different fibre phases embedded in the matrix (Fig. 3.1). By assuming that the fibres belonging to the same phase p have the same length $2L_f^p$ and cross section A_f^p, and that their orientations are randomly arranged in the solid angle, the following assumption can be made: each direction is equally represented. The direction of a single fibre can be identified by the unit vector $\boldsymbol{k}$ parallel to its axis; by using the polar angles φ and ϑ (Fig. 3.1), such a vector can be written as:

$$\boldsymbol{k} = \{k_1 \quad k_2 \quad k_3\} = \{\sin\vartheta \cdot \cos\varphi \quad \sin\vartheta \cdot \sin\varphi \quad \cos\vartheta\} \tag{3.4}$$

A fundamental hypothesis for the mechanical model developed is the assumptions that each fibre phase is homogeneously distributed inside the matrix and that a reference elementary volume (R.E.V.), having a characteristic length d, has the same average composition - and consequently the same mechanical properties - of the composite. Moreover, the characteristic length D of the body is assumed to be much greater than the characteristic length d, i.e. $d/D \ll 1$ and this implies that the composite is macroscopically homogeneous. By considering the R.E.V., the

following volume fractions of each component can be defined:

$$\begin{aligned} &\mu_m = V_m/V && \text{matrix volume fraction} \\ &\mu_f^p = V_f^p/V && \text{fibre volume fraction of the } p-th \text{ fibre phase} \end{aligned} \tag{3.5}$$

where V, V_m and V_f^p are the R.E.V. volume, the matrix volume and the $p-th$ fibre phase volume in the R.E.V., respectively. It is trivial to observe that:

$$V = V_m + \sum_{p=1}^{q} V_f^p \qquad \text{or} \qquad 1 = \mu_m + \sum_{p=1}^{q} \mu_f^p$$

3.3 Equivalent homogeneous material

Under the previous hypothesis, the average properties of the composite material can be determined. This goal can be obtained by equating the virtual work rate $\dot{w}$ evaluated in the composite material, with that in the homogenised equivalent material [15, 188]. By introducing a generic virtual displacement field $\tilde{\boldsymbol{u}}$, and the corresponding virtual strain tensor $\tilde{\boldsymbol{\varepsilon}}$ and virtual strain rate tensor $\dot{\tilde{\boldsymbol{\varepsilon}}}$, defined as follows:

$$\tilde{\boldsymbol{\varepsilon}} = sym(grad\, \tilde{\boldsymbol{u}}) = sym[\nabla \otimes \tilde{\boldsymbol{u}}], \qquad \dot{\tilde{\boldsymbol{\varepsilon}}} = \left[sym(\nabla \otimes \dot{\tilde{\boldsymbol{u}}})\right] \tag{3.6}$$

the stated condition can be written, for a generic composite volume V, equal or greater than the R.E.V. volume, as fallows:

$$\dot{w} = \overbrace{\int_V \kappa(\boldsymbol{x}) \cdot \dot{\tilde{\boldsymbol{\varepsilon}}} : \boldsymbol{\sigma} dV + \sum_{p=1}^{q} \int_V \chi(\boldsymbol{x}) \cdot \dot{\tilde{\boldsymbol{\varepsilon}}}_f \cdot \boldsymbol{\sigma}_f dV}^{\text{composite's work rate}} = \overbrace{\int_V \dot{\tilde{\boldsymbol{\varepsilon}}} : \boldsymbol{\sigma}_{eq} dV}^{\text{homogenized material's work rate}} \tag{3.7}$$

where $\tilde{\varepsilon}_f$ and σ_f are the virtual strain and the stress in a fibre belonging to the given $p-th$ phase, respectively. The scalar functions $\kappa(\boldsymbol{x})$ and $\chi_p(\boldsymbol{x})$ are defined as:

$$\kappa(\boldsymbol{x}) = \begin{cases} 1 & \text{if } (\boldsymbol{x}) \in V_m \\ 0 & \text{if } (\boldsymbol{x}) \notin V_m \end{cases} \qquad \text{and} \qquad \chi_p(\boldsymbol{x}) = \begin{cases} 1 & \text{if } (\boldsymbol{x}) \in V_f^p \\ 0 & \text{if } (\boldsymbol{x}) \notin V_f^p \end{cases} \tag{3.8}$$

They identify the location of the point $\boldsymbol{x}$ in the matrix or in the reinforced phase, respectively. The fibre stress can be evaluated by means of its elastic modulus E_f^p multiplied by the fibre strain ε_f, while the stress tensor of the homogenised equivalent material $\boldsymbol{\sigma}_{eq}$ can be obtained from the equivalent elastic tensor $\boldsymbol{C}_{eq}$ multiplied by the actual strain tensor $\boldsymbol{\varepsilon}$. If a linear elastic behaviour for the fibres and for the equivalent homogenised material is assumed, the following relationship can be written:

$$\sigma_f = E_f^p \cdot (\boldsymbol{k} \otimes \boldsymbol{k}) : \boldsymbol{\varepsilon}(\boldsymbol{x}) \tag{3.9a}$$

$$\boldsymbol{\sigma}_{eq}(\boldsymbol{x}) = \boldsymbol{C}_{eq}(\boldsymbol{x}) : \boldsymbol{\varepsilon}(\boldsymbol{x}) \tag{3.9b}$$

The expression (3.9a) is written by observing that the strain measured in the fibre direction is equal to $\varepsilon_f = (\boldsymbol{k} \otimes \boldsymbol{k}) : \boldsymbol{\varepsilon}(\boldsymbol{x})$, and analogous to the virtual strain $\tilde{\varepsilon}_f$ and virtual strain rate, $\dot{\tilde{\varepsilon}}_f$, are equal to $\tilde{\varepsilon}_f = (\boldsymbol{k} \otimes \boldsymbol{k}) : \tilde{\boldsymbol{\varepsilon}}(\boldsymbol{x})$, $\dot{\tilde{\varepsilon}}_f = (\boldsymbol{k} \otimes \boldsymbol{k}) : \dot{\tilde{\boldsymbol{\varepsilon}}}(\boldsymbol{x})$, respectively. By inserting Eqs. (3.9) in the expression of the virtual work rate (Eq. (3.7)), the following expression can be obtained:

$$\begin{aligned} \dot{w} = &\int_V \kappa(\boldsymbol{x}) \dot{\tilde{\boldsymbol{\varepsilon}}}(\boldsymbol{x}) : \boldsymbol{C}_m(\boldsymbol{x}) : \boldsymbol{\varepsilon}(\boldsymbol{x}) dV + \\ &+ \sum_{p=1}^{q} \int_V \chi_p(\boldsymbol{x}) \cdot (\boldsymbol{k} \otimes \boldsymbol{k}) : \dot{\tilde{\boldsymbol{\varepsilon}}}(\boldsymbol{x}) \cdot E_f^p \cdot (\boldsymbol{k} \otimes \boldsymbol{k}) : \boldsymbol{\varepsilon}(\boldsymbol{x}) dV = \\ &= \int_V \dot{\tilde{\boldsymbol{\varepsilon}}}(\boldsymbol{x}) : \boldsymbol{C}_{eq}(\boldsymbol{x}) : \boldsymbol{\varepsilon}(\boldsymbol{x}) dV \end{aligned} \tag{3.10}$$

where $\boldsymbol{\varepsilon}_f$ indicates the strain measured at the fibre location along its axis. The previous relationship can be rewritten as:

$$\begin{aligned} \int_V \dot{\tilde{\boldsymbol{\varepsilon}}}(\boldsymbol{x}) : \left\{ \kappa(\boldsymbol{x}) \boldsymbol{C}_m(\boldsymbol{x}) + \sum_{p=1}^{q} \chi_p(\boldsymbol{x}) \left[E_f^p \cdot (\boldsymbol{F} \otimes \boldsymbol{F}) \right] \right\} : \boldsymbol{\varepsilon}(\boldsymbol{x}) dV = \\ \int_V \dot{\tilde{\boldsymbol{\varepsilon}}}(\boldsymbol{x}) : \boldsymbol{C}_{eq}(\boldsymbol{x}) : \boldsymbol{\varepsilon}(\boldsymbol{x}) dV \end{aligned} \tag{3.11}$$

where the second-order tensor $\boldsymbol{F} = \boldsymbol{k} \otimes \boldsymbol{k}$ has been introduced. It is trivial to observe that, since the equivalent material is macroscopically homogeneous (at least at the scale of the R.E.V.), the elastic equivalent tensor $\boldsymbol{C}_{eq}(\boldsymbol{x})$ can be assumed to be constant with respect to the position vector $\boldsymbol{x}$, i.e. $\boldsymbol{C}_{eq}(\boldsymbol{x}) = \boldsymbol{C}_{eq}$. By comparing the first and the second member of Eq. (3.11), the equivalent elastic tensor can be

recognised, and its mean value over the volume V can be obtained:

$$\begin{aligned} \boldsymbol{C}_{eq} &= \frac{1}{V} \cdot \int_V \left\{ \kappa(\boldsymbol{x}) \boldsymbol{C}_m(\boldsymbol{x}) + \sum_{p=1}^{q} \chi_p(\boldsymbol{x}) \left[E_f^p \cdot (\boldsymbol{F} \otimes \boldsymbol{F}) \right] \right\} dV = \\ &= \mu_m \cdot \boldsymbol{C}_m + \sum_{p=1}^{q} \mu_f^p E_f^p \cdot \int_V \boldsymbol{F} \otimes \boldsymbol{F} dV \end{aligned} \tag{3.12}$$

where the following definitions of the fibre and matrix volume fractions (see Eq (3.5)) have been used:

$$\mu_m = \frac{1}{V} \int_V \kappa(\boldsymbol{x}) dV = \frac{V_m}{V} \qquad \mu_f^p = \frac{1}{V} \int_V \chi(\boldsymbol{x}) dV = \frac{V_f^p}{V} \tag{3.13}$$

The tangent elastic quantities of the materials must be introduced to calculate the increment of stresses in the matrix, $\dot{\boldsymbol{\sigma}}_m$, in the fibre, $\dot{\boldsymbol{\sigma}}_f$, and in the equivalent material, $\dot{\boldsymbol{\sigma}}_{eq}$, when an incremental condition is considered:

$$\dot{\boldsymbol{\sigma}}(\boldsymbol{\varepsilon}) = \boldsymbol{C}'_m(\boldsymbol{\varepsilon}) : \dot{\boldsymbol{\varepsilon}}, \quad \dot{\sigma}_f(\varepsilon_f^m) = \left(\frac{d\sigma_f}{d\varepsilon_f} \cdot \frac{d\varepsilon_f}{d\varepsilon_f^m} \right)_p \dot{\varepsilon}_f, \quad \dot{\boldsymbol{\sigma}}_{eq} = \boldsymbol{C}'_{eq}(\boldsymbol{\varepsilon}) : \dot{\boldsymbol{\varepsilon}} \tag{3.14}$$

where $\boldsymbol{C}'_m$ and $\boldsymbol{C}'_{eq}$ are the tangent elastic tensor of the matrix and of the equivalent material, respectively, while ε_f^m and ε_f are the strain in the matrix measured in the fibre direction and the actual fibre strain, respectively. For the sake of simplicity, all the equations are written with reference to the actual matrix strain tensor. In the following, in order to simplify the notation, the hypothesis of a single fibre phase present in the composite is made, and the sum over the index p is omitted. By remembering Eqs. (3.14), the equivalent tangent elastic tensor $\boldsymbol{C}'_{eq}(\boldsymbol{\varepsilon})$ of the equivalent homogenised material can be obtained from Eq. (3.12) as:

$$\begin{aligned} \boldsymbol{C}'_{eq} &= \frac{1}{V} \cdot \int_V \left[\kappa(\boldsymbol{x}) \cdot \boldsymbol{C}'_m + \chi(\boldsymbol{x}) \cdot \left(\frac{d\sigma_f}{d\varepsilon_f^m} \right) \cdot \boldsymbol{F} \otimes \boldsymbol{F} \right] dV = \\ &= \mu_m \cdot \boldsymbol{C}'_m + \mu_f \cdot \underbrace{\left(\frac{d\sigma_f}{d\varepsilon_f^m} \right) \cdot \int_V \boldsymbol{F} \otimes \boldsymbol{F} dV}_{\boldsymbol{C}'_f} = \mu_m \cdot \boldsymbol{C}'_m + \mu_f \cdot \boldsymbol{C}'_f \end{aligned} \tag{3.15}$$

In order to evaluate the tangent elastic tensor $\boldsymbol{C}'_{eq}$, the last integral in Eq. (3.15) can be computed on a hemisphere of radius R having a generic volume V_{hem}

(greater than the R.E.V. volume in order to be sufficiently representative of the macroscopic mechanical behaviour of the composite) and divided by the hemisphere volume itself, with the aim to represent all the possible fibre orientations inside the composite:

$$\begin{aligned}\frac{1}{V_{hem}}\int_V \boldsymbol{F}\otimes\boldsymbol{F}dV &= \int_0^R\int_0^{2\pi}\int_0^{\pi/2}(\boldsymbol{F}\otimes\boldsymbol{F})r\, r\sin\vartheta d\varphi d\vartheta dr = \\ &= \frac{R^3}{3}\frac{1}{\frac{2}{3}\pi R^3}\int_0^{2\pi}\int_0^{\pi/2}(\boldsymbol{F}\otimes\boldsymbol{F})\sin\vartheta d\varphi d\vartheta = \\ &= \frac{1}{2\pi}\int_0^{2\pi}\int_0^{\pi/2}(\boldsymbol{F}\otimes\boldsymbol{F})\sin\vartheta d\varphi d\vartheta\end{aligned} \tag{3.16}$$

In the case of a fibre phase homogeneously distributed and oriented inside the matrix, the elastic tensor contribution of the fibres, $\boldsymbol{C}_f$, to the elastic tensor of the composite, $\boldsymbol{C}_{eq}$, that is isotropic if also the matrix material is isotropic, can be simply estimated and the integral of Eq. (3.16) can be evaluated in a simple way.

Some terms of the elasticity tensor $\boldsymbol{C}_f$ are the following ones:

$$\begin{aligned}&C^f_{1111} = \frac{1}{5}\mu_f E_f, \quad C^f_{1122} = \frac{1}{15}\mu_f E_f, \quad C^f_{1133} = \frac{1}{15}\mu_f E_f, \\ &C^f_{1112} = C^f_{1123} = C^f_{1113} = 0 \quad C^f_{1212} = \frac{1}{15}\mu_f E_f, \quad .....\end{aligned} \tag{3.17}$$

where E_f is the elastic modulus of the fibres.

All the above relationships have been obtained under the hypothesis of perfect bond at fibre-matrix interface, i.e. the actual strain in the fibre can be simply written from the matrix strain tensor $\boldsymbol{\varepsilon}(\boldsymbol{x})$ as $\varepsilon^m_f(\boldsymbol{x}) = \varepsilon_f(\boldsymbol{x}) = (\boldsymbol{k}\otimes\boldsymbol{k}) : \boldsymbol{\varepsilon}(\boldsymbol{x})$.

3.4 Influence of fibre orientation

The reinforcing phase is assumed to be composed by fibres having length and cross section area equal to $2L_f$ and A_f, respectively. In order to generalize the above formulation, the fibre orientation is supposed to be described through Gaussian-like probability density functions, $p_\varphi(\varphi)$ and $p_\vartheta(\vartheta)$, where the angles φ and ϑ (characterised by mean values $\overline{\varphi}$ and $\overline{\vartheta}$ and the corresponding variations, δ_φ and δ_ϑ, respectively) are used to identify the fibre axial direction. In such a way, preferential orientations of the reinforcing fibres can be simply considered, whereas

the particular case of random fibre distribution can be also modelled by properly setting the functions $p_\varphi(\varphi)$ and $p_\vartheta(\vartheta)$. The probability distribution functions of the orientation angles can be written as:

$$p_\alpha(\alpha) = A_\alpha(\alpha) + B_\alpha(\alpha) + C_\alpha(\alpha) \tag{3.18}$$

with

$$\begin{aligned}
A_\alpha(\alpha) &= \frac{1}{\sqrt{2 \cdot \pi \cdot \delta_\alpha^2}} \cdot e^{-\frac{1}{2} \cdot \left(\frac{\alpha-\lambda}{\delta_\alpha}\right)^2} \\
B_\alpha(\alpha) &= \frac{1}{\sqrt{2 \cdot \pi \cdot \delta_\alpha^2}} \cdot e^{-\frac{1}{2} \cdot \left(\frac{\alpha-\lambda-\pi}{\delta_\alpha}\right)^2} \\
C_\alpha(\alpha) &= \frac{1}{\sqrt{2 \cdot \pi \cdot \delta_\alpha^2}} \cdot e^{-\frac{1}{2} \cdot \left(\frac{\alpha-\lambda+\pi}{\delta_\alpha}\right)^2} \\
\alpha &= \varphi, \quad \vartheta \qquad\qquad 0 \leq \alpha \leq \pi
\end{aligned}$$

where λ represents the mean value of the probability density functions (i.e. $\lambda = \overline{\varphi}$ or $\lambda = \overline{\vartheta}$). The assumed probability density functions satisfy the unit cumulated probability condition, i.e. $\int_0^\pi p_\varphi(\varphi) = 1$ and $\int_0^\pi p_\vartheta(\vartheta) = 1$ over the solid angle. The above definition of functions $p_\varphi(\varphi)$ and $p_\vartheta(\vartheta)$ allows to consider fibres lying along a given direction in the evaluation of the integral of (3.16). In such a case, the last integral in Eq. (3.16) can be rewritten as:

$$\begin{aligned}
&\int_{SolidAngle} p_\varphi(\varphi) \cdot p_\vartheta(\vartheta) \cdot \boldsymbol{F} \otimes \boldsymbol{F} d\varphi d\vartheta = \\
&= \int_0^\pi \int_0^\pi p_\varphi(\varphi) \cdot p_\vartheta(\vartheta) \cdot (\boldsymbol{F} \otimes \boldsymbol{F}) d\varphi d\vartheta
\end{aligned} \tag{3.19}$$

Consequently, Eq. (3.15) becomes:

$$\boldsymbol{C}'_{eq} = \mu_m \cdot \boldsymbol{C}'_m + \mu_f \cdot \left(\frac{d\sigma_f}{d\varepsilon_f^m}\right) \cdot \int_0^\pi \int_0^\pi p_\varphi(\varphi) \cdot p_\vartheta(\vartheta) \cdot (\boldsymbol{F} \otimes \boldsymbol{F}) d\varphi d\vartheta \tag{3.20}$$

The contribution of each fibre, quantified by means of the previous integral, is maximum when its direction is coincident with the mean value of the probability density functions ($\bar{\varphi}$ and $\bar{\vartheta}$), while it becomes equal to zero when the fibre axis is normal to the above directions (i.e. $\overline{\varphi} \pm \pi/2$ and $\overline{\vartheta} \pm \pi/2$) (Fig. 3.2).

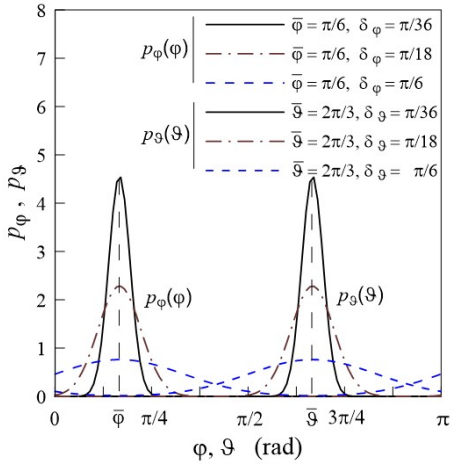

Figure 3.2: Probability distribution functions p_φ and p_ϑ used for the evaluation of the integral in Eq. (3.20).

The simple case of fibres randomly oriented in every direction of the solid angle can be obtained from Eq. (3.19) by setting $p_\varphi(\varphi) = \pi/2$ and $p_\vartheta(\vartheta) = \sin(\vartheta)$, leading to both the macroscopic fibre tangent tensor $\boldsymbol{C}'_f$ and the tangent tensor of the composite $\boldsymbol{C}'_{eq}$ to be isotropic.

In the case of fibres preferentially oriented along a given direction, the resulting composite material has generally an anisotropic behaviour with respect to a global coordinate system, while it can be considered to be transversally isotropic in a local coordinate system with the symmetry axis coincident with the fibre orientation direction.

All the above relations are based on the perfect bond hypothesis between the fibres and the matrix.

The formulation proposed is used to evaluate the elastic properties of a fibre reinforced material having randomly arranged or preferentially oriented fibres (a 2D material lying on the x-y plane and reinforced with fibres belonging to such a plane, i.e. $\overline{\vartheta} = \pi/2$ is assumed for the sake of simplicity). By considering different matrix-fibre Young modulus ratios, $\gamma = E_f/E_m$, and a matrix Poisson's ratio equal to $\nu_m = 0.33$, the mechanical properties of the obtained composite material, in terms of elastic moduli and Poisson's ratios, are determined. In Figure 3.3 the dimensionless elastic moduli in the x- and y- directions are represented against the

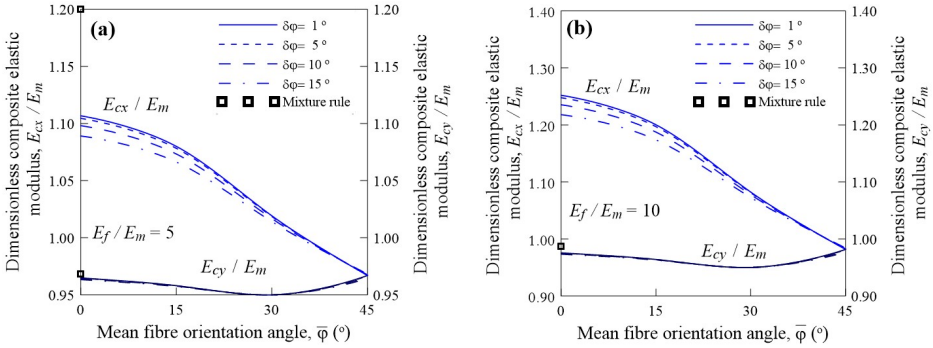

Figure 3.3: Dimensionless composite elastic modulus along the x- direction, E_{cx}/E_m, and the y- direction, E_{cy}/E_m, for fibre-matrix elastic modulus ratio $\gamma = 5$ (a) and $\gamma = 10$ (b), against the mean orientation angle $\overline{\varphi}$ of the fibres (measured counter clockwise with respect to the x-axis) for different fibre angle deviations δ_φ.

mean orientation angle of the fibres, $\overline{\varphi}$, by assuming the variance δ_φ of the angle in the range $1^o \div 15^o$. As can be observed, the elastic modulus tends to increase as the fibres approach the direction related to the elastic modulus under consideration; on the other hand it can be noticed as, by increasing the angle variance, the elastic modulus tends to decrease (increase) in the direction nearly parallel (perpendicular) to the fibres. The above described behaviour can be appreciated for both the considered fibre-matrix elastic modulus ratios $\gamma = 5$ and 10 (Fig. 3.3a and 3.3b).

In Figure 3.4, the variation of the Poisson's ratio ν_{xy} against the mean orientation angle of the fibres $\overline{\varphi}$ is represented; as can be observed, the value increases by increasing $\overline{\varphi}$. The effect of δ_φ is practically negligible.

In Figure 3.5, the elastic properties of a unidirectional fibre-reinforced composite (Fig. 3.5a) is represented against the fibre volume content for a material characterised by $E_m = 70GPa$, $E_f = 450GPa$ ($E_f/E_m = 6.4$) and $\nu_m = 0.3$, together with some results from Kari et al. [18]. As can be noted, the dimensionless elastic modulus E_{cx}/E_m is correctly represented by the present model. In Figure 3.5b, the case of a randomly distributed fibre-reinforced composite is represented against the fibre volume content for a material having $E_f/E_m = 10$, $E_f/E_m = 30$ and $\nu_m = 0.33$, together with some results from Kalamkarov et al. [15]. As can be noted, the isotropic elastic modulus and the Poisson's ratio are in good agreement with the literature results. It can be observed that the composite Poisson's ratio tends to decrease (approaching the value 1/4) by increasing the fibre volume content.

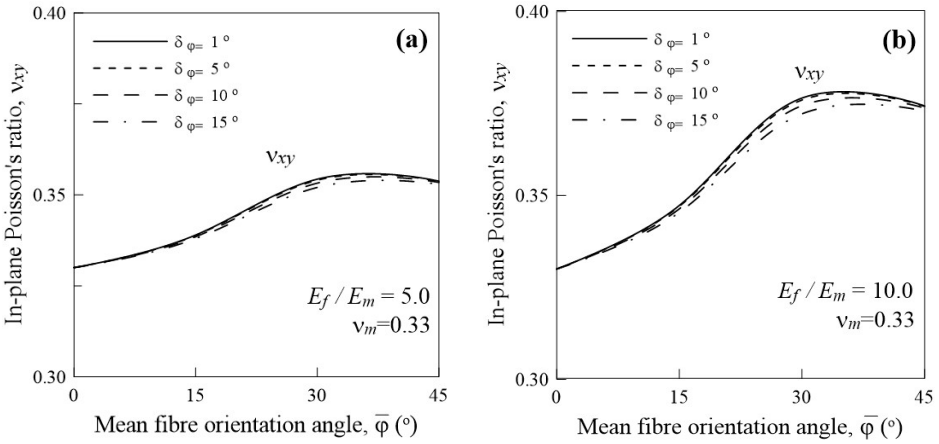

Figure 3.4: Composite Poisson's ratio in the x-y plane, ν_{xy} for fibre-matrix elastic modulus ratio $\gamma = 5$ (a) and $\gamma = 10$ (b), against the mean orientation angle $\overline{\varphi}$ of the fibres (measured counter clockwise with respect to the x-axis) for different fibre angle deviations δ_{φ}.

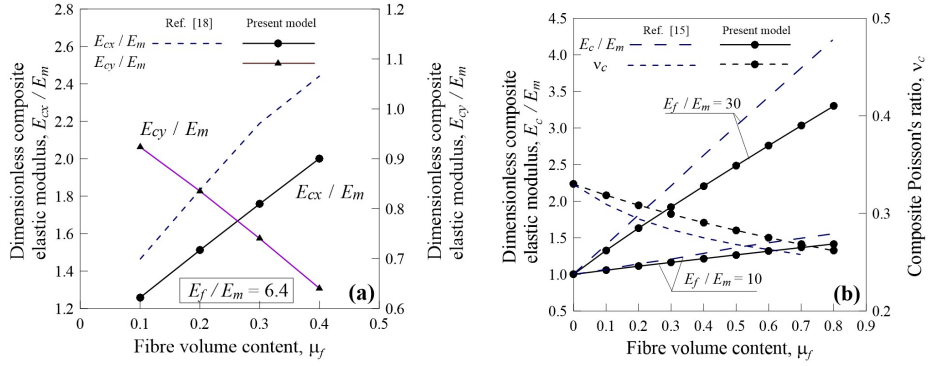

Figure 3.5: Dimensionless composite elastic modulus along the x- direction, E_{cx}/E_m, and the y- direction, E_{cy}/E_m, for unidirectional fibres (a) and dimensionless composite elastic modulus, E_c/E_m, for randomly arranged fibres (b), against the fibre volume content. Results by [15] and by [18] are also reported.

3.5 Fibre-matrix debonding

When an imperfect bond between the reinforcing fibre and the matrix can take place, a strain jump, $[[\varepsilon_{f-m}]]$, can be assumed to exist at the fibre-matrix interface. Such a strain jump can be written as:

$$[[\varepsilon_{f-m}(\boldsymbol{x})]] = \varepsilon_f^m(\boldsymbol{x}) - \varepsilon_f(\boldsymbol{x}) \tag{3.21}$$

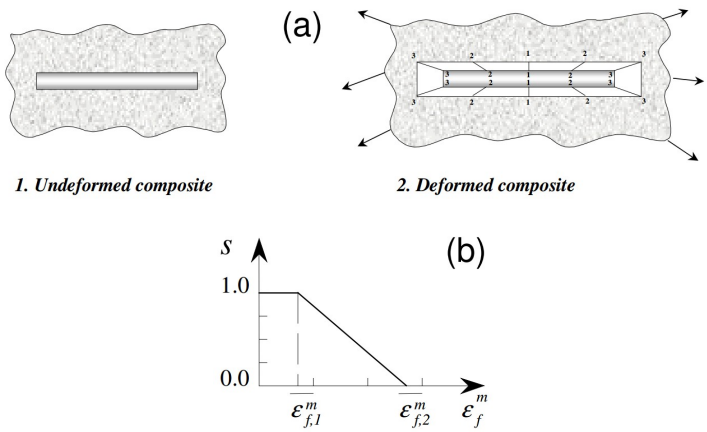

Figure 3.6: Imperfect bonds between the fibre and matrix (a). A simplified relationship assumed to describe strain jump at the interface (b)

where $\varepsilon_f^m(\boldsymbol{x})$ is the matrix strain along the fibre direction and $\varepsilon_f(\boldsymbol{x})$ is the strain in the fibre. In order to refer the actual fibre strain $\varepsilon_f(\boldsymbol{x})$ to the matrix strain, $\boldsymbol{\varepsilon}$, when the sliding occurs, the actual fibre strain can be written as:

$$\begin{aligned}\varepsilon_f(\boldsymbol{x}) &= \varepsilon_f^m(\boldsymbol{x}) - [[\varepsilon_{f-m}(\boldsymbol{x})]] = \varepsilon_f^m(\boldsymbol{x}) \cdot \Big[1 - \big(1 - s(\varepsilon_f^m(\boldsymbol{x}))\big)\Big] = \\ &= \varepsilon_f^m(\boldsymbol{x}) \cdot s(\varepsilon_f^m(\boldsymbol{x})) = \big[(\boldsymbol{k} \otimes \boldsymbol{x}) : \boldsymbol{\varepsilon}(\boldsymbol{x})\big]\end{aligned} \tag{3.22}$$

Consequently:

$$[[\varepsilon_{f-m}(\boldsymbol{x})]] = \varepsilon_f^m(\boldsymbol{x}) \cdot \big[1 - s(\varepsilon_f^m(\boldsymbol{x}))\big] \tag{3.23}$$

The scalar function $s(\varepsilon_f^m(\boldsymbol{x}))$ measures the local "*degree of sliding*" between the fibre and the matrix (i.e. at a given position along the fibre). When $s(\varepsilon_f^m(\boldsymbol{x})) = 0$, the sliding is complete, $[[\varepsilon_{f-m}(\boldsymbol{x})]] = \varepsilon_f^m(\boldsymbol{x})$, and no shear stress is transferred between the matrix and the fibre. In such a case, the fibre-matrix interface has no stiffness and the fiber doesn't bear any stress, that is to say, the composite material behaves as an elastic material with inclusion of voids having the shape of the fibres. When $s(\varepsilon_f^m(\boldsymbol{x}))$ tends to one, the interface is perfect, i.e. no strain jump occurs, $[[\varepsilon_{f-m}(\boldsymbol{x})]] = 0$. In this condition the shear stress transfer between the matrix and the fibre is maximum, and the reinforcing phase carries the maximum possible load (Fig. 3.6a).

It is reasonable to assume that the value of the function $s(\varepsilon_f^m(\boldsymbol{x}))$ depends on the amount of the matrix strain evaluated in the fibre direction, $\varepsilon_f^m(\boldsymbol{x})$. A very simple and reasonable relationship for $s(\varepsilon_f^m(\boldsymbol{x}))$ can be assumed to be, for instance, the piecewise linear dependence shown in Fig. 3.6b. Such a relationship requires the introduction of two characteristic strains, $\overline{\varepsilon_1^m}$, $\overline{\varepsilon_2^m}$, that define the matrix strain value at which debonding takes place ($\overline{\varepsilon_1^m}$) and the matrix strain value at which debonding is complete ($\overline{\varepsilon_2^m}$), i.e. $s(\varepsilon_f^m(\boldsymbol{x})) = 0$, respectively.

The quantification of the function $s(\varepsilon_f^m(\boldsymbol{x}))$ can be made on the basis of physical concepts as is illustrated in the following. Even if the sliding function is defined locally along the fibre, $s(\boldsymbol{x})$, in the hypothesis of very short fibres it is reasonable to consider it to be constant along the fibre, characterized by a value that can be assumed to be equal to the mean value of $s(\varepsilon_f^m(\boldsymbol{x}))$. Since the actual fibre strain is evaluated with reference to the matrix strain, even for a linear elastic fibre material (with Young's modulus E_f), the stress-strain relationship is non-linear when the sliding takes place. The tangent elastic modulus of the fibre evaluated with respect to the matrix strain, $E_f(\varepsilon_f^m(\boldsymbol{x})) = d\sigma_f(\boldsymbol{x})/d\varepsilon_f^m(\boldsymbol{x})$, can be defined as:

$$\begin{aligned} E_f(\varepsilon_f^m(\boldsymbol{x})) &= \frac{d}{d\varepsilon_f^m(\boldsymbol{x})}\left[E_f \cdot \overbrace{\left(\varepsilon_f^m(\boldsymbol{x}) - [[\varepsilon_{m-f}(\boldsymbol{x})]]\right)}^{\varepsilon_f(\boldsymbol{x}) = s(\varepsilon_f^m(\boldsymbol{x}))\cdot\varepsilon_f^m(\boldsymbol{x})}\right] = \\ &= E_f \cdot \left[s(\varepsilon_f^m(\boldsymbol{x})) + \varepsilon_f^m(\boldsymbol{x}) \cdot \frac{ds(\varepsilon_f^m(\boldsymbol{x}))}{d\varepsilon_f^m(\boldsymbol{x})}\right] \end{aligned} \tag{3.24}$$

By considering the above relationship, the tangent elastic tensor $\boldsymbol{C}'_{eq}(\boldsymbol{\varepsilon})$ of the equivalent homogenised material becomes (see Eq. (3.16)):

$$\begin{aligned} \boldsymbol{C}'_{eq} &= \mu \cdot \boldsymbol{C}'_m + \mu_f \left(\frac{d\sigma_f(\boldsymbol{x})}{d\varepsilon_f^m(\boldsymbol{x})}\right) \cdot \int_{S.\ a.} p_\varphi(\varphi) \cdot p_\vartheta(\vartheta) \cdot \boldsymbol{F} \otimes \boldsymbol{F} d\Omega = \mu \cdot \boldsymbol{C}'_m + \\ &+ \eta_p \cdot \left[s(\varepsilon_f^m(\boldsymbol{x})) + \varepsilon_f^m(\boldsymbol{x}) \cdot \frac{ds(\varepsilon_f^m(\boldsymbol{x}))}{d\varepsilon_f^m(\boldsymbol{x})}\right] \cdot \int_{S.\ a.} p_\varphi(\varphi) \cdot p_\vartheta(\vartheta) \cdot \boldsymbol{F} \otimes \boldsymbol{F} d\Omega \end{aligned} \tag{3.25}$$

In order to write explicitly the expression $s(\varepsilon_f^m(\boldsymbol{x}))$, the stress transferred between the matrix and the fibre must be taken into account.

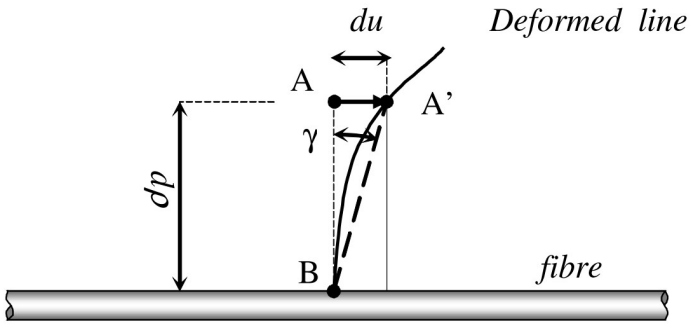

Figure 3.7: Scheme of the shear deformation around a single fibre

3.5.1 Equilibrium of the fibre-matrix system

By considering a cylinder of matrix material surrounding a single fibre, the equilibrium equation along the fibre direction can be written as:

$$\frac{df(x)}{dx} = -p \cdot \tau_i = -p \cdot \bar{k} \cdot (u_R - u_r) \tag{3.26}$$

where p, τ_i, $f(x)$, $\bar{k}$, u_R, and u_r are the fibre perimeter, the shear stress at the interface, the total axial force sustained by the fibre in the fibre section located at the abscissa x (Fig. 3.7), the stiffness of the fibre-matrix interface and the displacements measured in the fibre direction inside the matrix cylinder and at the interface, respectively. The parameter u_r is assumed to coincide with the displacement measured on the fibre axis, due to the negligibility of the fibre radius with respect to the radius R of the cylinder of material under study (this is correct for small content of fibres, i.e. $R \gg r$).

The stiffness $\bar{k}$ of the fibre-matrix interface can be calculated by writing the shear strain and stress at a generic distance ρ from the fibre centre as a function of the shear stress interface stress τ_i (Fig. 3.7):

$$\tau(\rho) = G_m \cdot \gamma(\rho) = G_m \cdot \frac{du}{d\rho} = \tau_i \frac{r}{\rho} \tag{3.27}$$

where G_m, r and ρ indicate the matrix shear modulus, the fibre radius and a generic radius measured from the fibre centre, respectively, and u is the displacement parallel to the fibre direction (Fig. 3.7). The last equality in Eq. (3.27) is written by considering the longitudinal equilibrium of the hollow cylinder defined by the

internal radius r and by the external radius ρ, i.e. $2\pi \cdot r \cdot \tau_i \cdot dx = 2\pi \cdot \rho \cdot \tau(\rho) \cdot dx$. By expressing the interface stress τ_i from the above relationships, the following expression can be obtained:

$$\frac{d\rho}{\rho}\tau_i = G_m \cdot \frac{du}{r} \tag{3.28}$$

Finally, by integrating the above equation between r and $\rho = R$ (where the displacements u are supposed to be known, $u_r = u(r)$ and $u_R = u(R)$), the following expression can be written:

$$\int_r^R \frac{d\rho}{\rho}\cdot\tau_i = \frac{G_m}{r}\cdot\int_{u(r)}^{u(R)} du \rightarrow \tau_i = \underbrace{\frac{G_m}{r}\cdot\frac{1}{\ln(R/r)}}_{\bar{k}}\cdot(u_R - u_r) = \bar{k}\cdot(u_R - u_r) \tag{3.29}$$

By considering the following relationships:

$$\begin{aligned} &\frac{du_r(x)}{dx} \approx \varepsilon_f(x) = \frac{\sigma_f(x)}{E_f} = \frac{\sigma_f(x)}{E_f}\cdot\frac{A_f}{A_f} = \frac{f(x)}{E_f\cdot A_f} \qquad \text{and} \\ &\frac{du_R(x)}{dx} \approx \varepsilon_m(x) = \frac{\sigma_m(x)}{E_m} \end{aligned} \tag{3.30}$$

and deriving Eq. (3.26) with respect to x, the following expression can be obtained [189]:

$$\frac{d^2 f(x)}{dx^2} + p\cdot\bar{k}\cdot\left(\frac{\sigma_m(x)}{E_m} - \frac{f(x)}{E_f\cdot A_f}\right) = 0 \tag{3.31}$$

or equivalently:

$$\frac{d^2 f(x)}{dx^2} + p\cdot\bar{k}\cdot\left(\frac{P - f(x)}{E_m\cdot A_m} - \frac{f(x)}{E_f\cdot A_f}\right) = 0 \tag{3.32}$$

since $\overbrace{\sigma_f\cdot A_f}^{f(x)} + \sigma_m(x)\cdot A_m = P$, where P is the total force sustained by the cylinder of composite under study. By making the position

$$\alpha = \frac{1}{E_m\cdot A_m} + \frac{1}{E_f\cdot A_f} \qquad \beta = \sqrt{p\cdot\bar{k}\cdot\alpha} \qquad F = \frac{P}{\alpha\cdot E_m\cdot A_m}$$

Eq. (3.32) can be rewritten in the following form:

$$\frac{d^2 f(x)}{dx^2} - \beta^2\cdot f(x) + \beta^2\cdot F = 0 \tag{3.33}$$

By integrating the previous second order differential equation and by imposing the boundary conditions at the fibre ends, $f(x = \pm L_f) = 0$ (the fibre is assumed to have length $2L_f$), the solution of Eq. (3.33) is [24]:

$$f(x) = F \cdot \left[1 - \frac{\cosh(\beta \cdot x)}{\cosh(\beta \cdot L_f)}\right] \tag{3.34}$$

and the shear stress $\tau_i = \tau(x)$ at the interface and the force sustained by the matrix can be calculated as follows:

$$\tau(x) = -\frac{1}{p} \cdot \frac{df(x)}{dx} = \frac{F \cdot \beta}{p} \cdot \left[\frac{\sinh(\beta \cdot x)}{\cosh(\beta \cdot L_f)}\right] \qquad \text{and} \tag{3.35a}$$

$$P - f(x) = \sigma_(x) \cdot A_m = F \cdot \left\{\alpha \cdot E_m \cdot A_m - \left[1 - \frac{\cosh(\beta \cdot x)}{\cosh(\beta \cdot L_f)}\right]\right\} \tag{3.35b}$$

3.5.2 Sliding function evaluation

In order to obtain the mean value $s(\overline{\varepsilon_f^m})$ of the sliding function $s(\varepsilon_f^m(x))$ along the fibre, the actual elastic energy density stored in the fibre can be determined by imposing that such a value is equal to the average energy due to a constant stress distribution, $\overline{\sigma_f}$, along the fibre. Since the reinforcing fibre is assumed to have a linear elastic behaviour, the above cited energy W must be evaluated according to the effective axial stress distribution inside the fibre:

$$\begin{aligned} W &= \frac{1}{2 \cdot V_f} \cdot \int_{V_f} \sigma_f(x) \cdot \varepsilon_f(x) dV_f = \frac{1}{2 \cdot V_f} \cdot \int_{-L_f}^{L_f} \sigma_f(x) \cdot \frac{\sigma_f(x)}{E_f} \cdot A_f dx \\ &= \frac{1}{2 \cdot V_f} \cdot \frac{A_f}{E_f} \cdot \int_{-L_f}^{L_f} \sigma_f^2(x) dx = \frac{1}{4 \cdot L_f \cdot E_f} \cdot \int_{-L_f}^{L_f} \sigma_f^2(x) dx \end{aligned} \tag{3.36}$$

where the fibre volume is written as $V_f = 2 \cdot L_f \cdot A_f$.

The corresponding average quantity, $\overline{W}$, can be obtained by considering an equivalent constant stress distribution, $\overline{\sigma_f}$, along the fibre length:

$$\overline{W} = \frac{1}{2} \cdot \overline{\sigma_f} \cdot \overline{\varepsilon_f} = \frac{1}{2} \cdot E_f \cdot \overline{\varepsilon_f}^2 = \frac{1}{2} \cdot E_f \cdot \left[s\left(\overline{\varepsilon_f^m}\right) \cdot \overline{\varepsilon_f^m}\right]^2 \tag{3.37}$$

where $\overline{\varepsilon_f} = s\big(\overline{\varepsilon_f^m}\big) \cdot \overline{\varepsilon_f^m}$ and the mean fibre stress is written as $\overline{\sigma_f} = E_f \cdot \overline{\varepsilon_f}$. In the above relationships the mean value of the matrix strain $\overline{\varepsilon_f^m}$ measured in the fibre direction is used. It can be computed as follows:

$$\overline{\varepsilon_f^m} = \frac{1}{2L_f} \cdot \int_{-L_f}^{L_f} \varepsilon_f^m(x)dx = \frac{1}{2L_f} \cdot \int_{-L_f}^{L_f} \Big[(\boldsymbol{k} \otimes \boldsymbol{k}) : \boldsymbol{\varepsilon}(x))\Big]dx \tag{3.38}$$

The (constant) value of $s(\overline{\varepsilon_f^m})$ can explicitly be written by solving Eq. (3.37):

$$s(\overline{\varepsilon_f^m}) = \frac{1}{\overline{\varepsilon_f^m}} \cdot \sqrt{\frac{2 \cdot \overline{W}}{E_f}} \tag{3.39}$$

and, by assuming $W = \overline{W}$, the following expression can be obtained:

$$\begin{aligned} s(\overline{\varepsilon_f^m}) &= \frac{1}{\overline{\varepsilon_f^m}} \cdot \sqrt{\frac{2 \cdot \int_{-L_f}^{L_f} \sigma_f^2(x)dx}{4L_f \cdot E_f^2}} = \frac{1}{\overline{\varepsilon_f^m} \cdot E_f} \cdot \sqrt{\frac{\int_{-L_f}^{L_f} \sigma_f^2(x)dx}{2L_f}} = \\ &= \frac{1}{\dfrac{E_f}{2L_f} \cdot \displaystyle\int_{-L_f}^{L_f} \varepsilon_f^m(x)dx} \cdot \sqrt{\frac{\int_{-L_f}^{L_f} \sigma_f^2(x)dx}{2L_f}} \end{aligned} \tag{3.40}$$

with

$$\varepsilon_f^m(x) = \frac{\sigma_m(x)}{E_m \cdot A_m} = \frac{P - f(x)}{E_m \cdot A_m} = F\left[\alpha - \frac{1}{E_m \cdot A_m}\left(1 - \frac{\cosh(\beta \cdot x)}{\cosh(\beta \cdot L_f)}\right)\right] \tag{3.41}$$

In the following, Eq. (3.40) is employed using the proper fibre stress law distribution in the pre-, post- and complete debonding stage.

Pre-debonding stage

Since the interface shear stress satisfies the condition $\tau_{i,max} = \tau_i(x = \pm L_f) < \tau_{au}$, during the pre-debonding stage (Fig. 3.8b), the stress inside the fibre can be expressed by using the function $f(x)$ obtained from Eq. (3.34):

$$\sigma_f = \frac{f(x)}{A_f} \qquad \text{with } -L_f \leq x \leq L_f$$

The constant value of the sliding function evaluated through the mean fibre strain can be expressed by:

$$s(\overline{\varepsilon_f^m}) = \frac{1}{\overline{\varepsilon_f^m} \cdot E_f} \cdot \sqrt{\frac{\displaystyle\int_{-L_f}^{L_f} \left[\frac{F}{A_f} \cdot \left(1 - \frac{\cosh(\beta \cdot x)}{\cosh(\beta \cdot L_f)}\right)\right]^2 dx}{2L_f}} = \\ = \frac{1}{\overline{\varepsilon_f^m}} \cdot \sqrt{\frac{\displaystyle\int_{-L_f}^{L_f} \left[\frac{F}{A_f} \cdot \left(1 - \frac{\cosh(\beta \cdot x)}{\cosh(\beta \cdot L_f)}\right)\right]^2 dx}{2L_f \cdot E_f^2}} \tag{3.42}$$

by using the analytical expression of the mean matrix strain parallel to the fibre direction, $\overline{\varepsilon_f^m}$, obtained as:

$$\begin{aligned} \overline{\varepsilon_f^m} &= \frac{1}{2L} \cdot \int_{-L_f}^{L_f} \varepsilon_f^m(x) dx = \\ &= \frac{1}{2L_f} \cdot \int_{-L_f}^{L_f} F\left\{\alpha - \frac{1}{E_m \cdot A_m}\left[1 - \frac{\cosh(\beta \cdot x)}{\cosh(\beta \cdot L_f)}\right]\right\} dx = \\ &= \frac{F}{E_f \cdot A_f} \cdot \left[1 + \frac{E_f \cdot A_f}{E_m \cdot A_m} \cdot \frac{\tanh(\beta \cdot L_f)}{\beta \cdot L_f}\right] \end{aligned} \tag{3.43}$$

By remembering that $\cosh^2(\beta \cdot x) = \left(e^{\beta \cdot x} + e^{-\beta \cdot x}\right)^2/4$, the integral of Eq. (3.42) becomes:

$$\int_{-L_f}^{L_f} \left[\frac{F}{A_f} \cdot \left(1 - \frac{\cosh(\beta \cdot x)}{\cosh(\beta \cdot L_f)}\right)\right]^2 dx = \\ = \frac{2L_f \cdot F^2}{A_f^2} \cdot \left[1 + \frac{1}{4\beta \cdot L_f} \cdot \frac{\sinh(2\beta \cdot L_f)}{\cosh^2(\beta \cdot L_f)} + \frac{1}{2\cosh^2(\beta \cdot L_f)} - \frac{\tanh(\beta \cdot L_f)}{\beta \cdot L_f}\right]$$

Consequently the sliding function given by Eq. (3.42) can be rewritten as follows:

$$s(\overline{\varepsilon_f^m}) = \frac{\sqrt{1 + \dfrac{1}{\cosh^2(\beta \cdot L_f)} + \dfrac{1}{4\beta \cdot L_f} \cdot \dfrac{\sinh(2\beta \cdot L_f)}{\cosh^2(\beta \cdot L_f)} - \dfrac{2\tanh(\beta \cdot L_f)}{\beta \cdot L_f}}}{\left[1 + \dfrac{E_f \cdot A_f}{E_m \cdot A_m} \cdot \dfrac{\tanh(\beta \cdot L_f)}{\beta \cdot L_f}\right]} \tag{3.44}$$

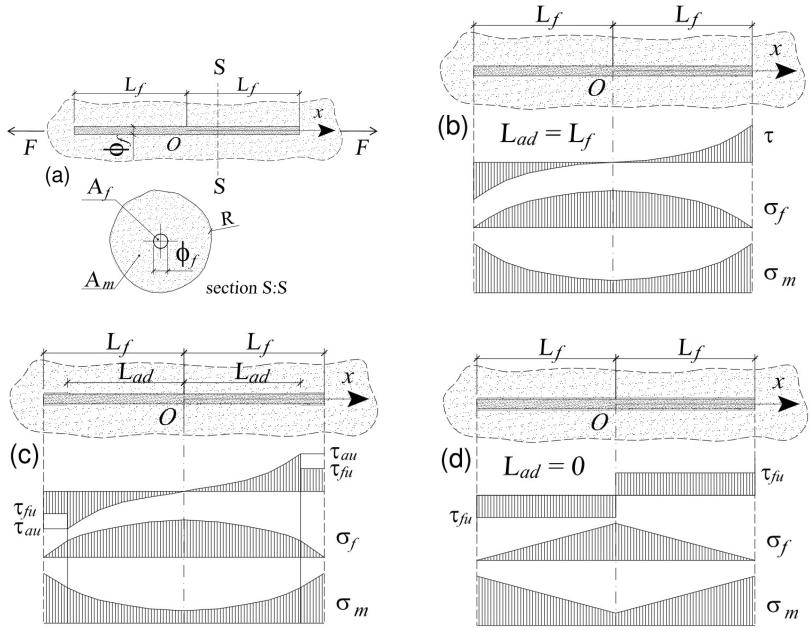

Figure 3.8: Cylinder of matrix material around a single fibre under tension (a); stress distributions around a single fibre in the predebonding stage (b); during the debonding stage (c); and at complete debonding stage (d).

Note that the dependence of the function s from the stress-strain state disappears in the previous equation, i.e. $s(\overline{\varepsilon_f^m}) = \bar{s}$, and it depends only on the geometrical characteristics (A_f, A_m, L_f, p) and upon the mechanical properties of the two materials (E_m, E_f, G_m).

Debonding initiation

When the shear stress transmitted from the matrix becomes equal to the ultimate interface shear stress τ_{au} at fibre extremities, $\tau_i(x = \pm L) = \tau_{au}$, the debonding phenomenon starts. By using Eq. (3.35a), the debonding initiation condition can be identified by:

$$\begin{aligned} \left|\tau_i(\pm L_f)\right| &= \frac{F \cdot \beta}{p} \cdot \left[\frac{\sinh(\beta \cdot L_f)}{\cosh(\beta \cdot L_f)}\right] = \frac{F \cdot \beta}{p} \cdot \tanh(\beta \cdot L_f) = \tau_{au} \\ \Rightarrow \quad F_{deb} &= \frac{\tau_{au} \cdot p}{\beta \cdot \tanh(\beta \cdot L_f)} \end{aligned} \tag{3.45}$$

where the subscript '*deb*' stands for debonding, the function, F_{deb}, indicates the minimum value of the total force applied to the single-fibre reinforced cylinder under study, that causes the starting of the debonding phenomenon. The corresponding mean strain in the matrix, measured in the fibre direction, becomes:

$$\overline{\varepsilon_f^m}_{,deb} = \frac{\tau_{au} \cdot p}{\beta} \cdot \left(\frac{1}{E_m \cdot A_m \cdot \beta} + \frac{1}{A_f \cdot E_f \tanh(\beta \cdot L_f)} \right) \tag{3.46}$$

Partial debonding stage

When the debonding phenomenon occurs in two limited zones (each one with length $(L_f - L_{ad})$) located at the extremities of the fibre, it can be assumed that, in such zones, the shear stress is constant and equal to the characteristic interface friction shear stress τ_{fu} (Fig. 3.8c). By integrating the differential Eq. (3.33) with the new boundary conditions $f(x = \pm L_{ad}) = p \cdot \tau_{fu} \cdot (L_f - L_{ad})$, the following expression can be obtained:

$$f(x) = \begin{cases} p \cdot \tau_{fu} \cdot (L_f - |x|) & \text{for } -L_f \leq x < -L_{ad} \text{ and } L_{ad} < x \leq L_f \\ F \cdot \left[1 + \dfrac{p \cdot \tau_{fu} \cdot (L_f - L_{ad}) - F}{F} \cdot \dfrac{\cosh(\beta \cdot x)}{\cosh(\beta \cdot L_f)} \right] & \text{for } -L_{ad} \leq x \leq L_{ad} \end{cases} \tag{3.47}$$

and the shear stress at the matrix-fibre interface can be written as follows:

$$\tau_i(x) = \begin{cases} \tau_{fu} & \text{for } -L_f \leq x < -L_{ad} \text{ and } L_{ad} < x \leq L_f \\ -\beta \cdot \left[\tau_{fu} \cdot (L_f - L_{ad}) - \dfrac{F}{p} \right] \cdot \dfrac{\sinh(\beta \cdot x)}{\cosh(\beta \cdot L_{ad})} & \text{for } -L_{ad} \leq x \leq L_{ad} \end{cases} \tag{3.48}$$

Since $\tau_i(x = \pm L_{ad}) = \tau_{au}$, the value of the corresponding $F = F_{deb}(L_{ad})$ can be determined as follows:

$$F_{deb}(l) = \frac{p \cdot \left[\tau_{au} + \beta \cdot \tau_{fu} \cdot (L_f - L_{ad}) \right]}{\beta} \cdot \coth(\beta \cdot L_{ad}) \tag{3.49}$$

The axial force in the fibre and the interface shear stress distribution in the non-debonded zone, in the limit condition of progressive debonding, can be rewritten

as follows:

$$f(x) = \begin{cases} p \cdot \tau_{fu} \cdot (L_f - |x|) & \text{for } -L_f \le x < -L_{ad} \text{ and } L_{ad} < x \le L_f \\ F_{deb}(L_{ad}) \cdot \left[1 - M \cdot \dfrac{\cosh(\beta \cdot x)}{\cosh(\beta \cdot L_f)}\right] & \text{for } -L_{ad} \le x \le L_{ad} \end{cases} \tag{3.50}$$

with

$$M = \frac{F_{deb}(L_{ad}) - p \cdot \tau_{fu} \cdot (L_f - L_{ad})}{F_{deb}(L_{ad})}$$

and

$$\tau_i(x) = \begin{cases} \tau_{fu} & \text{for } -L_f \le x < -L_{ad} \text{ and } L_{ad} < x \le L_f \\ -\beta \cdot \left[\tau_{fu} \cdot (L_f - L_{ad}) - \dfrac{F_{deb}(L_{ad})}{c}\right] \cdot \dfrac{\sinh(\beta \cdot x)}{\cosh(\beta \cdot L_{ad})} & \text{for } -L_{ad} \le x \le L_{ad} \end{cases} \tag{3.51}$$

By taking into account Eq. (3.38) and Eq. (3.39), the mean value of the sliding function $s(\overline{\varepsilon_f^m})$ in this stage can be obtained as follows:

$$\begin{aligned} s(\overline{\varepsilon_f^m}) &= \frac{1}{\overline{\varepsilon_f^m} \cdot E_f} \cdot \sqrt{\frac{\int_{-L_f}^{L_f} \sigma_f^2(x)dx}{2L_f}} = \\ &= \frac{1}{\overline{\varepsilon_f^m} \cdot E_f} \cdot \sqrt{\frac{\int_{-L_{ad}}^{L_{ad}} \sigma_f^2(x)dx + 2\int_{L_{ad}}^{L_f} \sigma_{f,deb}^2(x)dx}{2L_f}} \end{aligned} \tag{3.52}$$

Since, by introducing the previous expressions, the following terms can be acknowledged:

$$\int_{-L_{ad}}^{L_{ad}} \sigma_f^2(x)dx = \frac{F_{deb}^2}{A_f^2} \cdot \left[2L_{ad} + \right.$$
$$\left. + \frac{M^2}{\cosh^2(\beta \cdot L_{ad})} \cdot \left(L_{ad} + \frac{\sinh(2\beta \cdot L_{ad})}{2\beta}\right) - \frac{4M \cdot \sinh(\beta \cdot L_{ad})}{\beta \cdot \cosh(\beta \cdot L_{ad})}\right] \tag{3.53a}$$

and

$$2\int_{L_{ad}}^{L_f} \sigma_{f,deb}^2(x)dx = \frac{2}{3} \cdot \frac{p^2\tau_{fu}^2}{F_{deb}^2}(L_f - L_{ad})^3 \tag{3.53b}$$

the sliding function presents the following expression:

$$s(\overline{\varepsilon_f^m}) = \frac{F_{deb}}{\overline{\varepsilon_f^m} \cdot E_f \cdot A_f} \cdot \frac{1}{\sqrt{2L_f}} \cdot \left[2L_{ad} + \frac{M^2}{\cosh^2(\beta \cdot L_{ad})} \cdot \left(L_{ad} + \right.\right. \\ \left.\left. + \frac{\sinh(2\beta \cdot L_{ad})}{2\beta} \right) - \frac{4M \cdot \tanh(\beta \cdot L_{ad})}{\beta} + \frac{2}{3} \cdot \frac{p^2 \tau_{fu}^2}{F_{deb}^2} (L_f - L_{ad})^3 \right]^{\frac{1}{2}} \tag{3.54}$$

The matrix strain function evaluated in the fibre direction, $\varepsilon_f^m(x) = \sigma_m(x)/(E_m \cdot A_m)$, can be obtained:

$$\varepsilon_f^m(x) = \begin{cases} F_{deb}(L_{ad}) \cdot \alpha - \dfrac{p \cdot \tau_{fu} \cdot (L_f - |x|)}{E_m \cdot A_m} \text{ for } -L_f \leq x < -L_{ad} \text{ and } L_{ad} < x \leq L_f \\ F_{deb}(L_{ad}) \left[\dfrac{1}{E_f \cdot A_f} + \dfrac{M}{E_m \cdot A_m} \cdot \dfrac{\cosh(\beta \cdot x)}{\cosh(\beta \cdot L_{ad})} \right] \quad \text{for } -L_{ad} \leq x \leq L_{ad} \end{cases} \tag{3.55}$$

and, finally, its mean value along the fibre becomes:

$$\overline{\varepsilon_f^m} = \frac{1}{2L} \cdot \int_{-L_f}^{L_f} \varepsilon_f^m(x) dx = \frac{1}{2L} \cdot \left(\int_{-L_{ad}}^{L_{ad}} \varepsilon_f^m(x) dx + 2 \int_{L_{ad}}^{L_f} \varepsilon_f^m(x) dx \right) = \\ = \frac{1}{E_m \cdot A_m} \cdot \left\{ F_{deb}(L_{ad}) \cdot \left[\frac{M}{\beta \cdot L_f} \cdot \tanh(\beta \cdot L_{ad}) + \left(1 - \frac{L_{ad}}{L_f} \right) + \right.\right. \\ \left.\left. + \frac{E_m \cdot A_m}{E_f \cdot A_f} \right] + p \cdot \tau_{fu} \cdot \frac{L_f}{2} \left(1 + \frac{L_{ad}}{L_f} \right)^2 \right\} \tag{3.56}$$

In the partial debonding stage, once the fibre and interface parameters L_f, τ_{fu} and τ_{au} are known, the solution of the problem can be achieved, by using Eq. (3.51), determining first the distance L_{ad}, at which debonding starts, and setting $\tau_i(L_{ad}) = \tau_{au}$. From Eq. (3.56) the parameter $F_{deb}(L_{ad})$ can be expressed as a function of $\overline{\varepsilon_f^m}$. Finally, by substituting the result obtained for $F_{deb}(L_{ad})$ in Eq. (3.52), the constant value of the sliding function $s(\overline{\varepsilon_f^m})$ can be obtained.

In the particular case of $\tau_{fu} \approx 0$, the previous equations can be rewritten in a

simplified way as follows:

$$f(x) = \begin{cases} \sigma_{f,deb} \cdot A_f = 0 & \text{for } -L_f \le x < -L_{ad} \text{ and } L_{ad} < x \le L_f \\ \sigma_f(x) \cdot A_f = F_{deb}(L_{ad}) \cdot \left[1 - \dfrac{\cosh(\beta \cdot x)}{\cosh(\beta \cdot L_f)}\right] & \text{for } -L_{ad} \le x \le L_{ad} \end{cases} \tag{3.57}$$

since $M = 1$;

$$\tau_i(x) = \begin{cases} 0 & \text{for } -L_f \le x < -L_{ad} \text{ and } L_{ad} < x \le L_f \\ \beta \cdot \dfrac{F_{deb}(L_{ad})}{p} \cdot \dfrac{\sinh(\beta \cdot x)}{\cosh(\beta \cdot L_{ad})} & \text{for } -L_{ad} \le x \le L_{ad} \end{cases} \tag{3.58}$$

$$\varepsilon_f^m(x) = \begin{cases} F_{deb}(L_{ad}) \cdot \alpha & \text{for } -L_f \le x < -L_{ad} \text{ and } L_{ad} < x \le L_f \\ \dfrac{F_{deb}(L_{ad})}{E_f \cdot A_f} \cdot \left[1 + \dfrac{E_f \cdot A_f}{E_m \cdot A_m} \cdot \dfrac{\cosh(\beta \cdot x)}{\cosh(\beta \cdot L_{ad})}\right] & \text{for } -L_{ad} \le x \le L_{ad} \end{cases} \tag{3.59}$$

$$\overline{\varepsilon_f^m} = \frac{F_{deb}(L_{ad})}{E_f \cdot A_f} \cdot \left\{ \frac{E_f \cdot A_f}{E_m \cdot A_m} \cdot \left[1 - \frac{L_{ad}}{L_f} + \frac{\tanh(\beta \cdot L_{ad})}{\beta \cdot L_f}\right] + 1 \right\} \tag{3.60}$$

$$s(\overline{\varepsilon_f^m}) = \frac{\sqrt{\dfrac{L_{ad}}{L_f} + \dfrac{1}{2\cosh^2(\beta \cdot L_{ad})} \cdot \left(\dfrac{L_{ad}}{L_f} + \dfrac{\sinh(2\beta \cdot L_{ad})}{2\beta \cdot L_f}\right) - \dfrac{2\tanh(\beta \cdot L_{ad})}{\beta \cdot L_f}}}{\left[\dfrac{E_f \cdot A_f}{E_m \cdot A_m} \cdot \left(1 - \dfrac{L_{ad}}{L_f} + \dfrac{\tanh(\beta \cdot L_{ad})}{\beta \cdot L_f}\right)\right]} \tag{3.61}$$

Also for the case of partial debonding, the sliding function can be assumed to be dependent only on geometrical and mechanical parameters if the interface frictional shear stress is negligible with respect to the ultimate shear stress, τ_{au} ($\tau_{fu} \approx 0$).

Complete debonding stage

When the debonding phenomenon reaches the centre of the fibre and the bonded length, L_{ad}, vanishes, the shear stress transmitted from the matrix to the fibre is everywhere equal to the friction shear stress τ_{fu} (Fig. 3.8d). In this stage the force

carried by the fibre at a generic distance x from the fibre midpoint is expressed by:

$$f(x) = p \cdot \tau_{fu} \cdot (L_f - |x|) \qquad \text{for } -L_f \leq x \leq L_f \tag{3.62}$$

whereas the shear stress at the interface is a constant value, $\tau_i(x) = \tau_{fu}$. The sliding function $s(\overline{\varepsilon_f^m})$ in this stage can be finally obtained by simply setting $L_{ad} = 0$ in Eq. (3.52):

$$s(\overline{\varepsilon_f^m}) = \frac{1}{\overline{\varepsilon_f^m} \cdot E_f} \cdot \sqrt{\frac{2\int_0^{L_f} \sigma_f^2(x)dx}{2L_f}} = \sqrt{\frac{1}{3}} \cdot \frac{p \cdot \tau_{fu} \cdot L_f}{A_f} \cdot \frac{1}{E_f \cdot \overline{\varepsilon_f^m}} \tag{3.63}$$

The matrix strain distribution in the fibre direction becomes:

$$\varepsilon_f^m(x) = -\frac{p \cdot \tau_{fu} \cdot (L_f - |x|)}{E_m \cdot A_m} \qquad \text{for } -L_f \leq x \leq L_f \tag{3.64}$$

and

$$\overline{\varepsilon_f^m} = \int_{L_f}^{L_f} \frac{\varepsilon_f^m(x)}{2L_f} dx = -\frac{p \cdot \tau_{fu} \cdot L_f}{E_m \cdot A_m} \tag{3.65}$$

Finally, the sliding function, $s(\overline{\varepsilon_f^m})$, can be expressed by:

$$s(\overline{\varepsilon_f^m}) = \frac{1}{3} \frac{E_m \cdot A_m}{E_f \cdot A_f} \tag{3.66}$$

$s(\overline{\varepsilon_f^m})$ is constant, being its value dependent on the elastic modulus ratio, E_f/E_m, and on the fibre content value (expressed through the ratio between the matrix and fibre cross sections, A_m/A_f).

As a numerical example, a FRC square plate (having sizes equal to $1.0 \times 1.0m$ and thickness $0.1m$ and assumed to be in a plane stress condition) under upward top displacement applied to the upper edge (corresponding to stress σ_0) is examined (Fig. 3.9a).

The constants of the matrix material are assumed as follows: Young modulus $E_m = 10GPa$, Poisson's ratio equal to $\nu_m = 0.33$. A reinforcing fibre phase characterised by an elastic modulus equal to $E_f = 100GPa$ and a volume fraction equal to $\mu_f = 5\%$ is assumed to be in the composite, whereas the limit matrix-fibre interface shear stress is equal to $\tau_{au} = 1MPa$ and fibre length and diameter are

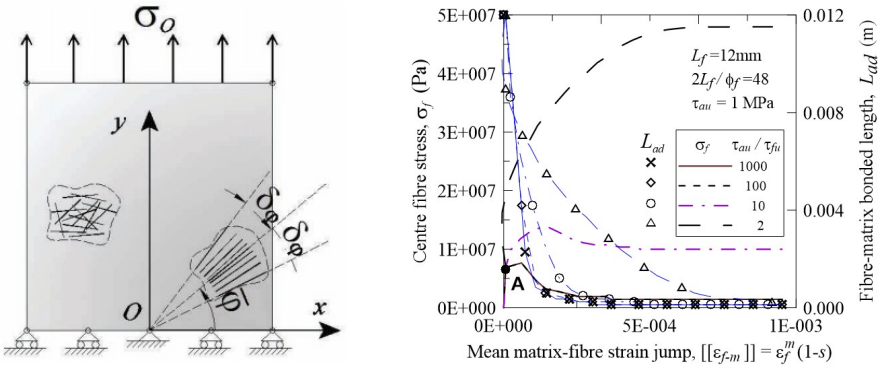

Figure 3.9: Rectangular panel under vertical top edge applied stress: scheme of the random (left) or preferentially oriented (right) reinforcing fibres (a); non-linear bond-slip law ($\sigma_f - [[\varepsilon_{f-m}]]$) for different τ_{au}/τ_{fu} ratios in the fibre-reinforced plate (with $\overline{\varphi} = \pi/2$, $\delta_\varphi = 1°$) and the evolution of the non-debonded length, L_{ad} (lines with symbols), (b).

equal to $2L_f = 24mm$ and $\phi_f = 0.5mm$, respectively. The stress state in the plate is approximately homogenous and uniaxial (in the y-direction, Fig. 3.9a). In Figure 3.9b, the bond-slip law, obtained through the present sliding model for different τ_{au}/τ_{fu} ratios in the case of vertically aligned fibres ($\overline{\varphi} = \pi/2$, $\delta_\varphi = 1°$), is represented. As can be noted, the stress σ_f in the fibre initially increases nearly instantaneously, since at the beginning of the loading process, the values of the sliding function are approximately equal to 1.0, to which corresponds a fibre-matrix strain jump $[[\varepsilon_{f-m}]] = \varepsilon_m^f \cdot (1-s) \cong 0$. In this stage, such a behaviour is governed by the geometry of the fibres and by the shear stress τ_{au}. Once the debonding is initiated in the fibre (point A in Fig. 3.9b), the role of the friction shear stress τ_{fu} becomes important: for low value of the τ_{au}/τ_{fu} ratio (such as in the case $\tau_{au}/\tau_{fu} = 2$), the $\sigma_f - [[\varepsilon_{f-m}]]$ curve continues to increase by increasing $[[\varepsilon_{f-m}]]$, since the non-debonded length L_{ad} slowly reduces (Fig. 3.9b). As far as the complete debonding is concerned, the stress σ_f tends to a constant value that depends on the fibre aspect ratio $\eta = 2L_f/\phi_f$ and τ_{fu}. On the other hand for higher τ_{au}/τ_{fu} ratios (such as in the cases $\tau_{au}/\tau_{fu} = 10$, 100, 1000 in Fig. 3.9b) the stress reaches a maximum value and subsequently a decreasing behaviour can be observed by increasing $[[\varepsilon_{f-m}]]$. As in the first case described above, when the complete debonding is approached (i.e. $L_{ad} \to 0$) the stress σ_f tends to a constant value characterised by lower value as much as the τ_{au}/τ_{fu} ratios increase. The fibre-matrix non-debonded length is also represented in Figure 3.9b (lines with

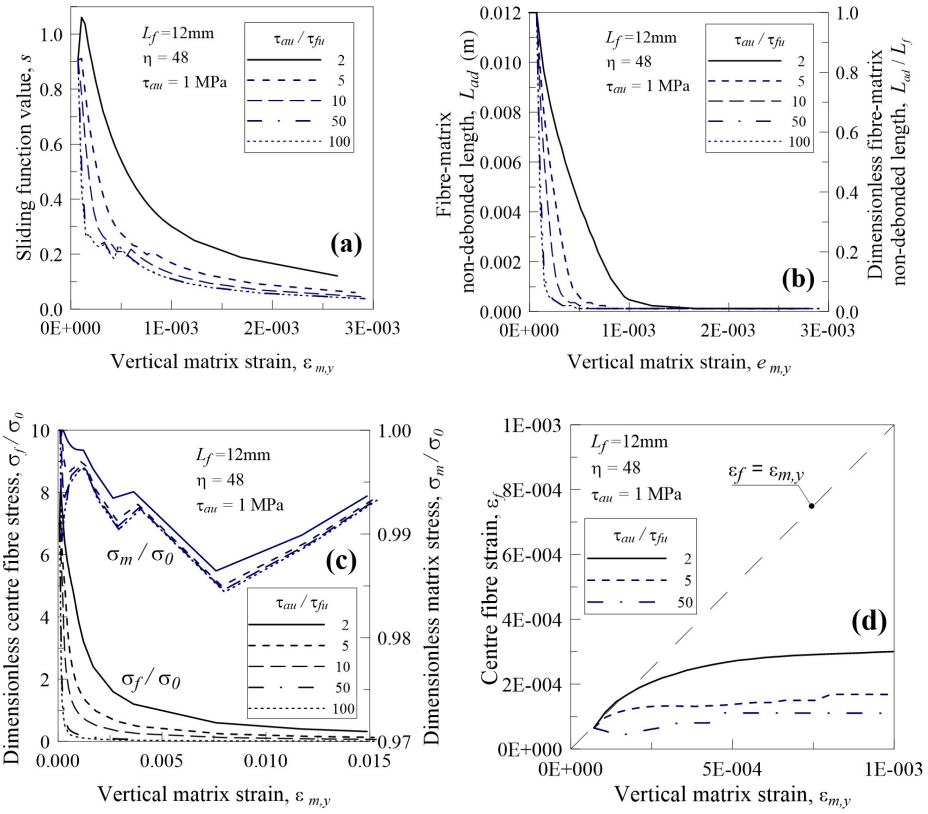

Figure 3.10: Fibre-reinforced plate, with unidirectional fibres characterised by $\overline{\varphi} = \pi/2$, $\delta_\varphi = 1°$, under vertical top edge applied stress for different τ_{au}/τ_{fu} ratios: sliding function value (a), fibre-matrix non debonded length (b), dimensionless fibre and matrix stresses (c) and fibre strain (d) against the vertical matrix strain.

symbols): it can be observed that such a quantity decreases with the increase of the matrix-fibre strain jump. Such a behaviour is much more pronounced by increasing the τ_{au}/τ_{fu} ratio.

In Figure 3.10a, the sliding function is represented against the vertical matrix strain ε_{my} for the same vertically fibre-reinforced plate examined above. In the first part of the graph the value of s increases only for low τ_{au}/τ_{fu} ratios; since the τ_{au} value is the same for all the examined cases, the debonding starts simultaneously for the same matrix strain value. As much as the reduction of the non-debonded length takes place (see Fig. 3.10b), the sliding function value decreases more significantly for high τ_{au}/τ_{fu} ratios. Also the non-debonded length L_{ad} (Fig. 3.10b) shows the

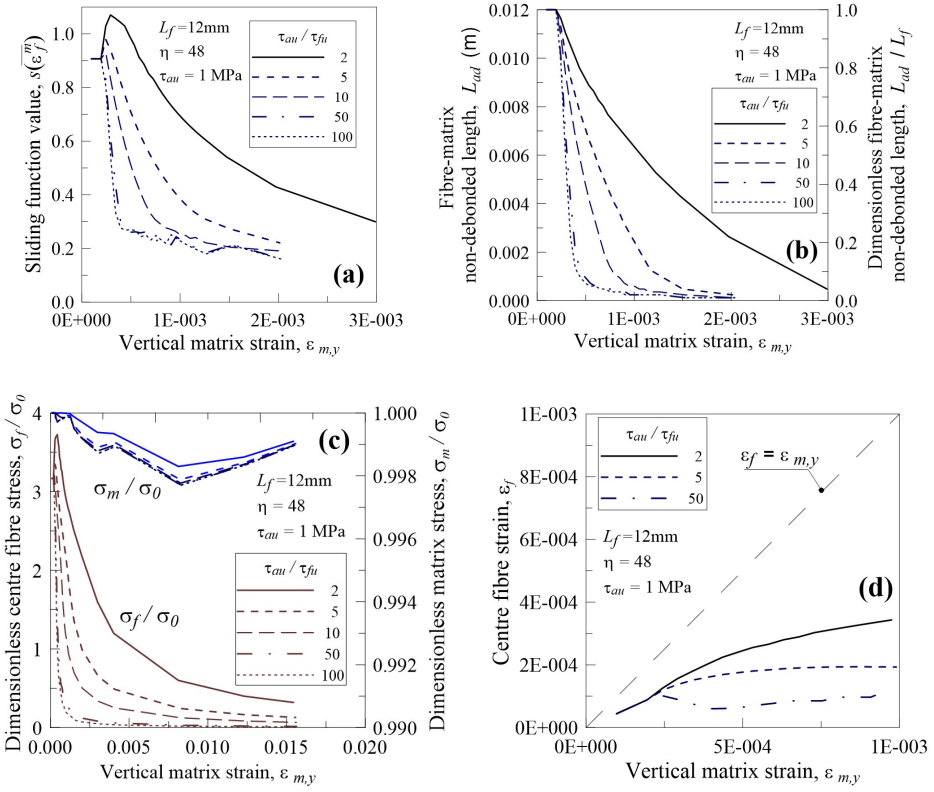

Figure 3.11: Fibre-reinforced plate, with randomly distributed fibres, under vertical top edge applied stress for different τ_{au}/τ_{fu} ratios: sliding function value (a), fibre-matrix non debonded length (b), dimensionless fibre and matrix stresses (c) and fibre strain (d) against the vertical matrix strain.

same qualitative pattern by increasing the strain ε_{my}.

In Figure 3.10c, the normalised stress carried by the matrix σ_m/σ_0 and by the fibres σ_f/σ_0 (where σ_0 is the actual stress applied to the plate) is reported. It can be noted that the relative stress σ_f/σ_0 in the centre of the fibre decreases depending on the τ_{au}/τ_{fu} ratio. The dimensionless stress carried by the matrix, σ_m/σ_0, initially oscillates and finally, for high strain values, increases to guarantee the global equilibrium of the plate. Note the different scales used for the vertical axes of Figure 3.10c, the stress in the matrix σ_m is practically equal to the applied stress (i.e. $\sigma_m/\sigma_0 \cong 1$), since the considered fibre content is very small and the fibre bearing capacity in the plate is very low. Finally, the central fibre strain ε_f is represented in Figure 3.10d against the mean vertical matrix strain ε_{my}. It can be

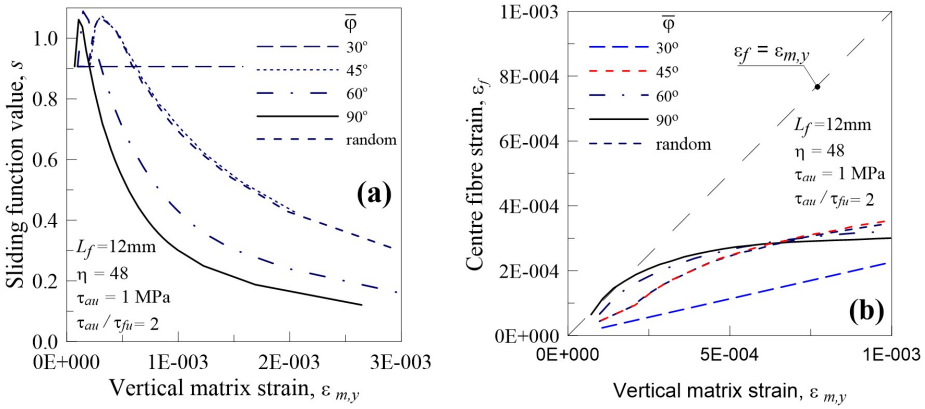

Figure 3.12: Fibre-reinforced plate, characterised by different mean values of the fibre orientation angle, under vertical top edge applied stress: sliding function value (a) and fibre strain (b) against the vertical matrix strain.

noted that the strain in the fibre is initially very similar to the matrix strain while, once the debonding is consistent, it tends to a constant value that depends on the η ratio as well as on the friction shear stress τ_{fu}.

In Figure 3.11, the same above described quantities are reported for the case of randomly distributed fibres. The trend shown is quite similar, for all the considered quantities, to the case of uniaxial vertical fibres discussed above.

It must be observed that in the case of randomly distributed fibres, the trend shown by the different quantities (s, L_{ad}, σ_f/σ_0, σ_m/σ_0, ε_f) is less pronounced with respect to the vertical matrix strain since the 2-D average strain $\overline{\varepsilon_f^m} \cong tr\boldsymbol{\varepsilon}/2 \cong \varepsilon_{my}/2$ (that is lower than $\overline{\varepsilon_f^m} = (\boldsymbol{\varepsilon} \cdot \boldsymbol{t}) \cdot \boldsymbol{t} \cong \varepsilon_{my}$ in the uniaxial case) is used in such a case to compute all the parameters related to the fibres. Moreover, the fibre strain is slightly higher than in the case of vertically aligned fibres since the debonding phenomenon is more limited in the present case.

In Figure 3.12, the effect of the fibres orientation is shown. In Figure 3.12a the sliding function is represented against the vertical matrix strain ε_{my} for an assumed $\tau_{au}/\tau_{fu} = 2$ ratio and different mean values of the fibre orientation, i.e. $\overline{\varphi} = 30°$, $45°$, $60°$, $90°$ (all with $\delta_\varphi = 1°$), as well as for randomly arranged fibres. It can be observed that s presents higher values by decreasing the angle $\overline{\varphi}$ from $90°$ to $45°$, whereas it is almost constant for $\overline{\varphi} = 30°$ since the fibres, nearly perpendicular to the applied stress, are very little strained in the latter case and debonding does not occur. The case of random fibres is, as expected, practically coincident with the

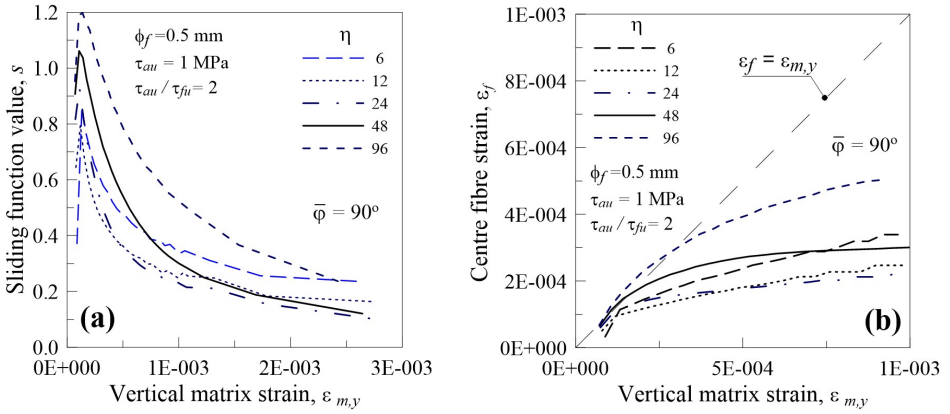

Figure 3.13: Fibre-reinforced plate under vertical top edge applied stress, with vertical reinforcing fibres (characterised by $\overline{\varphi} = \pi/2$, $\delta_\varphi = 1°$) with different fibre aspect ratios η: sliding function value (a) and fibre strain (b) against the vertical matrix strain.

case $\overline{\varphi} = 45°$. In Figure 3.12b, the centre fibre strain ε_f is represented against the vertical matrix strain ε_{my}: for the case $\overline{\varphi} = 30°$, ε_f varies almost linearly with ε_{my} since the debond is absent and the two strains are proportional each other, while ε_f tends to a constant value for high values of ε_{my} in the other cases. Note that, in the case of vertical fibres ($\overline{\varphi} = 90°$), the strain in the fibres initially increases as the matrix strain does and subsequently increases slower than the matrix strain does due to the severe debonding occurred in the fibres. For the other angles ($\overline{\varphi} = 45°$, $60°$) and for randomly oriented fibres, the fibre strain is initially lower than the matrix strain, but, subsequently, it increases more significantly than in the case of vertical fibres since the debonding in such cases is much more limited.

In Figure 3.13a, the influence of the fibre aspect ratio η is examined for the case of vertically aligned fibres ($\overline{\varphi} = \pi/2$, $\delta_\varphi = 1°$) and for $\tau_{au}/\tau_{fu} = 2$. The sliding function increases for very low values of the vertical matrix strain ε_{my} up to a maximum value that depends on the ratio η (the higher such a ratio, the higher the maximum value of s). The sliding function shows a decreasing trend with vertical matrix strain increasing: it is interesting to note that the value of the parameter s becomes greater for fibre with a low aspect ratio than for very slender fibres ($\eta \gg 1$). Finally, Figure 3.13b shows the centre fibre strain ε_f against the vertical matrix strain ε_{my}. Very long fibres are characterised by a central strain initially higher than that for short fibres, but, once the debonding proceeds, such a

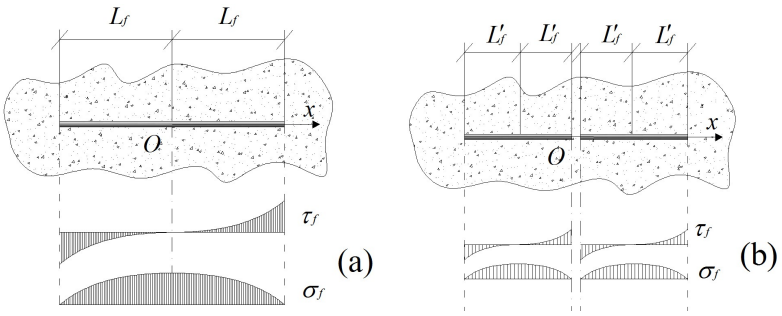

Figure 3.14: Stress distributions around a single fibre (a) and fibre broken into two parts (b).

behaviour tends to become the opposite. In other words, short fibres seem to be more effective than long ones regarding their bearing capacity in the composite.

3.6 Fibre failure and fibre reciprocal interaction

3.6.1 Fibre Failure

Apart the debonding phenomenon (see Sec. 3.5), the fibre failure can also be easily taken into account by observing that the maximum tensile stress along the fibre axis, according to the "Shear Lag" model, is always reached at its centre, $x = 0$ (Fig. 3.14a)[20, 190]. If such a maximum fibre stress $\sigma_f(0)$ is greater than the tensile strength of the fibre, $\sigma_f(0) > f_{t,f}$, the fibre is assumed to break (in a brittle manner) in two parts having the same half-lengths $L'_f = L_f/2$ (Fig. 3.14b).

The fibre effects on the composite can be updated through the non-linear iterative solution of the problem by considering such a new half length, whereas the total fibre volume fraction remains unchanged. If the subsequent applied load produces a the fulfillment of the above failure condition, the fibre length is halved again and the computational process proceeds further in the same way. In the case of fibre failure in presence of debonding, the fibre half-length is updated by considering $L'_{ad} = L_{ad}/2$, that is, the bonded part of the fibre in the subsequent calculations. The bond-slip law, which describes the tensile stress in the middle position of the fibre against the fibre-matrix strain jump $[[\varepsilon_{f-m}(x)]] = \varepsilon_f^m(x) \cdot \left[1 - s(\varepsilon_f^m(x))\right]$, can easily be obtained. In the pre-debonding stage, the quantity $F = F\big([[\varepsilon_{f-m}(x)]]\big)$

can be assessed from the following relationship [20]:

$$F\big([[\varepsilon_{f-m}]]\big) = (\sqrt{2}\cdot\overline{\varepsilon_f^m}\cdot E_f\cdot A_f)\cdot\Big(1-\frac{[[\varepsilon_{f-m}]]}{\overline{\varepsilon_f^m}}\Big)\cdot\Big[2+ \\ +\frac{1}{L_f\cdot\cosh^2(\beta\cdot L_f)}\cdot\Big(L_f+\frac{\sinh(2\beta\cdot L_f)}{2\beta}\Big)-\frac{4\cdot\sinh(\beta\cdot L_f)}{L_f\cdot\beta\cdot\cosh(\beta\cdot L_f)}\Big]^{-\frac{1}{2}} \tag{3.67}$$

and, by inserting Eq. 3.67 in the centre fibre stress expression, $\sigma_f = f(x)/A_f$, the relationship $\sigma_f(x=0,[[\varepsilon_{f-m}]])$ can be explicitly obtained:

$$\sigma_f(0) = \frac{F\big([[\varepsilon_{f-m}]]\big)}{A_f}\cdot\Big[1-\frac{1}{\cosh(\beta\cdot L_f)}\Big] \tag{3.68}$$

On the other hand, in the case of fibre debonding, by assuming the limit condition $\tau_i(\pm L_{ad}) = \tau_{au}$, the corresponding value of F, $F_{deb}(L_{ad})$, can be evaluated:

$$F_{deb}(L_{ad}) = \frac{\tau_{au}\cdot p}{\beta\cdot\tanh(\beta\cdot L_{ad})}+\tau_{fu}\cdot p\cdot(L_f-L_{ad})) \tag{3.69}$$

and substituted in the expression of the mean matrix strain measured in the fibre direction, $\overline{\varepsilon_f^m}$:

$$\overline{\varepsilon_f^m} = F_{deb}(L_{ad})\cdot\left[\alpha-\frac{L_{ad}}{L_f\cdot E_m\cdot A_m}\right]+ \\ +\frac{\sinh(\beta\cdot L_{ad})}{L_f\cdot E_m\cdot A_m}\cdot\left[\left(\frac{p\cdot\tau_{fu}\cdot(L_{ad}-L_f)+F_{deb}(L_{ad})}{\beta\cdot\cosh(\beta\cdot L_{ad})}\right)\right]+ \\ +\frac{p\cdot\tau_{fu}(L_{ad}-L_f)\cdot L_{ad}}{L_f\cdot E_m\cdot A_m}+\frac{p\cdot\tau_{fu}}{L_f\cdot E_m\cdot A_m}\cdot\left(\frac{L_{ad}^2+L_f^2}{2}-L_f\cdot L_{ad}\right) \tag{3.70}$$

in order to obtain the non-debonded length L_{ad}. The above procedure can easily be performed, once the strain $\overline{\varepsilon_f^m}$ is known, for instance, from the FE analysis of the structural component under study. Finally, by remembering that the fibre-matrix strain jump $[[\varepsilon_{f-m}]]$ depends on F_{deb} and L_{ad}, as provided by the following

expression:

$$\frac{[[\varepsilon_{f-m}]]}{\overline{\varepsilon_f^m}} = \left\{ 1 - \frac{F_{deb}}{\sqrt{2}\cdot\overline{\varepsilon_f^m}\cdot E_f\cdot A_f}\cdot\frac{1}{\sqrt{L_f}}\cdot\left[2L_{ad} + \frac{M^2}{\cosh^2(\beta\cdot L_{ad})}\cdot\Big(L_{ad}+ \right.\right.$$
$$\left.\left. + \frac{\sinh(2\beta\cdot L_{ad})}{2\beta}\Big) - \frac{4M\cdot\sinh(\beta L_{ad})}{\beta\cdot\cosh(\beta\cdot L_{ad})} + \frac{2}{3}\cdot\frac{\pi A_f^2\tau_{au}^2}{4F_{deb}^2}\cdot(L_f - L_{ad})^3\right]\right\} \tag{3.71}$$

F_{deb} can be expressed in terms of $[[\varepsilon_{f-m}]]$ with $M = \big(p\cdot\tau_{fu}\cdot(L_{ad}-L_f)+F_{deb}\big)/F_{deb}$.

The expression $\sigma_f(x=0,[[\varepsilon_{f-m}]])$ can be explicitly obtained:

$$\sigma_f(0) = \frac{F_{deb}([[\varepsilon_{f-m}]])}{A_f}\cdot$$
$$\cdot\left[1 + \frac{p\cdot\tau_{fu}\cdot(L_{ad}-L_f) + F_{deb}([[\varepsilon_{f-m}]])}{F_{deb}([[\varepsilon_{f-m}]])}\cdot\frac{1}{\cosh(\beta\cdot L_{ad})}\right] \tag{3.72}$$

The bond-slip relationship is characterised by decreasing values when the sliding function $s(\varepsilon_f^m)$ decreases (or equivalently the fibre-matrix strain jump $[[\varepsilon_{f-m}]]$ increases) whereas, once the debonding is complete ($L_{ad}=0$), the above equation depends only on the fibre geometry and on the fibre-matrix friction shear stress value τ_{fu}.

3.6.2 Fibre-fibre interaction effect

Fibres can interact each other when their distance is small and their reciprocal orientation leads to an overlapping. As a matter of fact, the matrix in such situations cannot easily fill the space around the fibres during the production process. The main result of the above phenomenon is the lack of matrix in some part of the composite, leading to a shorter effective fibre length for the stress transfer process between the matrix and the reinforcing fibre [191].

The probability to find a fibre in a generic point inside the composite can be assumed to be coincident with the fibre volume fraction μ_f. The probability to find two fibres in one point is equal to μ_f^2, and that to find m fibres in one point is μ_f^m. Since μ_f is usually a small number, only the first and second order terms can

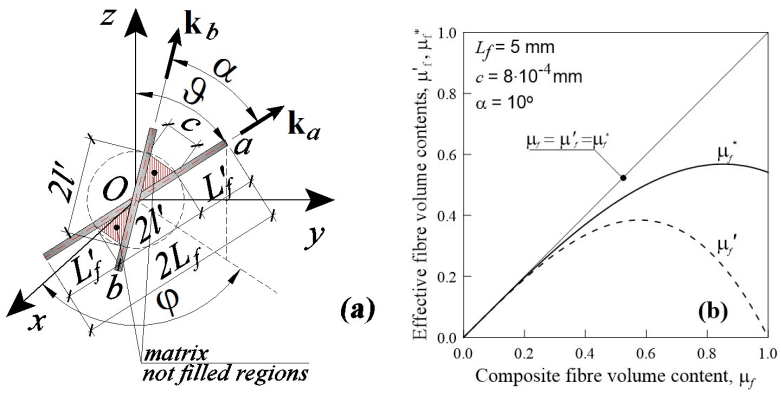

Figure 3.15: A couple of interacting fibres (a) and function μ'_f and μ^*_f (b).

be taken into account. The effective fibre volume μ'_f can be corrected as follows:

$$\mu'_f = \mu_f \cdot (1 - \mu_f^2)$$

if the fraction μ_f^2 is assumed to be completely ineffective in the composite (Fig. 3.15a), that is, fibres located at the same point are supposed to be not working due to their reciprocal interaction. Such a hypothesis is too much conservative and, therefore, the effective length of fibres located at the same point needs to be properly reduced.

In order to find out the size of the empty space around the fibres and the effective length, a composite characteristic length c can be assumed (for example, it could be identified with the typical aggregate or matrix grain size). The space that cannot be filled by the matrix material can be quantified through the effective fibre length $2L'_f$ (Fig. 3.15a) [192]:

$$2L'_f = 2L_f - \frac{c}{\sin(\alpha/2)} \qquad \text{with } c \leq 2L_f \cdot \sin(\alpha/2) = c_{max} \tag{3.73}$$

where $\alpha = arccos(\boldsymbol{k}_a \cdot \boldsymbol{k}_b)$ is the angle between the fibres a and b, with the fibre direction unit vector expressed through the Euler angles φ, ϑ: $\boldsymbol{k} = \{k_x\ k_y\ k_z\} = \{\sin\vartheta \cdot \cos\varphi\ \ \sin\vartheta \cdot \sin\varphi\ \ \cos\vartheta\}$. The effective matrix-fibre contact surface S_f (for one fibre) can be evaluated as follows:

$$S_f = p \cdot 2L_f - \frac{p}{2} \cdot 2l' = p \cdot (2L_f - l') \tag{3.74}$$

where p is the perimeter of the fibre. In Eq. (3.74), only half of the length l' (i.e. the portion of the fibre surface enclosed between the two fibres) is assumed to be ineffective, while the outer portion is still working. In such a way, the fibre contact area for two superposed aligned fibres ($l' = L_f$) reduces to that for a single fibre.

The fibre-matrix contact surface ratio can be expressed by $r = S_f/S_t$, where $S_t = p \cdot 2L_f$ is the contact surface of one isolated fibre. By taking into account the above ratio and the fibre-fibre interaction, the effective volume fraction μ_f^* of the composite can be updated as follows:

$$\mu_f^* = \mu_f \cdot [1 - (1-r) \cdot \mu_f^2], \qquad r = p \cdot (2L_f - l')/(p \cdot 2L_f) = 1 - l'/2L_f \quad (3.75)$$

i.e. the fibres located at the same position collaborate to the load bearing capability of the composite by the fraction $r \cdot \mu_f^2$, whereas the fraction $(1-r) \cdot \mu_f^2$ is completely ineffective for such a purpose. Eq. (3.75) is plotted in Fig. 3.15a for some specific values of the fibre parameters. The angle α between fibres is assumed to be equal to the variation of the mean angle for unidirectional FRC, whereas $\alpha = \pi/4$ is adopted for random fibres (that is, the maximum angle between fibres uniformly oriented in every spatial directions).

Chapter 4

A Computational Model for Matrix Materials

4.1 Introduction

The matrix phase requires the present Chapter due to the complexity of its mechanical aspects.

In the following, the behaviour of the matrix material under both static and cyclic loading is analysed. In the first case, both the elastic-plastic and brittle behaviours are examined, whereas a damage approach based on the Whöler curves is adopted, in the latter case, to describe the fatigue effects. The computational algorithm obtained from the present formulation is reported and discussed and some numerical examples are performed in order to clarify the mechanical model exposed below.

4.2 Matrix Material: Brittle Behaviour

Problems characterised by high strain localisation (such as diffuse micro-crack created in brittle or quasi-brittle materials), i.e. progressive strain concentration in a narrow zone identified as *fracture process zone*, are common in engineering applications. Their numerical simulation is a hard task due to the discontinuity of the displacement field in the cracked zones, which can produce computational

instability, divergence and non-uniqueness of the solution [193]. The simulation of a geometric discontinuity by using the finite element technique can be obtained by incorporating displacement functions in the FE formulation [194–196]. In this context, the developed models can be roughly divided into two classes, depending on the regularity of the kinematics description of the displacement field. The displacement field (and the corresponding strain field) can be considered to be:

- *Continuous*: when both the displacement and the strain fields do not present any jump, even if they have high gradient values in the process zone. Models belonging to this class are characterized by the continuity of both displacement and strain fields, and the process zone is represented by a band or layer of softening material where the strain gradually increases from the minimum value on the boundary of the band to its maximum value at its centre.

- *Weak discontinuity*: the displacement field is continuous but the strain field presents a discontinuity in a finite interval, i.e. it has a jump at the boundary of the process zone. Models belonging to this class use a continuous description of the displacement field but admit the presence of weak discontinuities.

- *Strong discontinuity*: the displacement field has a discontinuity in a single point, along a curve or on a surface, at which it presents a jump; the corresponding strain field becomes unbounded in correspondence of the displacement discontinuity. Models belonging to this class admit presence of a *strong discontinuity* along a curve (2D problems) or a surface (3D problems) across which the displacement field shows a jump.

The localization of strain corresponds to a damage that leads to a gradual development of macroscopic stress-free cracks. Furthermore, it is reasonable to assume that the discontinuity transmits some cohesive forces (traction) that are related to the opening and sliding component of the displacement jump through a particular traction-separation law. Consequently, the presence of the discontinuity can produce a cohesive crack, whose effects are usually assumed to decrease with crack opening and to vanish when the crack opening exceeds a certain value, corresponding to the condition of stress-free crack faces.

The progressive localised damage can be modelled through many approaches in the literature. By considering a perfect brittle behaviour, Rashid [197] proposed a model where a finite element is considered to be cracked when the stress level

inside it exceeds a fixed limit. Then the constitutive laws are modified in order to nullify the stress normal to the discontinuity. However, such an approach does not consider, even for brittle materials, the existence of a zone of finite dimension near the tip of the crack with non-linear behaviour. This aspect was introduced by Hillerborg [198] through the presence of a cohesive traction transmitted normal to the crack faces.

The *smeared crack approach* models the discontinuity through a suitable modification of the material properties. If the strain energy released by the modified elements during the softening phase is equal to the strain energy released by a discrete increment of the crack opening, the overall behaviour is equivalent. The smeared crack model is convenient when the orientation of the crack is not known a priori: it does not need remeshing or the introduction of new degrees of freedom. Consequently, the nucleation of one or more cracks in the finite element volume is related to the deterioration of the current stiffness matrix at the integration point level. This class of crack models has the drawback of producing a possible non-uniqueness of the solution and presenting an excessive mesh dependence.

In order to fix this problem and to regularize the solution, non-local models based on the smeared crack approach with an integral or differential formulation have been proposed [199, 200]. Two main classes of strategies can be distinguished to describe the crack formation in the finite elements: a local approach and a remeshing technique. In the first type of methods, the fracture process is described by using micromechanical models to represent the evolution of damage in the material. The presence of the crack is not geometrically introduced by modifying the mesh. In the latter class, the crack propagation in elastic or elastic-plastic materials can be analysed by suitable remeshing algorithms, in which the displacement discontinuity induced by the separation of the edges of a crack is physically introduced in the mesh to model the evolution of damage. The remeshing technique can be applied to the entire model at every step of the calculation or locally involving only the region of finite elements within a certain distance from the crack tip. In the first case, the generated finite elements are, generally, well shaped but the main disadvantage is the large number of field variables transferred from the old to the new mesh. In the letter case, the field variables are less numerous, but the generated finite elements may not be well-shaped due to the existing unchanged mesh surrounding the remeshed region.

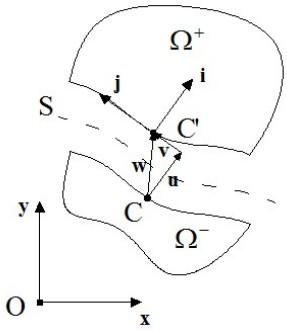

Figure 4.1: Example of a 2-D solid Ω having a discontinuous displacement field along the line S characterised by the normal and tangential versors $\boldsymbol{i}$ and $\boldsymbol{j}$ in the point C.

A different way to describe the crack propagation in solid can be formulated by introducing a detaching algorithm in order to properly separate adjacent finite elements when a crack develops between them. The earliest proposed approach uses a node decoupling technique with a simple nodal force release mechanism [201, 202]. Generally, such a method produces inaccurate results, because the node release technique requires an a priori knowledge of the crack path, and it is usually constrained to growth by following the mesh pattern. Furthermore, singular elements cannot be employed easily around the crack tip.

Another technique which allows geometry changes during the computation procedure is the Element-Free Galerkin (EFG) method [203]. The mesh of the domain is not necessary because it uses only nodal data and do not require any element connectivity. The shape functions describing the approximate displacement field are obtained though the moving least-square interpolants [204]. The slope functions of the EFG approach in presence of geometrical discontinuities can be obtained by adopting specific techniques such as the transparency one, the diffraction approach and so on.

Finally, the eXtended Finite Element Method (X-FEM) [205] allows to model the geometric quantities independent of the finite element mesh. It enriches a standard mesh-based approximations of the displacement field with additional discontinuous functions without the need of any remeshing. The geometry of the discontinuity is updated by means of the enrichment scheme.

4.2.1 Kinematic formulation

In the present approach, a solid occupying a region Ω within a discontinuity of the displacement field along the line S is examined. The normal and tangential directions to the discontinuity at a generic point C on S are identified by the versors **i** and **j**, respectively (Fig. 4.1).

The discontinuous displacement field in Ω can be written as [196]:

$$\boldsymbol{\delta}(\boldsymbol{x}) = \overline{\boldsymbol{\delta}}(\boldsymbol{x}) + H(\boldsymbol{x}) \cdot [[\boldsymbol{\delta}(\boldsymbol{x})]] = \overline{\boldsymbol{\delta}}(\boldsymbol{x}) + \underbrace{H(\boldsymbol{x}) \cdot \boldsymbol{w}(\boldsymbol{x})}_{\boldsymbol{\delta_d}(\boldsymbol{x})} \tag{4.1}$$

where the total displacement field $\boldsymbol{\delta}(\boldsymbol{x})$ is given by the sum of the continuous part $\overline{\boldsymbol{\delta}}(\boldsymbol{x})$ and the discontinuous one $\boldsymbol{\delta_d}(\boldsymbol{x}) = H(\boldsymbol{x}) \cdot [[\boldsymbol{\delta}(\boldsymbol{x})]] = H(\boldsymbol{x}) \cdot \boldsymbol{w}(\boldsymbol{x})$. The function $H(\boldsymbol{x})$ is the Heaviside jump function across the crack line and is defined as:

$$H(\boldsymbol{x}) = 0 \qquad \text{if} \quad \boldsymbol{x} \in \Omega^- \qquad \text{and} \qquad H(\boldsymbol{x}) = 1 \qquad \text{if} \quad \boldsymbol{x} \in \Omega^+$$

The displacement jump vector across the line S indicated with $[[\boldsymbol{\delta}(\boldsymbol{x})]] = \boldsymbol{w}(\boldsymbol{x})$ coincides with the displacement discontinuity vector. In Eq. (4.1) the discontinuity jump vector $\boldsymbol{w}(\boldsymbol{x})$ can be given by the sum of the normal ($\boldsymbol{u}(\boldsymbol{x})$) and the tangential ($\boldsymbol{v}(\boldsymbol{x})$) jump vectors, i.e. $\boldsymbol{w}(\boldsymbol{x}) = \boldsymbol{u}(\boldsymbol{x}) + \boldsymbol{v}(\boldsymbol{x})$ (Fig. 4.1).

Through the strain-displacement relationship, under the small deformation hypothesis, the strain tensor can be obtained [194]:

$$\boldsymbol{\varepsilon}(\boldsymbol{x}) = \underbrace{\nabla^s \overline{\boldsymbol{\delta}}(\boldsymbol{x}) + H(\boldsymbol{x}) \cdot \nabla^s \boldsymbol{w}(\boldsymbol{x})}_{\boldsymbol{\varepsilon^b}(\boldsymbol{x})} + \underbrace{\delta_s (\boldsymbol{w}(\boldsymbol{x}) \otimes \boldsymbol{i})^s}_{\boldsymbol{\varepsilon^u}(\boldsymbol{x})} \tag{4.2}$$

where ∇^s is the symmetric operator and δ_s is the Dirac delta function located on S, i.e.: $\delta_s = 0$ if $\boldsymbol{x} \in \Omega^+ \cup \Omega^- = \Omega \setminus S$ and $delta_s = \infty$ if $\boldsymbol{x} \in S$.

Note that the bounded, $\boldsymbol{\varepsilon^b}(\boldsymbol{x})$, and the unbounded, $\boldsymbol{\varepsilon^u}(\boldsymbol{x})$, parts of the strains along the discontinuity line S are outlined in Eq. (4.2). Since the narrow band, where the displacement discontinuity takes place, has thickness equal to zero, the strain and the stress fields are bounded in the region where the material is continuous (denoted by $\Omega^+ \cup \Omega^- = \Omega \setminus S$, Fig. 4.1). Consequently the stress tensor can be evaluated by an appropriate constitutive law and, in the simplest case of

a linear elastic material's behaviour, the bounded part of the stress field can be obtained:

$$\boldsymbol{\sigma}(\boldsymbol{x}) = \boldsymbol{C} : [\nabla^s \overline{\boldsymbol{\delta}}(\boldsymbol{x}) + H(\boldsymbol{x}) \cdot \nabla^s \boldsymbol{w}(\boldsymbol{x})] \qquad \text{with } \boldsymbol{x} \in \Omega^+ \cup \Omega^- = \Omega \setminus S \quad (4.3)$$

where $\boldsymbol{C}$ is the standard fourth order elastic tensor.

4.2.2 Variational formulation

The governing equation for the equilibrium problem of a body Ω with a crack along a line S can be written as follows:

$$\nabla\boldsymbol{\sigma} + \boldsymbol{b} = 0 \qquad \text{in } \Omega \setminus S \quad (4.4a)$$

$$\boldsymbol{s} = \hat{\boldsymbol{s}} \qquad \text{on } \Gamma_u \quad (4.4b)$$

$$\boldsymbol{\sigma} \cdot \boldsymbol{n} = \hat{\boldsymbol{t}} \qquad \text{on } \Gamma_t \text{ with } \Gamma_t \cup \Gamma_u = \partial\Omega \quad (4.4c)$$

$$\left.\begin{aligned} \boldsymbol{\sigma}^+ \cdot \boldsymbol{n}^+ &= \hat{\boldsymbol{t}}^+ \\ \boldsymbol{\sigma}^- \cdot \boldsymbol{n}^- &= \hat{\boldsymbol{t}}^- \end{aligned}\right\} \quad \boldsymbol{t}^+ = \boldsymbol{t}^- \qquad \text{on } S \quad (4.4d)$$

$$\boldsymbol{\varepsilon} = \nabla^s \boldsymbol{u}, \quad \boldsymbol{\sigma} = \boldsymbol{\sigma}(\boldsymbol{\varepsilon}) \qquad \text{in } \Omega \setminus S \quad (4.4e)$$

In the previous equations, $\boldsymbol{b}$ represents the body force vector, $\bar{\boldsymbol{u}}$ and $\boldsymbol{t}$ are prescribed displacement and tension vectors on Γ_u and on Γ_t, respectively, whereas $\boldsymbol{t}^+ = -\boldsymbol{t}^-$ are the tensions across the discontinuity line S. The last equations (4.4e) represent the linear strain-displacement and constitutive relationships, respectively.

By assuming that the condition $\boldsymbol{u} = \bar{\boldsymbol{u}}$ is exactly satisfied on Γ_u, the following three-fields weak form can be written [195]:

$$\begin{aligned}
&\left[\int_{\Omega^-} \delta\boldsymbol{u}^*(\nabla\boldsymbol{\sigma} + \boldsymbol{b})d\Omega + \int_{\Omega^+} \delta\boldsymbol{u}^*(\nabla\boldsymbol{\sigma} + \boldsymbol{b})d\Omega\right] + \\
&+\left[\int_{\Omega^-} \delta\boldsymbol{\sigma}^*(\boldsymbol{\varepsilon} - \nabla^s\boldsymbol{u})d\Omega + \int_{\Omega^+} \delta\boldsymbol{\sigma}^*(\boldsymbol{\varepsilon} - \nabla^s\boldsymbol{u})d\Omega\right] + \\
&+\left[\int_{\Omega^-} \delta\boldsymbol{\varepsilon}^*(\boldsymbol{\sigma} - \boldsymbol{\sigma}(\boldsymbol{\varepsilon})d\Omega + \int_{\Omega^+} \delta\boldsymbol{\varepsilon}^*(\boldsymbol{\sigma} - \boldsymbol{\sigma}(\boldsymbol{\varepsilon})d\Omega\right] + \\
&+\left[\int_{\Gamma_t^-} \delta\boldsymbol{u}^*(\boldsymbol{\sigma}\cdot\boldsymbol{n} - \hat{\boldsymbol{t}})d\Gamma + \int_{\Gamma_t^+} \delta\boldsymbol{u}^*(\boldsymbol{\sigma}\cdot\boldsymbol{n} - \hat{\boldsymbol{t}})d\Gamma\right] + \\
&+\left[\int_S \delta\boldsymbol{u}^{*-}(\boldsymbol{\sigma}^-\cdot\boldsymbol{n}^- - \hat{\boldsymbol{t}}^-)d\Gamma + \int_S \delta\boldsymbol{u}^{*+}(\boldsymbol{\sigma}^+\cdot\boldsymbol{n}^+ - \hat{\boldsymbol{t}}^+)d\Gamma\right] = 0
\end{aligned} \quad (4.5)$$

for any virtual displacement field $\delta\boldsymbol{u}^*$ to which corresponds the virtual strain $\delta\boldsymbol{\varepsilon}^* = \nabla^s\delta\boldsymbol{u}^*$ and the virtual stress field $\delta\boldsymbol{\sigma}^* = \boldsymbol{C}(\nabla^s\delta\boldsymbol{u}^*)$, where the symbol $\delta(\bullet)$ denotes a generic variation of the variable $(\bullet)$, $\Gamma_t^+ = \Gamma_t \cap \partial\Omega^+$ and $\Gamma_t^- = \Gamma_t \cap \partial\Omega^-$.

The terms $\int \delta\boldsymbol{u}^*\nabla\boldsymbol{\sigma}d\Omega = \int \delta\boldsymbol{u}^*(div\boldsymbol{\sigma})d\Omega$ in Eq. (4.5) in the sub-domains Ω^+ and Ω^- can be rewritten through the divergence theorem:

$$\begin{aligned}
&\int_{\Omega^-} \delta\boldsymbol{u}^*(div\boldsymbol{\sigma})d\Omega = \\
&\qquad = \int_{\Gamma_t^-} \delta\boldsymbol{u}^*(\boldsymbol{\sigma}\cdot\boldsymbol{n})d\Gamma + \int_S \delta\boldsymbol{u}^*(\boldsymbol{\sigma}^-\cdot\boldsymbol{n}^-)d\Gamma - \int_{\Omega^-} \nabla^s(\delta\boldsymbol{u}^*)\boldsymbol{\sigma}d\Omega \\
&\int_{\Omega^+} \delta\boldsymbol{u}^*(div\boldsymbol{\sigma})d\Omega = \\
&\qquad = \int_{\Gamma_t^+} \delta\boldsymbol{u}^*(\boldsymbol{\sigma}\cdot\boldsymbol{n})d\Gamma + \int_S \delta\boldsymbol{u}^*(\boldsymbol{\sigma}^+\cdot\boldsymbol{n}^+)d\Gamma - \int_{\Omega^+} \nabla^s(\delta\boldsymbol{u}^*)\boldsymbol{\sigma}d\Omega
\end{aligned} \tag{4.6}$$

Then, by considering the relationship reported in Eqs. (4.4), the following terms contained in Eq. (4.5) can be recognized to fulfil the following equalities::

$$\begin{aligned}
\left[\int_{\Omega^-} \delta\boldsymbol{\sigma}^*(\boldsymbol{\varepsilon} - \nabla^s\boldsymbol{u})d\Omega + \int_{\Omega^+} \delta\boldsymbol{\sigma}^*(\boldsymbol{\varepsilon} - \nabla^s\boldsymbol{u})d\Omega\right] &= 0 \\
\left[\int_{\Omega^-} \delta\boldsymbol{\varepsilon}^*(\boldsymbol{\sigma} - \boldsymbol{\sigma}(\boldsymbol{\varepsilon})d\Omega + \int_{\Omega^+} \delta\boldsymbol{\varepsilon}^*(\boldsymbol{\sigma} - \boldsymbol{\sigma}(\boldsymbol{\varepsilon})d\Omega\right] &= 0 \\
\left[\int_{\Gamma_t^-} \delta\boldsymbol{u}^*(\boldsymbol{\sigma}\cdot\boldsymbol{n} - \hat{\boldsymbol{t}})d\Gamma + \int_{\Gamma_t^+} \delta\boldsymbol{u}^*(\boldsymbol{\sigma}\cdot\boldsymbol{n} - \hat{\boldsymbol{t}})d\Gamma\right] &= 0 \\
\left[\int_S \delta\boldsymbol{u}^{*-}(\boldsymbol{\sigma}^-\cdot\boldsymbol{n}^- - \hat{\boldsymbol{t}}^-)d\Gamma + \int_S \delta\boldsymbol{u}^{*+}(\boldsymbol{\sigma}^+\cdot\boldsymbol{n}^+ - \hat{\boldsymbol{t}}^+)d\Gamma\right] &= 0
\end{aligned}$$

By using Eq. (4.6), the weak form of Eq. (4.5) becomes:

$$\int_{\Omega\setminus S} \nabla^s(\delta\boldsymbol{u}^*)\boldsymbol{\sigma}d\Omega = \int_{\Omega\setminus S} (\delta\boldsymbol{u}^*)\boldsymbol{b}d\Omega + \int_{\Gamma_t} \delta\boldsymbol{u}^*\hat{\boldsymbol{t}}d\Gamma + \int_S (\delta\boldsymbol{u}^{*+} - \delta\boldsymbol{u}^{*-})\hat{\boldsymbol{t}}d\Gamma \tag{4.7}$$

By introducing the classical FE notation, the quantities related to the virtual displacement field $\delta\boldsymbol{u}^*$ can be written as follows:

$$\begin{aligned}
&\delta\boldsymbol{u}^* = \boldsymbol{N}\cdot\delta\boldsymbol{\delta}^* + \left[H\boldsymbol{I} - \boldsymbol{N}^+\right]\delta\boldsymbol{w}_n^* \\
&\nabla^s(\delta\boldsymbol{u}^*) = \delta\boldsymbol{\varepsilon}^* = \boldsymbol{B}\cdot\delta\boldsymbol{\delta}^* - \left[\boldsymbol{B}^+\otimes\delta\boldsymbol{w}_n^*\right]^s \qquad \text{in } \Omega\setminus S
\end{aligned} \tag{4.8}$$

$$\begin{aligned} \delta \boldsymbol{w}^* &= \delta \boldsymbol{u}^{*+} - \delta \boldsymbol{u}^{*-} = \delta[[\boldsymbol{u}^*]] \qquad \text{in } S \\ \int_{\Omega \setminus S} \nabla^s(\delta \boldsymbol{u}^*) \boldsymbol{\sigma} d\Omega &= \int_{\Omega \setminus S} \delta \boldsymbol{\varepsilon}^* \boldsymbol{\sigma} d\Omega = \int_{\Omega \setminus S} \delta \boldsymbol{\varepsilon}^* \boldsymbol{C} \boldsymbol{\varepsilon} d\Omega \end{aligned} \tag{4.9}$$

where the sum of the shape functions evaluated at the location $\boldsymbol{x} \in \Omega_e^+$ has been indicated with $\boldsymbol{N}^+(\boldsymbol{x}) = \sum_{i \in \Omega_e^+} N_i(\boldsymbol{x})$.

In Eq. (4.8), the discontinuity vector is assumed to be associated to the element's node (n) in order to be interpolated through the modified shape functions $\left[H\boldsymbol{I} - \boldsymbol{N}^+\right]$, i.e. $\boldsymbol{w} = \left[H\boldsymbol{I} - \boldsymbol{N}^+\right] \cdot \boldsymbol{w}_n$.

The same relationship can be assumed for the virtual displacement jump field: $\delta \boldsymbol{w}^* = \left[H\boldsymbol{I} - \boldsymbol{N}^+\right] \cdot \delta \boldsymbol{w}_n^*$. By using the previous equations, Eq. (4.7) can be rewritten as follows:

$$\begin{aligned} &\int_{\Omega \setminus S} \Big[\boldsymbol{B} \cdot \delta \boldsymbol{\delta}^* - \left[\boldsymbol{B}^+ \otimes \delta \boldsymbol{w}_n^*\right]^s\Big]^t \boldsymbol{C} \Big[\boldsymbol{B} \cdot \boldsymbol{\delta} - \left[\boldsymbol{B}^+ \otimes \boldsymbol{w}_n\right]^s\Big] d\Omega = \\ &= \int_{\Omega \setminus S} \Big[\boldsymbol{N} \cdot \delta \boldsymbol{\delta}^* + \left[H\boldsymbol{I} - \boldsymbol{N}^+\right] \delta \boldsymbol{w}_{\boldsymbol{n}}^*\Big]^t \boldsymbol{b} d\Omega + \\ &+ \int_{\Gamma_t} \Big[\boldsymbol{N} \cdot \delta \boldsymbol{\delta}^* + \left[H\boldsymbol{I} - \boldsymbol{N}^+\right] \delta \boldsymbol{w}_{\boldsymbol{n}}^*\Big]^t \hat{\boldsymbol{t}} d\Gamma + \int_S \delta \boldsymbol{w}^* \hat{\boldsymbol{t}} d\Gamma \end{aligned} \tag{4.10}$$

where the nodal discontinuous displacement vector $\boldsymbol{w}_n$ is now made explicit present in the formulation.

Since the virtual displacement $\delta \boldsymbol{\delta}^*$ and the virtual displacement jump vector $\delta \boldsymbol{w}^*$ are chosen arbitrarily, they can be assumed independent of each other, and the following two expressions can be obtained:

$$\begin{cases} \displaystyle\int_{\Omega \setminus S} \left[\boldsymbol{B} \cdot \delta \boldsymbol{\delta}^*\right]^t \boldsymbol{C} \Big[\boldsymbol{B} \cdot \boldsymbol{\delta} - \left[\boldsymbol{B}^+ \otimes \boldsymbol{w}_n\right]^s\Big] d\Omega = \\ \qquad\qquad = \displaystyle\int_{\Omega \setminus S} \left[\boldsymbol{N} \cdot \delta \boldsymbol{\delta}^*\right]^t \boldsymbol{b} d\Omega + \int_{\Gamma_t} \left[\boldsymbol{N} \cdot \delta \boldsymbol{\delta}^*\right]^t \hat{\boldsymbol{t}} d\Gamma \\ \displaystyle\int_{\Omega \setminus S} \Big[- \left[\boldsymbol{B}^+ \otimes \delta \boldsymbol{w}_n^*\right]^s\Big]^t \boldsymbol{C} \Big[\boldsymbol{B} \cdot \boldsymbol{\delta} - \left[\boldsymbol{B}^+ \otimes \boldsymbol{w}_n\right]^s\Big] d\Omega = \\ \qquad = \displaystyle\int_{\Gamma_t} \Big[\left[H\boldsymbol{I} - \boldsymbol{N}^+\right] \delta \boldsymbol{w}_{\boldsymbol{n}}^*\Big]^t \hat{\boldsymbol{t}} d\Gamma + \int_S \Big[\left[H\boldsymbol{I} - \boldsymbol{N}^+\right] \delta \boldsymbol{w}^*\Big]^t \hat{\boldsymbol{t}} d\Gamma \end{cases} \tag{4.11}$$

Furthermore, by eliminating the arbitrary variations of the displacement vector, $\delta \boldsymbol{\delta}^*$, and of the discontinuity vector for the nodal dofs, $\delta \boldsymbol{w}_n^*$; the following

relationship can be got:

$$\begin{bmatrix} \int_{\Omega\setminus S} \boldsymbol{B}^t \boldsymbol{C} \boldsymbol{B} d\Omega & -\int_{\Omega\setminus S} \boldsymbol{B}^t \boldsymbol{C} \boldsymbol{B}^+ d\Omega \\ -\int_{\Omega\setminus S} \boldsymbol{B}^{+t} \boldsymbol{C} \boldsymbol{B} d\Omega & \int_{\Omega\setminus S} \boldsymbol{B}^{+t} \boldsymbol{C} \boldsymbol{B}^+ d\Omega \end{bmatrix} \begin{Bmatrix} \boldsymbol{\delta} \\ \boldsymbol{w}_n \end{Bmatrix} = \\ = \begin{Bmatrix} \int_{\Omega\setminus S} \boldsymbol{N}^t \boldsymbol{b} d\Omega + \int_{\Gamma_t} \boldsymbol{N}^t \hat{\boldsymbol{t}} d\Gamma \\ \int_{\Gamma_t} \left[H\boldsymbol{I} - \boldsymbol{N}^+\right]^t \hat{\boldsymbol{t}} d\Gamma + \int_S \left[H\boldsymbol{I} - \boldsymbol{N}^+\right]^t \hat{\boldsymbol{t}} d\Gamma \end{Bmatrix} \tag{4.12}$$

By considering the traction-jump law having the incremental form: $d\hat{\boldsymbol{t}} = \boldsymbol{T} \cdot d\boldsymbol{w}$ on the crack line S, where $\boldsymbol{T}$ is a proper operator which relates the crack traction to the crack jump displacements, the second element of the right-hand side vector of the previous equation can be expressed in the following form:

$$\int_S \left[H\boldsymbol{I} - \boldsymbol{N}^+\right]^t \boldsymbol{T} \cdot d\boldsymbol{w} d\Gamma = \int_S \left[H\boldsymbol{I} - \boldsymbol{N}^+\right]^t \boldsymbol{T} \cdot \left[H\boldsymbol{I} - \boldsymbol{N}^+\right] d\boldsymbol{w}_n d\Gamma \tag{4.13}$$

Then Eq. (4.12) can be rewritten in incremental form as follows:

$$\begin{bmatrix} \int_{\Omega\setminus S} \boldsymbol{B}^t \boldsymbol{C} \boldsymbol{B} d\Omega & -\int_{\Omega\setminus S} \boldsymbol{B}^t \boldsymbol{C} \boldsymbol{B}^+ d\Omega \\ -\int_{\Omega\setminus S} \boldsymbol{B}^{t+} \boldsymbol{C} \boldsymbol{B} d\Omega & \int_{\Omega\setminus S} \boldsymbol{B}^{t^+} \boldsymbol{C} \boldsymbol{B}^+ d\Omega + K_s \end{bmatrix} \begin{Bmatrix} d\boldsymbol{\delta} \\ d\boldsymbol{w}_n \end{Bmatrix} = \\ = \begin{Bmatrix} \overbrace{\int_{\Omega\setminus S} \boldsymbol{N}^t d\boldsymbol{b} d\Omega + \int_{\Gamma_t} \boldsymbol{N}^t d\hat{\boldsymbol{t}} d\Gamma}^{d\boldsymbol{f_1}} \\ \int_{\Gamma_t} \left[H\boldsymbol{I} - \boldsymbol{N}^+\right]^t d\hat{\boldsymbol{t}} d\Gamma \end{Bmatrix} \tag{4.14}$$

where d denotes a generic increment and

$$K_s = -\int_S \left[H\boldsymbol{I} - \boldsymbol{N}^+\right]^t \boldsymbol{T} \cdot \left[H\boldsymbol{I} - \boldsymbol{N}^+\right] d\Gamma$$

Now, by considering the hypotheses that the incremental traction forces introduced at the discontinuity are equal to zero, i.e. $\int_{\Gamma_t} \left[H\boldsymbol{I} - \boldsymbol{N}^+\right]^t d\hat{\boldsymbol{t}} d\Gamma = 0$, the above equations can be rewritten in a compact form:

$$\begin{bmatrix} \boldsymbol{K}_{\delta\delta} & \boldsymbol{K}_{\delta w} \\ \boldsymbol{K}_{w\delta} & \boldsymbol{K}_{ww} + \boldsymbol{K}_s \end{bmatrix} \begin{Bmatrix} d\boldsymbol{\delta} \\ d\boldsymbol{w} \end{Bmatrix} = \begin{bmatrix} \boldsymbol{K}_{\delta\delta} & \boldsymbol{K}_{\delta w} \\ \boldsymbol{K}_{w\delta} & \boldsymbol{K}_{ww-S} \end{bmatrix} \begin{Bmatrix} d\boldsymbol{\delta} \\ d\boldsymbol{w} \end{Bmatrix} = \begin{Bmatrix} d\boldsymbol{f_1} \\ d\boldsymbol{0} \end{Bmatrix} \tag{4.15}$$

where $\boldsymbol{K}_{ww-S} = \boldsymbol{K}_{ww} + \boldsymbol{K}_s$. Finally, the unknown vectors can be found by

performing a static condensation:

$$\begin{cases} d\boldsymbol{w} = \boldsymbol{K}_{ww,S}^{-1}\left(-\boldsymbol{K}_{w\delta}d\boldsymbol{\delta}\right) \\ d\boldsymbol{\delta} = \left(\boldsymbol{K}_{\delta\delta} - \boldsymbol{K}_{\delta w}\boldsymbol{K}_{ww,S}^{-1}\boldsymbol{K}_{w\delta}\right)^{-1} d\boldsymbol{f}_1 = \overline{\boldsymbol{K}_{\delta\delta}}^{-1} d\boldsymbol{f}_1 \end{cases} \tag{4.16}$$

The matrix

$$\overline{\boldsymbol{K}_{\delta\delta}} = \boldsymbol{K}_{\delta\delta} - \boldsymbol{K}_{\delta w}\boldsymbol{K}_{ww-S}^{-1}\boldsymbol{K}_{w\delta} \tag{4.17}$$

can be considered to be the condensed incremental tangent stiffness matrix of the cracked finite element.

4.2.3 Stress-based discontinuous approach

By assuming the hypothesis that the discontinuity of the displacement field, occurred along a straight line S, is centred in the geometrical centre C of the cracked finite element and that such a discontinuity is characterised by an arbitrary direction (identified by the unit vector $\boldsymbol{j}$), the displacement field $\boldsymbol{\delta}(\boldsymbol{x})$ (see Eq. (4.1)) can be written as indicated by Eq. (4.8) (Fig. 4.2a):

$$\boldsymbol{\delta}(\boldsymbol{x}) = \boldsymbol{N}(\boldsymbol{x}) \cdot \boldsymbol{\delta} + \left[H\boldsymbol{I}(\boldsymbol{x}) - \boldsymbol{N}^{+}(\boldsymbol{x})\right] \cdot \boldsymbol{w}_n \tag{4.18}$$

$\boldsymbol{\delta}(\boldsymbol{x})$ is the sum of the classical continuous displacement field $\boldsymbol{N}(\boldsymbol{x}) \cdot \boldsymbol{\delta}$ (where $\boldsymbol{N}(\boldsymbol{x})$ is the FE shape function matrix) and of the discontinuous part of the displacements $\left[H\boldsymbol{I}(\boldsymbol{x}) - \boldsymbol{N}^{+}(\boldsymbol{x})\right] \cdot \boldsymbol{w}_n$.

The vector $\boldsymbol{\delta}$ contains the standard nodal dofs, whereas the vector $\boldsymbol{w}_n$ the nodal discontinuities that allow to represent the displacement discontinuity along the line S. Consequently, the displacement jump vector can be written as $\boldsymbol{w}_c = \boldsymbol{u}_c + \boldsymbol{v}_c$, where $\boldsymbol{u}_c$ and $\boldsymbol{v}_c$ are the displacement jumps normal and parallel to the crack line at point C, respectively (Fig. 4.2b). By using the nodal counterparts, the above relationship becomes: $\boldsymbol{w}_n = \boldsymbol{u}_n + \boldsymbol{v}_n$, where $\boldsymbol{u}_n$ and $\boldsymbol{v}_n$ are the nodal displacement jumps normal and parallel to the crack line. The corresponding small strain field can be obtained as follows:

$$\boldsymbol{\varepsilon}(\boldsymbol{x}) = \underbrace{\boldsymbol{B}(\boldsymbol{x})\boldsymbol{\delta} - \left[\boldsymbol{B}^{+}(\boldsymbol{x}) \otimes \boldsymbol{w}_n\right]^{s}}_{\boldsymbol{\varepsilon}^{b}(\boldsymbol{x})} + \underbrace{\delta_s \boldsymbol{w}(\boldsymbol{x})}_{\boldsymbol{\varepsilon}^{u}(\boldsymbol{x})} \tag{4.19}$$

where $\boldsymbol{B}(\boldsymbol{x})$ is the compatibility matrix, $\boldsymbol{B}^{+}(\boldsymbol{x}) = \sum_{i \in \Omega_e^{+}} B_i(\boldsymbol{x})$ and δ_s is the Dirac

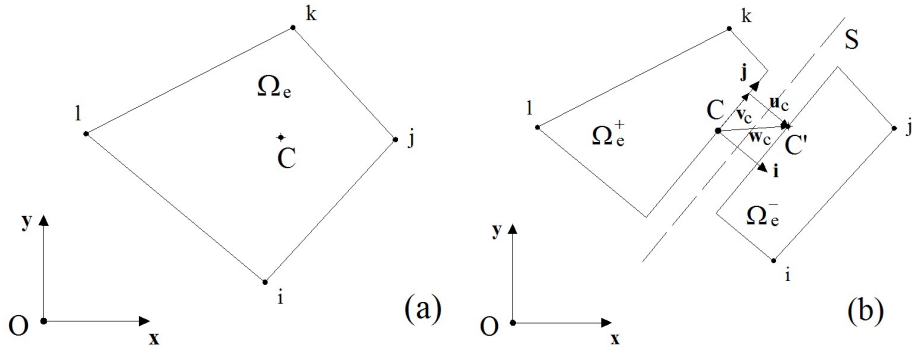

Figure 4.2: Finite element having an embedded discontinuity of the displacement field: no cracked (a) and cracked four noded finite element (b)

delta function placed on S, $(\boldsymbol{\varepsilon}^b(\boldsymbol{x}))$ and $(\boldsymbol{\varepsilon}^u(\boldsymbol{x}))$ are the bounded and unbounded parts of the strain. As can be noted, Eq. (4.19) is the discretised counterpart of Eq. (4.2).

As is stated in the previous section, since the narrow band, where the discontinuity takes place, has width tending to zero, the material can be assumed to remain continuous outside S (i.e. in the regions Ω_e^- and Ω_e^+ in Fig. 4.2b) and, consequently, the strains and stresses are bounded in $\Omega \setminus S$. For a linear elastic material, the stress tensor can be evaluated as follows:

$$\boldsymbol{\sigma}(\boldsymbol{x}) = \boldsymbol{C} : \boldsymbol{\varepsilon}^b(\boldsymbol{x}) = \boldsymbol{C} : \left[\boldsymbol{B}(\boldsymbol{x})\boldsymbol{\delta} - \left[\boldsymbol{B}^+(\boldsymbol{x}) \in \boldsymbol{w}_n\right]^s\right] \qquad \text{on } \Omega \setminus S \qquad (4.20)$$

Here, the nodal crack jump displacement vector $\boldsymbol{w}_n$ is unknown and must be evaluated through a properly material's cohesive law. As is well-known, it is reasonable to assume the existence of a bridging and/or a frictional stress in the process zone around the crack tip, which is usually well described by a decreasing function of the jump displacement $\boldsymbol{w}$.

The mechanical effects due to the discontinuity of the displacement field can be simulated through an ad-hoc FE stress field reduction in order to represent the damage phenomenon produced by the existence of the crack. Such a stress reduction can conveniently be evaluated on the basis of the stress-crack opening displacement relationship adopted for the material being examined. This formulation has the advantage to keep the continuity of the effective displacement field inside each finite

element, since the discontinuity is considered only at the stress level, without the need of special or enriched shape functions to modify the displacement field. By treating such a phenomenon in a way similar to the non-linear behaviour typical of the elastic-plastic FE problems, the equilibrium equations are fulfilled iteratively by driving the unbalanced nodal force vector $\boldsymbol{f}_{e-u}^{(i)}$ to very small values, according to a proper vector norm. For a given load step i, the unbalanced nodal force vector $\boldsymbol{f}_{e-u}^{(i)}$ can be evaluated over the finite elements domain Ω_e as follows:

$$\boldsymbol{f}_{e-u}^{(i)} = \boldsymbol{f}_{e,ext}^{(i)} - \int_{\Omega_e} \boldsymbol{B}^t \cdot \boldsymbol{\sigma}_{red}(\boldsymbol{w}_c) d\Omega \tag{4.21}$$

where $\boldsymbol{f}_{e,ext}^{(i)}$ is the corresponding external nodal force vector, and $\boldsymbol{\sigma}_{red}(\boldsymbol{w}_c)$ is the reduced stress tensor evaluated in the finite element by modifying the existing stress tensor $\boldsymbol{\sigma}(\boldsymbol{x})$ evaluated before the crack formation. This stress field correction can be performed by means of the knowledge of the relative displacement vector $\boldsymbol{w}_c = \boldsymbol{u}_c + \boldsymbol{v}_c = u_c\boldsymbol{i} + v_c\boldsymbol{j}$ across the crack. Such a vector is needed in order to evaluate the bridging stress $\sigma_c(u_c)$ transmitted across the crack faces in the process zone (see Sec. 4.2.3). Note that u_c and v_c represent the amount of the displacement jump measured normal (opening mode, u_c) and parallel (sliding mode, v_c) to the crack direction, respectively. The non-linear analysis process proceeds till some convergence requirements are fulfilled. In other words, at each load step increment, the FE model is solved, and the stress field is determined at each Gauss point of each cracked finite element by assuming an elastic or elastic-plastic material behaviour, and then it is properly modified for the next iteration. For the sake of simplicity, the hypotheses that the crack is located in the centre of the finite element and only its orientation can vary are made. In order to evaluate such an orientation, the stress state is computed in the centre of each finite element and the corresponding principal stress and strain directions are determined. When the maximum principal stress $\sigma_1(C)$ reaches the material tensile strength f_t, a straight crack S is introduced in the centre of the finite element under consideration (Fig. 4.2b) having an orientation, identified by the versor $\boldsymbol{i}$, normal to the current maximum principal stress ($\sigma_1(C)$) direction. The orientation of the versor $\boldsymbol{j}$ can vary also in the subsequent load steps up to the satisfaction of the same convergence requirements. After such a positive convergence check the current determined direction is kept constant through the remaining computational process.

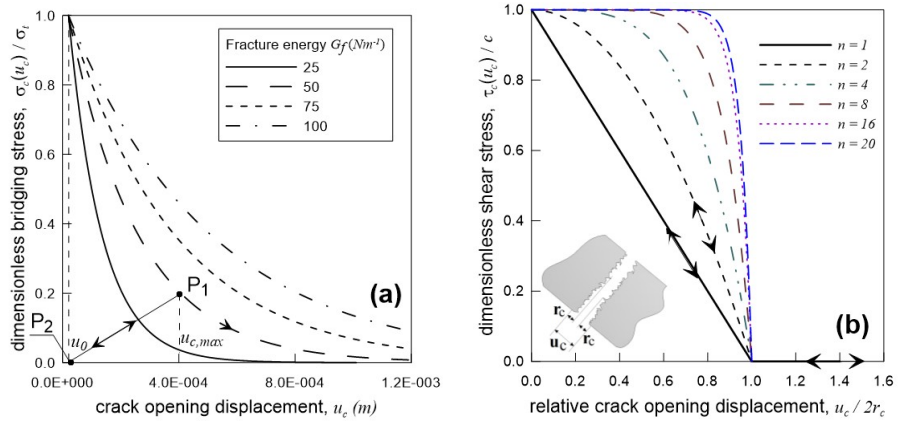

Figure 4.3: Examples of dimensionless bridging stress vs crack opening displacement u_c (a) and dimensionless shear stress transmitted across the crack faces vs relative crack opening displacement (b).

Crack bridging law

In order to describe the fracture process, a cohesive-friction law is introduced to simulate the mechanical behaviour of the cracked zone whereas an elastic or an elastic-plastic law is adopted for the non-cracked (continuous) region. In other words, the crack faces are assumed to transmit a non-zero stress which depends on a decreasing function of the relative crack face opening displacement u_c [206]. An example of such a relationship was proposed by Sancho [196] by assuming a piecewise linear decreasing function of u_c.

In the present Ph.D. Thesis, a continuous decreasing exponential law is adopted [195, 196]. The continuous bridging stress-crack opening relationship $\sigma_c(u_c)$ is written as follows:

$$\sigma_c(u_c) = f_t \cdot e^{\left\{\frac{2f_t(u_0 - u_c)}{2\mathcal{G}_f - f_t \cdot u_0}\right\}} \tag{4.22}$$

where f_t is the maximum tensile strength of the material, $\boldsymbol{u}_0$ is the lower crack opening limit at which the bridging process starts, and $\mathcal{G}_f$ is the fracture energy of the material (energy for unit surface crack [198]). This expression has the advantages to be continuous, derivable and with an asymptotic behaviour, i.e. $\sigma_c(u_c) \xrightarrow[u_c \to \infty]{} 0^+$.

The assumed cohesive law is graphically represented in Fig. 4.3a for different values of the fracture energy $\mathcal{G}_f$ of the material. Such a parameter, that governs

the decreasing slope of the function, is equal to the area under the curve $\sigma_c(u_c)$ [198], and physically represents the dissipated energy per unit surface crack area produced by the cracking process. By computing the integral in Eq. (4.22) for the integration variable v ranging in the interval $[u_0, +\infty)$, the value $\mathcal{G}_f$ of the exponential expression is found:

$$\mathcal{G}_f = \int_{u_0}^{+\infty} f_t \cdot e^{\left\{\frac{2f_t(u_0 - u_c)}{2\mathcal{G}_f - f_t \cdot u_0}\right\}} dv \tag{4.23}$$

The bridging stress-crack opening displacement relationship must be defined also for the case of unloading. In such a case, the bridging stress behaviour is assumed to be represented by a straight line defined by points $P_1 = \big(u_{c,max}, \sigma_c(u_{c,max})\big)$ and $P_2 = (u_0, 0)$. In the case of a subsequent reloading, the straight line is assumed to be followed till the previous maximum opening crack displacement $u_{c,max}$ is reached again [196].

When reloading occurs, for values of u_c greater than $u_{c,max}$, the original decreasing $\sigma_c(u_c)$ curve is followed again (Fig. 4.3a).

Furthermore, it is advisable to consider also the presence of a friction shear stress between the crack faces during the fracture process. With this aim, the crack surface roughness r_c that represents the mean asperity size measured perpendicular to the crack faces, can be introduced, and the shear stress can be reasonable assumed to be described by the following expression:

$$\tau_c(u_c) = \begin{cases} c \cdot \left(1 - \left(\dfrac{u_c}{2 \cdot r_c}\right)^n\right) & \text{if } 0 < u_c \leq 2 \cdot r_c \\ 0 & \text{if } u_c > 2 \cdot r_c \end{cases} \tag{4.24}$$

When the crack is completely closed ($u_c = 0$), the crack is assumed to be able to transmit a maximum shear stress equal to the material cohesion coefficient c.

When the opening process begins and the crack surface asperity are still in contact ($0 < u_c \leq 2 \cdot r_c$), a certain amount of shear stress exists between the crack faces, and is expressed by a decreasing law of the relative crack distance u_c.

Finally, when the crack opening distance exceed the double of the surface roughness, i.e. $u_c > 2 \cdot r_c$, the contact between the two surfaces vanishes, and the shear stress reaches the zero value, $\tau_c(u_c) = 0$.

The exponent n in Eq. (4.24) allows to control the shear stress decreasing rate

as a function of the relative crack distance (Fig. 4.3b). The above expression (Eq. (4.24)) is assumed to represent both the loading and the unloading situations.

FE formulation

As is previously mentioned, since during the crack process the strain is assumed to be concentrated in a very narrow band corresponding to the crack location, the knowledge of the crack jump displacement vector $\boldsymbol{w}(\boldsymbol{x})$, quantifying the relative crack opening displacement, is fundamental for the solution of the fracture problem. In order to do that, the FE mean nodal displacement values across the crack, projected in a direction normal ($\boldsymbol{u}_c$) and parallel ($\boldsymbol{v}_c$) to the crack direction, are defined:

$$\begin{aligned} \boldsymbol{w}_c = \boldsymbol{u}_c + \boldsymbol{v}_c = u_c \cdot \boldsymbol{i} + v_c \cdot \boldsymbol{j}, \qquad & \text{with} \\ u_c = \big[\boldsymbol{Q} \cdot (\boldsymbol{\delta} \cdot \boldsymbol{i})\big]/n_n, \qquad v_c = \big[\boldsymbol{Q} \cdot (\boldsymbol{\delta} \cdot \boldsymbol{j})\big]/n_n & \end{aligned} \tag{4.25}$$

where n_n is the nodal number of finite element nodes. The matrix $\boldsymbol{Q}$ is the nodal discontinuity matrix, and $\boldsymbol{\delta}$ is the element nodal displacement vector.

The nodal discontinuity matrix $\boldsymbol{Q}$ can easily be determined by considering the nodes of the finite element that lie in one or in the other part of the element defined by the crack line. As a matter of fact, by referring to Fig. 4.2b where a 2D problem with a 4 node cracked FE is represented, the above discontinuity matrix can explicitly be written as follows:

$$\boldsymbol{Q}^t = \begin{bmatrix} \overbrace{-1 & 0}^{\text{node } i} & \overbrace{+1 & 0}^{\text{node } j} & \overbrace{+1 & 0}^{\text{node } k} & \overbrace{-1 & 0}^{\text{node } l} \\ 0 & -1 & 0 & +1 & 0 & +1 & 0 & -1 \end{bmatrix} \begin{matrix} \\ \leftarrow \text{ dofs along } x \\ \leftarrow \text{ dofs along } y \end{matrix} \tag{4.26}$$

The simplest way to proceed is to consider the normal and the tangential values of the displacement jump across the crack faces independent of each other.

Firstly, the normal component $\boldsymbol{u}_c$ of $\boldsymbol{w}_c$ is examined (Fig. 4.2b). By using the above mean nodal normal displacement u_c across the crack given by Eq. (4.25) in Eq. (4.22), the crack bridging stress $\sigma_c = \sigma_c(u_c)$ value can be determined as a first attempt.

To physically represent the presence of the crack, the stress state must be modified in order to have exactly the stress σ_c normal to the crack faces. The

stress state can be *elastically-corrected* as follows:

$$\begin{aligned}\boldsymbol{\sigma}_{red(u)} &= \boldsymbol{\sigma} - \boldsymbol{C} : \left[\nabla^s(\boldsymbol{N}\cdot\boldsymbol{\delta}_{u(s)})\right] = \\ &= \boldsymbol{\sigma} - \boldsymbol{C} : \left[\nabla^s(\boldsymbol{N}\cdot s_n\cdot\boldsymbol{\delta}_u)\right] = \boldsymbol{\sigma} - \underbrace{\boldsymbol{C} : (s_n\cdot\boldsymbol{B}\cdot\boldsymbol{\delta}_u)}_{\boldsymbol{\sigma}_{\boldsymbol{c(u)}}}\end{aligned} \tag{4.27}$$

where $\boldsymbol{\sigma}$ is the effective stress tensor, and $\boldsymbol{\delta}_{u(s)} = (s_n\cdot\boldsymbol{\delta}_u)$ is a fictitious nodal displacement vector which is assumed to be proportional to the nodal displacement vector $\boldsymbol{\delta}_u$, through the coefficient s_n. The vector $\boldsymbol{\delta}_u$ is determined by considering the projection of the current nodal displacement vector $\boldsymbol{\delta}$ on the direction $\boldsymbol{i}$, i.e. $\boldsymbol{\delta}_u = (\boldsymbol{\delta}\cdot\boldsymbol{i}) = \boldsymbol{D}\cdot\boldsymbol{\delta}$. In the previous expression $\boldsymbol{D}$ is the operator which transforms the nodal displacement $\boldsymbol{\delta}$ into the normal nodal displacement components. Therefore, the stress tensor correction is performed by using a proper nodal displacement vector which is assumed to be the current FE nodal displacement vector projected on the direction $\boldsymbol{i}$.

The correction factor s_n can easily be determined as is described below. The normal traction $\sigma_{c(n)}$ acting at the middle point C of the crack and corresponding to the correction elastic tensor $\boldsymbol{\sigma}_{c(u)} = \boldsymbol{C} : (\boldsymbol{B}\cdot\boldsymbol{\delta}_{u(s)}))$ can be evaluated:

$$\sigma_{c,n} = (\boldsymbol{\sigma}_{c,u}\cdot\boldsymbol{i})\cdot\boldsymbol{i} = \left[\boldsymbol{C} : (\boldsymbol{B}\cdot\boldsymbol{\delta}_{u,s})\cdot\boldsymbol{i}\right]\cdot\boldsymbol{i}$$

where $\boldsymbol{B}$ is the compatibility matrix evaluated at point C. The effective normal stress $\sigma_{e(n)}$ on the crack plane, produced by the modified stress tensor $\boldsymbol{\sigma}_{red(n)}$, is expressed by:

$$\sigma_{e(n)} = (\boldsymbol{\sigma}_{red(n)}\cdot\boldsymbol{i})\cdot\boldsymbol{i}$$

Then, by imposing that $\sigma_{e(n)} = \sigma_c(u_c)$, the following expression can be obtained

$$\sigma_{e(n)} = (\boldsymbol{\sigma}_{red(n)}\cdot\boldsymbol{i})\cdot\boldsymbol{i} = \left[\left(\boldsymbol{\sigma} - \boldsymbol{C} : (s_n\cdot\boldsymbol{B}\cdot\boldsymbol{\delta}_u)\right)\cdot\boldsymbol{i}\right]\cdot\boldsymbol{i} = \sigma_c(u_c) \tag{4.28}$$

and the correction factor s_n can be determined:

$$s_n = \frac{(\boldsymbol{\sigma}\cdot\boldsymbol{i})\cdot\boldsymbol{i} - \sigma_c(u_c)}{\left[(\boldsymbol{C} : \boldsymbol{B}\cdot\boldsymbol{\delta}_u)\cdot\boldsymbol{i}\right]\cdot\boldsymbol{i}} = 1 - \frac{\sigma_c(u_c)}{\left[(\boldsymbol{C} : \boldsymbol{B}\cdot\boldsymbol{\delta}_u)\cdot\boldsymbol{i}\right]\cdot\boldsymbol{i}} \tag{4.29}$$

In the following, the friction shear stress transmitted across the crack faces is examined. From Eq. (4.24), once the crack opening is known, the shear stress

$\tau_c(u_c)$ which corresponds to the Mode II of fracture can be evaluated. Analogous to Mode I, the effective stress state must be modified in order to physically represent the friction shear stress across the crack faces. The nodal displacement vector $\boldsymbol{\delta}_v$ is determined by considering the projection $\boldsymbol{\delta}_v = (\boldsymbol{\delta} \cdot \boldsymbol{j}) \cdot \boldsymbol{j} = \boldsymbol{E} \cdot \boldsymbol{\delta}$ of the current nodal displacement vector $\boldsymbol{\delta}$ on the direction $\boldsymbol{j}$ (analogous to $\boldsymbol{D}$, $\boldsymbol{E}$ is the operator which transforms the nodal displacement $\boldsymbol{\delta}$ into the tangential nodal displacement components). The nodal displacement vector can be used to evaluate a fictitious displacement vector $\boldsymbol{\delta}_{v,s}$ which is assumed to be proportional to $\boldsymbol{\delta}_v$ ($\boldsymbol{\delta}_{v(s)} = s_s \cdot \boldsymbol{\delta}_v$) through the coefficient s_s. The reduced stress state can be written as follows:

$$\begin{aligned} \boldsymbol{\sigma}_{red(v)} &= \boldsymbol{\sigma} - \boldsymbol{C} : \left[\nabla^s(\boldsymbol{N} \cdot \boldsymbol{\delta}_{v(s)})\right] = \\ &= \boldsymbol{\sigma} - \boldsymbol{C} : \left[\nabla^s(\boldsymbol{N} \cdot s_s \cdot \boldsymbol{\delta}_v)\right] = \boldsymbol{\sigma} - \boldsymbol{C} : (s_s \cdot \boldsymbol{B} \cdot \boldsymbol{\delta}_v) \end{aligned} \tag{4.30}$$

By evaluating the shear stress $\tau_{c(n)}$ acting at the middle point C of the crack plane, corresponding to the correction elastic stress tensor $\boldsymbol{\sigma}_{c(v)} = \boldsymbol{C} : (\boldsymbol{B} \cdot \boldsymbol{\delta}_{v(s)}$

$$\tau_{c(n)} = (\boldsymbol{\sigma}_{c(v)} \cdot \boldsymbol{i}) \cdot \boldsymbol{j} = \left[\boldsymbol{C} : (\boldsymbol{B} \cdot \boldsymbol{\delta}_{v(s)}) \cdot \boldsymbol{i}\right] \cdot \boldsymbol{j}$$

and the effective shear stress $\tau_{e(n)}$, acting at the same point of such a fracture plane, produced by the modified stress tensor $\boldsymbol{\sigma}_{red(s)}$,

$$\tau_{e(n)} = (\boldsymbol{\sigma}_{red(s)} \cdot \boldsymbol{i}) \cdot \boldsymbol{j}$$

the correction factor s_s can be determined by imposing that $\tau_{e(n)} = \tau_c(u_c)$:

$$\tau_{e(n)} = (\boldsymbol{\sigma}_{red(s)} \cdot \boldsymbol{i}) \cdot \boldsymbol{j} = \left[\left(\boldsymbol{\sigma} - \boldsymbol{C} : (s_s \cdot \boldsymbol{B} \cdot \boldsymbol{\delta}_v)\right) \cdot \boldsymbol{i}\right] \cdot \boldsymbol{j} = \tau_c(u_c) \tag{4.31}$$

Then:

$$s_s = \frac{(\boldsymbol{\sigma} \cdot \boldsymbol{i}) \cdot \boldsymbol{j} - \tau_c(u_c)}{\left[(\boldsymbol{C} : \boldsymbol{B} \cdot \boldsymbol{\delta}_v) \cdot \boldsymbol{i}\right] \cdot \boldsymbol{j}} = 1 - \frac{\tau_c(u_c)}{\left[(\boldsymbol{C} : \boldsymbol{B} \cdot \boldsymbol{\delta}_v) \cdot \boldsymbol{i}\right] \cdot \boldsymbol{j}} \tag{4.32}$$

Finally, by considering the two above stress tensor corrections at the same time, the modified stress tensor in the considered FE can be written as follows:

$$\begin{aligned} \boldsymbol{\sigma}_{red} &= \boldsymbol{\sigma} - \boldsymbol{C} : \left[\nabla^s\big(\boldsymbol{N} \cdot (\boldsymbol{\delta}_{u(s)} + \boldsymbol{\delta}_{v(s)})\big)\right] = \\ &= \boldsymbol{\sigma} - \boldsymbol{C} : \left[\nabla^s\big(\boldsymbol{N} \cdot (s_n \boldsymbol{D} + s_s \boldsymbol{E}) \cdot \boldsymbol{\delta}\big)\right] = \\ &= \boldsymbol{\sigma} - \boldsymbol{C} : \left[\nabla^s(\boldsymbol{N} \cdot \boldsymbol{\delta}_{w(s)})\right] \end{aligned} \tag{4.33}$$

By considering, for simplicity, a 2-D plane stress problems, the reduced stress tensor $\boldsymbol{\sigma}_{red}$ in the crack co-ordinate system ξ, η can be written as (Fig. 4.2):

$$\boldsymbol{\sigma}_{red,S}(\boldsymbol{w}_c) = \boldsymbol{\sigma}_{red,S}(\boldsymbol{Q}, \boldsymbol{\delta}) = \begin{bmatrix} \sigma_c(u_c) & \tau_c(u_c) \\ \tau_c(u_c) & \sigma_\eta \end{bmatrix} \tag{4.34}$$

where σ_η is the stress present in the material acting in the direction parallel to crack that is not affected by the stress reduction. By properly rotating the above stress tensor in the global co-ordinate system, $x - y$ (Fig. 4.2), the reduced stress tensor, used in Eq. (4.21), can be obtained:

$$\boldsymbol{\sigma}_{red}(\boldsymbol{w}_c) = \boldsymbol{R}^t \cdot \boldsymbol{\sigma}_{red,S}(\boldsymbol{w}_c) \cdot \boldsymbol{R} = \boldsymbol{\sigma} - \boldsymbol{\sigma}_{jump}(\boldsymbol{w}_c) \tag{4.35}$$

where $\boldsymbol{R}$ is the rotation matrix between the $x-y$ and the $\xi-\eta$ co-ordinate systems. In Eq. (4.35) the desired reduced stress tensor is written as the difference between the current stress tensor $\boldsymbol{\sigma}$ and a corrective stress tensor, $\boldsymbol{\sigma}_{jump}(\boldsymbol{w}_c) = \boldsymbol{\sigma} - \boldsymbol{\sigma}_{red,S}(\boldsymbol{w}_c)$, which represents the stress tensor difference between the pre-existing stress tensor and those required after the formation of the crack.

The incremental strain tensor can be obtained from the above stress tensor, i.e.

$$d\boldsymbol{\varepsilon} = \boldsymbol{C}^{-1}\big[d\boldsymbol{\sigma} - \boldsymbol{\sigma}_{jump}(d\boldsymbol{w}_c)\big] = \boldsymbol{B} \cdot d\boldsymbol{\delta} - \big[\boldsymbol{C}^{-1} \cdot \boldsymbol{T} d\boldsymbol{w}_c\big]$$

where $\boldsymbol{C}^{-1} \cdot \boldsymbol{\sigma}_{jump}(d\boldsymbol{w}_c) = \boldsymbol{C}^{-1} \cdot \boldsymbol{T} d\boldsymbol{w}_c$, $\boldsymbol{T}$ is a proper tensor that gives the stress jump from the crack faces relative displacement jump vector $\boldsymbol{w}_c$.

It can be observed that the discontinuity vector $\boldsymbol{w}_c$, evaluated at the centre of the finite element and assumed to be constant across the element, can give raise to an apparently discontinuous crack opening displacement across the elements boundaries. Since the crack is herein modelled not as an effective displacement discontinuity but only through its static effect, the stress reduction in the cracked FE produces also an increasing of the nodal displacement of the adjacent elements, assuring a globally continuous displacement field.

Variational interpretation

The above stress-based formulation of the discontinuous displacement field can be reinterpreted by using a variational approach analogous to Sec. 4.2.2.

By starting from the variational expression (weak form) of the problem for a

continuous body

$$\int_{\Omega} \nabla^s(\delta \boldsymbol{u}^*)\boldsymbol{\sigma} d\Omega = \int_{\Omega} \delta \boldsymbol{u}^* \boldsymbol{b} d\Omega + \int_{\Gamma_t} \delta \boldsymbol{u}^* \boldsymbol{t} d\Gamma \tag{4.36}$$

and by introducing the reduced stress field given by Eq. (4.33) in the classical FE notation, the above variational expression becomes:

$$\begin{aligned} \int_{\Omega} \nabla^s(\delta \boldsymbol{u}^*)\boldsymbol{\sigma}_{red} d\Omega &= \int_{\Omega} \nabla^s(\delta \boldsymbol{u}^*)\big\{\boldsymbol{\sigma} - \boldsymbol{C} : \big[\nabla^s\big(\boldsymbol{N} \cdot (\delta_{w(s)})\big)\big]\big\} d\Omega = \\ &= \int_{\Omega} \delta \boldsymbol{u}^* \boldsymbol{b} d\Omega + \int_{\Gamma_t} \delta \boldsymbol{u}^* \boldsymbol{t} d\Gamma \end{aligned} \tag{4.37}$$

Then, after some rearrangements, the following relationship can be obtained:

$$\int_{\Omega} \delta \boldsymbol{\delta}^{*t} \boldsymbol{B}^t \boldsymbol{\sigma} d\Omega = \int_{\Omega} \delta \boldsymbol{\delta}^{*t} \boldsymbol{B}^t \boldsymbol{C} \boldsymbol{B} \cdot \boldsymbol{\delta}_{w(s)} d\Omega + \int_{\Omega} \delta \boldsymbol{\delta}^{*t} \boldsymbol{N}^t \boldsymbol{b} d\Omega + \int_{\Gamma_t} \delta \boldsymbol{\delta}^{*t} \boldsymbol{N}^t \boldsymbol{t} d\Gamma \tag{4.38}$$

Since the variation of the displacement field is arbitrary, the fictitious displacement vector $\delta\boldsymbol{\delta}^*$ can be eliminated:

$$\begin{aligned} &\underbrace{\int_{\Omega} \boldsymbol{B}^t \boldsymbol{C} \boldsymbol{B} d\Omega}_{\boldsymbol{K}} \cdot \boldsymbol{\delta} = \underbrace{\int_{\Omega} \boldsymbol{N}^t \boldsymbol{b} d\Omega + \int_{\Gamma_t} \boldsymbol{N}^t \boldsymbol{t} d\Gamma}_{\boldsymbol{f_1}} + \underbrace{\int_{\Omega} \boldsymbol{B}^t \boldsymbol{C} \boldsymbol{B} d\Omega}_{\boldsymbol{K}} \cdot \boldsymbol{\delta}_{w(s)} \qquad \text{i.e.} \\ &\boldsymbol{\delta} = \boldsymbol{K}^{-1}\big(\boldsymbol{f}_1 + \boldsymbol{K}\boldsymbol{\delta}_{w(s)}\big) \end{aligned} \tag{4.39}$$

By considering a generic increment, the following expression can be obtained:

$$\begin{aligned} &\underbrace{\int_{\Omega} \boldsymbol{B}^t \boldsymbol{C} \boldsymbol{B} d\Omega}_{\boldsymbol{K}} \cdot d\boldsymbol{\delta} = \underbrace{\int_{\Omega} \boldsymbol{N}^t d\boldsymbol{b} d\Omega + \int_{\Gamma_t} \boldsymbol{N}^t d\boldsymbol{t} d\Gamma}_{d\boldsymbol{f_1}} + \underbrace{\int_{\Omega} \boldsymbol{B}^t \boldsymbol{C} \boldsymbol{B} d\Omega}_{\boldsymbol{K}} \cdot d\boldsymbol{\delta}_{w(s)} \\ &\text{i.e.} \qquad \boldsymbol{K} d\boldsymbol{\delta} - \boldsymbol{K} d\boldsymbol{\delta}_{w(s)} = \boldsymbol{K} d\boldsymbol{\delta} - \boldsymbol{K}(s_n \boldsymbol{D} + s_s \boldsymbol{E}) d\boldsymbol{\delta} = d\boldsymbol{f}_1 \end{aligned} \tag{4.40}$$

and, remembering Eq. (4.29) and (4.32), the following relationship is obtained:

$$d\boldsymbol{\delta}_{w(s)} = \underbrace{\left\{ \frac{\sigma_c(u_c)}{\big[(\boldsymbol{C} : \boldsymbol{B}^t \cdot \delta_u) \cdot \boldsymbol{i}\big] \cdot \boldsymbol{i}} - 1 \right\}}_{A} \cdot \boldsymbol{N}(\boldsymbol{x}) \cdot d\boldsymbol{\delta}_u + \tag{4.41}$$

$$+\underbrace{\left\{\frac{\tau_c(u_c)}{\big[(\boldsymbol{C}:\boldsymbol{B}^t\cdot\boldsymbol{\delta}_v)\cdot\boldsymbol{i}\big]\cdot\boldsymbol{j}}-1\right\}}_{B}\cdot\boldsymbol{N}(\boldsymbol{x})\cdot d\boldsymbol{\delta}_v=$$

$$=+\boldsymbol{N}(\boldsymbol{x})\Big[A\big(\boldsymbol{Q},\boldsymbol{\delta},\sigma_c(u_c)\big)\cdot d\boldsymbol{\delta}_u+B\big(\boldsymbol{Q},\boldsymbol{\delta},\tau_c(u_c)\big)\cdot d\boldsymbol{\delta}_v\Big]=$$

$$=+\boldsymbol{N}(\boldsymbol{x})\Big[A\big(\boldsymbol{Q},\boldsymbol{\delta},\sigma_c(u_c)\big)\cdot\boldsymbol{D}+B\big(\boldsymbol{Q},\boldsymbol{\delta},\tau_c(u_c)\big)\cdot\boldsymbol{E}\Big]\cdot d\boldsymbol{\delta}$$

The equation (4.40) can be rewritten:

$$\underbrace{\int_\Omega \boldsymbol{B}^t\boldsymbol{C}\boldsymbol{B}d\Omega}_{\boldsymbol{K}}\cdot d\boldsymbol{\delta}=d\boldsymbol{f}_1+\underbrace{\int_\Omega \boldsymbol{B}^t\boldsymbol{C}\boldsymbol{B}\cdot\boldsymbol{N}(\boldsymbol{x})\cdot A\big(\boldsymbol{Q},\boldsymbol{\delta},\sigma_c(u_c)\big)\cdot\boldsymbol{D}d\Omega}_{\boldsymbol{K}_n}\cdot d\boldsymbol{\delta}+$$

$$+\underbrace{\int_\Omega \boldsymbol{B}^t\boldsymbol{C}\boldsymbol{B}\cdot\boldsymbol{N}(\boldsymbol{x})\cdot B\big(\boldsymbol{Q},\boldsymbol{\delta},\tau_c(u_c)\big)\cdot\boldsymbol{E}d\Omega}_{\boldsymbol{K}_s}\cdot d\boldsymbol{\delta} \tag{4.42}$$

$$\text{or}\qquad \boldsymbol{K}d\boldsymbol{\delta}-(\boldsymbol{K}_n+\boldsymbol{K}_s)d\boldsymbol{\delta}=d\boldsymbol{f}_1$$

Finally, the solution can be expressed as follows:

$$d\boldsymbol{\delta}=\big[\underbrace{\boldsymbol{K}-(\boldsymbol{K}_n+\boldsymbol{K}_s)}_{\overline{\boldsymbol{K}}}\big]^{-1}d\boldsymbol{f}_1=\overline{\boldsymbol{K}}^{-1}d\boldsymbol{f}_1 \tag{4.43}$$

where the matrices $\boldsymbol{K}_n$, $\boldsymbol{K}_s$ are expressed as follows:

$$\boldsymbol{K}_n=\int_\Omega \boldsymbol{B}^t\boldsymbol{C}\boldsymbol{B}\cdot\boldsymbol{N}(\boldsymbol{x})\big[A\big(\boldsymbol{Q},\boldsymbol{\delta},\sigma_c(u_c)\big)\cdot\boldsymbol{D}\big]d\Omega,$$

$$\boldsymbol{K}_s=\int_\Omega \boldsymbol{B}^t\boldsymbol{C}\boldsymbol{B}\cdot\boldsymbol{N}(\boldsymbol{x})\big[B\big(\boldsymbol{Q},\boldsymbol{\delta},\tau_c(u_c)\big)\cdot\boldsymbol{E}\big]d\Omega$$

and the matrix $\overline{\boldsymbol{K}}=\big[\boldsymbol{K}-(\boldsymbol{K}_n+\boldsymbol{K}_s)\big]$ can be considered as the condensed incremental tangent stiffness matrix of the cracked finite element. The expressions of Eq. (4.42) are similar to Eq. (4.16) where the discontinuity vector $\boldsymbol{\delta}_{w(s)}=\boldsymbol{\delta}_{u(s)}+\boldsymbol{\delta}_{v(s)}$ corresponds to the terms $\boldsymbol{w}_c=\boldsymbol{u}_c+\boldsymbol{v}_c$, and must be evaluated through an iterative process (see Sec 4.4).

4.3 Matrix Material: Elastic-Plastic Behaviour

If the matrix phase has an elastic-plastic behaviour, the well-known elastic-plastic constitutive equations can be expressed in an incremental form:

$$\dot{\boldsymbol{\varepsilon}} = \dot{\boldsymbol{\varepsilon}}^{el} + \dot{\boldsymbol{\varepsilon}}^{pl} = \dot{\boldsymbol{C}}^{-1} \cdot \boldsymbol{\sigma} + \dot{\boldsymbol{\varepsilon}}^{pl} \tag{4.44}$$

where $\dot{\boldsymbol{\varepsilon}}^{el}$ and $\dot{\boldsymbol{\varepsilon}}^{pl}$ stand for the elastic and plastic part of the strain rate tensor, whereas $\boldsymbol{\sigma}$ is the stress rate tensor and $\dot{\boldsymbol{C}}$ is the fourth order tangent elastic tensor rate.

The elastic-plastic behaviour can be classically defined by the yield function $\mathcal{F}(\sigma_{ij}, k_1, \ldots, k_m) = 0$, where $k_1, \ldots, k_m$ are the hardening parameters. Different behaviours can be distiguished:

$$\begin{aligned}
&\text{(i) elastic behaviour when} && \mathcal{F}(\sigma_{ij}, k_1, \ldots, k_m) < 0 \\
&\text{(ii) plastic flow when} && \mathcal{F}(\sigma_{ij}, k_1, \ldots, k_m) = 0 \quad \text{and} \\
& && \mathcal{F}'(\sigma_{ij}, k_1, \ldots, k_m) = 0 \\
&\text{(iii) elastic unloading when} && \mathcal{F}(\sigma_{ij}, k_1, \ldots, k_m) = 0 \quad \text{and} \\
& && \mathcal{F}'(\sigma_{ij}, k_1, \ldots, k_m) < 0
\end{aligned} \tag{4.45}$$

The yielding condition for a perfectly plastic (or hardening) material can be written (Fig. 4.4):

$$\begin{aligned}
&\mathcal{F}(\sigma_{ij}, k_1, \ldots, k_m) = 0 \quad \text{and} \\
&\begin{cases}
d\mathcal{F} = \frac{\partial \mathcal{F}_0}{\partial \boldsymbol{\sigma}} d\boldsymbol{\sigma} = 0 & \text{perfectly plastic material} \\
d\mathcal{F} = \frac{\partial \mathcal{F}_0}{\partial \boldsymbol{\sigma}} d\boldsymbol{\sigma} + \frac{\partial \mathcal{F}_0}{\partial k_h} dk_h = 0 & \text{hardening material}
\end{cases}
\end{aligned} \tag{4.46}$$

A simple standard flow rule, suitable for most of the engineering materials, is assumed to describe the plastic strain increment:

$$\begin{aligned}
&\dot{\boldsymbol{\varepsilon}} = \dot{\boldsymbol{\varepsilon}}^{el} + \dot{\boldsymbol{\varepsilon}}^{pl} = \dot{\boldsymbol{C}}_m^{-1} : \dot{\boldsymbol{\sigma}} + \dot{\lambda} \frac{\partial \boldsymbol{Q}}{\partial \boldsymbol{\sigma}} \\
&\text{with} \qquad \dot{\lambda} = \frac{\boldsymbol{f} : \boldsymbol{C}'_m : \dot{\boldsymbol{\varepsilon}}}{H + \boldsymbol{f} : \boldsymbol{C}'_m : \boldsymbol{f}} \quad \text{and} \qquad \boldsymbol{f} = \frac{\partial \boldsymbol{Q}}{\partial \sigma_{ij}}
\end{aligned} \tag{4.47}$$

where H is the hardening parameter which can be related to the post-yielding stress-strain slope E_t: $H = E_t/(1 - E_t/E)$ and $\boldsymbol{Q}$ represents the plastic potential function. The plastic multiplier $\dot{\lambda}$ is defined through:

$$\begin{aligned} &\dot{\lambda} \geq 0 && \text{if } \mathcal{F} = 0 \text{ and } d\mathcal{F} = 0 \\ &\dot{\lambda} = 0 && \text{if } \mathcal{F} = 0 \text{ and } d\mathcal{F} < 0 \text{ or } \mathcal{F} < 0 \end{aligned}$$

In the simple case that the plastic strain increment is proportional to the gradient $\boldsymbol{f} = \partial Q/\partial\sigma_{ij} = \partial\mathcal{F}/\partial\sigma_{ij}$ of the plastic surface (i.e. $\boldsymbol{Q} = \mathcal{F}$), the so-called associated flow rule can be used. This can allow some relevant simplifications in the mathematical treatment of the problem and can be used for a wide class of materials.

For an isotropic material the yielding criterion must be independent from the reference system adopted to express the stress components, so the stress tensor (σ_{ij}) invariants $(I_1,\, I_2,\, I_3)$ and the deviatoric stress tensor (σ'_{ij}) invariants $(J_1,\, J_2,\, J_3)$ can be used to write the yield function. Such invariants are defined as follows:

$$I_1 = \sigma_{ii}, \quad I_2 = \frac{1}{2}\sigma_{ij}\sigma_{ji}, \quad I_3 = \frac{1}{3}\sigma_{ij}\sigma_{jk}\sigma_{ki} \tag{4.48}$$

$$\begin{aligned} &J_1 = \sigma'_{ii}, \quad J_2 = \frac{1}{2}\sigma'_{ij}\sigma'_{ji}, \quad J_3 = \frac{1}{3}\sigma'_{ij}\sigma'_{jk}\sigma'_{ki} \quad \text{or} \\ &J_1 = s_1 + s_2 + s_3 \\ &J_2 = \frac{1}{2}(s_1^2 + s_2^2 + s_3^2) = \frac{1}{6}\left[(\sigma_1 - \sigma_2)^2 + (\sigma_2 - \sigma_3)^2 + (\sigma_3 - \sigma_1)^2\right] \\ &J_3 = s_1 \cdot s_2 \cdot s_3 \quad \text{with} \quad \sigma'_{ij} = \sigma_{ij} - \frac{1}{3}\delta_{ij}\sigma_{kk} = \sigma_{ij} - \delta_{ij} \cdot p, \quad p = \sigma_{kk}/3 \end{aligned} \tag{4.49}$$

The yield criterion thus becomes:

$$\mathcal{F}(I_1,\, I_2,\, I_3,\, J_1,\, J_2,\, J_3,\, k_1, \ldots, k_m) = 0 \tag{4.50}$$

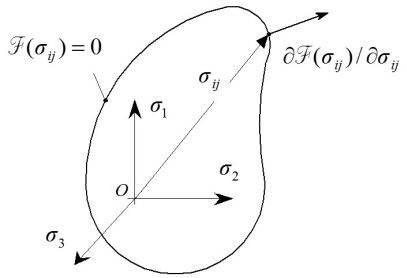

Figure 4.4: Generic yield surface; the normal to such surface $\boldsymbol{f} = \partial\mathcal{F}/\partial\sigma_{ij}$ is also indicated.

4.4 Computational algorithm for brittle and elastic-plastic materials

The computational algorithm can be summarized as follows:

1. Solve the equilibrium problem for the current load step level, by considering linear or elastic-plastic material behaviour;
2. Check whether a crack develops in one or more finite elements. The crack conditions are:
   (a) the maximum principal stress is greater than the material strength;
   (b) the "computed" opening crack displacement exceeds a minimum value below which the crack cannot be considered to exist.
3. Determine the orientation orthogonal to the maximum principal stress direction as a first attempt, in the case of a new crack;
4. Determine the mean normal and tangential nodal displacement with respect to the crack direction through the quantities u_c and v_c (see Eq. (4.25);
5. Evaluate the normal and shearing bridging stresses by using the proper cohesive laws expressed by Eq. (4.25) and (4.24);
6. Determine the stress correction (reduction) $\boldsymbol{\sigma}_{red} = \boldsymbol{\sigma} - \boldsymbol{C} : \left[\nabla^s(\boldsymbol{N}\cdot\boldsymbol{\delta}_{w(s)})\right]$ expressed through the factors s_s and s_n by using Eq. (4.29) and (4.32), respectively;
7. Determine unbalanced force vector $\boldsymbol{f}^{(i)}_{e(u)}$ at the current step by using Eq. (4.21);

8. Update element's total nodal displacements by adding up the converged displacements at the previous load step $\boldsymbol{\delta}_{i-1}$ and those determined at the current increment $d\boldsymbol{\delta}_i$, i.e. $\boldsymbol{\delta}_i = \boldsymbol{\delta}_{i-1} + d\boldsymbol{\delta}_i$;

9. Determine again the mean normal and tangential nodal displacements with respect to the crack direction through Eq. (4.26) by using $\boldsymbol{\delta}_i$, and the normal and shearing bridging stresses evaluated by using the proper cohesive laws (4.25), (4.24);

10. Since the computational process is non-linear, it requires some appropriate convergence requirements. Check for convergence must be performed by standard assessment criteria (displacements, unbalanced forces, energy convergence) and also by checking the convergence of the normal and shearing bridging stresses, according to the assumed cohesive laws:

$$\begin{aligned} \left|\sigma_{e(n)} - \sigma_c(u_c)\right| &= \left|(\boldsymbol{\sigma} \cdot \boldsymbol{i} \cdot \boldsymbol{i} - \sigma_c(u_c)\right| \leq tol\ \sigma_c \\ \left|\tau_{e(n)} - \tau_c(u_c)\right| &= \left|(\boldsymbol{\sigma} \cdot \boldsymbol{i} \cdot \boldsymbol{j} - \tau_c(u_c)\right| \leq tol\tau_c \end{aligned}$$

where $\sigma_e(n)$ and $\tau_e(n)$ are the effective normal and shearing stresses and $tol\sigma_c$ and $tol\tau_c$ are suitable tolerances. In order to control the crack opening convergence, the following crack opening tolerance is introduced:

$$\left|u_c^j - u_c^{j-1}\right| / u_c^j \leq tol\ u_c^j$$

where u_c^j, u_c^{j-1} are crack opening displacements at the iteration j and $j-1$, respectively, obtained from the following relationships:

$$u_c^j = \left[\boldsymbol{Q} \cdot (\boldsymbol{\delta}^{(i)} \cdot \boldsymbol{i})\right] / n_n u_c^{j-1} = \left[\boldsymbol{Q} \cdot (\boldsymbol{\delta}^{(i-1)} \cdot \boldsymbol{i})\right] / n_n$$

11. Store total displacements, strains, stresses and the related quantities and go to the subsequent load step, if all the convergence requirements are fulfilled. Otherwise go to step No.7 and repeat steps 7-10 up to the fulfilment of the convergence conditions;

12. Repeat the computational process from step No.1 by considering the subsequent new load step.

In regions of the body with high stress level, for example due to coarse mesh or to the use of low order elements, the crack formation condition (see step No.2) can be reached simultaneously by many finite elements at a given load step. Consequently, a criterion to avoid that the crack can be "smeared" over all the finite element of that regions must be adopted. A "crack driving algorithm" is proposed: it assumes that a main crack develops from a very highly stressed zone (such as near a pre-existing notch or crack), and the further crack propagation is assumed to be produced by the growth of such a dominant crack which can extend only in adjacent finite elements which are embedded in a potentially cracked region around the current dominant crack.

Details of the cited algorithm can be found in [207].

4.5 Static loading numerical examples

The discontinuous FE formulation, proposed in the previous Sections, is used to simulate the behaviour of simple structures to assess its capability in the prediction of the fracture process in brittle solids.

The algorithm described in Section 4.4 has been implemented in a non-linear 2-D FE code. All the analyses below are conducted by assuming that, for brittle matrix materials, the fracture process is governed by the value of the exponent n equal to 6 for shear stress decreasing rate control (Eq. (4.24)).

The tolerances used to check the convergence of the non-linear iterative solution process are assumed to be equal to $2 \cdot 10^{-4}$ for both the incremental displacement norm and incremental nodal residual force vector norm, while the incremental tolerance used to check the crack opening and sliding has been assumed to be equal to 10^{-4}.

All the numerical examples are performed under displacement control in order to be able to follow the softening branch of the load-displacement curves. The non-linear analyses have been performed by progressively increasing the displacement of one (or more) FE node(s), up to the final value required by the test.

4.5.1 Square plate under tension

In order to verify the mesh dependence of the presented formulation, the simple case of a square plate (assumed to be in plane stress condition) under upward

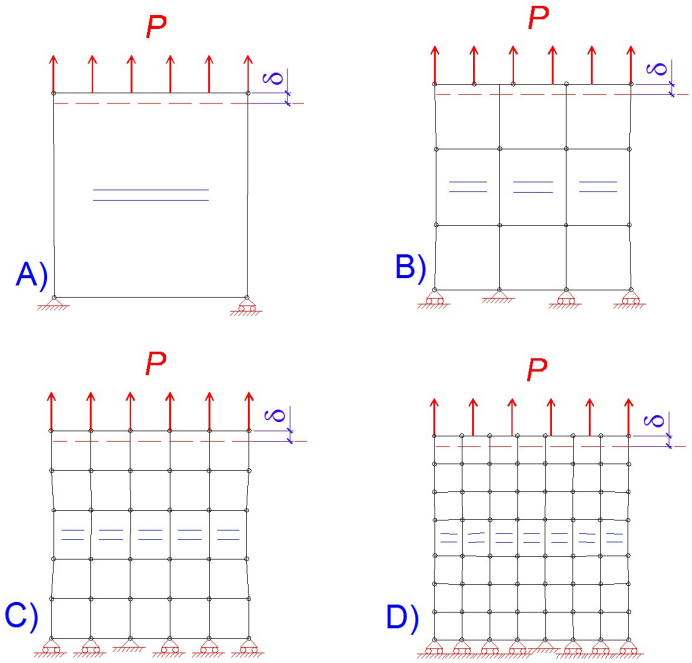

Figure 4.5: Different meshes adopted for the simulation of tensile tests on a square brittle plate and developed crack patterns: 1 FE (mesh A), 9 FE (mesh B), 25 FE (mesh C) and 49 FE (mesh D).

increasing top displacement, is examined (Fig. 4.5).

The material's constants are assumed as follows: Young modulus $E = 20GPa$, Poisson's ratio equal to $\nu = 0.15$, ultimate tensile strength equal to $f_t = 2.5MPa$, whereas two unit surface fracture energies $\mathcal{G}_f = 100N/m$ and $\mathcal{G}_f = 50N/m$ are assumed.

Four different meshes are analysed (Fig. 4.5), named A, B, C and D, characterised by 1, 9, 25 and 49 elements, respectively. In the same Figure the crack patterns evaluated numerically by the present approach are also drawn: the couple of straight line segments indicates the crack opening developed in the material for the given top displacement δ.

In Figure 4.6 the obtained load-displacement curves are reported for the different meshes. Note that they are almost identical for the different meshes considered, regardless of the assumed value of the fracture energy (Fig. 4.6a and 4.6c): some differences can be appreciated in the post-peak branch of the curves for the one-

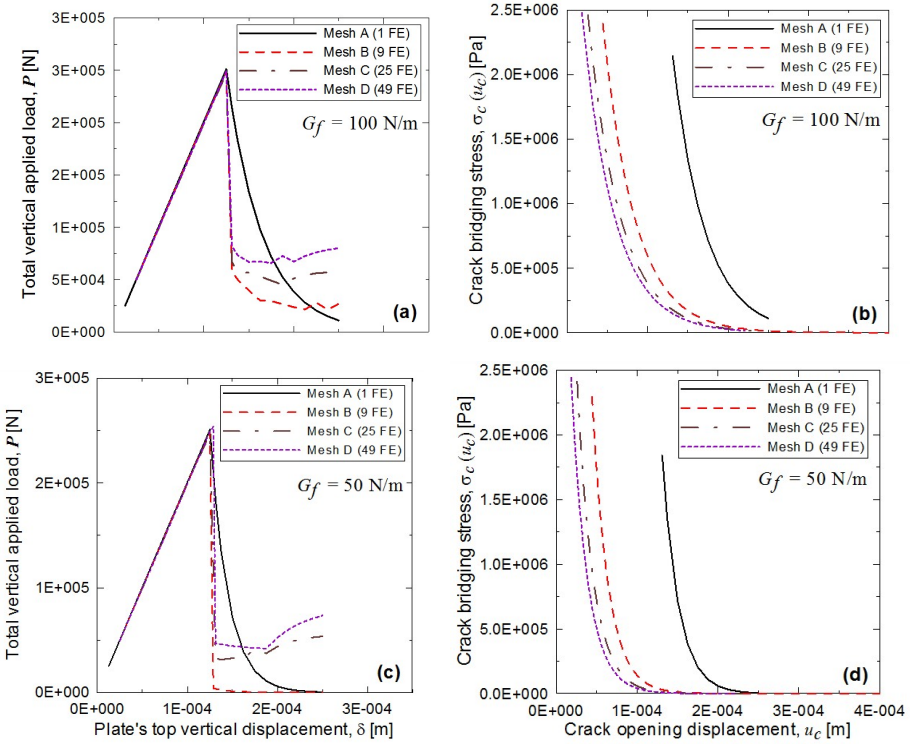

Figure 4.6: Load P vs vertical displacement δ (a) and (c) and crack bridging stress vs crack opening displacement u_c at the central FE (b) and (d) for a square brittle plate with $\mathcal{G}_f = 100N/m$ (a) and (b) and $\mathcal{G}_f = 50N/m$ (c) and (d) for the four meshes in Fig. 4.5.

element FE model, due to the too poor mesh used, which cannot represent the actual stress distribution in the cracked section. In Figure 4.6b and 4.6d, the bridging stress against the crack opening displacement u_c is reported for the central element of meshes A, B, C, D in Figure 4.5. It is evident as the initial crack opening at which the fracture process starts (i.e. $\sigma_c(u_0) = f_t$) is different for different values of the element size: in fact the displacement u_0 at which the crack process starts, depends on the element relative node displacement which produces a tensile stress equal to f_t: obviously such a critical relative displacement depends on the element size and it is intuitive that $u_0(1FE) > u_0(9FE) > u_0(25FE) > u_0(49FE)$. On the other hand the curve patterns are almost identical for the four cases considered (Fig. 4.6). In order to verify the correctness of the simulated fracture process, the crack opening displacement u_c is represented against the top displacement δ in

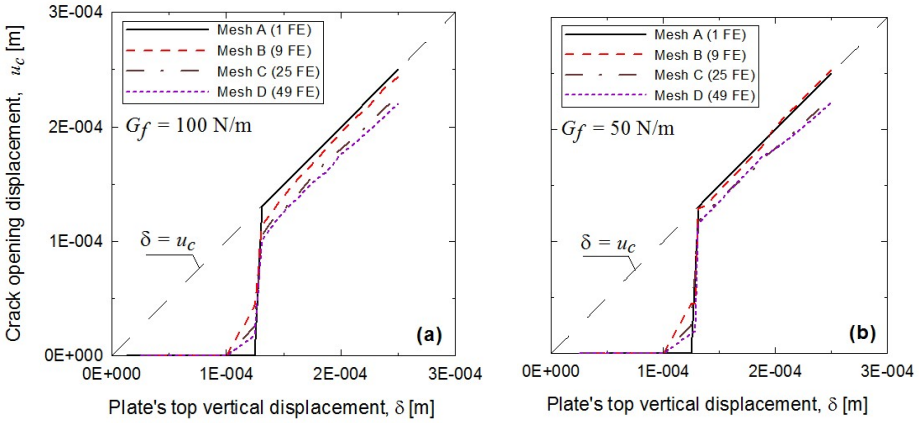

Figure 4.7: Crack opening displacement u_c vs plate top vertical displacement δ for a square brittle plate in the case $\mathcal{G}_f = 100N/m$ (a) and $\mathcal{G}_f = 50N/m$ (b).

Figure 4.7.

For both the considered values of the fracture energy ($\mathcal{G}_f = 100N/m$ and $\mathcal{G}_f = 50N/m$), the crack remains initially closed ($u_c = 0$) for low value of the top displacement and, after the appearance of the fracture, the crack opening u_c tends quickly to become equal to the plate's top displacement δ, $u_c \cong \delta$. In other words, the deformation of the plate, once the crack has appeared, becomes localised in the narrow band of the fracture zone. This confirms that the proposed model is able to effectively reproduce the crack formation in a brittle solid independently by the mesh discretization adopted.

4.5.2 Single-edge notched beam under four-point shear

The mechanical behaviour of a four-point shear loaded single-edge notched beam is herein examined. Such a beam configuration has been used by several Authors as a benchmark test for numerical analyses [195, 208]. The geometrical parameters of the structure and the two considered FE discretisations are displayed in Figure 4.8 (four-noded elements in Fig. 4.8a and three-noded elements in Fig. 4.8b). A beam thickness equal to 0.1 m is adopted and plane stress condition is assumed to exist in the beam.

The mechanical parameters of the beam material are the following: Young modulus equal to $E = 35GPa$, Poisson's ratio $\nu = 0.15$, ultimate tensile strength

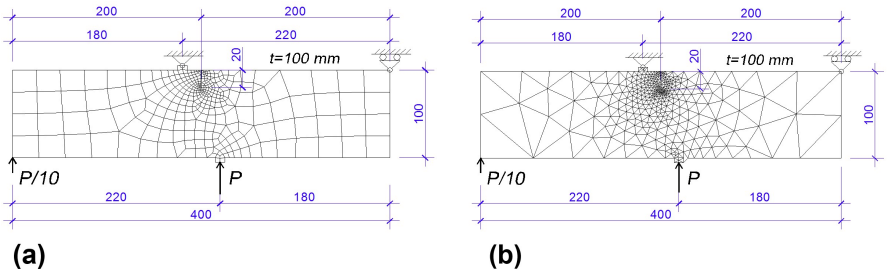

Figure 4.8: Single-edge notched beam under four point shear: discretisation with 301 four-noded bilinear elements and 343 nodes (a), discretisation with 660 triangular constant stress elements and 378 nodes (b). Dimensions in millimetres.

$f_t = 2.8MPa$, unit surface fracture energy $\mathcal{G}_f = 100N/m$. A linear-elastic behaviour of the uncracked material is assumed.

Non structured meshes with an irregular arrangements of elements with 301 four noded bilinear elements and 343 nodes (Fig. 4.8a) and a mesh with 660 constant stress triangular elements and 378 nodes (Fig. 4.8b) are considered in the analyses that are performed under displacement control, by imposing a progressive vertical displacement at the two bottom loaded points (Fig. 4.8). The ratio between displacements of the two above points has been kept equal to that obtained in the same linear-elastic structure under a load controlled test, by applying the forces P and $P/10$ to the corresponding bottom points of the beam. The crack mouth sliding displacement d (CMSD) is evaluated by measuring the relative vertical displacement of the two nodal points lying on the top opposite crack faces. The CMSD vs the vertical bottom applied load P is graphically represented in Figure 4.9a, together with some literature's results [195].

As can be observed, the load against the displacement curves are in satisfactory agreement with the literature results even if some differences can be appreciated in the decreasing branch of the numerical curves for the two considered discretisations. In Figure 4.9a the elastic-plastic case is also shown: the Drucker-Prager plasticity criterion is assumed for the uncracked material with tensile yield stress equal to $\sigma_{y,t} = 2.8MPa$ and hardening parameter equal to $H = 0$ (no softening is considered since it is assumed to be completely represented by the cracking process). The plastic behaviour effect modifies the load-relative displacement curve which has a lower peak with respect to the elastic cases, and an approximately elastic-perfectly plastic behaviour can be recognised. In Figure 4.9b, and 4.9c the crack patterns

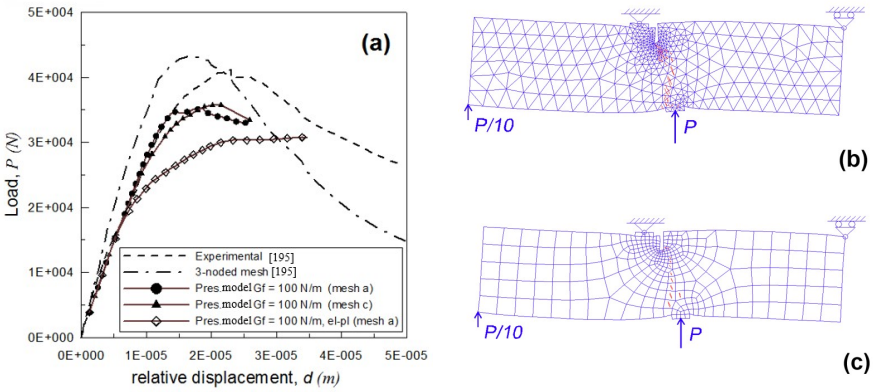

Figure 4.9: Single-edge notched beam under four point shear: load P vs vertical relative crack displacement (a); final crack patterns corresponding to mesh a) (b) and mesh b) (c) of Fig. 4.8.

for the four- and three-noded meshes are displayed. The expected crack path is reproduced by the numerical simulation (the crack tends to grow from the initial crack tip to the bottom loaded edge of the beam where the load P is applied) even considering a diffuse crack pattern which develops in the beam.

4.5.3 L-Shaped slab

An L-shaped slab is herein considered, the FE simulation performed through the above formulation is compared with the numerical solution provided by Oliver and Mosler [199]. The geometrical dimensions are displayed in Figure 4.10a (with $L = 0.5m$, while the slab thickness is equal to $t = 0.2m$) where the FE discretization with four-noded elements is also represented.

The mechanical parameters of the structural component under study are the following: Young modulus equal to $E = 10GPa$, Poisson's ratio $\nu = 0.20$, ultimate tensile strength $f_t = 1.0MPa$, unit surface fracture energy $\mathcal{G}_f = 20N/m$.

A simple linear-elastic behaviour of the slab's material is assumed in the uncracked zones. The top edge of the slab is restrained while the right bottom vertical edge is subjected to a prescribed downward displacement δ.

In Figure 4.10b the deformed cracked mesh as well as the crack path developed are represented, while the overall structural response can be quantified through the vertical load against the vertical displacement δ. As can be observed in Figure 4.10b

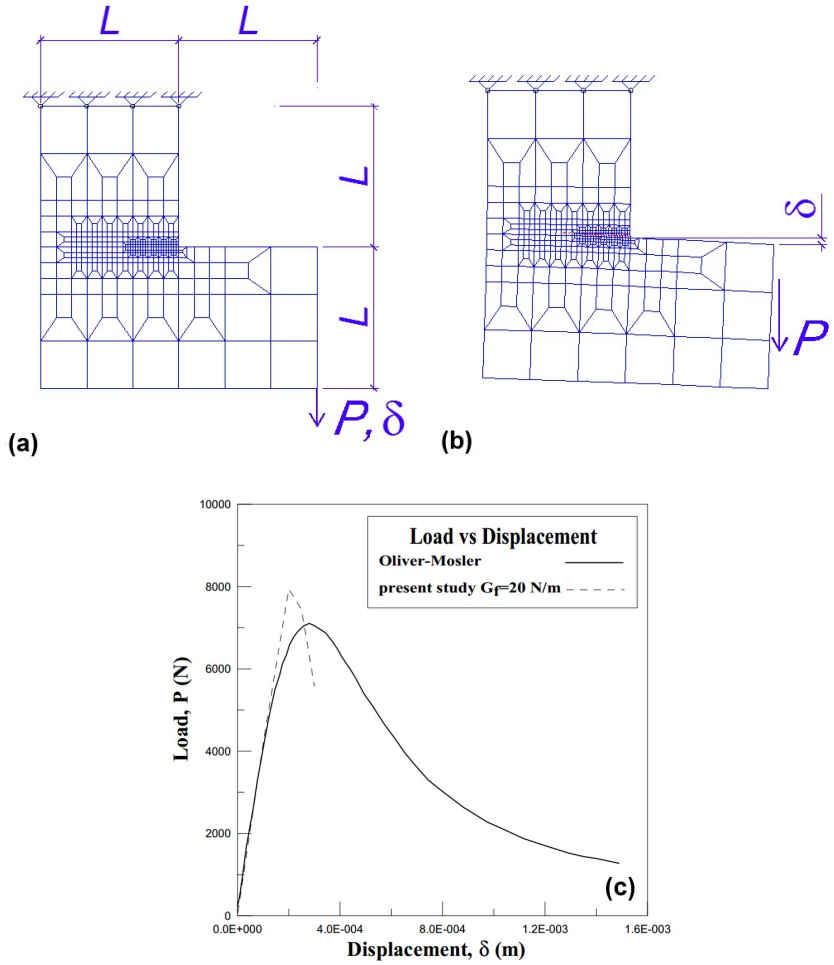

Figure 4.10: L-shaped slab under prescribed vertical displacement. Geometrical parameters and FE discretisation with 366 four-noded bilinear elements and 355 nodes (a), deformed mesh and developed crack path during the loading process(b). Load P vs the vertical displacement δ in the L-shaped slab for $\mathcal{G}_f = 20N/m$(c).

the crack develops in a nearly horizontal direction, growing toward the left hand side of the slab.

In Figure 4.10c, the load P against the vertical displacement δ in the L-shaped slab is displayed together with Oliver and Mosler's results [199]. As can be observed, the present results show a behaviour characterised by a more brittle behaviour with respect to literature's results, with a slightly higher load peak.

4.6 Matrix Material Behaviour under Cyclic Loads

The fatigue effects in a homogeneous material under uniaxial constant amplitude cyclic load can be tackled through the experimental-based Wöhler diagrams (S-N curves), which determine the number of load cycles to failure for a given load ratio, $R^* = \sigma_{min}/\sigma_{max}$ (Fig. 4.11).

As experimental tests have confirmed, such curves in their descending part (Fig. 4.11) can be empirically approximated by $\sigma = A \cdot N^{-B}$ or $N = \big(\sigma/A\big)^{-\frac{1}{B}} = const \cdot \sigma^{-\frac{1}{B}}$ (where $A, B > 0$ are the Wöhler fatigue constants of the material) which, in a logarithmic plane, describes a straight line:

$$\ln \sigma = \ln A - B \cdot \ln N$$

Such a line, for stress level below the threshold value σ_0 (fatigue limit), becomes horizontal and no fatigue effects occur in the material, i.e. the fatigue life can be considered unlimited with respect to the number of loading cycles (Fig. 4.11). Consequently, the fatigue curves can thus be described by the following relationship:

$$N = \begin{cases} c\big(\sigma/A\big)^{-\frac{1}{B}} = const \cdot \sigma^{-\frac{1}{B}} & \text{if } \sigma > \sigma_0 \\ \infty & \text{if } \sigma \leq \sigma_0 \end{cases} \tag{4.51}$$

In the case of cyclic uniaxial stress state considered, the number of loading cycles N^* to failure at the location x inside the body (characterised by maximum stress value $\sigma^* \geq \sigma_0$) can be written as follows:

$$N^* = A^{\frac{1}{B}} \cdot \sigma^{*-\frac{1}{B}} \tag{4.52}$$

Once the number of loading cycles N^* has acted on the structure, the failure

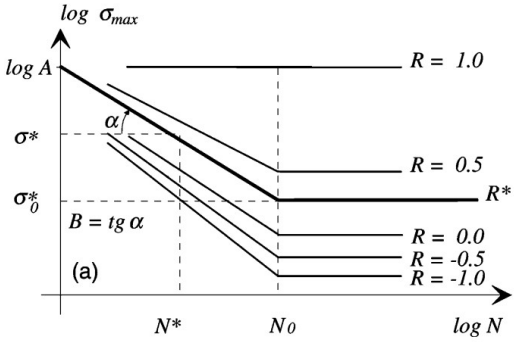

Figure 4.11: Qualitative fatigue life diagram for different fatigue stress ratio R^*.

condition is reached at the location x, and the scalar damage parameter D_c can be assumed to be equal to one, $D_c(\sigma^*, R^*, N^*, x) = 1$ (the subscript c refers to a particular material's mechanical characteristic). The effects of the damage process occurring after a number of loading cycles $N < N^*$ can be considered as a reduction of the mechanical properties [209, 210].

It is reasonable to consider such a damage scalar quantity as a piecewise linear function of the number of loading cycles:

$$D_c(\sigma^*, R^*, N, x) = \begin{cases} \frac{N}{N^*} = \frac{N}{(\sigma^*/A)^{-1/B}} < 1 & \text{if } \sigma^* > \sigma_0 \\ 0 & \forall N \text{ if } \sigma^* \leq \sigma_0 \end{cases} \tag{4.53}$$

Obviously in the case of cyclic loads with $\sigma^* \leq \sigma_0$, the damage parameter is assumed to be equal to zero, and no degradation of the material's mechanical properties occurs.

This approach can also be interpreted as the way to update the mechanical properties of the matrix, reduced by the damaging effect of the progressive fatigue loading [20]. The above assessment can be done according to the following relationship:

$$P_m(N) = P_{m0} \cdot \left[1 - D_c(\sigma^*, R^*, N, x)\right] \tag{4.54}$$

where P_{m0} is the value of an undamaged generic mechanical parameter of the material, and P_m is the corresponding damaged one. The above reduction is written through the damage parameter D_c that is assumed to be expressed in the form (4.53)..

In the case of multiaxial stress states, the previous equations can be applied by replacing σ^* with the combined stress σ_{eq} related to the yielding or failure criteria of the matrix material under study. Alternatively, the principal stress amplitude can be applied. An advisable choice to take into account the fatigue effects is to impose $P_{m0} = E_{m0}$ (undamaged Young modulus of the material), whereas its damaged corresponding counterpart is the damaged Young modulus $E_m(N)$:

$$E_m(N) = E_{m0} \cdot \left[1 - D_{cm}(\sigma^*, R^*, N, x)\right] \tag{4.55}$$

Chapter 5

Mechanics of the fiber-matrix detachment

5.1 Introduction

The mechanical behaviour of fibre-reinforced materials depends on the properties of their constituents, i.e. bulk material (matrix) and fibres, and also on the reciprocal bonding at their interface. Typical damage phenomena occurring in such materials, responsible for a significant decrease of their mechanical performance, can be related to the fibre-matrix delamination (or debonding) [192, 211].

In composites, where the reinforcing fibres are shorter than a critical length (depending on the geometry, fibre tensile strength and matrix-fibre limit shear stress), the damage associated with the fibre pull out, is generally predominant with respect to fibre breaking, and it must be carefully evaluated in order to quantify the loss of load bearing capacity of the reinforced structural elements.

As a matter of fact, the fibre-fibre interaction could also be of remarkable importance in the mechanics of fibre-reinforced composites. However, it should be considered that the interaction appears to be of significant importance only when the fibre volume content is high ($>20\%$): in the present study, the so-called dilute hypothesis is made and, therefore, such a phenomenon can be neglected [212].

Failure mechanisms corresponding to fibre instabilities have also been taken into account as relevant damaging effects in fibre-reinforced solids; they easily

occur in presence of fibre-matrix detachment. Buckling in aligned fibres under compressive loads has been studied by Kyriakides at al. [213] and Vogler et al. [214], whereas micro-buckling occurring in partially debonded fibres in periodic composites, responsible for size effect and loss of the periodic structure characteristic, has been examined by Greco and Luciano [215] by also taking into account the crack faces contact.

In the present Ph.D. Thesis, this aspect has been neglected, since the buckling phenomenon is typically relevant for long fibres. For short fibre-reinforced materials, the fibre-matrix detachment is more significant in determining the decrease of the effectiveness of the fibre bearing capacity [212].

5.2 Debonding phenomenon

Multiphase materials suffer from loss of fibre-matrix bond effectiveness, with a consequent detrimental effect on the stress transfer between the different constituents. Such a phenomenon, known as debonding, is represented by a partial or complete detachment between the phases of the composite. In the case of fibre-reinforced materials, such a debonding appears as a separation between the matrix and the fibres, generally starting from the fibre extremities when the applied stress level exceeds a critical value. In such a context, by recognising that the edge of the fibre-matrix detached region can be treated as the crack front in a 3D fracture problem (Fig. 5.1), the debonding phenomenon can conveniently be studied through fracture mechanics concepts. In other words, the Stress-Intensity Factor arising along the crack front can be determined and used for the mechanical assessment of the composite, in particular to quantify the development of the debonding itself.

Due to the geometry of the fibre extremities, a singular stress field arises around the fibre ends even without any fibre-matrix debonding [216, 217]. The related SIFs can be used to determine whether the effective detachment takes place or not.

This represents an innovative alternative to the well-known "Shear Lag" model for the assessment of fibre debonding initiation. In the above context, some basic researches conducted during last decades to solve the stated problem can usefully be recalled. In particular, Chen and Nisitani [218] and Noda [219] have examined the stress field near a corner of joined dissimilar materials and that arising at

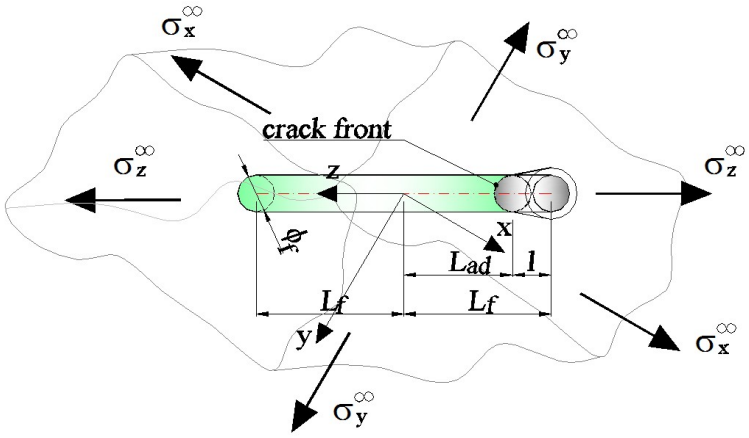

Figure 5.1: A 3D linear-elastic infinite domain with a partially detached embedded cylindrical elastic inclusion with total length, $2L_f$, diameter, ϕ_f, and deboned length, l.

the end of a cylindrical inclusion, respectively, whereas the problem of the elastic singular stress field near a partially longitudinally debonded rigid fibre in an infinite medium has analytically been solved by Chaundhuri [220]. The fundamental 2D problem of an arc-shaped crack located along the interface of a circular elastic inclusion in an infinite elastic material was solved by Toya [221] adopting a complex function solution, by Mantic [11] using a coupled stress and energy approach and by Varna et al. [222] through experimental tests, whereas the case of a curvilinear inclusion under shear was studied by Sendenckyj [223].

The problem of a cylindrical crack at the fibre-matrix interface in an infinite medium has been analysed by Demir [224] and by Zbib et al. [225], whereas a cylindrical crack in a long cylinder has been examined by Wüthrich [226].

In a 3D linear-elastic infinite domain with a partially detached cylindrical elastic inclusion (i.e. a partially debonded fibre), the longitudinal remote stress (σ_z^∞, i.e. stress parallel to the fibre axis) is responsible for Mode I and II stress-intensity factors (SIFs), whereas the transversal remote stresses (σ_x^∞, σ_y^∞) are responsible for Mode I, II and III SIFs along the crack front. The above problem is very complex since the debonded crack is located between two dissimilar materials (the matrix and the fibre, Fig. 5.1).

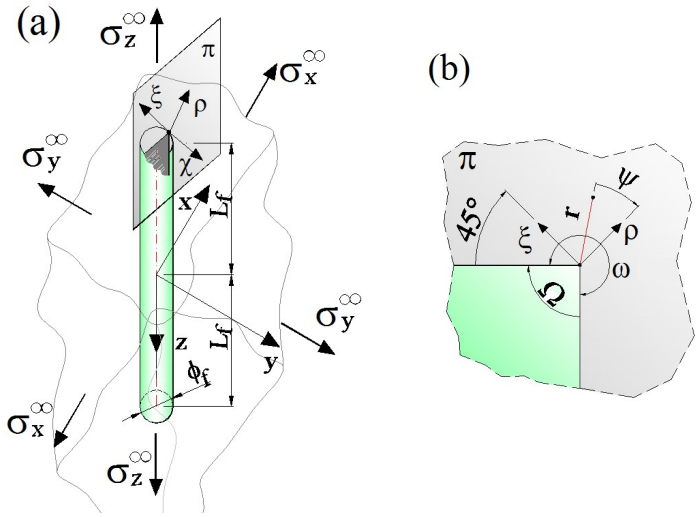

Figure 5.2: Extremity of a fibre (a) as a wedge embedded in an infinite elastic solid (b).

5.3 SIFs arising at the tip of a corner joint between two different materials

In order to assess whether the debonding phenomenon can initiate, the knowledge of the SIFs arising at the circular shape edges of a bonded fibre is needed. As a matter of fact, a singular stress field arises at the extremities of a non-debonded fibre [219], and the related SIFs can be used to assess the occurrence of interface failure once the interface critical energy is known. This case (Fig. 5.2a) can be assimilated to the stress field problems studied by Chen and Nisitani [218] related to a 2D elastic wedge inclusion, and by Noda [219] related to a cylindrical inclusion embedded in a different elastic material (Fig. 5.2b).

By considering a section plane π crossing the fibre along its axis (Fig. 5.2a), a generic point on the circular edge at the fibre extremity corresponds to a 2D wedge problem characterised by an internal corner angle Ω equal to 90° (Fig. 5.2b). The SIFs $K_{I,w}$ and $K_{II,w}$ at the corner of the wedge can be used to determine an equivalent SIF ($K_{eq,w}$). By applying the complex potentials method, Chen and Nisitani [218] determined the singular stress field and the displacement field around the corner of a diamond inclusion. In polar coordinates (note that the axis ρ in Fig. 5.2b is assumed to be the bisector line of the internal angle Ω), the singular

stress field can be written as follows [218]:

$$\begin{aligned}
\sigma_{r,i} &= \frac{K_{I,\lambda_1}}{r^{1-\lambda_1}} \cdot f^I_{r,i}(\psi) + \frac{K_{II,\lambda_2}}{r^{1-\lambda_2}} \cdot f^{II}_{r,i}(\psi) \\
\sigma_{\psi,i} &= \frac{K_{I,\lambda_1}}{r^{1-\lambda_1}} \cdot f^I_{\psi,i}(\psi) + \frac{K_{II,\lambda_2}}{r^{1-\lambda_2}} \cdot f^{II}_{\psi,i}(\psi) \\
\tau_{r\psi,i} &= \frac{K_{I,\lambda_1}}{r^{1-\lambda_1}} \cdot f^I_{r\psi,i}(\psi) + \frac{K_{II,\lambda_2}}{r^{1-\lambda_2}} \cdot f^{II}_{r\psi,i}(\psi)
\end{aligned} \tag{5.1}$$

where the subscript $i = 1, 2$ indicates whether material 1 (matrix) or 2 (inclusion) is considered, $(1-\lambda_1)$ and $(1-\lambda_2)$ (with $0 < \lambda_1,\ \lambda_2 < 1$) are the stress singularities which depend on the elastic characteristics of the two materials and the internal inclusion angle Ω, K_{I,λ_1} and K_{I,λ_2} are Mode I and Mode II SIFs, and $f^I_{j,i}$ and $f^{II}_{j,i}$ are angular functions (with $j = r,\ \psi,\ r\psi$).

In the above relationships, the eigenvalues $\lambda_1,\ \lambda_2$ can be obtained as the roots of the following eigenequations:

$$\begin{aligned}
&D_1(\alpha_D,\ \beta_D,\ \omega,\ \lambda_1) = \\
&= (\alpha_D - \beta_D)^2\lambda_1^2(1-\cos 2\omega) + 2\lambda_1(\alpha_D - \beta_D)\sin\omega\big[\sin\lambda_1\omega + \\
&+ \sin\lambda_1(2\pi-\omega)\big] + 2\lambda_1(\alpha_D - \beta_D)\beta_D\sin\lambda_1\big[\sin\lambda_1(2\pi-\omega) - \sin\lambda_1\omega\big] + \\
&+ (1-\alpha_D^2) - (1-\beta_D^2)\cos 2\lambda_1\pi + (\alpha_D^2 - \beta_D^2)\cos\big[2\lambda_1(\omega-\pi)\big] = 0
\end{aligned} \tag{5.2}$$

for Mode I deformation and:

$$\begin{aligned}
&D_2(\alpha_D,\ \beta_D,\ \omega,\ \lambda_2) = \\
&= (\alpha_D - \beta_D)^2\lambda_2^2(1-\cos 2\omega) - 2\lambda_2(\alpha_D - \beta_D)\sin\omega\big[\sin\lambda_2\omega + \\
&+ \sin\lambda_2(2\pi-\omega)\big] - 2\lambda_2(\alpha_D - \beta_D)\beta_D\sin\lambda_2\big[\sin\lambda_2(2\pi-\omega) - \sin\lambda_2\omega\big] + \\
&+ (1-\alpha_D^2) - (1-\beta_D^2)\cos 2\lambda_2\pi + (\alpha_D^2 - \beta_D^2)\cos\big[2\lambda_2(\omega-\pi)\big] = 0
\end{aligned} \tag{5.3}$$

for Mode II deformation, where α_D and β_D are Dunders' composite constants [227] and are related to the elastic constants of each constituent:

$$\alpha_D = \frac{G_1(\kappa_2+1) - G_2(\kappa_2-1)}{G_1(\kappa_2+1) + G_2(\kappa_1+1)}, \qquad \beta_D = \frac{G_1(\kappa_2+1) - G_2(\kappa_2-1)}{G_1(\kappa_2+1) + G_2(\kappa_1+1)}$$

where $\omega = 3/2\pi$ is the angle outside the fibre vertex (note that the angle Ω in Fig. 5.2b is assumed to be equal to $\pi/2$). In order to apply such concepts to the case of a non-debonded fibre, the above solution can be locally adopted (Fig. 5.2a), by

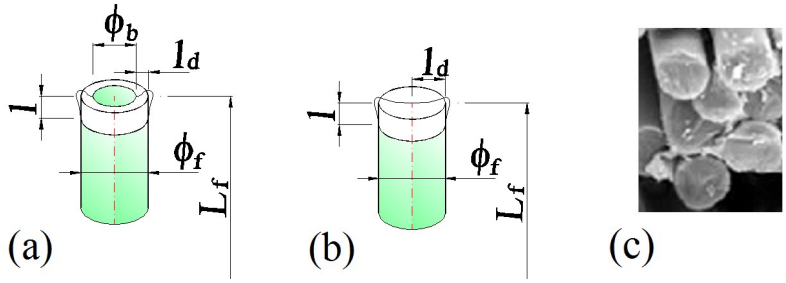

Figure 5.3: (a) Partial detachment at the fibre extremity; (b) case of complete top debonding of the fibre. Hatched zones indicate bonding between the fibre and the matrix. (c) Typical extremities of small cylindrical fibres.

using the elastic parameters of the matrix and the fibres (i.e. $G_1 = G_m$, $G_2 = G_f$ and $\nu_1 = \nu_m$, $\nu_2 = \nu_f$) to determine the stress singularities. In other words, the SIFs at the extremities of the fibre are assumed to be equal to those of a wedge inclusion, i.e. $K_{I,w} = K_{I,\lambda_1}$, $K_{II,w} = K_{II,\lambda_2}$. An equivalent Mode I SIF can be defined also in this case:

$$K_{Ieq,w} = \sqrt{K_{I,\lambda_1}^2 + K_{II,\lambda_2}^2} \tag{5.4}$$

Once the above equivalent SIF $K_{Ieq,w}$, evaluated at the corner of the fibre base reaches the critical value K_{ic} for the interface , a 3D crack appears (Fig. 5.3a) determining a circular bonded area (identified by the diameter ϕ_b) at the top of the fibre, and a cylindrical lateral detachment with length l. It has been demonstrated that, in the case of an annular surface crack (corresponding to the detachment at the top of the fibre), the SIF for a given applied stress is an increasing function of the detached length l_d [228]. Therefore, the bonded circular area becomes smaller and smaller, up to its complete disappearance (i.e. $l_d \to \phi_f/2$ or $\phi_b \to 0$, Fig. 5.3b).

In Figure 5.4a and 5.4b, the equivalent SIF of the bonded fibre ($K_{b,eq} = K_{Ieq,w}$, Eq. 5.4) against the dimensionless remote axial/radial stress ratio $\sigma_z^\infty/\sigma_r^\infty$ is represented for two different constant values of the remote radial stress σ_r^∞. The continuous lines represent the case related to $\sigma_r^\infty = 1\,MPa$, whereas the dashed lines refer to $\sigma_r^\infty = 5\,MPa$. It can be observed that $K_{b,eq}$ attains a minimum for $\sigma_z^\infty/\sigma_r^\infty \cong 1$, and increases almost linearly by increasing the ratio $\sigma_z^\infty/\sigma_r^\infty$. The above minimum condition allows us to state that, when the axial remote stress

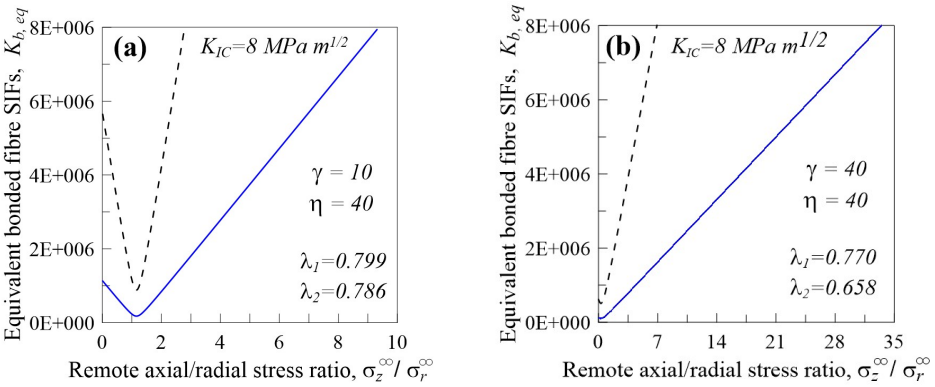

Figure 5.4: Influence of the remote axial-radial stress ratio $\sigma_z^\infty/\sigma_r^\infty$ for different levels of $\sigma_r^\infty = 1.0,\ 5.0\ MPa$ and $\eta = 2L_f/\phi_f = 40$ (a) $\gamma = 10$, (b) $\gamma = 40$.

is equal to about the radial one, the equivalent SIF attains a minimum value, i.e. this represents the safest condition against debonding initiation. The ratio $\sigma_z^\infty/\sigma_r^\infty$ should attain higher values by increasing the Young modulus ratio $\gamma = E_f/E_m$ to reach the critical condition.

Regarding the crack initiation and propagation from the fibre's extremities, it must be recalled that such a case corresponds to the crack appearance and growth from a V-notch, where the singular stress field is given by the classical Williams' solution [229]. As a matter of fact, Leguillon [230] and Yosibash et al. [231] have pointed out that the fracture (energy) and the strength criteria lead to a paradox in the case of mixed mode loading, when applied to a problem involving a singular stress field without a preexisting crack, as occurs in the case of a V-notch. Only when the fracture takes place, the toughness-based approach fully describes the process, and the stress-based approach is simultaneously satisfied. On the basis of the classical strain energy density criterion and the above recalled Leguillon's approach, others criteria have been proposed such that by Li and Zhang ($S-\sigma$ criterion) [232] and that by Greco et al. [233] both related to the behaviour of periodic composites involving matrix-fibre debonding analysed by means of the fracture mechanics concepts. In the present Ph.D. Thesis, in order to overcome the above contradiction and to use a single energy SIF-based criterion for crack initiation and extension, a small crack along the circumferential edge of the fibre (due to the unavoidable imperfections in fibre geometry and in joining between matrix and fibre material in such a sharp region, Fig. 5.3c) is reasonably assumed

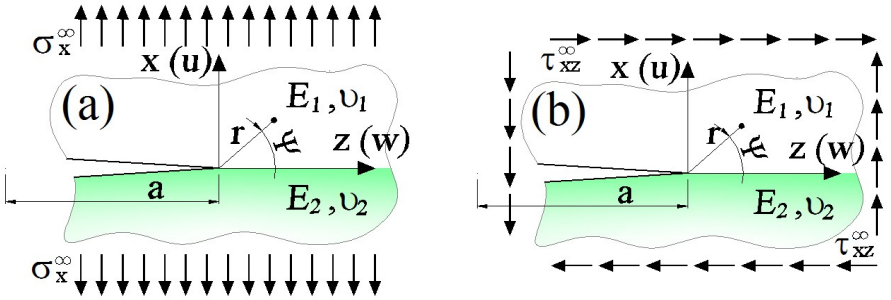

Figure 5.5: Crack at the interface between two different materials: (a) Mode I loading and (b) Mode II loading and fibre-reinforced composite material.

to exist. Consequently, a small cylindrical lateral crack having length $l = a \cdot L_f$ (with $a \ll 1$) is considered, with the constant a assumed in the numerical examples equal to 0.05. Such a small value does not significantly influence the further crack growth along the fibre due to the remote applied increasing load and thus not affect the generality of the adopted approach.

5.4 Straight crack between two dissimilar materials

In order to define the three-dimensional fracture mechanics problem, the case of a straight crack located at the boundary between a bi-material plane is examined, since the solution for such an elementary case can be locally used to describe the problem of a cylindrical crack. The singularity of the stress field arising around the tip of a straight crack between two dissimilar materials depends on the effects of the different elastic properties of the two materials joined along the interface line, $\Psi = 0°$ (Fig. 5.5).

This aspect has widely been examined for both Mode I and Mode II loading in the literature [234–239]. In more detail, it has been shown that the stress singularity at the crack tip presents a singular oscillatory behaviour (Fig. 5.6).

In the case of a straight crack with length $2a = l$ (for an edge crack with length a, l is defined in the same way, i.e. $l = 2a$) placed along the interface of two elastic materials under a remote tension normal to the crack line, the stress field along the

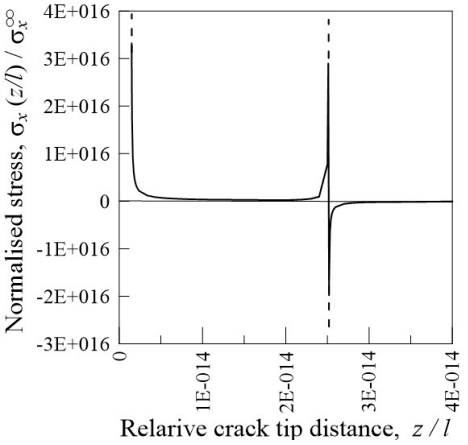

Figure 5.6: Oscillatory behaviour of the stress parallel to the applied load, approaching the tip of a crack between two dissimilar elastic materials.

interface ($\Psi = 0°$, Fig. 5.5) is expressed through complex functions as follows [240]:

$$\begin{aligned}\sigma_x + i\tau_{xy} &= \frac{K_1 + iK_2}{\sqrt{2\pi r}} \cdot \left(\frac{r}{l}\right)^{i\zeta} = \frac{K_1 + iK_2}{\sqrt{2\pi r}} \cdot e^{i\zeta \ln\left(\frac{r}{l}\right)} = \\ &= \frac{K_1 + iK_2}{\sqrt{2\pi r}} \cdot \left\{\cos\left[\zeta \cdot \ln\left(\frac{r}{l}\right)\right] + i \sin\left[\zeta \cdot \ln\left(\frac{r}{l}\right)\right]\right\}\end{aligned} \tag{5.5}$$

whereas the crack faces relative displacement field along the interface ($\Psi = 180°$, Fig. 5.5a) is given by:

$$\delta u + i\delta w = \frac{K_1 + iK_2}{2(1 + 2i\zeta)\cosh(\pi\zeta)} \cdot \left[\frac{\kappa_1 + 1}{G_1} + \frac{\kappa_2 + 1}{G_2}\right] \cdot \sqrt{\frac{r}{2\pi}} \cdot \left(\frac{r}{l}\right)^{i\zeta} \tag{5.6}$$

with $\delta u = u(r,\, \pi) - u(r,\, -\pi)$ and $\delta w = w(r,\, \pi) - w(r,\, -\pi)$ (Fig. 5.5). The bi-material mechanical coefficients in Eqs. 5.5 and 5.6 are given by:

$$\begin{aligned}&\zeta = \frac{1}{2\pi} \cdot \ln\left[\left(\frac{\kappa_1}{G_1} + \frac{1}{G_2}\right) \Big/ \left(\frac{\kappa_2}{G_2} + \frac{1}{G_1}\right)\right] \\ &\text{with} \\ &\kappa_j = \begin{cases} 3 - 4\nu_j & \text{plane strain} \\ \dfrac{3 - \nu_j}{1 + \nu_j} & \text{plane stress} \end{cases} \quad \text{and } j = 1, 2\end{aligned} \tag{5.7}$$

ν_1, ν_2 and G_1, G_2 being the Poisson ratio and shear modulus of the materials 1 and 2, respectively. Note that the stresses tend to infinity (and the displacements tend to zero) by approaching the crack tip, with an oscillatory fashion due to the complex exponential function in the above expressions (Eq. (5.5)). It can be noted that even a simple remote tension acting perpendicular to the crack is responsible for both Mode I (K_1) and Mode II (K_2) SIFs. This phenomenon is due to the different elastic properties of the joined materials, whereas the Mode II SIF vanishes for homogeneous cracked material and such a loading condition. By separating the real and the imaginary part of the above relationships, the Mode I (K_1) and Mode II (K_2) SIFs can be explicitly obtained as a function of the stresses at the crack tip:

$$\begin{aligned} K_1(\sigma_x^\infty) = K_{1x} &= \left\{ \tau_{xz} \cdot \sin\left[\zeta \cdot \ln\left(\frac{r}{l}\right)\right] + \sigma_x \cdot \cos\left[\zeta \cdot \ln\left(\frac{r}{l}\right)\right] \right\} \cdot \sqrt{2\pi r} \\ K_2(\sigma_x^\infty) = K_{2x} &= \left\{ \tau_{xz} \cdot \cos\left[\zeta \cdot \ln\left(\frac{r}{l}\right)\right] - \sigma_x \cdot \sin\left[\zeta \cdot \ln\left(\frac{r}{l}\right)\right] \right\} \cdot \sqrt{2\pi r} \end{aligned} \tag{5.8}$$

where the stresses σ_x, τ_{xz} are evaluated at the distance r from the crack tip for $\Psi = 0°$. By considering the displacements $\delta u(r)$, $\delta w(r)$ along the crack faces ($\Psi = 180°$, Fig. 5.5), the following expressions can be obtained:

$$\begin{aligned} K_1(\sigma_x^\infty, \delta u, \delta w) &= \sqrt{\frac{2\pi}{r}} \cdot \frac{1}{B} \cdot \left[\delta u(2\zeta S + C) + \delta w(S - 2\zeta C)\right] \\ K_2(\sigma_x^\infty, \delta u, \delta w) &= \sqrt{\frac{2\pi}{r}} \cdot \frac{1}{B} \cdot \left[\delta u(2\zeta C - S) + \delta w(C + 2\zeta S)\right] \end{aligned} \tag{5.9}$$

where

$$B = \frac{c_1 + c_2}{2(1 + 4\zeta^2)\cosh(\pi\zeta)}, \quad \text{with} \quad c_1 = \frac{\kappa_1 + 1}{G_1} \quad \text{and} \quad c_2 = \frac{\kappa_2 + 1}{G_2} \tag{5.10}$$

and $S = \sin(\zeta \cdot \ln(r/l))$, $C = \cos(\zeta \cdot \ln(r/l))$. The equivalent interface SIF, $K_i(\sigma_x^\infty)$, due to the remote stress σ_x^∞can be defined by means of energetic considerations [234]:

$$K_i(\sigma_x^\infty) = K_{ix} = \sqrt{K_1^2(\sigma_x^\infty) + K_2^2(\sigma_x^\infty)} \tag{5.11}$$

On the other hand, for Mode II loading (Fig. 5.5b), the SIFs equations can be observed to have the same structure as for the above case, since the solutions

for opening and sliding mode, in term of stress (along the line $\Psi = 0°$) and displacements (along the line $\Psi = 180°$), are characterised by the same form as those for an isotropic homogeneous elastic material. Note that, in the case of a remote uniform tension acting parallel to the crack line (z-axis), σ_z^∞, a Mode II SIF arises due to the different elastic properties of the two dissimilar materials. Such a stress intensity factor can approximately be determined by using the displacements w measured on the crack face parallel to the z direction (Fig. 5.5):

$$\begin{aligned} & K_2(\sigma_z^\infty) = \left[K_{2(1)}(\sigma_z^\infty) + K_{2(2)}(\sigma_z^\infty)\right]/2 \\ \text{where} \quad & K_{2(1)}(\sigma_z^\infty) = \frac{2G_1}{\kappa_1 + 1}\sqrt{\frac{2\pi}{r}} \cdot w_{(1)}(r) \\ \text{and} \quad & K_{2(2)}(\sigma_z^\infty) = -\frac{2G_2}{\kappa_2 + 1}\sqrt{\frac{2\pi}{r}} \cdot w_{(2)}(r) \end{aligned} \tag{5.12}$$

i.e. the Mode II SIF can be computed as the mean value of the SIF evaluated by employing the displacements (measured related to the crack tip position) and the mechanical properties of the material (1) ($w_{(1)}(r)$) and material (2) ($w_{(2)}(r)$), respectively. It can be noted that $K_2(\sigma_z^\infty) = 0$ for a homogeneous cracked material, i.e. material (1) is identical to material (2), since $K_{2(1)}(\sigma_z^\infty) = -K_{2(2)}(\sigma_z^\infty)$.

For *3D antiplane loading* (occurring when the body is loaded by a remote stress parallel to the y axis, normal to the $x - z$ plane), also the Mode III SIF arises [241]. Such a stress-intensity factor can approximately be determined by using the displacements v measured on the crack face parallel to the y direction (Fig. 5.5):

$$\begin{aligned} & K_3(\sigma_z^\infty) = \left[K_{3(1)}(\sigma_z^\infty) + K_{3(2)}(\sigma_z^\infty)\right]/2 \\ \text{where} \quad & K_{3(1)}(\sigma_z^\infty) = \frac{2G_1}{\kappa_1 + 1}\sqrt{\frac{2\pi}{r}} \cdot w_{(1)}(r) \\ \text{and} \quad & K_{3(2)}(\sigma_z^\infty) = \frac{2G_2}{\kappa_2 + 1}\sqrt{\frac{2\pi}{r}} \cdot w_{(2)}(r) \end{aligned} \tag{5.13}$$

i.e. the Mode III SIF is computed as the mean value of the SIF evaluated by using the displacements (measured close to the crack tip position) and the mechanical properties of the material (1) ($v_{(1)}(r)$) and material (2) ($v_{(2)}(r)$), respectively. By considering at the same time the three Modes produced by the remote stresses, σ_x^∞, σ_y^∞, σ_z^∞ and τ_{xz}^∞, the equivalent interface SIF can be written as follows (see

Eq. (5.11)):

$$K_i = \sqrt{\left(K_1(\sigma_x^\infty) + K_1(\tau_{xz}^\infty)\right)^2 + \left(K_2(\sigma_x^\infty) + K_2(\tau_{xz}^\infty) + K_2(\sigma_z^\infty)\right)^2 + K_3^2(\sigma_y^\infty)} \tag{5.14}$$

Under such a mixed mode, the above equivalent SIF can be used to determine the condition of incipient crack propagation

$$K_i = K_{ic} = \begin{cases} \sqrt{E_i \cdot \mathcal{G}_{ic}} & \text{plane stress} \\ \sqrt{\dfrac{E_i \cdot \mathcal{G}_{ic}}{1-\nu^2}} & \text{plane strain} \end{cases} \tag{5.15}$$

where $\mathcal{G}_{ic}$ is the interface fracture energy and K_{ic} the corresponding fracture toughness, whereas E_i and ν_i are the Young modulus and Poisson's ratio of the interface. The above described solutions are assumed to be locally applicable to 3D fracture problems [242] by employing the displacements, u (w), and the normal stresses orthogonal, σ_x (parallel, σ_z), to the fracture plane at the crack front point being considered (Fig. 5.7a), whereas the shear stress $\tau_{nx} = \tau_{xn}$ (on a plane perpendicular to the crack front normal, n, and directed normal to the crack plane) corresponds to the shear stress τ_{xz} of Eq. (5.4).

5.5 Fibre debonding as a fracture mechanics problem

The above 2D crack problem solution can locally be applied to the case of a crack arising between a fibre and the surrounding matrix when a partial fibre-matrix detachment takes place. In this case, the fracture problem is fully three-dimensional, and the mechanical characteristics of the fibre-reinforced composite are those of both the fibre and the matrix. By considering a cylindrical straight fibre embedded in an infinite isotropic elastic domain under remote tension (Fig. 5.7b), the fibre is assumed to be characterised by length $2L_f$, diameter ϕ_f, elastic modulus E_f and Poisson's ratio ν_f. The surrounding elastic medium (matrix material) is assumed to present elastic modulus E_m and Poisson's ratio ν_m (Fig. 5.7).

An orthogonal reference system, centred in the fibre midsection with the z-axis parallel to the fibre midline and the x and y axes belonging to the midspan fibre cross section (Fig. 5.7), is considered. A remote stress field, characterised by a

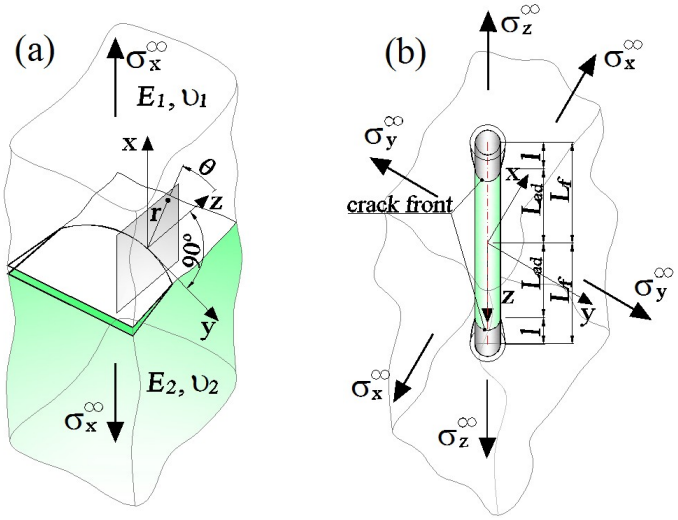

Figure 5.7: (a) 3D crack at the interface between two different materials under remote stress σ_x^∞. Definition of the local co-ordinate system centred on a point on the crack front. (b) Case of a partially symmetrically detached fibre representing debonding.

component σ_z^∞ acting parallel to the fibre direction and components σ_x^∞, σ_y^∞ acting transversal to the fibre axis, is supposed to be applied to the matrix material.

Note that the presence of remote stresses σ_x^∞ and σ_y^∞ acting transversal to the fibre facilitates the debonding since those stresses produce further Mode I, II and Mode III SIFs along the crack front, and such SIFs must be superposed to the existing Mode II SIF produced by the longitudinal remote stress σ_z^∞ (Fig. 5.7b).

5.5.1 Remote stresses acting transversal to the fibre axis

Stresses normal to the fibre axis (Fig. 5.8a) are responsible for Mode I, II and III of fracture as can be deduced from the relative displacements arising between the fibre and the matrix near the crack front.

Note that the effect of the remote stress σ_x^∞ (in term of SIFs) is equivalent to that of the remote stress σ_y^∞, since the problem does not change with a $\pi/2$ rotation of the $x-y$ axes:

$$\begin{aligned} &K_1(\sigma_x^\infty,\theta) = K_1(\sigma_y^\infty,\pi/2-\theta), \qquad K_2(\sigma_x^\infty,\theta) = K_2(\sigma_y^\infty,\pi/2-\theta), \\ &K_3(\sigma_x^\infty,\theta) = K_3(\sigma_y^\infty,\pi/2-\theta) \end{aligned} \tag{5.16}$$

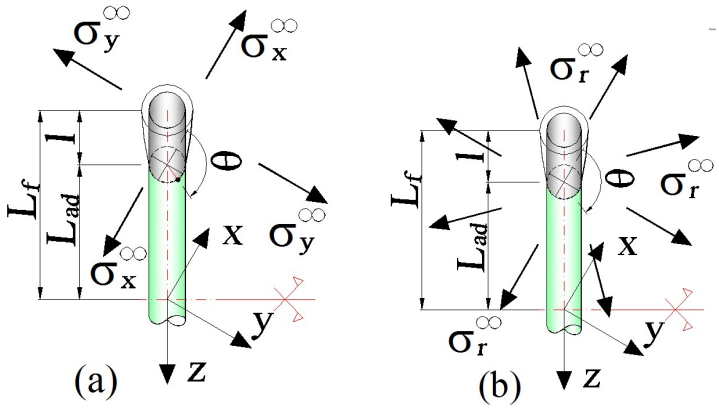

Figure 5.8: Scheme of the debonded end part of a fibre: (a) under biaxial remote stresses σ_x^∞ and σ_y^∞; (b) under remote uniform radial stress σ_r^∞.

that is, the interface Mode I, II and III SIFs due to the remote stress σ_x^∞, evaluated at a crack front point identified by the position angle θ, are identical to the interface Mode I, II and III SIFs due to the remote stress $\sigma_y^\infty = \sigma_x^\infty$ at the crack front point identified by the position angle $\pi/2 - \theta$ (Fig. 5.8a). Moreover, the SIFs, $K_1(\sigma_r^\infty)$ and $K_2(\sigma_r^\infty)$ for constant radial stress, σ_r^∞, normal to the fibre axis (Fig. 5.8b) can be obtained from the SIFs due to the remote stress σ_x^∞. As a matter of fact, such a situation can be obtained from the superposition of the effects due to the remote stress σ_x^∞ for different values of the position angle:

$$K_1(\sigma_r^\infty) = \frac{1}{2\pi}\int_0^{2\pi} K_1(\sigma_x^\infty, \theta)d\theta, \qquad K_2(\sigma_r^\infty) = \frac{1}{2\pi}\int_0^{2\pi} K_2(\sigma_x^\infty, \theta)d\theta \tag{5.17}$$

Further, note that the uniform remote stress σ_r^∞ does not produce any Mode III SIF ($K_3(\sigma_r^\infty) = 0$) due to the radial symmetry of the loading condition.

5.5.2 Remote stresses acting parallel to the fibre axis

The case of stresses acting parallel to the fibre axis corresponds to Mode I and Mode II of fracture, whereas Mode III is equal to zero due to the axisymmetric characteristic of the problem (Fig. 5.7b). Since the fibre is assumed to be embedded in an infinite domain, the Mode I and Mode II SIFs due to the remote stress σ_z^∞ are constant along the crack front and do not depend on θ, i.e. $K_{1z} = K_1(\sigma_z^\infty) = const.$ and $K_{2z} = K_2(\sigma_z^\infty) = const.$

The Mode I, II and III SIFs can conveniently be expressed in a dimensionless form as follows:

$$\begin{aligned}
&K^*_{Ix}(\theta) = \frac{K_{1x}(\theta)}{\sigma^\infty_x\sqrt{\pi l}}, \quad K^*_{Iy}(\theta) = \frac{K_{1y}(\theta)}{\sigma^\infty_y\sqrt{\pi l}},\\
&K^*_{IIx}(\theta) = \frac{K_{2x}(\theta)}{\sigma^\infty_x\sqrt{\pi l}}, \quad K^*_{IIy}(\theta) = \frac{K_{2y}(\theta)}{\sigma^\infty_y\sqrt{\pi l}},\\
&K^*_{IIIx}(\theta) = \frac{K_{3x}(\theta)}{\sigma^\infty_x\sqrt{\pi l}}, \quad K^*_{IIIy}(\theta) = \frac{K_{3y}(\theta)}{\sigma^\infty_y\sqrt{\pi l}},\\
&K^*_{Iz}(\theta) = \frac{K_{1z}(\theta)}{\sigma^\infty_z\sqrt{\pi l}}, \quad K^*_{IIz}(\theta) = \frac{K_{2z}(\theta)}{\sigma^\infty_z\sqrt{\pi l}}, \qquad K^*_{IIIz}(\theta) = \frac{K_{3z}(\theta)}{\sigma^\infty_z\sqrt{\pi l}}
\end{aligned} \tag{5.18}$$

that is in a compact form:

$$K^*_{Mw}(\theta) = \frac{K_{jw}(\theta)}{\sigma^\infty_w\sqrt{\pi l}} \tag{5.19}$$

where $K_{jw}(\theta)$ indicates the Mode M SIF ($M = I,\ II,\ II$ and $j = 1,\ 2,\ 3$) at the point (identified by the angle θ) along the crack front, due to the remote stress σ^∞_w ($w = x,\ y,\ z$), whereas $K^*_{Mw}(\theta)$ is the corresponding dimensionless value.

5.5.3 Multiaxial stress state

In general situations, the applied remote stress state is multiaxial, i.e. all the stresses σ^∞_x, σ^∞_y and σ^∞_z are present at the same time (for the sake of simplicity, the shear stresses are assumed to be not present). As is stated above, the remote stress $\sigma^\infty_x(\sigma^\infty_y)$ is responsible for $K_1(\sigma^\infty_x)$, $K_2(\sigma^\infty_x)$ and $K_3(\sigma^\infty_x)$ ($K_1(\sigma^\infty_y)$, $K_2(\sigma^\infty_y)$ and $K_3(\sigma^\infty_y)$), whereas the remote stress σ^∞_z is responsible for $K_1(\sigma^\infty_z)$ and $K_2(\sigma^\infty_z)$ ($K_3(\sigma^\infty_z)$=0) along the crack front. However, it can be remarked that the following SIFs can be neglected with respect to the other ones:

$$K_3(\sigma^\infty_x) \approx 0, \qquad K_1(\sigma^\infty_z) \approx 0 \tag{5.20}$$

and the equivalent interface SIF (see Eq. (5.14)) along the crack front can thus be simplified as follows:

$$\begin{aligned}
K_i(\theta) \cong \Big[&\big(K_1(\sigma^\infty_x,\theta) + K_1(\sigma^\infty_y,\theta)\big)^2 +\\
&+ \big(K_2(\sigma^\infty_x,\theta) + +K_2(\sigma^\infty_y,\theta) + K_2(\sigma^\infty_z)\big)^2\Big]^{\frac{1}{2}}
\end{aligned} \tag{5.21}$$

where the dependence on the angular coordinate θ is explicitly shown (Fig. 5.8), except for $K_2(\sigma_z^\infty)$ which is constant along the crack front.

By considering the generic case of a cylindrical fibre embedded in an elastic matrix under remote axial (σ_z^∞) and radial (σ_r^∞) stresses, the energetically equivalent SIF can be defined as follows:

$$K_i = \begin{cases} \sqrt{K_I^2(\sigma_r^\infty) + \left[K_{II}(\sigma_r^\infty) + K_{II}(\sigma_z^\infty)\right]^2}, & \text{if} \quad \sigma_r^\infty > 0 \\ K_{II}(\sigma_z^\infty), & \text{if} \quad \sigma_r^\infty \leq 0 \end{cases} \tag{5.22}$$

5.6 Fracture-shear strength relationship for fibre debonding

As said in Chapter 3, the maximum value of the interface shear stress is attained at the extremities of the adhesion length, L_{ad}, and the shear stress-based critical condition for the fibre detachment extension, according with the shear lag model [24], can be expressed as fallows:

$$\tau_{max} = \tau(L_{ad}) = \sigma_z^\infty \cdot \frac{\beta}{p \cdot (\alpha \cdot E_m)} \cdot \tanh(\beta \cdot L_{ad}) = \tau_{au} \tag{5.23}$$

where τ_{au} is the ultimate adhesion fiber-matrix interface shear stress for the joined materials, α and β are the fibre parameters defined in Sect. 3.5.1 in Chapter 3.

The stress-based critical condition for detachment extension becomes:

$$\sigma_{z,c}^\infty \geq \frac{\tau_{au} \cdot p \cdot \alpha \cdot E_m}{\beta \cdot \tanh(\beta \cdot L_{ad})} \tag{5.24}$$

Along the debonded length $l = L_f - L_{ad}$, the shear stress arising between the matrix and the fibre can be assumed to be equal to the friction stress, τ_{fu}, usually much lower than the ultimate adhesion fibre-matrix interface shear stress τ_{au}. For the sake of simplicity, such a friction stress is assumed to be negligible in the following.

The above critical condition (Eq. (5.24)) for detachment growth can be restated by using fracture mechanics concepts, by considering the critical condition,

expressed through the use of Eq. (5.22), due to the remote axial stress only:

$$K_i = K_{IIz} = K_{II}(\sigma_z^\infty) = K_{IIz}^* \cdot \sigma_z^\infty \sqrt{\pi l} \qquad \rightarrow \qquad \sigma_{z,c}^\infty \geq \frac{\sqrt{E_i \cdot \mathcal{G}_{ic}}}{K_{IIz}^* \cdot \sqrt{\pi l}} \tag{5.25}$$

By equating the two above critical conditions (Eqs. (5.24) and (5.25)), both expressed in terms of the remote critical axial stress $\sigma_{z,c}^\infty$, the relationship between the ultimate adhesion fibre-matrix interface shear stress τ_{au} and the fibre-matrix interface fracture toughness K_{ic} (or equivalently the interface fracture energy $\mathcal{G}_{ic}$) can be obtained, once the dimensionless SIF, $K_{IIz}^*(l)$, is known for a given detached length (l) and loading condition (σ_z^∞). This comparison is restricted to the case of remote stresses acting in the fibre direction, which corresponds to the only case admitted by the shear lag model.

In real cases, the stress state in the composite is not uniaxial and cannot be tackled by using the classical shear lag theory, whereas it can easily be treated by the general fracture mechanics approach proposed in the Ph.D. Thesis.

The presence of stresses σ_r^∞ transversal to the fibre could be considered in the shear lag theory by replacing the ultimate adhesion fibre-matrix interface shear stress τ_{au}, with $\tau_{au}(\sigma_r^\infty)$. Consequently, by equating the expressions of the two critical condition for the detachment extension, Eq. (5.24) and Eq. (5.25), the following relationships can be written:

$$K_{ic} = \tau_{au}(\sigma_r^\infty) \cdot \left[\frac{p \cdot \alpha \cdot E_m}{\beta \cdot \tanh(\beta \cdot L_{ad})}\right] \cdot \left[\sqrt{b^2 \cdot K_{Ir}^{*2} + (b \cdot K_{IIr}^* + K_{IIz}^*)^2} \cdot \sqrt{\pi l}\right] \tag{5.26a}$$

$$\mathcal{G}_{ic} = \tau_{au}^2(\sigma_r^\infty) \cdot \left[\frac{p \cdot \alpha \cdot E_m}{\beta \cdot \tanh(\beta \cdot L_{ad})}\right]^2 \cdot \frac{\left[b^2 \cdot K_{Ir}^{*2} + (b \cdot K_{IIr}^* + K_{IIz}^*)^2\right] \cdot \pi l}{E_i} \tag{5.26b}$$

where E_i is the elastic modulus of the fibre-matrix interface and p is the fibre cross section perimeter. Further, the remote radial stress is assumed to be equal to $\sigma_r^\infty = b \cdot \sigma_z^\infty$ (with b a constant). Since the interface fracture toughness K_{ic} is a characteristic value of the joined materials, the limit interface shear stress under

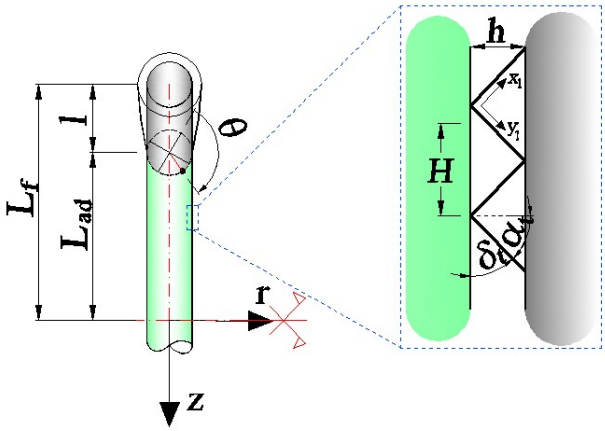

Figure 5.9: Scheme of the truss-like interface micro-structure for the bonded fibre-matrix region.

the remote radial stress value, $\tau_{au}(\sigma_r^{\infty})$, can be obtained from Eq. 5.26a:

$$\tau_{au}(\sigma_r^{\infty}) = \tau_{au} \cdot \overbrace{\frac{K^*_{IIz}}{\sqrt{b^2 \cdot K^{*2}_{Ir} + (b \cdot K^*_{IIr} + K^*_{IIz})^2}}}^{B(\sigma_r^{\infty})} \tag{5.27}$$

where τ_{au} must be considered as the limit shear stress without any radial stress. In other words, the knowledge of the dimensionless SIFs in Eq. 5.26 allows us to define the ultimate fiber-matrix shear stress in presence of a tensile remote radial stress. In practical cases, Eq. 5.26 can be used to evaluate the fiber-matrix interface fracture energy $\mathcal{G}_{ic}$ (or the corresponding fracture toughness K_{ic}), once the ultimate shear strength τ_{au} is known.

5.7 A simple mechanical model for the fiber-matrix interface layer

In order to establish a relationship between the fracture and the strength characteristics of the fibre-matrix interface, the mechanical properties of the fibre-matrix bonding are needed (see Eq. (5.26)). The so-called interface layer can elastically be characterized through a micro-mechanical structural model for such a layer. A simple and effective structural model for the interface can be adopted

by assuming a truss scheme for the material joining two continuous media, which mimics commonly observed interface structures in both artificial and natural materials [22, 243, 244]. Based on this model, the axial forces in the truss elements can be expressed as a function of the relative radial and axial displacements taking place between the matrix and the fibre (Fig. 5.9):

$$N_1 = \boldsymbol{A}^T \cdot \boldsymbol{K} \cdot \Delta\boldsymbol{u} \qquad \text{with} \tag{5.28}$$

$$\boldsymbol{A}^T = \left\{ \frac{1}{2\cos\delta_t} \quad \frac{1}{2\sin\delta_t} \right\}, \quad \boldsymbol{K} = \frac{2 \cdot E_b \cdot \mathcal{A}}{h/\sin\delta_t} \begin{bmatrix} 1+\alpha_t & 0 \\ 0 & 1-\alpha_t \end{bmatrix}, \quad \Delta\boldsymbol{u} = \begin{Bmatrix} \Delta u_z \\ \Delta_r \end{Bmatrix}$$

where $\boldsymbol{K}$ is the stiffness matrix (with components k_{ij}) of the truss-like structure, under the hypothesis: $\delta_t = \pi/2 - \alpha_t$, $0 < \alpha_t \ll 1$ (E_b, $\mathcal{A}$ and $h/\sin\delta_t$ being the elastic modulus, the cross-section area and the length of the bars, respectively), and $\Delta\boldsymbol{u}$ is the vector of the matrix-fibre relative displacements. In the above relationship, the truss elements of the interface are assumed to have an elastic modulus E_b generally different from that of the matrix one, E_m.

The stress tensors, $\boldsymbol{\sigma}_1$ in the local coordinate system $x_1 - y_1$ of the bar and $\boldsymbol{\sigma}$ in the global coordinate system $z - r$ can be defined as follows (Fig. 5.9):

$$\boldsymbol{\sigma}_1 = \begin{bmatrix} \sigma_{x1} & 0 & 0 \\ 0 & 0 & 0 \\ 0 & 0 & 0 \end{bmatrix}, \quad \boldsymbol{\sigma} = \boldsymbol{T}^T \boldsymbol{\sigma}_1 \boldsymbol{T} \quad \text{with} \quad \boldsymbol{T} = \begin{bmatrix} c & s & 0 \\ -s & c & 0 \\ 0 & 0 & 1 \end{bmatrix} \tag{5.29}$$

where $c = \cos\delta_t$, $s = \sin\delta_t$, $\boldsymbol{T}$ is the rotation matrix and $\boldsymbol{\sigma}$ is assumed corresponding to that for a plane stress condition. From Eq. (5.28), the stress in the bar element can be obtained:

$$\sigma_{x1} = \frac{N_1}{\mathcal{A}} = \frac{\boldsymbol{A}^T \cdot \boldsymbol{K} \cdot \Delta\boldsymbol{u}}{\mathcal{A}} = \frac{\boldsymbol{A}^T \cdot \boldsymbol{K} \cdot \boldsymbol{U}}{\mathcal{A}} \cdot \underline{\boldsymbol{\varepsilon}}_1 = \frac{h}{2} \cdot \tag{5.30}$$

$$\text{with} \quad \boldsymbol{U} = \begin{bmatrix} 0 & 0 & h & 0 \\ 0 & h & 0 & 0 \end{bmatrix}, \quad \underline{\boldsymbol{\varepsilon}}_1 = \begin{Bmatrix} \varepsilon_z \\ \varepsilon_r \\ \gamma_{rz} \\ \varepsilon_\theta \end{Bmatrix}, \quad \text{and} \quad \Delta\boldsymbol{u} = \boldsymbol{U} \cdot \underline{\boldsymbol{\varepsilon}}_1$$

The stress tensor $\boldsymbol{\sigma}$ (see Eq. (5.29)), expressed through the stress components in

the global coordinate system, becomes:

$$\boldsymbol{\sigma} = \begin{bmatrix} \sigma_z & \tau_{rz} & 0 \\ \tau_{zr} & \sigma_r & 0 \\ 0 & 0 & \sigma_\theta \end{bmatrix} = \begin{bmatrix} c^2 \cdot \sigma_{x1} & -c \cdot s \cdot \sigma_{x1} & 0 \\ -c \cdot s \cdot \sigma_{x1} & (1-c^2) \cdot \sigma_{x1} & 0 \\ 0 & 0 & \sigma_\theta \end{bmatrix} \tag{5.31}$$

or explicitly, by using Eq. (5.30) for σ_{x1}, the stress tensor is equal to:

$$\underline{\boldsymbol{\sigma}} = \begin{Bmatrix} \sigma_z \\ \sigma_r \\ \tau_{rz} \\ \sigma_\theta \end{Bmatrix} = \begin{Bmatrix} \dfrac{h(1-c^2)}{2} \cdot \dfrac{(k_{22} \cdot c + k_{12} \cdot s)\varepsilon_r + (k_{11} \cdot s + k_{21} \cdot c)\gamma_{rz}}{\mathcal{A} \cdot c \cdot s} \\ \dfrac{hc}{2} \cdot \dfrac{(k_{22} \cdot c + k_{12} \cdot s)\varepsilon_r + (k_{11} \cdot s + k_{21} \cdot c)\gamma_{rz}}{\mathcal{A} \cdot s} \\ -\dfrac{h}{2} \cdot \dfrac{(k_{22} \cdot c + k_{12} \cdot s)\varepsilon_r + (k_{11} \cdot s + k_{21} \cdot c)\gamma_{rz}}{\mathcal{A}} \\ \sigma_\theta \end{Bmatrix} \tag{5.32}$$

since the non-zero components of the stress tensor correspond to an axi-symmetric behaviour of the interface. By assuming a continuous distribution of the bars representing the interface material, the linear elastic constitutive equations in the axi-symmetric isotropic case (i.e. the material constituting the interface is assumed to be linear elastic and isotropic) are given by:

$$\underline{\boldsymbol{\sigma}} = \underbrace{\frac{E_i \cdot (1-\nu_i)}{(1+\nu_i)(1-2\nu_i)} \cdot \begin{bmatrix} 1 & \dfrac{\nu_i}{1-\nu_i} & 0 & \dfrac{\nu_i}{1-\nu_i} \\ \dfrac{\nu_i}{1-\nu_i} & 1 & 0 & \dfrac{\nu_i}{1-\nu_i} \\ 0 & 0 & \dfrac{1-2\nu_i}{2-2\nu_i} & 0 \\ \dfrac{\nu_i}{1-\nu_i} & \dfrac{\nu_i}{1-\nu_i} & 0 & 1 \end{bmatrix}}_{\boldsymbol{C}_i} \cdot \begin{Bmatrix} \varepsilon_z \\ \varepsilon_r \\ \gamma_{rz} \\ \varepsilon_\theta \end{Bmatrix} = \tag{5.33}$$

$$= \boldsymbol{C}_i \cdot \boldsymbol{S} \cdot \Delta\boldsymbol{u}$$

where $\boldsymbol{C}_i$ (characteristic of the interface) has the well-known form typical of an axi-symmetric elastic problem, and the strain components arranged in the strain vector $\underline{\boldsymbol{\varepsilon}}$ of the interface layer (having thickness equal to h) in the global coordinate

system can approximately be evaluated as follows:

$$\underline{\boldsymbol{\varepsilon}} = \begin{Bmatrix} \varepsilon_z \\ \varepsilon_r \\ \gamma_{rz} \\ \varepsilon_\theta \end{Bmatrix} = \begin{bmatrix} 0 & 0 \\ 0 & 1/h \\ 1/h & 0 \\ 0 & 1/\overline{r} \end{bmatrix} \begin{Bmatrix} \Delta u_z \\ \Delta u_r \end{Bmatrix} = \boldsymbol{S} \cdot \Delta \boldsymbol{u} \tag{5.34}$$

where $\boldsymbol{S}$ is the compatibility matrix, and $\overline{r}$ is the mean value of the radius of the interface layer measured with respect to the fiber axis. Since $\Delta u_r = h\varepsilon_r = \varepsilon_\theta \overline{r}$, the strain components ε_r, ε_θ must fulfil the relationship $\varepsilon_\theta = \varepsilon_r \cdot (h/\overline{r})$. By assuming that the deformation is small in the circumferential direction, the corresponding strain ε_θ can be neglected. Further, by considering that $\varepsilon_z = 0$ and by assuming the relative radial displacement Δu_r (i.e. $\varepsilon_r = \Delta u_r/h \cong 0$, $\varepsilon_\theta = \Delta U_r/\overline{r} \cong 0$) to be negligible, the stress vector in the interface layer can thus be simplified as follows:

$$\begin{aligned} \underline{\boldsymbol{\sigma}} &= \begin{Bmatrix} \dfrac{E_i(1-\nu_i)}{(1+\nu_i)(1-2\nu_i)} \cdot \varepsilon_z + \dfrac{E_i\nu_i}{(1+\nu_i)(1-2\nu_i)} \cdot (\varepsilon_r + \varepsilon_\theta) \\ \dfrac{E_i(1-\nu_i)}{(1+\nu_i)(1-2\nu_i)} \cdot \varepsilon_r + \dfrac{E_i\nu_i}{(1+\nu_i)(1-2\nu_i)} \cdot (\varepsilon_z + \varepsilon_\theta) \\ \dfrac{E_i}{2(1+\nu_i)(1-2\nu_i)} \cdot \gamma_{rz} \\ \dfrac{E_i(1-\nu_i)}{(1+\nu_i)(1-2\nu_i)} \cdot \varepsilon_\theta + \dfrac{E_i\nu_i}{(1+\nu_i)(1-2\nu_i)} \cdot (\varepsilon_r + \varepsilon_z) \end{Bmatrix} \cong \\ &\cong \begin{Bmatrix} 0 \\ 0 \\ \dfrac{E_i}{2(1+\nu_i)(1-2\nu_i)} \cdot \gamma_{rz} \\ 0 \end{Bmatrix} \end{aligned} \tag{5.35}$$

that was expected, since only the shear stress τ_{rz} is present according to the shear lag model. On the other hand, by writing the stress components in the global coordinate system through Eqs. (5.33) and (5.34) and by taking into account the previous hypothesis of small deformation in circumferential direction together with $\alpha_t \ll 1$, $\delta_t \to \pi/2$, $s = \sin\delta_t \cong 1$ and $c = \cos\delta_t \cong 0$), the following equation can

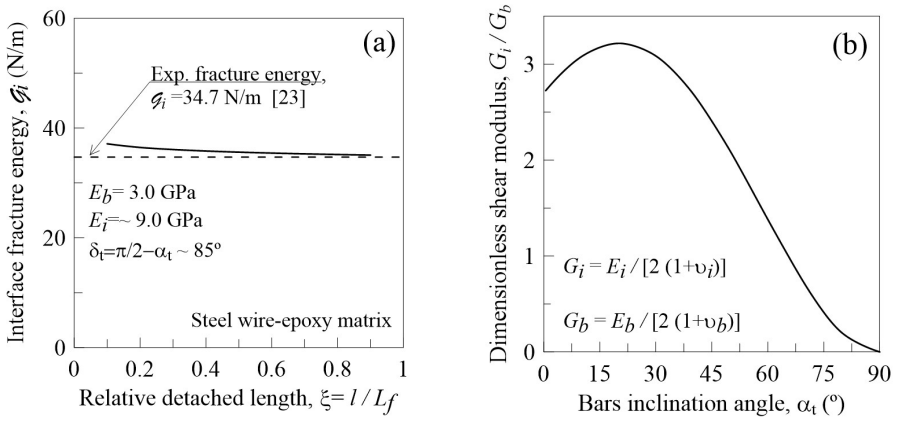

Figure 5.10: (a) Pattern of interface fracture energy $\mathcal{G}_i$ vs fiber dimensionless detached length, ξ; (b) Dimensionless shear modulus of the interface, G_i/G_b, vs inclination angle of the bars.

be obtained:

$$\underline{\boldsymbol{\sigma}} = \begin{Bmatrix} c^2 \cdot \sigma_{x1} \\ (1-c^2)\sigma_{x1} \\ -cs \cdot \sigma_{x1} \\ \sigma_\theta \end{Bmatrix} \cong \begin{Bmatrix} 0 \\ \sigma_{x1} \\ -cs \cdot \sigma_{x1} \\ 0 \end{Bmatrix} = \begin{Bmatrix} c \cdot \dfrac{h}{2} \cdot \dfrac{(k_{11} \cdot s + k_{21} \cdot c)}{\mathcal{A} \cdot s} \gamma_{rz} \\ \dfrac{h}{2} \cdot \dfrac{(k_{11} \cdot s + k_{21} \cdot c)}{\mathcal{A} \cdot c \cdot s} \gamma_{rz} \\ -\cdot \dfrac{h}{2} \cdot \dfrac{(k_{11} \cdot s + k_{21} \cdot c)}{\mathcal{A}} \gamma_{rz} \\ 0 \end{Bmatrix} \tag{5.36}$$

and, by comparing the shear stress in Eq. (5.36) with that in Eq. (5.35), the following expression for the shear modulus G_i of the interface can be deduced:

$$G_i = \frac{E_i}{2(1+\nu_i)} = \frac{h}{2} \cdot \frac{|k_{11} \cdot s + k_{21} \cdot c|}{\mathcal{A}} = \left| E_b \cdot (1+\alpha_t) \cdot s^2 \right| \tag{5.37}$$

Note that G_i is independent of the interface layer thickness and of the cross-section area $\mathcal{A}$ of the truss elements, while it depends on its elastic modulus E_b and on the angle δ_t defining the orientation of the truss elements. The interface elastic modulus E_i can finally be obtained once the Poisson's ratio ν_i of the fiber-matrix bonding is known (for the sake of simplicity, $\nu_i = \nu_m$ is assumed).

In order to show an application of the present interface model, the results reported in Ref. [23] (where the interface fracture energy and the limit shear stress have been examined through experimental tests performed on different

composite's constituents) are herein analysed. In particular, a steel-wire epoxy matrix composite has been studied, and its mechanical characteristics can be summarized as follows: $E_m = 3.0\,GPa$ and $E_f = 179\,GPa$ are the Young modulus of the matrix and fibres, respectively, $\nu_m = 0.35$ and $\nu_f = 0.3$ are the Poisson's ratio for the matrix and fibres, respectively. For this composite, the limit shear stress and the interface critical fracture energy are obtained from experimental tests and are taken equal to $\tau_{au} = 8.96\,MPa$ and to $\mathcal{G}_{ic} = 34.7\,J/m^2$ [23]. Based on Eq. (5.26b), the elastic modulus E_i (and consequently the corresponding shear modulus G_i) of the interface can be evaluated once the limit shear stress, τ_{au}, the Mode II SIF, $K^*_{IIz}(l)$, for a given debonded length l, and the interface critical energy, $\mathcal{G}_{ic}$, are known (Fig. 5.10a).

If the interface elastic modulus is assumed to be equal to about $E_i \cong 9.0\,GPa$, the approximate value $\mathcal{G}_{ic}(l) \cong 34.7\,J/m^2$, is obtained from Eq. (5.26b). As can be noted in Fig. 5.10a, the interface fracture energy $\mathcal{G}_{ic}$ computed through the above relationship is not perfectly constant but slightly varies with l, and that is due to the little variation of the function $K^{*2}_{IIz}(l) \cdot \pi l$ (in Eq. (5.26b)) with the debonded length, l. Once the interface elastic modulus E_i is known, the inclination angle δ_t, representing the arrangement of the truss elements of the interface, can be determined by solving Eq. (5.37), where the inclination angle appears in the terms $s = \sin\delta$ and $\alpha_t = \pi/2 - \delta_t$.

In the present simulation of the results reported by Kim et al. [23], the bars elastic modulus E_b is assumed equal to E_m, i.e. $E_b = 3.0\,GPa$. Then, Eq. (5.37) provides an inclination angle of the bars equal to about $\delta_t \cong 85°$ ($\alpha_t \cong 5°$), corresponding to an interface/truss shear modulus ratio G_i/G_b equal to about 2.87 (Fig. 5.10b).

5.8 Finite element analyses

In order to determine the SIFs for the above loading cases, numerical FE analyses have been herein performed by employing 20-noded solid elements. Due to the presence of three axes of symmetry, one-fourth of the fibre surrounded by a conveniently large region of matrix material is modelled (Fig. 5.11a). The influence of other neighbour fibres and that of the matrix boundary conditions are neglected [212] (i.e. the dilute hypothesis is made). Different values of the

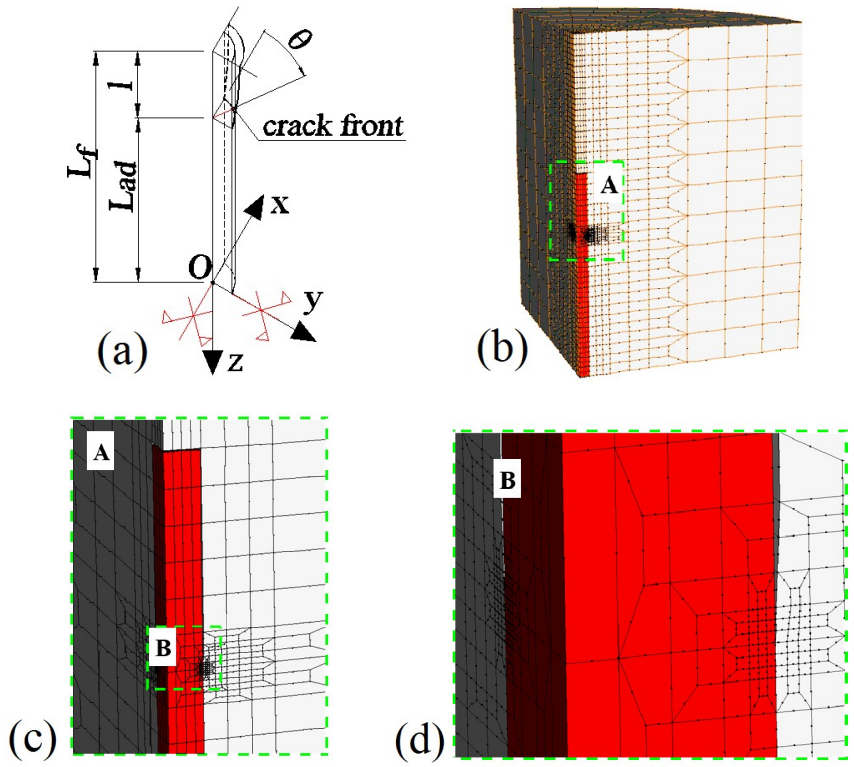

Figure 5.11: (a) Portion of a fibre and of the surrounding matrix material, (b) and (c) FE mesh of 1/8 of the fibre and matrix, and (d) crack front FE arrangement detail.

fibre/matrix elastic modulus ratio are examined, i.e. $\gamma = E_f/E_m = 1,\ 10,\ 25,\ 40$, whereas the Poisson's ratios are assumed to be equal to $\nu_m = 0.1$ and $\nu_f = 0.3$ for the matrix and the reinforcing phase, respectively. The fibre is assumed to be characterised by total length $2L_f$ and diameter ϕ_f, whereas its debonded parts (both with length equal to l) are assumed to be symmetrically placed at the fibre extremities. The fibre aspect ratio $\eta = 2L_f/\phi_f$ is assumed equal to 20, 40, 80, whereas the dimensionless crack length $\xi = l/L_f$ are taken equal to 0.05, 0.1, 0.2, 0.3, 0.4, 0.5, 0.6, 0.7, 0.8, 0.9. Quarter-point quadratic elements (Fig. 5.11b, (c) and (d)) are used along the crack front in order to simulate the square-root singularity of the stress and strain fields in such a zone. Then the SIFs are obtained from the expressions reported in the previous Sections by using the displacements measured on the crack faces.

In order to assure good numerical results, several convergence tests (h-convergence

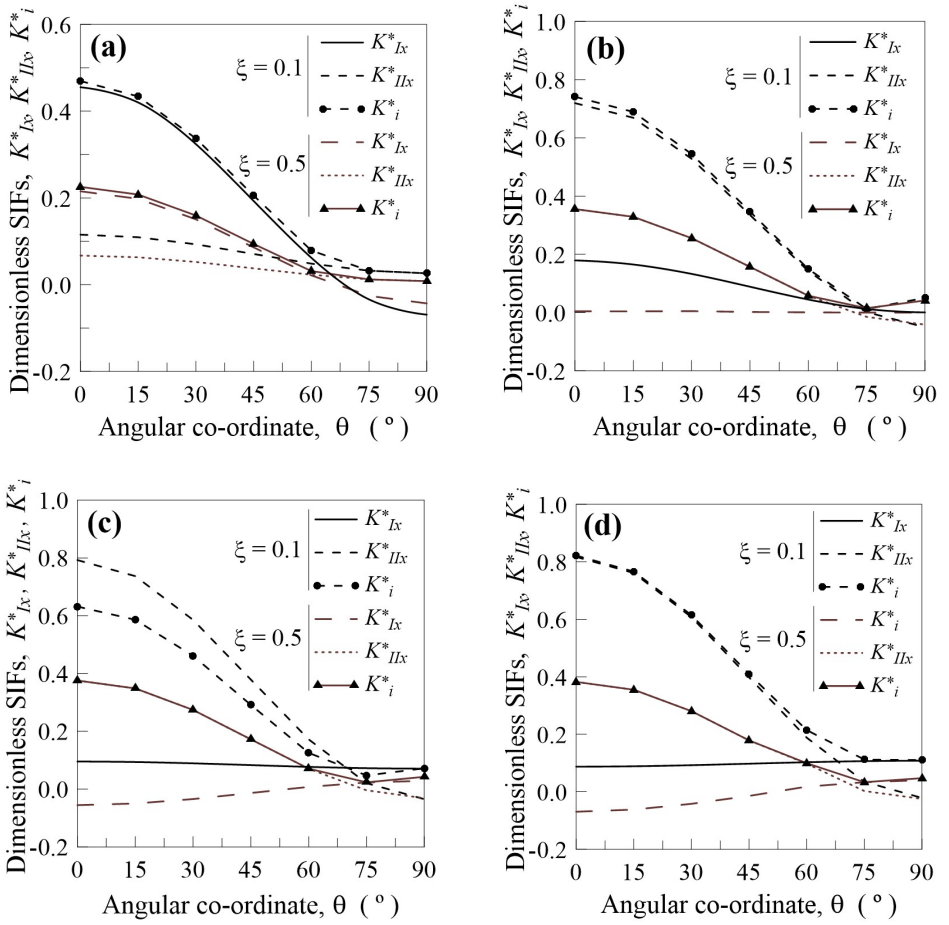

Figure 5.12: Dimensionless SIFs along the crack front ($0° \leq \theta \leq \pi/2$) for relative crack lengths $\xi = 0.1$ and $\xi = 0.5$ ($\eta = 20$): (a) $\gamma = 1$, (b) $\gamma = 10$, (c) $\gamma = 25$ and (d) $\gamma = 40$.

tests) are conducted to determine the optimum FE size and arrangement around the cracked zone.

5.8.1 Mode I and Mode II SIFs due to transversal stress

The effects of the transversal stress, σ_x^{∞}, on the Mode I, II and III dimensionless SIFs are herein examined.

In Figure 5.12 the dimensionless Mode I, Mode II and interface SIFs are plotted along the crack front for a fibre aspect ratio $\eta = 20$, different values of fibre/matrix elastic modulus ratio γ, and relative dimensionless crack length equal to $\xi = 0.1$

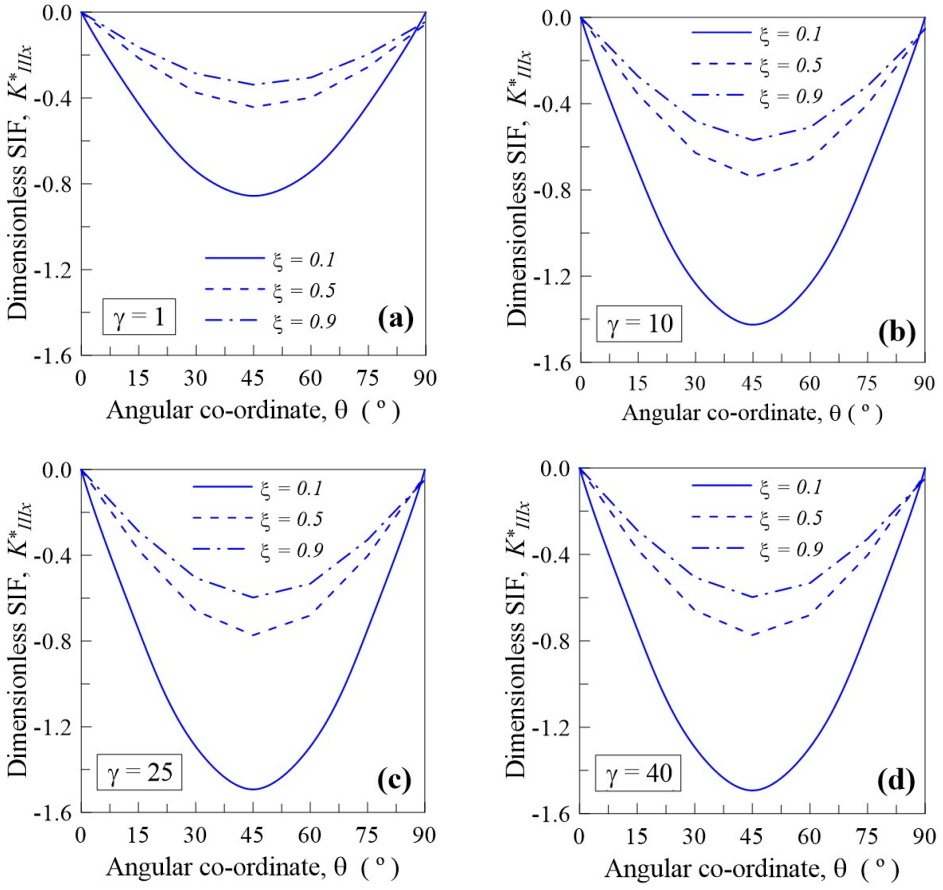

Figure 5.13: Dimensionless Mode III SIF along the crack front ($0° \leq \theta \leq \pi/2$) due to σ_x^∞ for relative crack lengths $\xi = 0.1$, $\xi = 0.5$ and $\xi = 0.9$ ($\eta = 20$): (a) $\gamma = 1$, (b) $\gamma = 10$, (c) $\gamma = 25$ and (d) $\gamma = 40$.

(short crack) and $\xi = 0.5$ (deep crack). Note that the SIFs increase by increasing the γ ratio. The minimum values of K^*_{Ix} and K^*_{IIx} are attained at the point identified by $\theta \cong \pi/2$ along the crack front. Negative values of K^*_{Ix} indicate the tendency of the crack faces to close and, therefore, these values must be neglected in practice. Analogous behaviour can be observed for other values of η.

Figure 5.13 shows the Mode III dimensionless SIF against the angular co-ordinate ($0° \leq \theta \leq \pi/2$). Such a SIF is equal to zero for $\theta = 0°$ and $\pi/2$, whereas the SIF is maximum for $\theta = \pi/4$ (maximum relative displacement parallel to the crack front). The above SIF increases by increasing γ and ξ. Note that

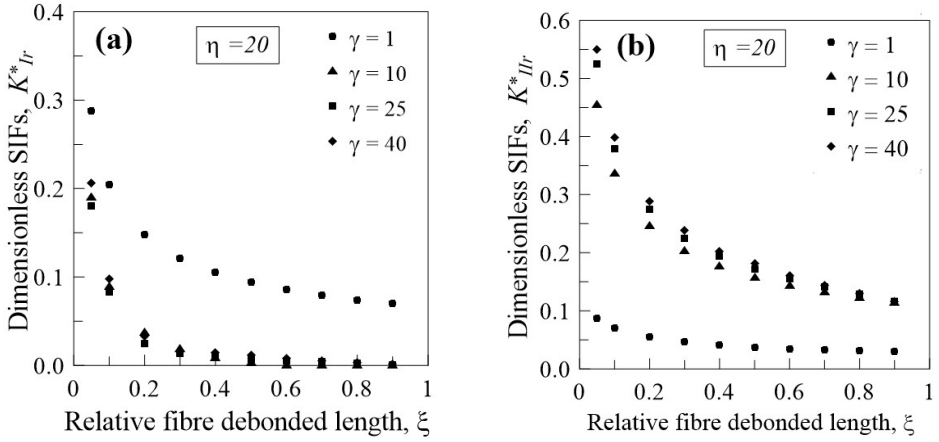

Figure 5.14: Dimensionless (a) Mode I and (b) Mode II SIFs due to the radial stress against the relative crack length ξ, for $\gamma = 1$, $\gamma = 10$, $\gamma = 25$ and $\gamma = 40$ ($\eta = 20$).

negative values of the Mode III SIF are related to the assumption of the positive displacements along the crack front, but that does not affect the results. Quite similar trends can be observed for other values of η.

5.8.2 Mode I and Mode II SIFs due to radial stress

In the present subsection, the effects of the uniform transversal radial stress, σ_r^∞, (Fig. (5.8b)) on Mode I and II SIFs are examined. The expressions used for the SIFs computations are reported in Eqs. (5.17). Due to the axisymmetry of the case analysed, no dependency on the angular co-ordinate θ can be noted. The graphs in Figure 5.14 display the dimensionless SIFs against the relative crack length ξ. In this case, the dimensionless Mode I SIF is lower for high value of the Young modulus ratio, γ, while the opposite occurs for the dimensionless Mode II SIF. Moreover, the SIFs tend to decrease by increasing ξ, i.e. the effect of the crack on the stress field tends to vanish as the crack extension tends to the fibre length.

5.8.3 Mode II SIF due to longitudinal stress

Finally, the case of the longitudinal stress, σ_z^∞, is examined. As is discussed above, the most significant SIF for this loading condition is the Mode II SIF. In Figure 5.15, the dimensionless SIF along the crack front is reported against the relative crack length for different values of γ. Such a SIF tends to increase

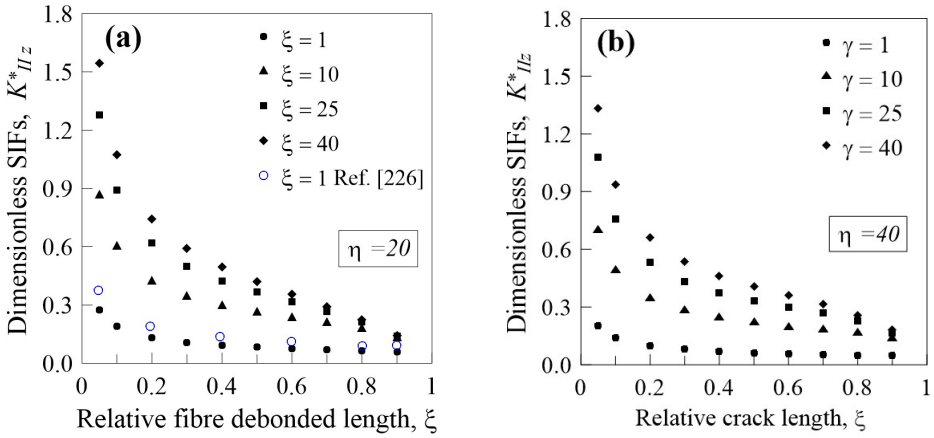

Figure 5.15: Dimensionless Mode II SIF due to σ_z^{∞} against relative crack length ξ, for $\gamma = 1$, $\gamma = 10$, $\gamma = 25$ and $\gamma = 40$: (a) $\eta = 20$; (b) $\eta = 40$. Results by Ref. [226] are also reported for $\gamma = 1$.

by increasing the Young modulus ratio, γ, and, as occurs in the case of radial stresses, it tends to vanish for very long cracks ($l \to L_f$, i.e. $\xi \to 1$) corresponding to a complete debonded fibre. Such a decrease is more evident for fibres having greater aspect ratio values, η. In Figure 5.15a, the results by Wüthrich [226] for a cylindrical crack and for $\gamma = 1$ are reported . Note that such results are related to a loading condition not exactly equal to the present one, and they do not depend on the ratio η (in Fig. 5.15a, they are plotted only for $\eta = 20$).

In conclusion, from the above discussion based on the obtained results under a given loading condition, the fibre debonding can be identified to occurs when the critical load is reached (crack propagation); however it does not develop further unless the load is increased. As a matter of fact, the SIFs show a decreasing tendency by increasing ξ.

5.8.4 Analytical interpolation of the SIFs values

In order to determine SIF expressions useful in practical applications, characterised by values of the dimensionless parameters γ, η, ξ falling in the above ranges (i.e. $1 \leq \gamma \leq 40$, $20 \leq \eta \leq 80$ and $0.05 \leq \xi \leq 0.9$), an interpolation of the obtained dimensionless SIFs is performed by using a polynomial equation having

the following form:

$$K^*_{Ir}(\bar{\gamma},\eta,\xi) = a_0+a_1\eta+a_2\eta^2+a_3\eta^3+b_1\xi+b_2\xi^2+b_3\xi^3+c_1\xi\eta+c_2\xi\eta^2+c_3\xi^2\eta \quad (5.38)$$

where the Young modulus ratio $\gamma = E_f/E_m = \bar{\gamma}$ is assumed constant when determining the coefficients a_0, a_1, a_2, ..., c_3 (see Appendix A). Graphical representations of Eq. (5.38) are plotted in Figure 5.16 ($\gamma = 10$) and Figure 5.17 ($\gamma = 40$), where the dimensionless Mode I and Mode II SIFs produced by a radial stress are represented against the relative crack length, ξ, and the fibre aspect ratio, η (Figs. 5.16a, 5.16b and 5.17a, 5.17b). The dimensionless Mode II SIF produced by a remote axial stress (Figs. 5.16c and 5.17c) is also displayed. Note that all the SIF results are heavily affected by the relative crack length ξ, while they are slightly influenced by the fibre aspect ratio. Further, the higher the fibre-matrix elastic modulus ratio γ, the higher the SIFs values. In the limit case $\gamma \to 0$ (or $\xi \to 1$, which is equivalent from the mechanical point of view), the fibre can be considered as a simple cylindrical void inside the matrix, and the stress singularity disappears. In the following, the influence of each parameter characterising the fibre-reinforced composite is examined in terms of its effect on the SIF values.

5.8.5 Influence of the relative crack length ξ on the SIFs

Mode I and II produced by the radial stress as well as Mode II produced by the axial stress are determined for the above range values of ξ. Figure 5.18 shows the dimensionless Mode I and Mode II SIFs due to a remote uniform radial stress and the Mode II SIF for an axial remote stress against the relative crack length ξ, for two values of the fibre aspect ratio ($\eta = 20,\ 80$) and different Young modulus ratios γ. For all cases, the SIFs tend to decrease by increasing the relative crack length. As a limit case, the SIFs tend to disappear as the debonding spreads along the whole fibre length. Under radial stress, the Mode I SIF is greater for lower values of the elastic modulus ratio γ, while the opposite occurs for the Mode II SIF due to both radial and axial stresses. In all the considered cases, the SIFs are more severe for short fibres, i.e. for low values of η. The continuous curves reported in Figure 5.18 represent the values obtained through the interpolation equations, Eq. (5.38), by using the coefficients a_0, a_1, a_2, ..., c_3 reported in Table A.4 (see Appendix A).

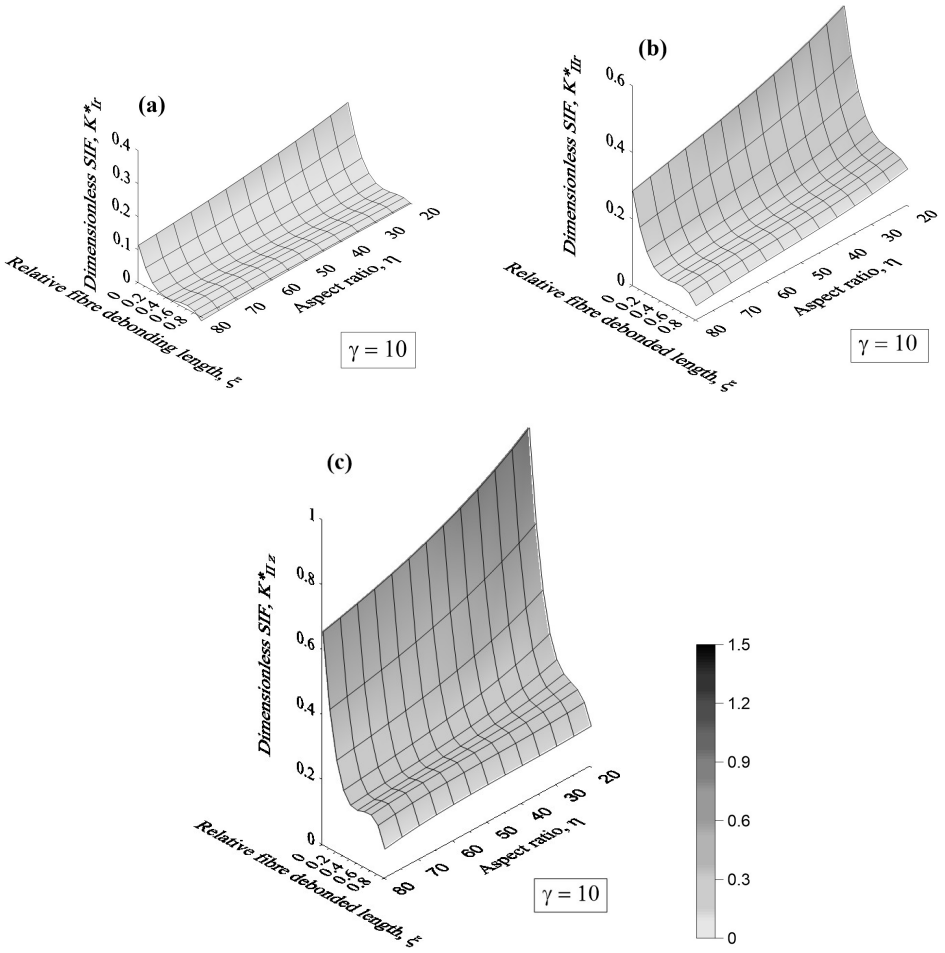

Figure 5.16: 3D interpolation (Eq. (5.38)) for $\gamma = 10$: (a) Mode I and (b) Mode II SIFs for the remote radial stress, (c) Mode II SIF for the remote longitudinal stress. Results are plotted against the relative crack length ξ and the fibre aspect ratio η.

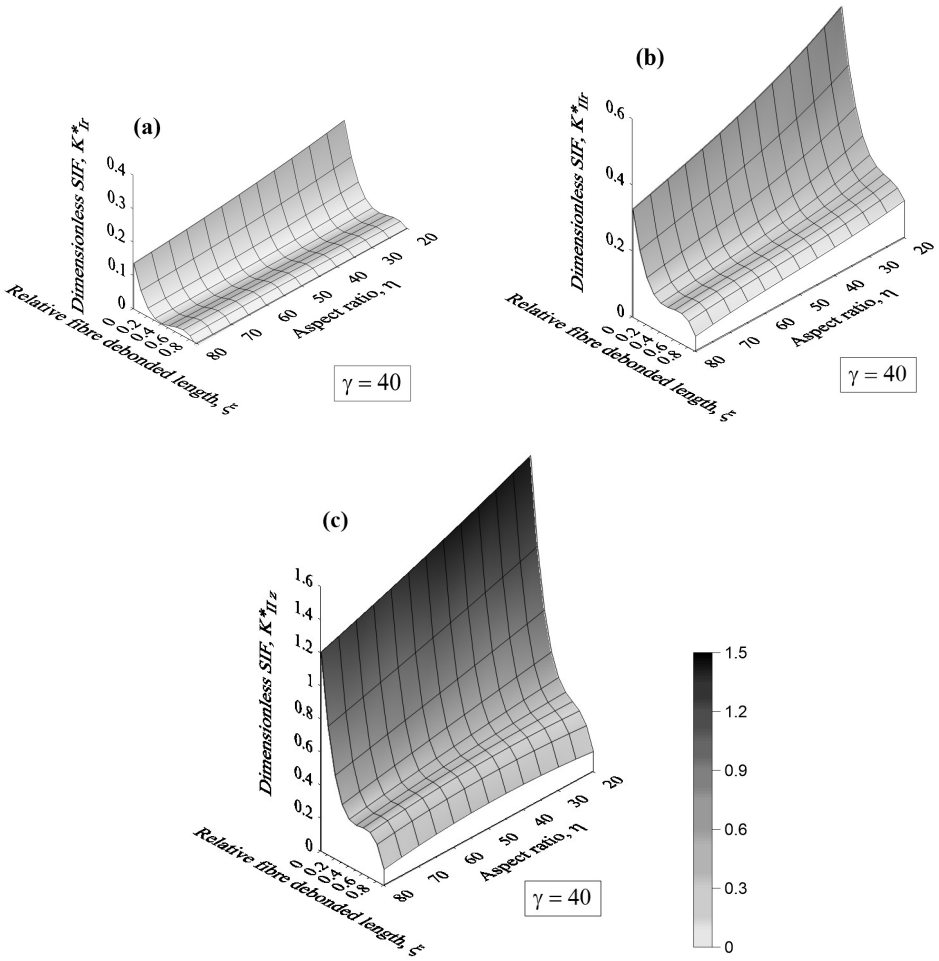

Figure 5.17: 3D interpolation (Eq. (5.38)) for $\gamma = 40$: (a) Mode I and (b) Mode II SIFs for the remote radial stress, (c) Mode II SIF for the remote longitudinal stress. Results are plotted against the relative crack length ξ and the fibre aspect ratio η.

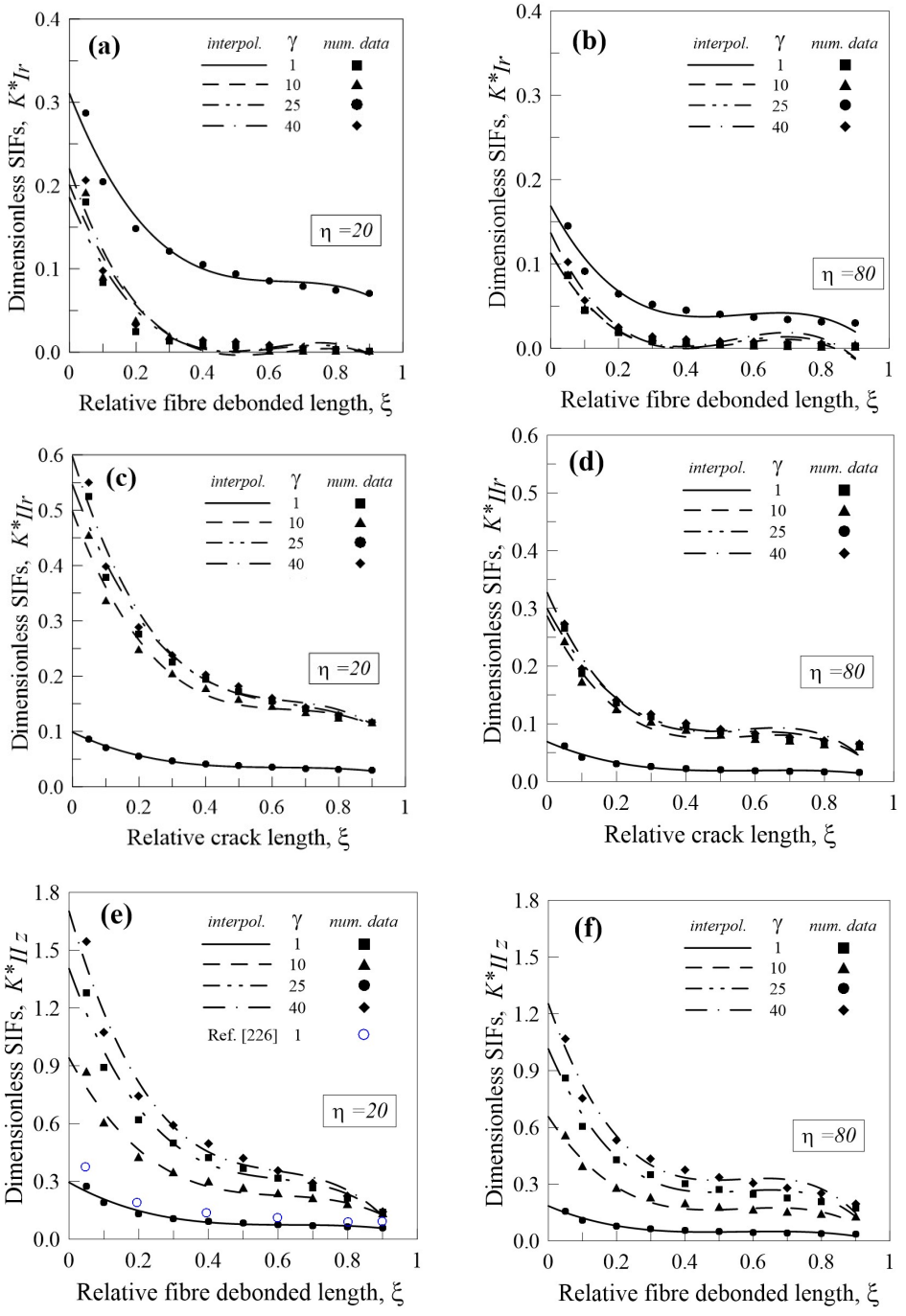

Figure 5.18: Dimensionless (a), (b) Mode I and (c), (d) Mode II SIFs due to a remote uniform radial stress. (e), (f) Mode II SIF for an remote axial stress against ξ, for $\eta = 20$, 80 and different values of γ.

5.8.6 Influence of the fibre aspect ratio η on the SIFs

Figure 5.19 shows the influence of the fibre aspect ratio on the Mode I and II SIFs, for both radial and axial remote stresses. It can be noticed that, for low values of η, the SIFs present higher values than those for longer fibres. Such a behaviour is more evident for short detached region, i.e. for low values of ξ. The observed trend is not influenced by the fibre-matrix elastic modulus ratio that simply determines different absolute SIF values, whereas the influence of the η parameter remains almost the same (Figures 5.19a, (c) and (e) are related to $\xi = 10$, while Figures 5.19b, (d) and (f) are related to $\xi = 40$). The continuous curves reported in Figure 5.19 represent the values obtained through interpolation, Eq. (5.38), by using the coefficients a_0, a_1, a_2, ..., c_3, reported in Table A.4 (see Appendix A), which provide a sufficiently accurate estimation of the numerical values.

5.8.7 Influence of the fibre-matrix Young modulus ratio γ on the SIFs

As has been already observed in the previous Sections, the ratio γ produces a significant variation of the SIFs for a partially detached fibre. In particular, it can be noted that the Mode I SIF for radial stress decreases by increasing γ (Fig. 5.20a, 5.20b) and stabilizes to an almost constant value for $\gamma \geq 10$. On the other hand, the behavior is the opposite for the Mode II SIF due to remote radial stress and for the Mode II SIF due to remote axial stress (Fig. 5.20c, 5.20d and Fig. 5.20e, 5.20f, respectively). Also the relative crack length seems to be not affecting the described trend of the SIFs against the γ. All the numerical SIFs and the interpolation coefficients related to Eq. (5.38) are reported in Table A.4 (see Appendix A).

5.9 Applications

5.9.1 Remote stress causing progressive fibre debonding

In the present Section, a fibre-reinforced composite with aligned fibres under a tensile remote stress acting parallel to the fibres direction is analysed. The fibres are assumed to be non interacting and, therefore, the solution for a single fibre can

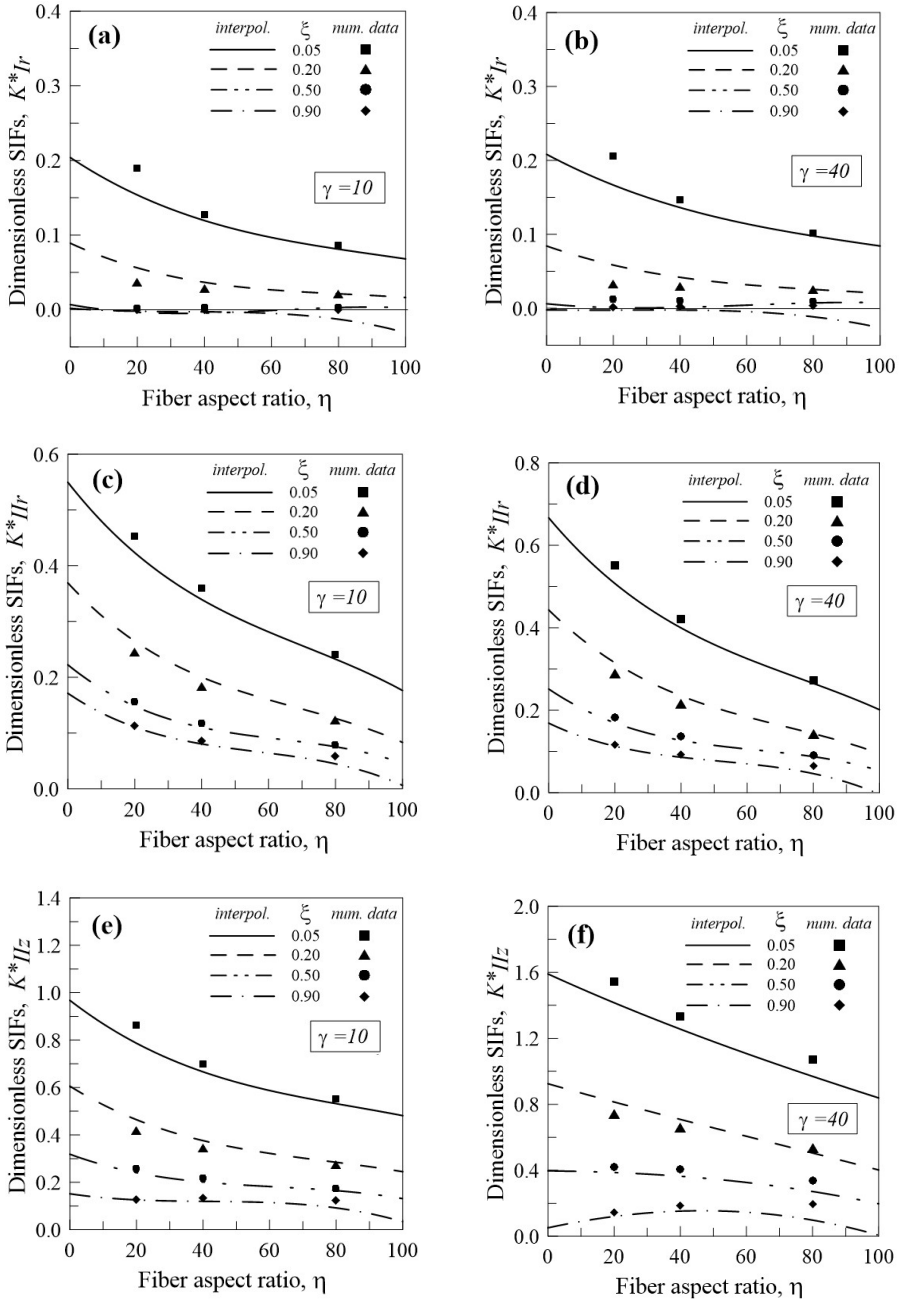

Figure 5.19: Dimensionless (a), (b) Mode I and (c), (d) Mode II SIFs due to a remote uniform radial stress. (e) and (f) Mode II SIF for an remote axial stress against η, for $\gamma = 10,\ 40$ and different values of ξ.

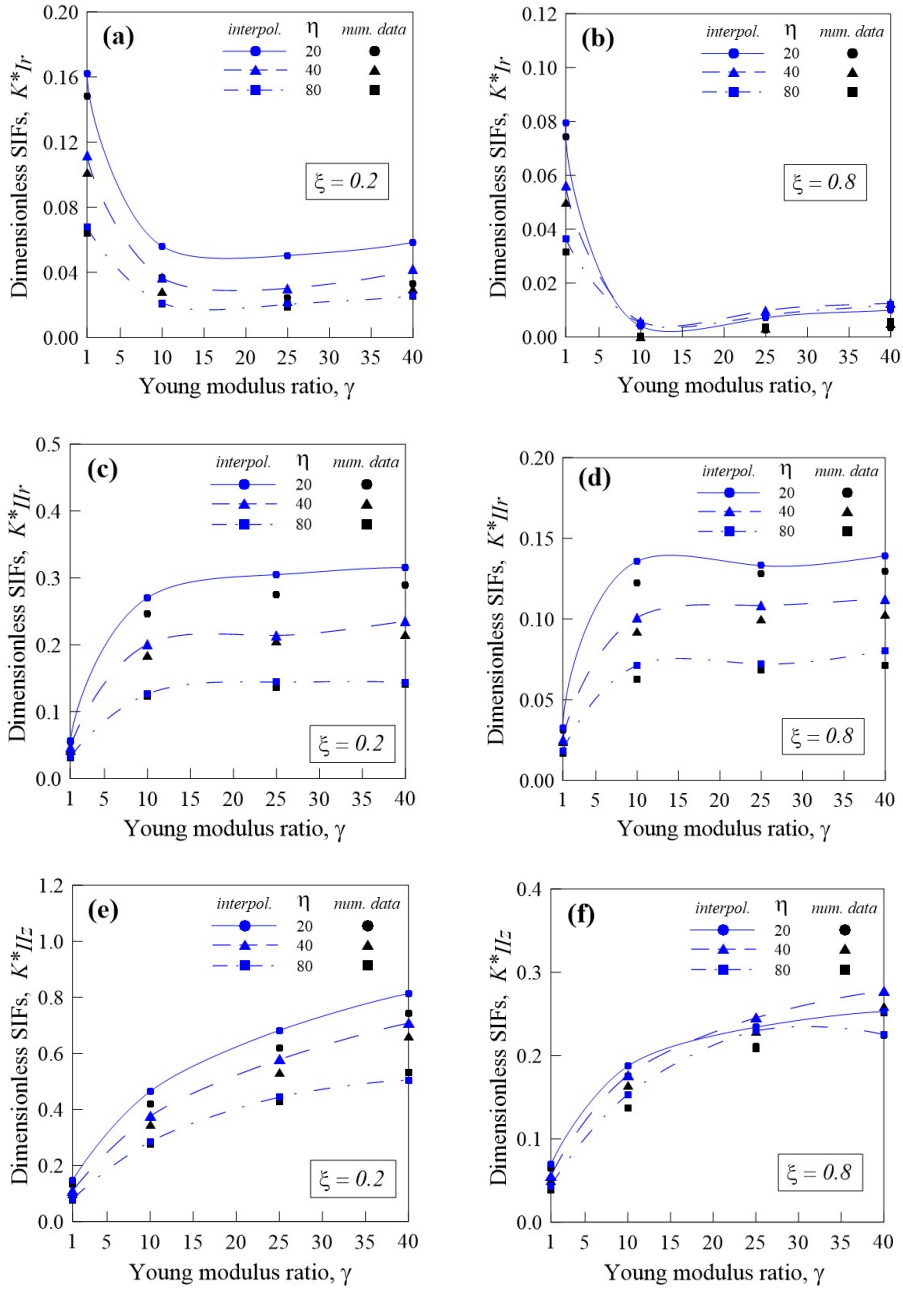

Figure 5.20: Dimensionless (a) and (b) Mode I and (c) and (d) Mode II SIFs due to a remote uniform radial stress. (e) and (f) Mode II SIF for an remote axial stress against γ for $\xi = 0.2$, 0.8 and different values of η.

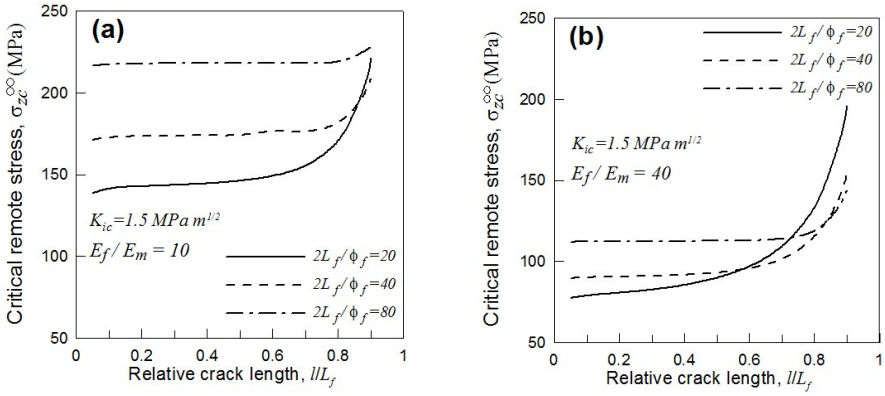

Figure 5.21: Critical remote stress σ_{zc}^{∞} against ξ, for different values of η: (a) $\gamma = 10$ and (b) $\gamma = 40$.

be assumed to be representative of the case being studied. The critical remote stress parallel to the fibres, σ_{zc}^{∞}, that produces a progressive fibre-matrix detachment is herein determined. The stress value to reach the interface fracture toughness K_{ic} for a given debonded length can be evaluated as follows (see Eq. 5.22):

$$\sigma_{zc}^{\infty} = \frac{K_{ic}}{K_2^*(\sigma_{zc}^{\infty}) \cdot \sqrt{\pi l}} \tag{5.39}$$

In Figure 5.21, such a remote critical stress is plotted against the relative crack length, ξ, for different values of η, Young modulus ratios equal to $\gamma = 1$ and $\gamma = 40$, and an interface fracture toughness equal to $K_{ic} = 1.5\, MPa\sqrt{m}$.

As has been remarked above, the critical stress required to obtain a progressive fibre debonding is an increasing function of the detached length. In other words, as the crack propagates, the applied stress must continuously be increased to maintain active the detachment phenomenon. Such a critical stress is almost constant for low values of ξ, whereas it sharply increases for $\xi \to 0.9$ (the last value of the numerical interpolation adopted) when the debonded part of the fibre tends to become almost equal to the whole fibre length. The critical stress is lower for high values of γ since it is inversely proportional to the SIF (see Fig. 5.21). Also the fibre aspect ratio η affects the critical stress: in particular such a stress, for value of the debonded length $\xi \leq 0.7$, is lower for low values of η.

In Figure 5.22a and 5.22b, the remote stress ratio $\sigma_z^{\infty}/\sigma_r^{\infty}$ is represented against the relative debonded length ξ, for a given value of σ_r^{∞}. The curves are deduced

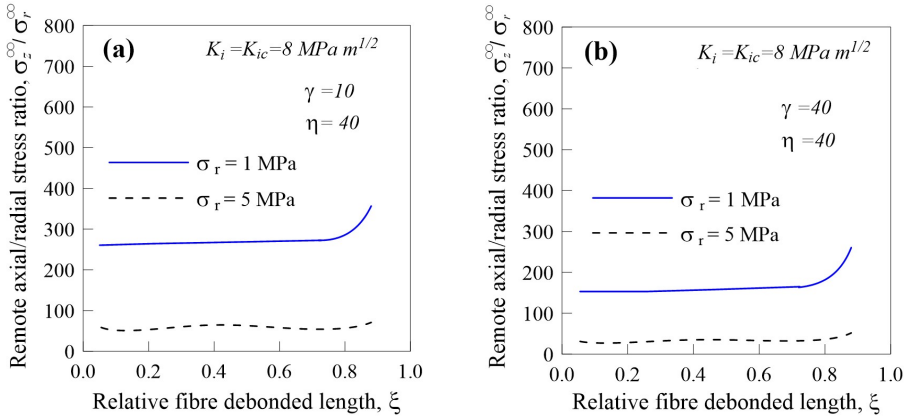

Figure 5.22: Dimensionless remote axial stress $\sigma_z^\infty/\sigma_r^\infty$ against ξ: (a) $\gamma = 10$, (b) $\gamma = 40$.

determining the $\sigma_z^\infty/\sigma_r^\infty$ ratio (by keeping σ_r^∞ constant) for which the critical condition $K_i = K_{ic}$ is attained. In other words, the curves represent the axial stress, for a given fixed radial stress, corresponding to the critical condition for progressive fibre debonding. The curves show an increasing trend by increasing ξ, i.e. the axial stress applied to the composite must continuously be increased in order to grow the detachment length. The above described behaviour is significantly affected by the Young modulus ratio γ: the axial remote stress that allows a debonding growth decreases by increasing the Young modulus ratio γ (see Fig. 5.22a and 5.22b).

5.9.2 Single fibre pull-out test

The developed fracture mechanics approach is here applied to simulate a single-fibre pull-out test for a polytetrafuoloethylene (PTFE) fibres-polypropilene (PP) matrix composite. One single fibre with diameter $\phi_f = 30\,\mu m$ is partially embedded in the matrix for a half of its length, i.e. L_f ($2L_f$ is the total length of the fibre), whereas the detached length is measured through a microscope during the loading process. The diagram of fibre load against detached length has been determined by Wang [245], for different values of the embedded fibre length. The above FRC material is characterized by Young modulus $E_m = 0.72\,GPa$ and Poisson's ratio $\nu_m = 0.3$ for the matrix, and $E_f = 0.9\,GPa$ and $\nu_f = 0.33$ for the reinforcing phase. The interface fracture energy is assumed to be equal to $\mathcal{G}_{ic} = 0.96\,Nm$ (corresponding to interface critical fracture toughness $K_{ic} =$

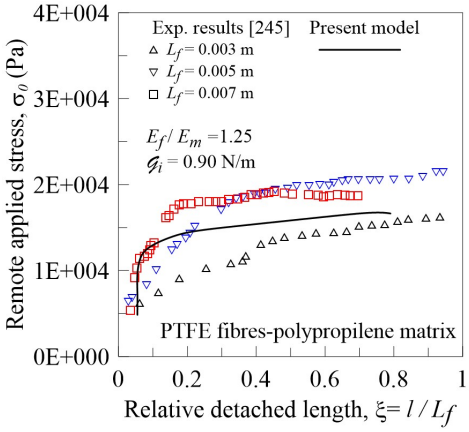

Figure 5.23: Remote matrix stress vs relative fibre debonding: experimental results by Wang [245] and present model results are shown.

$\sqrt{E_i \cdot \mathcal{G}_{ic}} = 29.4\, MPa\sqrt{m}$). The experiments found that the detachment for such a composite starts from the embedded extremity of the fibre [245]. This observation is assumed to be representative of a half fibre in the present numerical model. Further, L_f is herein assumed equal to $12\, mm$ in order to have a fibre geometrical ratio η within the range of the available SIFs [246]. Such an assumption is irrespective of the fibre geometrical ratio used in the experiments, since this parameter does not heavily influence the results of the model.

The experimental data and the present model results are compared in Figure 5.23. As can be observed, different values of embedded fibre length give slightly different curves, and the results obtained from the proposed numerical approach are in a satisfactory agreement with the experimental data. In particular, the remote applied stress significantly increases for small debonded values (i.e. for small values of ξ), while it remains almost constant for higher detached lengths.

5.10 Fatigue effects on the interface fibre-matrix detachment

As is well-known, the cyclic loading reduces the mechanical properties of materials due to the irreversible rearrangement of the lattice structure at the microscopic level. In composite materials the repeated loads are responsible of

the decreasing mechanical properties of the matrix and of the reduction of the of the fibre-matrix bond effectiveness. The progressive fibre-matrix debonding can be quantified through exponential fatigue propagation laws, applied to the crack representing the discontinuity at the detached extremities of the fibres.

The crack propagation assessment can be estimated through the debonding length rate, v_{cg}, law, or crack growth velocity quantified with respect to the number of loading cycles, defined by the classical Paris law:

$$v_{cg} = dl/dN = C_i \cdot \Delta K_i^{m_i}, \qquad \Delta K_{th} < \Delta K_i \leq K_{ic} \tag{5.40}$$

where C_i, m_i are the Paris constants of the interface, l is the debonded length and ΔK_i is the equivalent stress intensity factor range produced by the cyclic remote stresses. For the sake of simplicity, the far field cyclic stressed is assumed to vary with a constant amplitude. The cycles are assumed to be in phase in order to be able to define an equivalent SIF range. The above relationship can be used to determine the critical detached length against the number of loading cycles N_c necessary to get such a critical condition under repeated loading:

$$l(N_c) = l_c = \int_0^{N_c} C_i \cdot \Delta K_i^{m_i} dN, \quad \text{such that} \quad \Delta K_i(l_c, \sigma_z^\infty, \sigma_r^\infty) = K_{ic} \tag{5.41a}$$

$$D_i(N) = l(N)/l_c \geq 0 \tag{5.41b}$$

where the interface equivalent SIF (see Eq. (5.22)), $\Delta K_i(l_c, \sigma_z^\infty, \sigma_r^\infty)$, depends on the remote stress field and on the current debonded length for the given composite material. Once the critical detached length is known, also the sliding function parameter $s\left(\overline{\varepsilon_f^m}\right)$ can be evaluated, and consequently the equivalent tangent elastic tensor $\boldsymbol{C}'_{eq}$ of the homogenized material can be obtained through Eq. (3.25) of Chapter 3. According to the above relationship, a debonding-related damage D_i (Eq. (5.41b)) can be also defined as the ratio between the current debonded length and the critical length. The debonded critical length l_c corresponds to the condition of unstable crack propagation, i.e. the condition of complete fibre detachment from the matrix material and complete damage, i.e. $D_i(N_c) = 1$. On the other hand, as shown in the previous sections, $K_i(l_c, \sigma_z^\infty, \sigma_r^\infty)$ is a decreasing function of l: therefore the SIF decreases as the detached length increases, implying that the critical condition (Eq. (5.41a)) cannot be reached during the crack propagation.

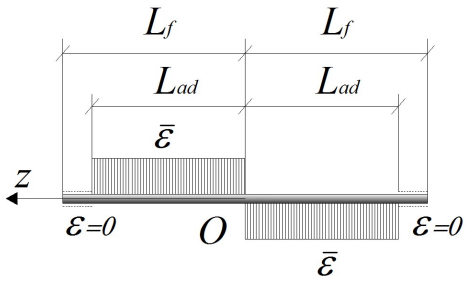

Figure 5.24: Qualitative approximation of sliding function s.

The debonding-related damage D_i can more conveniently be defined in this case as follows:

$$0 \leq D_i = l/L_f \leq 1 \tag{5.42}$$

Such a degrading parameter refers to the interface region, and quantitatively describes the effectiveness of the fibre in the bearing mechanism of the composite material.

Since the detachment phenomenon could synthetically be quantified through the sliding function $s(\overline{\varepsilon_f^m})$ (see Chap. 3), the interface damage can thus be quantified as $D_i = 1 - s(\overline{\varepsilon_f^m})$.

By considering the average matrix strain $\overline{\varepsilon_f^m} = (2L_{ad}\bar{\varepsilon})/(2L_f)$ along the fibre length (Fig. 5.24) and by remembering that $s(\varepsilon_f^m) = \varepsilon_f/\varepsilon_f^m$, an approximation of the scalar function can be written as follows:

$$s(\overline{\varepsilon_f^m}) \simeq \frac{L_{ad}}{L_f} = \frac{L_f - l}{L_f} = 1 - D_i = 1 - \xi, \quad \text{or} \quad D_i = \xi \tag{5.43}$$

5.11 Conclusions

As far as the computational model proposed in the present Chapter is concerned, some observations can be made:

- A computational model based on the Linear Elastic Fracture Mechanics (LEFM) concepts is herein proposed to describe the fibre-matrix phenomenon. Such a model is then correlated with the classical "Shear Lag" model;
- An initial detachment, quantified as a percentage of the fibre length, is considered at the fibre extremities;
- The progressive debonding, treated as the propagation of a three-dimensional cylindrical crack between two different linear elastic materials, is quantified through the sliding function determined by means of suitable equivalent SIFs obtained from FE simulations;
- The proposed approach, based on the LEFM, and the classical Shear Lag model are correlated and, through a simple mechanical model of the fibre-matrix interface layer, the interface critical parameters, such as the interface fracture toughness and interface fracture energy, are determined;
- The progressive debonding due to the action of cyclic loads is quantified through a fatigue power law by applying the calculated SIFs;
- The developed approach is applicable for both static and cyclic loading conditions.

Chapter 6

Computational Implementation and Numerical Applications

6.1 Introduction

The mechanical model, described in the previous Chapters, has been implemented in a non-linear 2-D FE code enabling the study of real structures. Some relevant examples are presented in this Chapter, in order to assess its capability to predict mechanical behaviour of FRC materials subjected to fracture process and/or fatigue loadings. In the following, the main features of the developed software, written in standard FORTAN77 language, are outlined and finally some numerical applications are shown.

6.2 Computational program

6.2.1 Main program

The developed FE software is characterised by the following 2D finite elements: three-node straight-side triangle, four-node straight-side quadrilateral and eight- and nine-node curved-side quadrilateral. Moreover, lumped nodal force vectors and

lumped mass matrix have been implemented for the sake of simplicity, whereas the well-known Lagrange multiplier approach has been adopted for the fulfilment of the essential boundary conditions. Finally, the stress and strain recovery in finite elements has been obtained from the corresponding values evaluated at the Gauss points and subsequently extrapolated at nodes. A non-linear iterative procedure, based on the convergence check of the displacements, unbalanced forces, stresses, energy and fracture, has been implemented.

A flow-chart of the developed program is illustrated in Figure 6.1.

The developed code has been conceived to solve both static and cyclic problems. In the case of time-dependent analyses, the well-known Newmark integration scheme in the time domain has been adopted. According to such finite-difference based methods, the fundamental relationships can be written as follows:

$$\begin{aligned} \boldsymbol{\delta}_{n+1} &= \boldsymbol{\delta}_n + dt \cdot \dot{\boldsymbol{\delta}}_n + dt^2 \cdot \left[\left(\frac{1}{2} - \beta \right) \ddot{\boldsymbol{\delta}}_n + \beta \cdot \ddot{\boldsymbol{\delta}}_{n+1} \right] \\ \dot{\boldsymbol{\delta}}_{n+1} &= \dot{\boldsymbol{\delta}}_n + dt \cdot \left[(1-\gamma) \ddot{\boldsymbol{\delta}}_n + \gamma \cdot \ddot{\boldsymbol{\delta}}_{n+1} \right] \end{aligned} \tag{6.1}$$

where $\boldsymbol{\delta}$ is the displacement vector, $\dot{\boldsymbol{\delta}}$ is the first order time-derivative of the displacement vector, and $\ddot{\boldsymbol{\delta}}$ is the second order time-derivative of the displacement vector. Values of the two parameters β and γ can be chosen in order to define the specific method used. For instance, the assumption $\beta = 1/4$ and $\gamma = 1/2$ (as taken into account in the program) leads to the average acceleration method or trapezoidal rule (also known as Crank-Nicolson method), that represents an implicit, unconditionally stable scheme for linear analyses without numerical dissipation (by assuming $\gamma = 0$, the method becomes explicit). After substituting the above expressions in the dynamic equilibrium equations,

$$\boldsymbol{M} \cdot \ddot{\boldsymbol{\delta}}(t) + \boldsymbol{D} \cdot \dot{\boldsymbol{\delta}}(t) + \boldsymbol{F}_{int}(t) = \boldsymbol{F}_{ext}(t) \tag{6.2}$$

written at the time instant $t_{n+1} = t_0 + (n+1)\Delta t$ (where Δt is the time step), the following system of equations can be written:

$$\boldsymbol{K}_{eff} \cdot \boldsymbol{\delta}_{n+1} = \boldsymbol{F}_{eff,\, n+1} \tag{6.3}$$

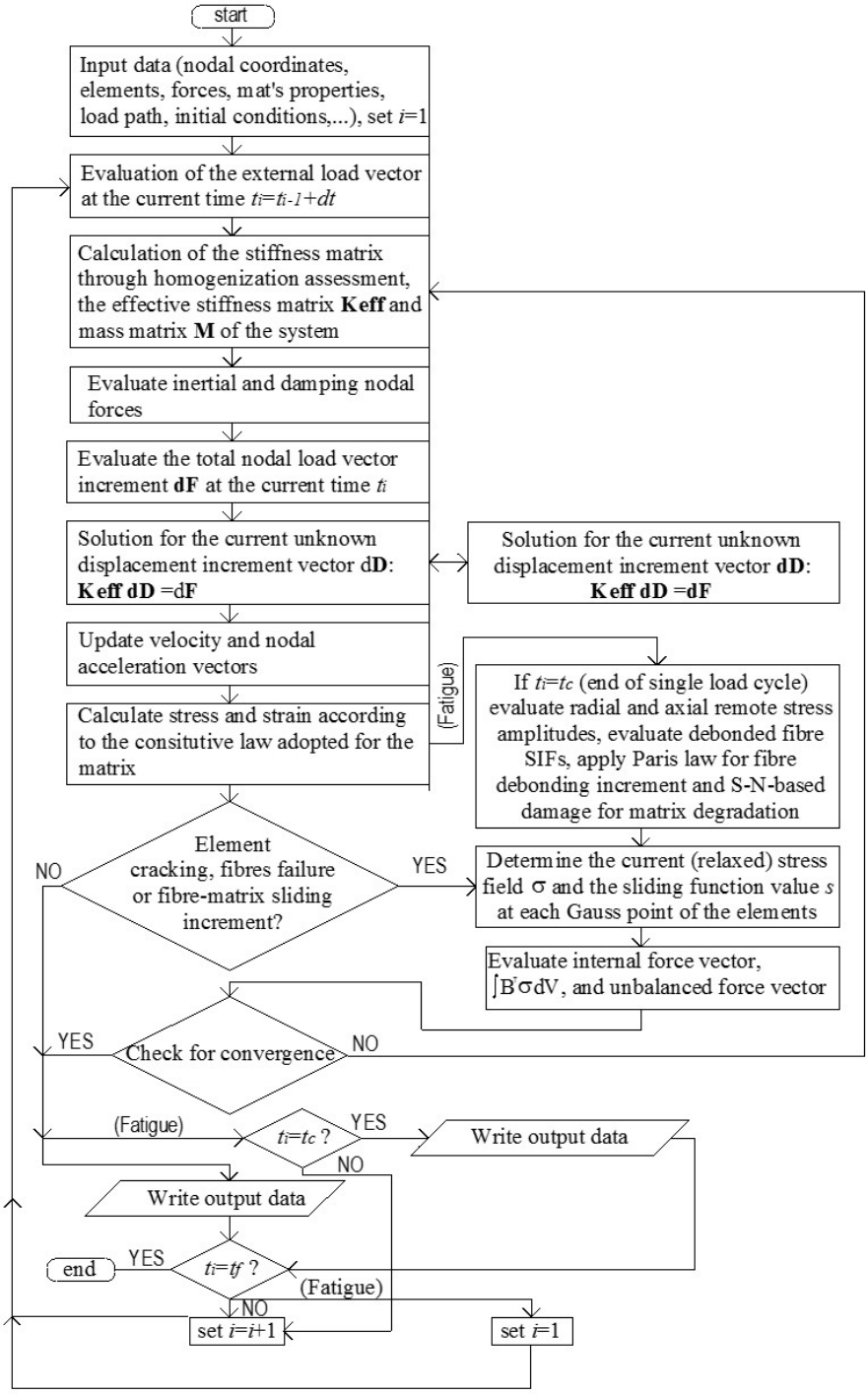

Figure 6.1: Flow-chart of the computational program.

where

$$\begin{aligned} \boldsymbol{K}_{eff} &= \frac{4}{\Delta t^2}\boldsymbol{M} + \frac{2}{\Delta t}\boldsymbol{D} + \boldsymbol{K} \\ \boldsymbol{F}_{eff,\, n+1} &= \boldsymbol{F}_{ext,\, n+1} + \boldsymbol{M}\Big[\frac{4}{\Delta t^2}\cdot\boldsymbol{\delta}_n + \frac{4}{\Delta t}\cdot\dot{\boldsymbol{\delta}}_n + \ddot{\boldsymbol{\delta}}_n\Big] + \boldsymbol{D}\Big[\frac{2}{\Delta t}\cdot\boldsymbol{\delta}_n + \dot{\boldsymbol{\delta}}_n\Big] \end{aligned} \tag{6.4}$$

Equation (6.4) is written by considering the internal forces to be expressed as a simple linear constitutive law: $\boldsymbol{F}_{int,\, n+1} = \boldsymbol{K}\cdot\boldsymbol{\delta}_{n+1}$. In the case of non-linear stress-strain relationships the internal force vector at the current time step, $\boldsymbol{F}_{int,\, n+1}$, must be evaluated after calculating the actual stress state $\boldsymbol{\sigma}$ (determined according to the current mechanical behaviour of the matrix material, such as elastic-plastic or brittle) in the finite elements:

$$\boldsymbol{F}_{int\, n+1} = \mathsf{A}_{i=1}^{n} \int_{V_{e,i}} \boldsymbol{B}^T \boldsymbol{\sigma} dV_e \tag{6.5}$$

where A is the assembling operator, $\boldsymbol{B}$ is the compatibility matrix. The case of static analyses is solved through the same algorithm by adopting a very slow variation of the external applied loads, $\boldsymbol{F}_{ext}(t)$, from the initial value up to the final one.

The developed software allows the treatment of different mechanical behaviours of the material: in particular, an elastic-plastic constitutive model for ductile materials and a discontinuous-like behaviour for fracture simulation of brittle materials are implemented.

The elastic-plastic constitutive relationship is suitable in describing mechanical behaviour of the material when an irreversible plastic flow takes place beyond the elastic limit, corresponding to a re-arrangement of its lattice structure. A detailed description of the elastic-plastic model adopted is reported in Section 4.3 of Chapter 4.

In the developed computer program, four yielding criteria have been implemented, namely the Tresca, the Von Mises, the Mohr-Coulumb and the Drucker-Prager Criterion. The mechanical parameters required by each criterion are listed in Table 6.1.

In the present FE implementation, the yielding functions are assumed to depend on a single yielding parameter k that corresponds to the uniaxial yield stress σ_{y0} of the material: $F(\sigma, k) = F(\sigma, \sigma_{y0}) = 0$. The evolution of the yielding parameter

Table 6.1: Yield criteria implemented in the FE software: definition of the yield surface $\mathcal{F}(\dots) = 0$ and the required materials parameters for its definition.

Yield Criterion	**Yield Function,** $F(\sigma_{ij}) = \mathcal{F}(\sigma_{ij}) - k(\kappa) = 0$	**Parameters in the case of uniaxial stress state**
Tresca	$\mathcal{F} = \tau_{max} = max\Big(\frac{1}{2}\lvert\sigma_1 - \sigma_2\rvert, \frac{1}{2}\lvert\sigma_2 - \sigma_3\rvert, \frac{1}{2}\lvert\sigma_3 - \sigma_1\rvert\Big) = k$ σ_1, σ_2, σ_3: principal stresses	$k = \sigma_{y0}/2 = \tau_{y0}$ τ_{y0}: yielding shear stress
Mises	$\mathcal{F}(J_2) = J_2 = k^2$ J_2: second deviatoric stress invariant	$k = \sigma_{y0}/\sqrt{3} = \tau_{y0}$ τ_{y0}: yielding shear stress
Mohr Coulomb	$\mathcal{F} = \lvert\tau\rvert = c - \sigma \cdot \tan\phi$ ($\sigma > 0$ traz.) c, ϕ: cohesion and internal friction angle of the material	$\sigma_{yt} = \frac{2c\cos\phi}{1+\sin\phi}$, $\sigma_{yc} = \frac{2c\cos\phi}{1-\sin\phi}$ σ_{yt}, σ_{yc}: yielding stresses under tension and compression
Drucker Prager	$\mathcal{F}(I_1, J_2) = \alpha \cdot I_1 + \sqrt{J_2} - k = 0$ I_1: first stress tensor invariant J_2: second deviatoric stress invariant k, α: material parameters	$\sigma_{yt} = \frac{\sqrt{3}k}{1+\sqrt{3}\alpha}$, $\sigma_{yc} = \frac{\sqrt{3}k}{1-\sqrt{3}\alpha}$ σ_{yt}, σ_{yc}: yielding stresses under tension and compression

k is described by the following simple linear law: $\sigma_{y0} = \sigma_y + H \cdot \dot{\varepsilon}^{pl}$, where H is the hardening parameter.

The non-linear behaviour of brittle-like materials is simulated through the fracture mechanics approach whose theoretical formulation and computational algorithm are described in Chapter 4 (see Sect. 4.2 and Sect. 4.4).

6.2.2 Implementation of the fracture mechanics approach to fiber-matrix detachment

The non-linear mechanical problem arising from the mesomechanical model, described in Chapter 5, has been implemented in the above FE model. The computational implementation can briefly be described by underlying its main steps as follows:

1. For a given level of applied loads, the stress field is firstly determined through a linear incremental analysis: the stress components at the Gauss point of

interest are used to determine the remote radial and axial stresses, σ_r^∞ and σ_z^∞. As matter of fact, by assuming a small fibre content, the local stress field is supposed to represent the remote one, i.e. the local stress field is considered to be not influenced by the other fibres around the point of interest (the so-called dilute hypothesis is made), and is used to quantitatively assess the fibre-matrix detachment.

2. In FRC materials with randomly arranged fibres, the axial (σ_z^∞) and radial (σ_r^∞) stresses in the REV can be assumed to be equal to the mean stress at the point examined, i.e. $\sigma_r^\infty = \sigma_z^\infty = \sigma_{ii}/3$. In unidirectional reinforced composites, they can be obtained as follows:

$$\sigma_z^\infty = (\boldsymbol{k} \otimes \boldsymbol{k}) : \boldsymbol{\sigma}, \qquad \sigma_r^\infty = \sigma_{t,ii}/2 \tag{6.6}$$

where $\sigma_{t,ii}$ represent the normal stress tensor components acting in a plane normal to the fibre axis.

3. Once the remote stresses are known, the interface SIF K_i at the fibre debonded edge can be assessed for the current debonded length, by using Eq. (5.22) in Chapter 5, once the relationships $K_I(\sigma_r^\infty)$, $K_{II}(\sigma_r^\infty)$ and $K_{II}(\sigma_z^\infty)$, obtained through the analytical interpolation described in Sections 5.8, are available.

4. By comparing this interface SIF with the interface fracture toughness K_{ic}, that can be expressed through the interface critical energy $\mathcal{G}_{ic}$, the occurrence of crack growth can be evaluated.

5. If this is the case (crack growing), the crack is extended for a small amount, and the interface SIF is recalculated up to the fulfilment of the incipient condition of crack propagation, i.e. $K(\xi) = K_{ic}$. Since $K(\xi)$ is a decreasing function of ξ for a given remote stress, a proper extension of the fibre detached length satisfies such a condition of incipient crack propagation, i.e. the crack stays.

6. After obtaining the current value of the mean debonded fibre length l (referred to the fibres in the region around the Gauss point under consideration) in correspondence of the condition of incipient crack propagation, $K(l = \xi \cdot L_f) = K_{ic}$, the sliding function s is determined by assuming a shear stress distribution equal to that shown in Figure 3.8 of Chapter 3. Once

the effective bonded length $L_{ad} = L_f - l$ and the fibre-matrix interface shear stress distribution $\tau_f(x)$ are known, the energy balance $W_f \cong \overline{W}_f$ can be written, and the averaged value of the sliding function, $s(\overline{\varepsilon_m^f})$, can finally be computed through Eq. (3.39) in Chapter 3. This scalar parameter represents an internal damage-related quantity, $d = 1 - s(\overline{\varepsilon_m^f})$, where d is the local value of the damage associated to fibre debonding. A strain-based progressive damage model for an anisotropic material can be derived from a thermodynamic potential such as the free-energy potential:

$$\Phi := \frac{1}{2}\boldsymbol{\varepsilon} : \boldsymbol{C}'(d) : \boldsymbol{\varepsilon} - \Gamma \tag{6.7}$$

where $\boldsymbol{C}'(d)$ is a fourth-order damaged tangent stiffness tensor, (it accounts for the degradation of stiffness components due to damage internal variables), whereas Γ is the dissipation potential associated to plastic deformation and hardening. Such a dissipation can be discarded in case of non-ductile matrix composites. The tangent stiffness tensor can finally be computed as follows:

$$\boldsymbol{C}'(d) = 2\frac{\partial \Phi}{\partial \boldsymbol{\varepsilon} \otimes \boldsymbol{\varepsilon}} \tag{6.8}$$

7. In the case of fibre-reinforced composites, the homogenized tangent stiffness tensor $\boldsymbol{C}'_h$ at the Gauss point GP in the $i-th$ finite element, corresponding to $\boldsymbol{C}'(d)$ in Eq. (6.8), is determined through the homogenization integral described by Eq. (3.25) in Chapter 3.

8. The convergence of the calculation at the current load step is checked in terms of incremental displacement norm and incremental unbalanced forces.

9. If the required tolerances are satisfied:

   - the calculation can proceed to the further load step, otherwise
   - the problem is solved again for the current applied load level but with a new stiffness matrix, evaluated at the actual load step j, determined by using an updated tangent elastic tensor $\boldsymbol{C}_h'^{(j)}$ for each Gauss point of the FE discretizion, i.e.

$$\boldsymbol{K}'^{(j)} = \mathsf{A}_{i=1}^{ne} \int_{V_{e,i}} \boldsymbol{B}^T \cdot \boldsymbol{C}_h'^{(j)} \cdot \boldsymbol{B} dV \tag{6.9}$$

10. The above calculations are repeated starting from step No. 2, up to the fulfilment of the convergence requirements before moving to the next load step.

As can be deduced, the equilibrium takes place at the state of incipient crack debonding propagation, i.e. the fibres are assumed to be equally detached in a given small region represented by the single Gauss point. The mechanical model does not physically take into account the presence of fibres, but it considers the reinforcing phase through its mechanical effects on the plain material by the homogenization procedure for the evaluation of the composite tangent stiffness tensor $\boldsymbol{C}'_h$.

6.2.3 Fatigue simulation

For the sake of computational applicability of the model, the remotely applied cyclic stresses σ_z^∞ and σ_r^∞ (evaluated at the Gauss point) are needed for the assessment of the fibre-matrix degradation during fatigue. The remote stress field must be decomposed as is shown in Eq. (6.6) in Section 6.2.2.

The fatigue effects on the matrix material are taken into account by means of Wöler's curves as is described in Sec. 4.5 (Chapter 4): the total number of load cycles N acting on the material is considered applied in N_{blocks} blocks with N_{cycles} cycles for each block (Fig. 6.2), i.e. $N = N_{blocks} \cdot N_{cycles}$. The damage fatigue algorithm is applied at the first cycle of every block, and the damaged mechanical characteristics (determined using the total number of load cycles that have already acted on the structure) are kept constant through the block without any further changing till a new block is examined.

The theoretical formulation related to the progressive fibre-matrix detachment produced by the cyclic loads is shown is Sect. 5.10 (Chapter 5). The interface SIF range evaluated through the stresses in Eqs. (6.6) is computed.

For numerical purposes, the fibre detachment increment during fatigue loads is assessed by subdividing the whole stress history in N_{blocks} blocks, and by applying the fatigue growth equation (Eq. (5.40), Chapter 5) after N_{cycles} of each fatigue block (Fig. 6.2).

Once the current debonded fibre length $l(N)$ (Eq. (5.41), Chapter 5) is known, the sliding function parameter $s(\varepsilon_f^m)$ can be evaluated (see Chapter 3) and, conse-

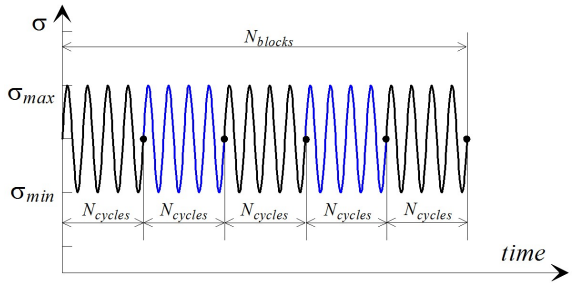

Figure 6.2: Constant amplitude stress cycles subdivided in N_{blocks} with N_{cycles} for each block.

quently, the equivalent tangent elastic tensor $\boldsymbol{C}'_{eq}$ of the homogenized material is updated through Eq. (3.25) (Chapter 3).

6.2.4 Convergence criteria

The FE numerical solution of the problem is determined iteratively, and such a process ends when a convergence criterion is fulfilled. The criteria that may be adopted in the present code (stress and crack opening displacement convergence checks are adopted only for fracture problems) are:

Displacement Convergence Criteria

Being $\boldsymbol{\delta}$ the displacement vector and $\delta\boldsymbol{\delta}$ its increment the norms of both $\boldsymbol{\delta}$ and $\delta\boldsymbol{\delta}$ vectors, are calculated at every load step and iteration i. The convergence criterion is fulfilled if the following inequality is satisfied:

$$e_{displ} = \frac{||\delta\boldsymbol{\delta}||_2}{||\boldsymbol{\delta}||_2} \leq t_d \tag{6.10}$$

where e_{displ} is the error measured in the displacement evaluation, and t_d is the setted tolerance.

Total Unbalanced Nodal Forces Convergence Criteria

At every load step and iteration i, the convergence is verified if

$$e_f = \frac{||\delta\boldsymbol{f}_i||_1 - ||\delta\boldsymbol{f}_{i-1}||_1}{||\delta\boldsymbol{f}_i||_1} \leq t_f \tag{6.11}$$

where e_f is the error related to the unbalanced force vector, $||\boldsymbol{\delta f}_i||_1$ and $||\boldsymbol{\delta f}_{i-1}||_1$ are the norms of the total unbalanced nodal forces vector at $i-th$ and $(i-1)-th$ iterations, respectively, and t_d is the adopted tolerance.

Single Unbalanced Nodal Forces Convergence Criteria

At every load step and iteration i, the following ratio is computed:

$$e_f = max_{k=1,n_{nod}\cdot n_{dof}} \left| \frac{\delta f_i^k}{load_i^k + reaz_i^k} \right| \tag{6.12}$$

where e_f is the error related to the single unbalanced force vector term, δf_i^k is the $k-th$ component of the unbalanced nodal force vector, $load_i^k$ and $reaz_i^k$ are the $k-th$ components of load and reaction force vectors at the $i-th$ iteration, respectively. The convergence is fulfilled if $e_f \leq t_{f_1}$, where t_{f_1} is the assumed tolerance.

Energetic Convergence Criteria

At every load step and iteration i, the elastic energy due to the displacement increment $\delta\boldsymbol{\delta}$ is calculated:

$$e_{En} = \frac{\frac{1}{2}\delta\boldsymbol{\delta}^t \cdot \boldsymbol{K}\delta\boldsymbol{\delta}}{E_{tot}} \tag{6.13}$$

In the above expression, e_{En} is the error related to the elastic energy, E_{tot} is the total elastic energy. The convergence is fulfilled if $e_{En} \leq t_{En}$, where t_{En} is the adopted tolerance.

Stress Convergence Criteria

At every load step, every iteration i and for each cracked element k, the convergence criteria can be written as follows:

$$e_{str} = max_{k=1,n_{elem}} \left| \frac{\sigma_{real} - \sigma_w}{f_t} \right|_{i,k} \leq t_\sigma \tag{6.14}$$

where σ_{real} is the real stress, σ_w is the cohesive stress transferred between the crack faces, f_t is the fracture strength, and t_σ is the assumed tolerance.

Crack opening displacement Convergence Criteria

At every load step, every iteration i and for each cracked element k, the convergence criteria can be written as follows:

$$e_{open} = max_{k=1,n_{elem}} \left| \frac{dw_c}{w_c} \right|_{i,k} \leq t_w \tag{6.15}$$

where w_c is the total opening displacement, dw_c is the corresponding increment at a given iteration and load step and t_w is the setted tolerance.

6.3 Static load examples

In the present Section, some simple examples related to loading condition not involving fatigue effects are analysed. All the analyses for brittle matrix materials are conducted by assuming the fracture process governed by the exponent n equal to 6 for shear stress decreasing rate control (see Eq. (4.24) Chapt. 4).

The tolerances used to check the convergence of the non-linear iterative solution process are assumed to be equal to $2 \cdot 10^{-4}$ for both the incremental displacement norm and incremental nodal residual force vector norm, whereas the incremental tolerance used to check the crack opening and sliding is assumed to be equal to 10^{-3}. The non-linear numerical examples presented below are performed under *displacement control*, in order to be able to follow the softening branch of the load-displacement curves.

6.3.1 FRC square plate subjected to simple tension

The tensile behaviour of a brittle matrix FRC square plate, having sizes equal to $1.0 \times 1.0 \times 0.1$(thickness)m, subjected to an upward displacement applied to the top edge, is examined by assuming a plane stress condition (Fig. 6.3).

The mechanical constants of the matrix material are assumed as follows: Young modulus $E_m = 20GPa$, Poisson's ratio equal to $\nu_m = 0.15$, ultimate tensile strength equal to $f_t = 2.8MPa$, unit surface fracture energy equal to $\mathcal{G}_f = 50N/m$. A steel reinforcing phase, constituted by fibres with length $2L_f = 24mm$, diameter $\phi_f = 0.5mm$, elastic modulus $E_f = 200MPa$, tension strength $f_{t,f} = 300MPa$, respectively, and a volume fraction ratio equal to $\mu_f = V_f/V = 2\%$, is assumed in the composite. Different preferential fibre orientations are examined as well as the

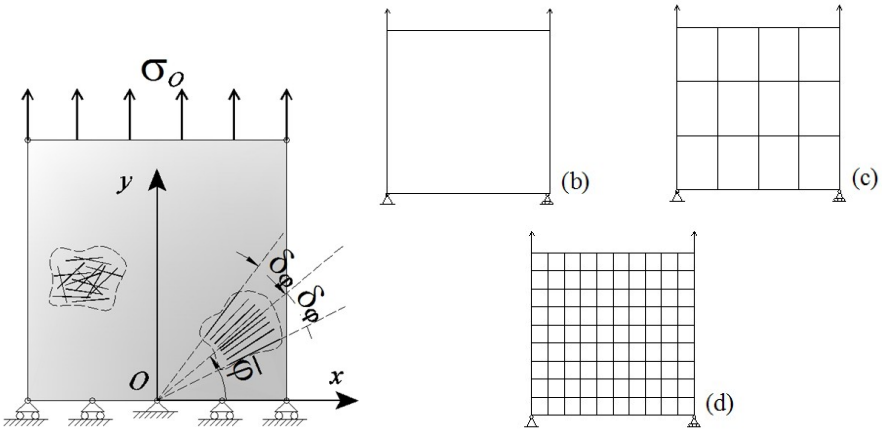

Figure 6.3: Square FRC plate under upward top edge displacement: (a) geometry and (b) meshes adopted.

random arrangement. In order to force the crack to appear in the centre of the plate, the finite elements lying on the horizontal central row of the mesh allow the fracture occurrence while fracture is not permitted for the remaining elements.

In Figure 6.4a, the vertical load against the increasing upward vertical displacement Δ of the top edge of the unreinforced plate ($\mu_f = 0\%$) is represented for different FE discretisations. As can be observed, the peak load corresponding to the crack appearance is well-represented independent of the assumed discretisation, and a steep softening branch occurs after such a peak, up to the achievement of very low values of the load corresponding to higher displacement due to the cohesive law adopted (Eq. (4.23)) governed by $\mathcal{G}_f$.

In Figure 6.4b the vertical load against the top displacement Δ for a fibre-reinforced material (for which the angle variance δ_φ is assumed to be equal to 1°) is represented for different fibre orientations and FE discretisations. As can be noted, the case $\overline{\varphi} = 0°$ corresponds to the unreinforced case (Fig. 6.4a), i.e. without significant effect of the fibres. A different behaviour arises for other orientation angles: after the peak load, a sudden decrease of the applied load can be appreciated due to the matrix fracture and, due to the bonding fibres, the load continues to increase after such a condition.

The crack patterns and the deformed meshes at the end of the loading process ($\Delta = 10^{-3}m$) are represented in Figure 6.5. As can be noted, the above described

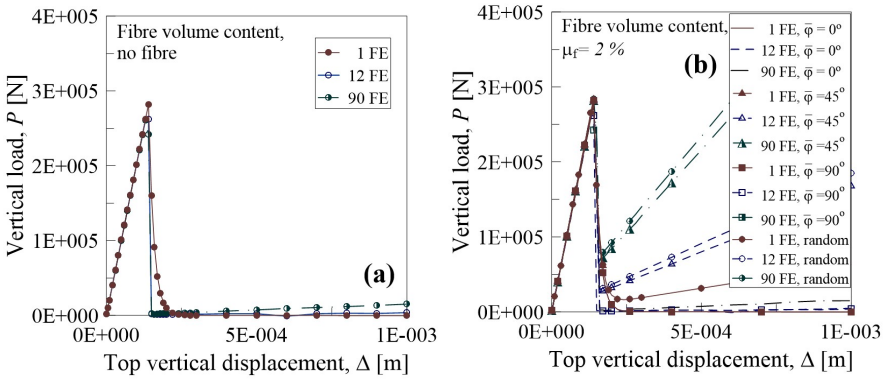

Figure 6.4: Load-displacement curves for the tensioned plate of Figure 6.3 for different FE discretisations: (a) unreinforced material and (b) fibre-reinforced material with different fibres orientations.

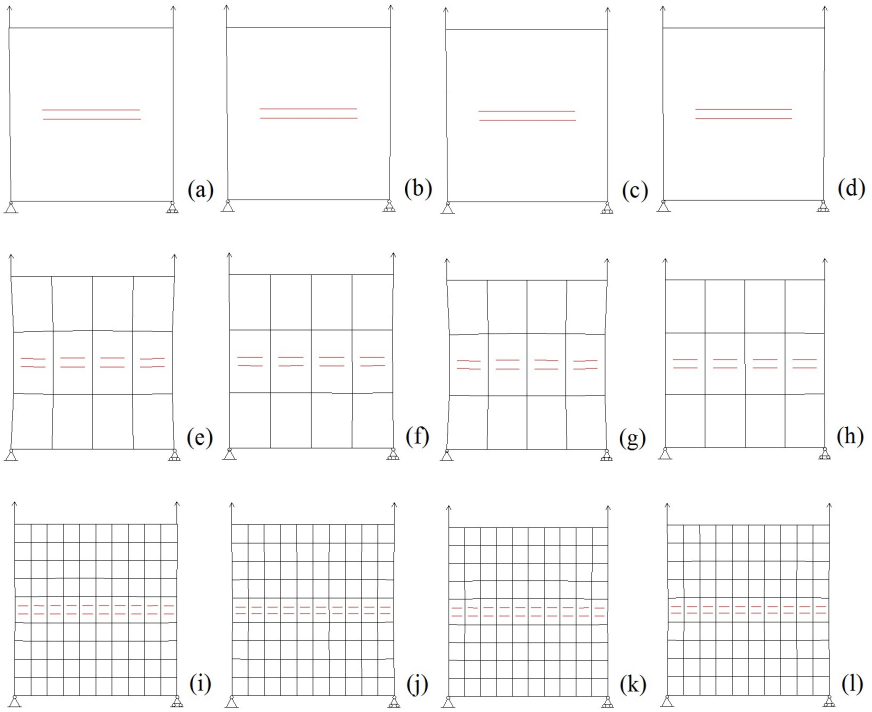

Figure 6.5: Deformed meshes (1FE mesh, first row; 12FE mesh, second row; 90FE mesh, third row). Developed crack pattern at the end of the loading process: (a, e, i) unreinforced material and fibre-reinforced material with (b, f, j) $\overline{\varphi} = \pi/4$, (c, g, k) $\overline{\varphi} = \pi/2$, and (d, h, l) random arrangement.

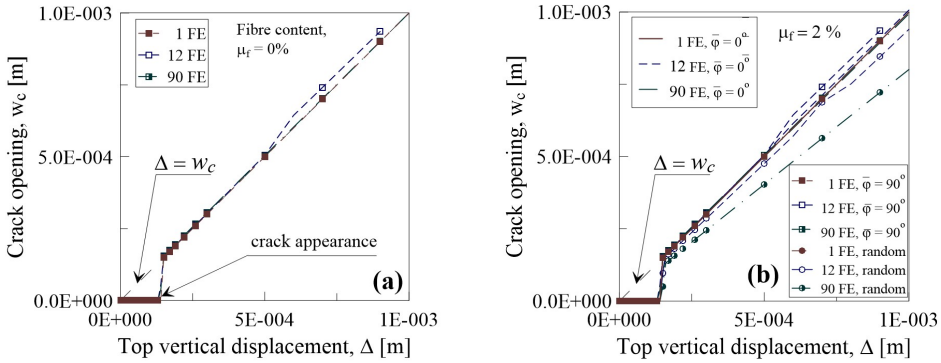

Figure 6.6: Crack opening vs plate top vertical displacement for different FE discretisations (see Fig. 6.5): (a) unreinforced material and (b) fibre-reinforced materials with different fibres orientations.

behaviour is almost independent of the adopted FE discretisation.

Finally, the crack opening w_c in the central finite element of the discretized plate is represented in Figure 6.6a against the top vertical displacement Δ. Up to the crack appearance, the crack opening displacement w_c remains equal to zero and, once the crack appears, such a quantity quickly becomes equal to the vertical displacement Δ for all the FE discretisations, i.e. the plate after cracking behaves as a couple of two independent rigid bodies. In Figure 6.6b, the same graph is provided for the fibre-reinforced case.

6.3.2 Single-edge notched specimen under tension loading

The following example analyses the tensile behaviour of a notched rectangular plate characterised by a polypropylene matrix with randomly distributed glass fibres [247]. The geometrical characteristics of the specimen as well as the FE discretisation are illustrated in Figure 6.7a. The polypropylene matrix material, assumed to be in plane stress condition, has the following mechanical properties: Young modulus $E_m = 2.0GPa$, Poisson's ratio equal to $\nu = 0.3$, ultimate tensile strength equal to $f_t = 120MPa$, unit surface fracture energy equal to $\mathcal{G}_f = 700N/m$; the glass reinforcing fibres are characterised by length $2L_f = 50mm$, diameter $\phi_f = 23.5\mu m$, elastic modulus $E_f = 72.3GPa$, tensile strength $f_{t,f} = 345MPa$ and by volume fraction ratio equal to $\mu_f = 19\%$. The fibres are supposed to be randomly oriented and homogeneously distributed in the matrix.

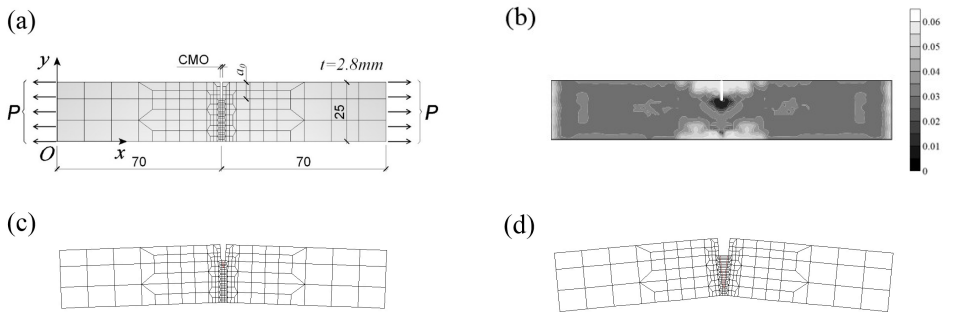

Figure 6.7: Single-edge notched specimen under tension loading and FE discretisation: (a) geometrical dimensions (in mm); (c) crack patterns, (d) for notch depth equal to 7 mm for the CMOD values corresponding to the two points on the P vs CMO graph 6.8. (b) Half fibre length (L_f,expressed in m) at the end of the numerical test for notch depth equal to 7 mm.

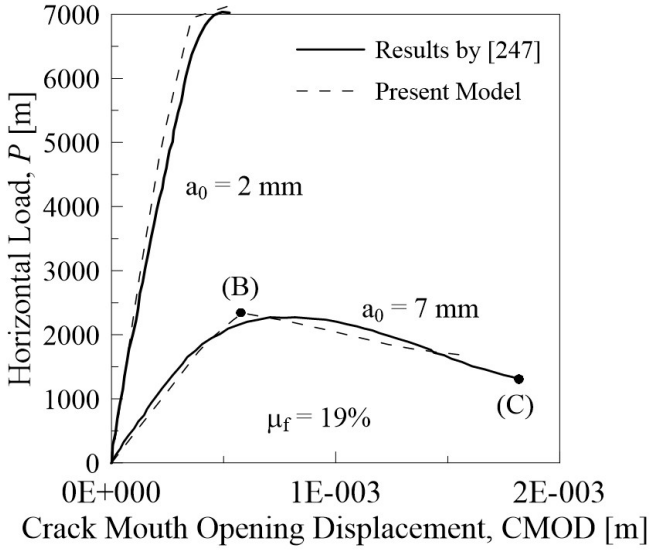

Figure 6.8: Load vs crack mouth opening displacement (CMOD) for specimens with notch depth equal to $a_0 = 2mm$ and $a_0 = 7mm$.

In Figure 6.8 the crack mouth opening displacement (CMOD) against the horizontal load applied to the specimen is represented for two different initial notch depths, $a_0 = 2mm$ and $a_0 = 7mm$. As can be observed, the literature's results are in good agreement with the present study results regarding both the initial specimen stiffness as well as the peak load and the softening branch of the *P-CMOD*

curves. In Figure 6.7c and 6.7d, the crack patterns are represented, for the case characterised by $a_0 = 7mm$ corresponding to the points (B) and (C) of Figure 6.8, respectively.

In Figure 6.7b, the fibre length distribution obtained from the present model at the end of the test (point (C) in Fig. 6.8 for $a_0 = 7mm$) is represented by using a grey-scale contour map. As can be noted, the fibres decrease their initial length (and reach very low values) in the fracture process zone located below the initial notch where the crack develops. The initial length of the fibres is maintained (i.e. no fibres failure occurs) in the central top and bottom part of the specimen, where unstressed and compressive stresses regions develop, respectively.

6.3.3 Fracture behaviour of FRC coupon under tensile loading

An experimental campaign related to prismatic Reactive Powder Concrete (RPC) specimens subjected to tensile stress is herein analysed [248]. The specimens have a total length equal to $700mm$, cross-section equal to $50 \times 20mm$, discretized through 438 four node elements.

The mechanical parameters of the RPC concrete are the following: Young modulus $E_m = 50GPa$, ultimate tensile strength $f_t = 8.0MPa$, fracture energy $\mathcal{G}_f = 30N/m$ [248]. The relevant parameters for unidirectional steel fibres are: fibre volume $\mu_f = 2.0\%$, Young modulus $E_f = 210GPa$, fibre length $2L_f = 13mm$ and diameter $\phi_f = 0.16mm$.

The analysis is performed under displacement control by imposing a progressive upward vertical displacement at the top of the specimen. A plane stress condition is assumed. Five orientations of fibres are examined ($\overline{\varphi} = 0°$, $30°$, $45°$, $60°$, $90°$) together with the case of fibres randomly arranged and the case of plain concrete (no fibres).

Vertical load against top vertical displacement curves provided by the numerical analyses are reported in Figure 6.9a. Note that the presence of the fibres produces an increment of the peak load with respect to the case of plain concrete (that is coincident to the case of fibres oriented with an angle equal to $\overline{\varphi} = 0°$). Further, the peak load is greater in the case of fibre oriented parallel to the load direction, $\overline{\varphi} = 90°$, and decreases by reducing the orientation angle. In Figure 6.9b, the results related to the crack orientation α against the average value of the fibre

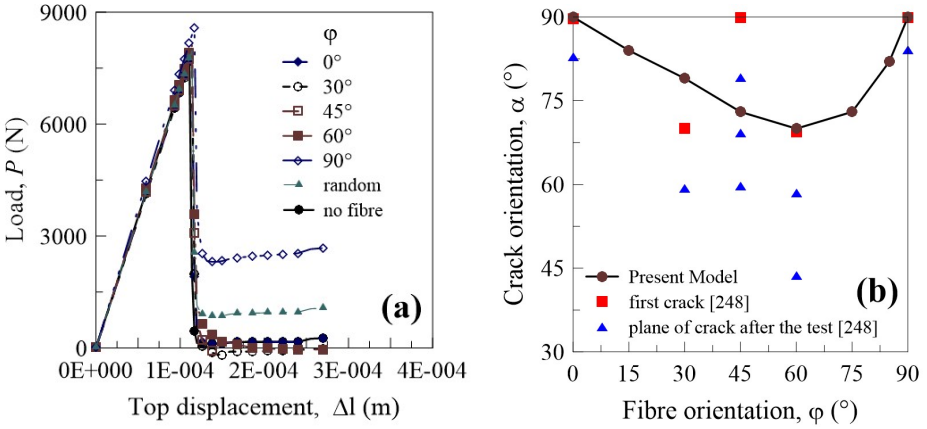

Figure 6.9: (a) Vertical load against top displacement and (b) crack orientation against fibre orientation according to experimental data.

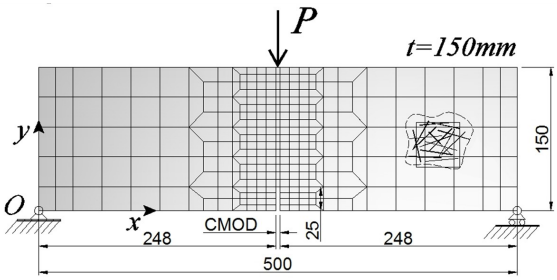

Figure 6.10: A three-point bending (plain and fibre-reinforced) concrete beam [249] with geometrical dimensions expressed in mm.

orientation $\overline{\varphi}$ are compared with those experimentally observed [248]: an evident dependence of the crack angle on the fibre orientation can be appreciated according to the experimental data.

6.3.4 Three Point Bending Behaviour of a single edge notched FRC beam

In the present Section, the failure behaviour of a FRC prismatic single-edge notched concrete beam under three-point bending is examined [249]. The specimens have span of $500mm$ and cross-section equal to $150 \times 150mm$; the notch depth is equal to $25mm$ and its width is equal to $4mm$ (Fig. 6.10).

Plain and steel fibre-reinforced concrete (with random arrangement and two

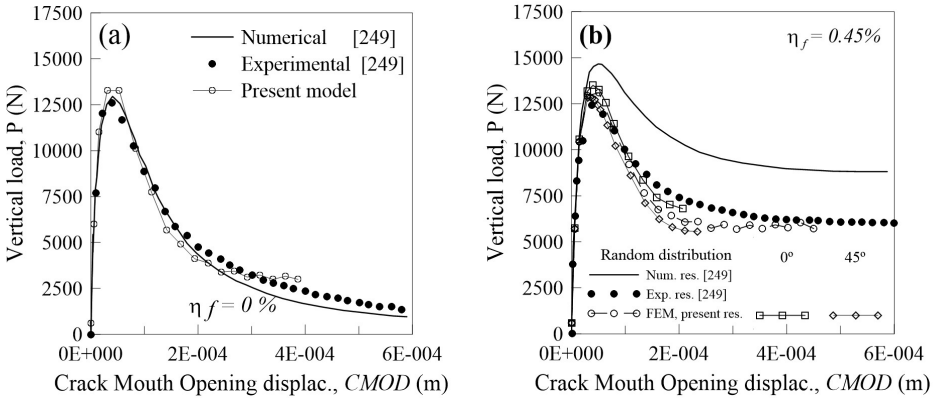

Figure 6.11: Vertical load vs crack mouth opening displacement (CMOD) for a three-point bending concrete beam [249]: (a) without steel fibers; (b) with steel fibers.

different fibre orientations, $\overline{\varphi} = 0°$ and $\overline{\varphi} = 45°$) are analysed. The mechanical parameters of the beam material are the following: Young modulus $E_m = 32GPa$, ultimate tensile strength $f_t = 2.6MPa$, fracture energy $\mathcal{G}_f = 94N/m$. The relevant parameters for the steel fibres are: $\mu_f = 0.45\%$, $E_f = 210GPa$, $2L_f = 50mm$, $\phi_f = 1mm$. The analyses are performed under displacement control, by imposing a progressive vertical displacement at the top central loaded point and measuring the corresponding reaction force. A plane stress condition is assumed. Vertical load against crack mouth opening displacement (CMOD) for plain concrete and for steel fibre-reinforced concrete specimens are shown in Figures 6.11a and 6.11b, respectively.

Literature numerical and experimental results [249] are also reported. As can be noted, the presence of the reinforcing fibres produces a slight increment of the peak load, but the most evident effect is an increase of ductility, as is shown by the decreasing branch of the force-CMOD curve. This behaviour is significant for fibres oriented normally to the crack direction ($\overline{\varphi} = 0°$), whereas it is less pronounced for random orientation and for $\overline{\varphi} = 45°$. The agreement of the present results with the experimental and numerical ones appears to be satisfactory.

6.3.5 Mechanical behaviour of a 3 point bending FRC beam

As a further example, the mechanical behaviour of a fibre-reinforced concrete beam under three-point bending is examined. The purpose of this example is

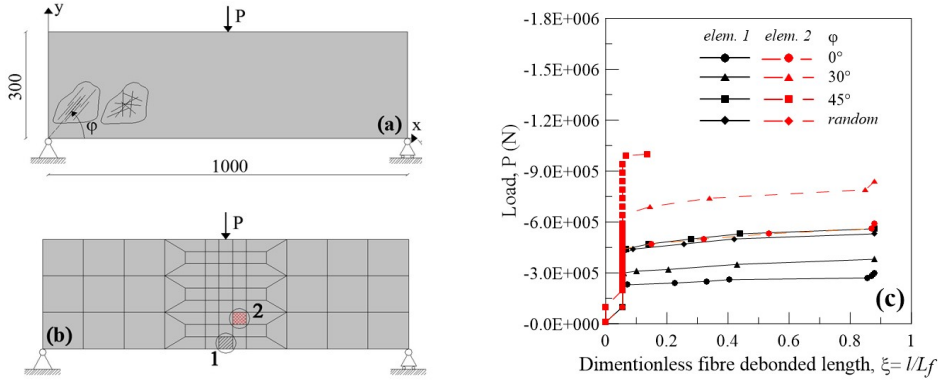

Figure 6.12: Three point bending of a fibre-reinforced concrete beam: (a) geometry (sizes in mm), (b) F.E. discretization, and (c) applied load P vs the dimensionless fibre debonded length ξ with various orientations (for elements 1 and 2).

to study the fibre debonding phenomenon through the fracture mechanics model presented in Chapter 4. The geometrical parameters of the structure and the considered FE discretisation (70 four-noded elements and 85 nodes) are displayed in Figure 6.12a and 6.12b. The beam thickness is assumed to be equal to $0.1m$, and a plane stress condition is adopted. The mechanical constants of the matrix material are assumed as follows: Young's modulus $E_m = 10GPa$, Poisson's ratio $\nu_m = 0.33$ and fracture energy $\mathcal{G}_f = 100N/m$. A reinforcing fibre phase characterised by elastic modulus equal to $E_f = 210GPa$, Poisson's ratio $\nu_f = 0.33$ and a volume fraction ratio $\mu_f = 5\%$ is taken into account, whereas the fibre length and diameter are assumed to be equal to $2L_f = 24mm$ and $\phi_f = 0.5mm$, respectively.

Non-linear analyses are performed under load control by imposing a progressive vertical downward force to the top point of the beam mid-section. Three unidirectional fibre orientations are considered ($\overline{\varphi} = 0°$, $30°$, $45°$ measured with respect to the x-axis, Fig. 6.12a) together with the case of random fibre arrangement. In Figure 6.12c, the applied load is plotted against the relative fibre debonded length ξ, evaluated in two finite elements (Fig. 6.12b) for different fibre orientations and for an interface fracture toughness equal to $K_{ic} = \sqrt{E_m \cdot \mathcal{G}_f} = 1.0MPa\sqrt{m}$. It can be remarked that, as the crack propagates along the fibres, the applied load becomes almost constant for ξ in the range 0.1 to 0.8 (values for $\xi > 0.9$ are not plotted because they exceed the range of validity of the proposed model). The continuous black curves refer to an element (No. 1, Fig. 6.12b) placed in the lower

mid-section of the beam and subjected to a pure traction, whereas the dashed red curves refer to the element No. 2 (Fig. 6.12b). As can be noted, for a given relative debonded length ξ, the applied load P related to the second element is greater than that for the first one. For $\overline{\varphi} = 45°$ and random fibre arrangement cases, the fibre detachment remains at an initial stage ($\xi \leq 0.1$), even for high level of applied load. Note that, in the case of horizontal fibre orientation ($\overline{\varphi} = 0°$), the load value needed to have the fibre-matrix detachment is lower than those in the other cases and in particular, at a given relative debonded length. The load increases by increasing the angle of the fibre orientation. The random fibre arrangement case is similar to the case of $\overline{\varphi} = 45°$.

6.3.6 Tensile behaviour of glass fibre-reinforced polyamide PA66 (GFRP) composite

The next example analyses the behaviour of a glass fibre-reinforced polymer (GFRP) specimen under tension, characterised by a polyamide 6.6 matrix material and short glass fibres as reinforcement [250]. Both unreinforced case and glass fibre-reinforced case are taken into account. The examined polyamide matrix material has the following mechanical characteristics: Young modulus $E_m = 3.1GPa$, Poisson's ratio $\nu = 0.35$, yield stress $\sigma_y = 60MPa$. The matrix material is assumed to follow the Mises yielding criterion with a zero post yield stress-strain slope, $E'_m \cong 0$ ($H = 0$) (perfect ductile behaviour). The glass reinforcing fibres are characterised by the following mechanical characteristics: Young modulus $E_f = 72.45GPa$, Poisson's ratio $\nu_f = 0.3$ and fibre diameter equal to $\phi_f = 11 \cdot 10^{-6}m$.

The fibres are distributed in the specimen with a preferential direction produced by the injection molding process of the coupons. Such an anisotropic spatial fibre distribution can be quantified through the so-called MIL (Mean Intercept Length) fabric tensor, which is a second order symmetric tensor whose eigenvectors define the directions of preferred fibre orientation [250]. The MIL fabric tensor eigenvalues (T_1, T_2, T_3 listed in decreasing value order) can be used to define an index of anisotropy, I_A [250, 251]. By assuming the first (greatest) eigenvalue T_1 as representative of the preferential fibre orientation direction, such an index can be evaluated for instance as $I_A = 1 - T_3/T_1 \cong 1 - T_2/T_1$, which is a measure of the orientation around the main direction 1 (note that $I_A = 0$ corresponds to randomly arranged fibres, whereas $I_A = 1$ indicates perfectly aligned fibres along

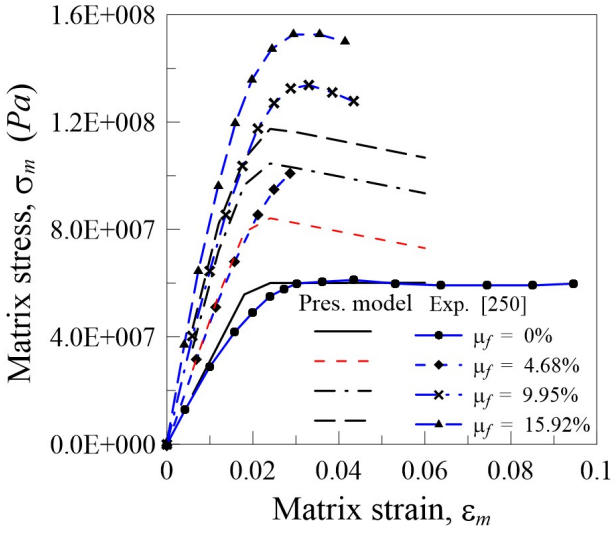

Figure 6.13: Stress-strain curves obtained for GFRP polyamide matrix composite with different glass fibre volume content. Numerical (present model) and experimental results [250] are reported.

the direction 1).

By considering the experimental values reported in [250], for which an index of anisotropy $I_A \cong 0.6$ has been found, the corresponding Gaussian probability distribution (Eq. (3.18) in Chapter 3) is approximately characterised by $\overline{\varphi} = \pi/2$, $\delta_\varphi = 49.5$ (by assuming a 2D problem with $\overline{\vartheta} = \pi/2$, $\delta_\vartheta = 1°$) for the specimen loaded in the y direction. The above values of the fibre probability density function has been obtained by taking into account the following probability ratio, $p(\overline{\varphi} + \delta_\varphi, \overline{\vartheta})/p(\overline{\varphi}, \overline{\vartheta}) \cong 0.6$, i.e. the ratio between the probability to find fibres oriented in the direction $(\overline{\varphi} + \delta_\varphi, \overline{\vartheta})$ is 0.6 times the probability to find fibres oriented in the direction $(\overline{\varphi}, \overline{\vartheta})$, with $\delta_\varphi = \pi/2$.

Four different fibre volume contents are examined [250]: $\mu_f = V_f/V = 0\%$ (plain polyamide material), $\mu_f = 4.68\%$, $\mu_f = 9.95\%$ and $\mu_f = 15.92\%$, and the corresponding weight averaged fibre lengths have been found experimentally [250] to be equal to $2L_f = 4.73 \cdot 10^{-4} m$, $2L_f = 3.54 \cdot 10^{-4} m$ and $2L_f = 2.76 \cdot 10^{-4} m$, respectively. By using the above parameters, the stress-strain curves of the GFRP material are obtained from the present model.

In Figure 6.13, the numerical results are compared with the experimental data reported in [250]. As can be observed, the case of unreinforced material is well

represented by the model. For glass fibre reinforced polyamide, the initial stiffness of the composite is slightly underestimated by the numerical approach and the failure stress is underestimated by the model, with an error equal to about 18% for $\mu_f = 4.68\%$, 10% for $\mu_f = 9.95\%$ and 19% for $\mu_f = 15.92\%$. It must be remarked that the represented stress corresponds only to the matrix one, i.e. it is the stress carried only by the matrix material in the continuum with the reinforcing fibres.

The above described results mismatch can be justified by considering that the assumed value of the anisotropy index does not correspond exactly to the fibre orientation description through the mean fibre orientation angle $\overline{\varphi}$ and its variance δ_φ. The adopted values of such quantities can be considered to be a rough representation of the experimental values of I_A, and the adopted geometrical and mechanical characteristics calculated for the fibres could not be exactly those of the real tested specimen. Moreover, the use of the Mises yielding criterion for the matrix may not be fully appropriate for the description of the polyamide mechanical behaviour.

Nevertheless, the trends shown by the curves for the different fibre volume fractions and spatial orientations reasonably reflect the experimental patterns.

6.3.7 Single edge notched FRC beam under four point shear

The mechanical behaviour of a four-point shear loaded single-edge notched beam is examined. Such a structural configuration has been used by several Authors as a benchmark test for numerical analyses in fracture mechanics of brittle solids [208]. The geometrical parameters of the structure and the examined FE discretisations (characterised by 776 four-noded elements and 817 nodes) are displayed in Figure 6.14a and 6.14b, respectively. A beam thickness equal to 0.1m is adopted and a plane stress condition is assumed in the numerical analyses.

The constants of the matrix material are assumed as follows: Young modulus $E_m = 35GPa$, Poisson's ratio equal to $\nu = 0.33$ and ultimate strength $f_t = 28MPa$. Reinforcing steel fibres are characterised by an elastic modulus equal to $E_f = 200GPa$ and a volume fraction ratio equal to $\mu_f = 5\%$. The fibre length and diameter are assumed to be equal to $2L_f = 24mm$ and $\phi_f = 0.5mm$, respectively.

A fibre tensile strength equal to $f_{t,f} = 100MPa$ has firstly been examined. Such a high value assures the absence of fibre breaking in the case under study.

The non-linear analyses are performed under displacement control by imposing a

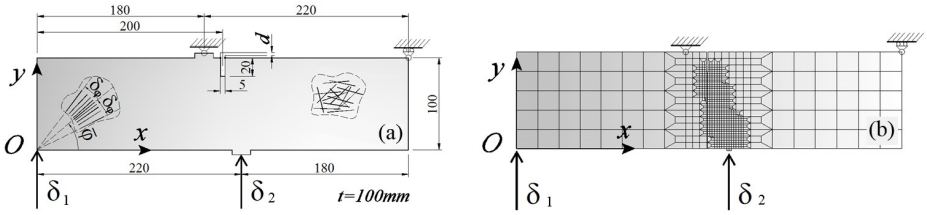

Figure 6.14: Single-edge notched beam under four point shear: (a) geometrical characteristics and (b) discretisation with 776 four-noded bilinear elements and 817 nodes.

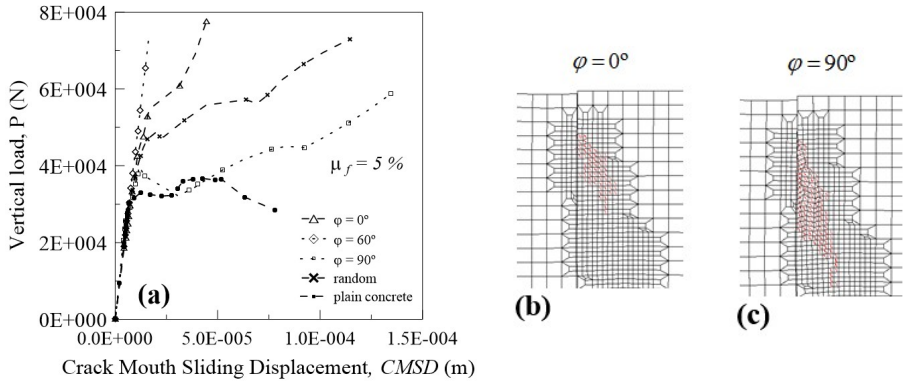

Figure 6.15: Single-edge notched beam under four point shear: (a) load P vs crack mouth sliding displacement $CMSD$. Crack patterns obtained for different fibre orientations ((b) $\overline{\varphi} = 0°$ and (c) $\overline{\varphi} = 90°$).

progressive vertical displacement at the two bottom loaded points, δ_1, δ_2 (Fig. 6.14); the ratio between the imposed displacements is $\delta_1/\delta_2 \cong 1.227$, which corresponds to that obtained in the same structure, assumed to be linear-elastic, under loads $P/10$ and P applied to the above mentioned bottom points of the beam (Fig. 6.14a), respectively.

Several fibre arrangements have been examined: randomly arranged fibres and aligned fibres having their preferential orientation angle described through a Gaussian probability distribution function with $\overline{\varphi} = 0°$, $60°$, $90°$ and $\delta_\varphi = 1°$. The load P (i.e. the reaction force measured at the central bottom point of the beam where the upward displacement δ_2 is imposed, Fig. 6.14) against the crack mouth sliding displacement $CMSD$ curves are plotted in Figure 6.15a, whereas the evaluated crack paths for horizontal ($\overline{\varphi} = 0°$) and vertical ($\overline{\varphi} = 90°$) fibres are reported in Figures 6.15b and 6.15c.

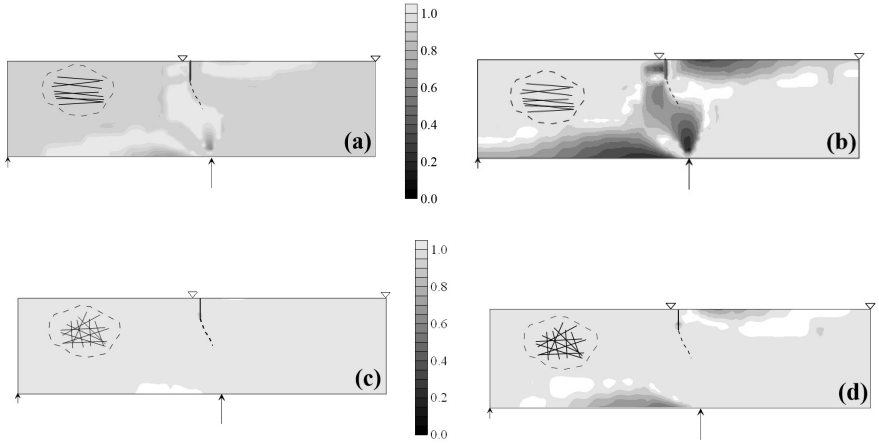

Figure 6.16: Dimensionless sliding function, s, in the notched beam for the case of horizontal fibres ($\overline{\varphi} = 0°$) for load level equal to (a) and 50% and (b) 100% of its final value, and for the case of fibre randomly arranged for load level equal to (c) and 50% and (d) 100% of its final value.

As can be noted by observing the P-CMSD curves, the effectiveness of the reinforcing fibres in enhancing fracture resistance is given by arrangement corresponding to fibres perpendicular to the crack ($\overline{\varphi} = 0°$). The case of horizontal fibres ($\overline{\varphi} = 0°$) appears to be more effective than the case of vertical fibres ($\overline{\varphi} = 90°$) due to the most pronounced bridged effect of the reinforcing phase in the former case. As can be noted the presence of the reinforcement phase increases the peak load and it is lower for the case of plain concrete, whereas the softening branches are slightly noticeable due to the effect of the reinforcing phase.

The spatial distribution of some mechanical parameters has been plotted only for two fibre orientations: horizontally aligned fibres ($\overline{\varphi} = 0°$, $\delta_{\varphi} = 1°$) and randomly arranged fibres.

The distribution of the sliding function s is plotted in Figure 6.16 for load levels equal to 50% and 100% of the maximum applied load and for two fibre arrangements (horizontal fibres and random arrangement). As can be noted, the fibre effectiveness decreases with the load increment in the tensile zones of the beam, and the sliding function s tends to the unity in the unstressed or compressed zones.

The dimensionless fibre debonded length $\xi = l/L_f$ pattern is plotted in Figure 6.17 for load levels equal to 50% and 100% of the maximum applied load and

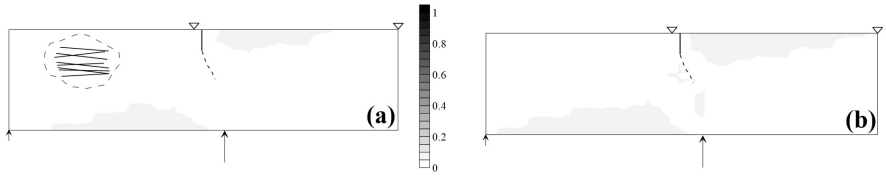

Figure 6.17: Dimensionless fibredebonded length, ξ, in the notched beam for the case of horizontal fibres ($\overline{\varphi} = 0°$) for load level equal to (a) 50% and (b) 100% of its final value.

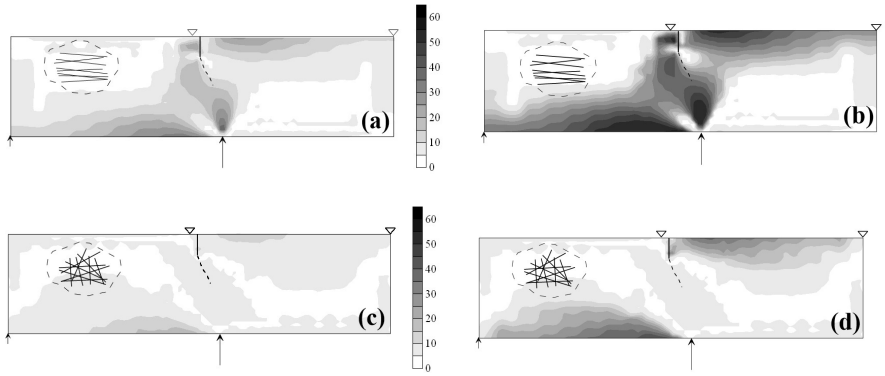

Figure 6.18: Stress evaluated in the centre of the fibres, σ_f (MPa), in the single-edge notched beam under four point shear: (a) case of a load level equal to 50% and (b) equal to 100% of its final value, for horizontal fibres; (c) case of a load level equal to 50% and (d) equal to 100% of its final value, for random orientation.

for horizontal fibres. As can be noted, the fibre debonding increases with the load increment in the tensile zones of the beam, and appears to occur nearly in the same regions where the sliding function reduces its value. The expected overall behaviour of the beam is physically consistent and correctly represented by the proposed model.

In Figure 6.18, the fibre stress distribution, σ_f, in the beam is mapped in the case of unidirectional horizontal fibres, for a load level equal to 50%(Fig. 6.18a) and 100% (Fig. 6.18b) of its final load, respectively. The same quantities are represented in Figure 6.18c and 6.18d for randomly oriented fibres. As can be noted, the case of horizontal reinforcement produces fibre stresses much higher than in the case of random orientation, with stress values approaching the fibre tensile strength in the right upper and left bottom parts of the beam as well as in the area just above the central applied upward displacement.

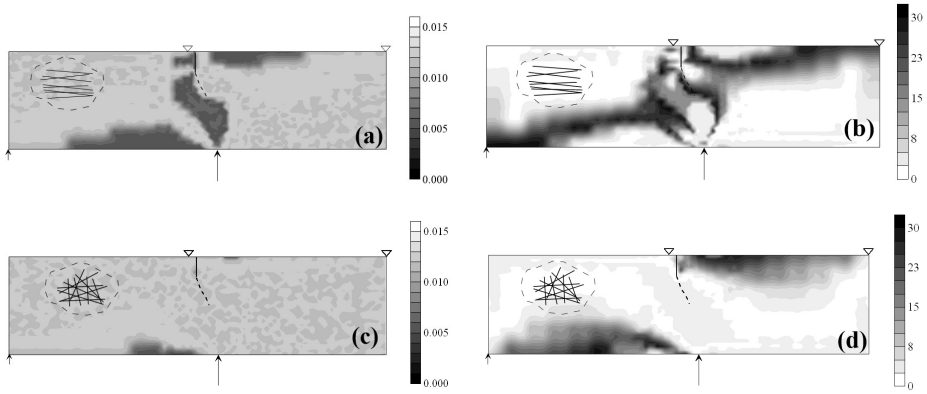

Figure 6.19: Single-edge notched beam under four point shear for a load level equal to 100% of its final value: (a) half fibre length, L_f (m), and (b) fibre stress, σ_f (MPa), for horizontal fibres; (c) half fibre length, L_f (m), and (d) fibre stress, σ_f (MPa), for random arrangement. Fibre tensile strength equal to $f_{t,f=30MPa}$.

In order to study the effect of fibre failure, a low value of the fibre tensile strength, assumed equal to $f_{t,f} = 30MPa$, has been examined in the following.

In Figure 6.19, the final fibre length distribution in the beam (Fig. 6.19a) and the fibre tensile stress (Fig. 6.19b) are mapped in the case of unidirectional horizontal fibres and of randomly oriented fibres (Figs. 6.19c and 6.19d), respectively, for a load level equal to 100% of its final value. It can be observed as the fibre failure occurs more easily in the case of horizontal reinforcements (see light zones in Fig. 6.19a corresponding to short - broken - fibres), as the small final fibre length (reached after one or more breakings) denotes. Fibre rupture is more localised in the right upper and left bottom parts of the beam as well as in the area just above the central applied upward load (Fig. 6.19a). In the case of randomly arranged fibres, the fibre failure occurs only in a very limited region of the beam located in the left bottom part of the structural component (Fig. 6.19c).

On the other hand, the stresses in the fibres are more severe in the case of horizontal unidirectional fibres (Fig. 6.19b) than for randomly distributed fibres (Fig. 6.19d) due to the fibre orientation that, especially in the most stretched zones of the beam, approximately corresponds to the maximum principal stress field direction.

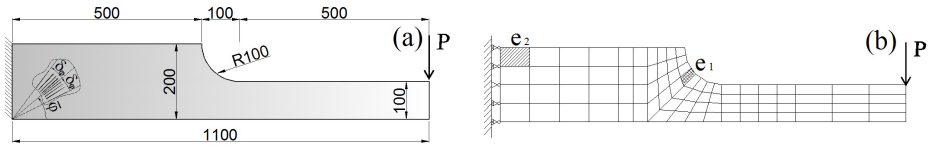

Figure 6.20: (a) Notched FR cantilever beam under a concentrated load (dimensions in mm, thickness equal to $t = 100mm$); (b) finite element discretization.

6.3.8 Parametric example

Finally, a parametric example regarding a notched Fibre-Reinforced cantilever beam under static monotonic concentrated load applied at its extremity is examined. The main involved mechanical parameters are made to vary in order to demonstrate the capability of the developed model to represent the progressive fibre-matrix detachment under different conditions. It is supposed that the material damaging effect is only represented by the fibre debonding, i.e. the fibres can progressively decrease their initial adhesion length with respect to the matrix material which is assumed to be linearly elastic. In the present example, the notched cantilever beam is discretized through 84 bilinear 4-noded finite elements (Fig. 6.20), and is assumed to be in plane stress condition. Two different composite materials are examined:

(1) A FRC material characterized by Young modulus $E_m = 10GPa$ and Poisson's ratio $\nu_m = 0.1$ for the bulk material. For the reinforcing fibres: Young modulus $E_f = 210GPa$, Poisson's ratio $\nu_f = 0.33$, semi-length $L_f = 24mm$ and diameter $\phi_f = 0.5mm$, respectively, and interface fracture energy equal to $\mathcal{G}_f = 100N/m$ (corresponding to interface critical fracture toughness $K_{ic} = \sqrt{E_i \cdot \mathcal{G}_{ic}} = 10^6 Pa\sqrt{m}$, having assumed $E_i = E_m$ for the sake of simplicity), whereas the fibre volume content is assumed to be equal to $\mu_f = 5\%$. Such mechanical characteristics are those of a *concrete-like steel fibre-reinforced composite*;

(2) A FRC material characterized by Young modulus $E_m = 31GPa$ and Poisson's ratio $\nu_m = 0.35$ for the matrix material. For the reinforcing fibres: Young modulus $E_f = 72,45GPa$, Poisson's ratio $\nu_f = 0.3$, semi-length and diameter $L_f = 0.473mm$ and $\phi_f = 0.011mm$ of the fibres, respectively, and interface fracture energy equal to $\mathcal{G}_{ic} = 150N/m$ (corresponding to interface critical fracture toughness $K_{ic} = \sqrt{E_m \cdot \mathcal{G}_{ic}} = 2.16MPa\sqrt{m}$, having assumed $E_i = E_m$ for the sake of

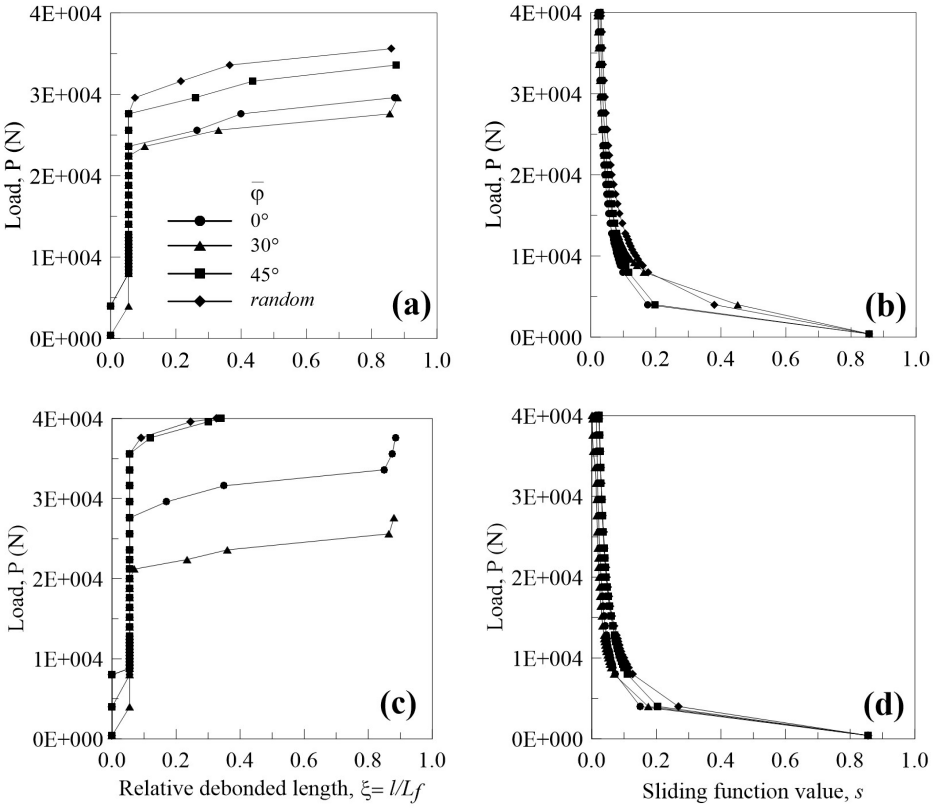

Figure 6.21: Relative fibre detachment for finite elements e_1 (a) and e_2 (c) (Fig. 6.20b) and sliding function value (e_1 (b); e_2 (d)) against the applied load P, for different fibre arrangements and for $K_{ic} = 1MPa\sqrt{m}$ of the concrete-like FR material.

simplicity), whereas the fibre volume content is equal to $\mu_f = 5\%$. Such mechanical characteristics are those of a *polymer-like glass fibre-reinforced composite*.

Being a plane problem, the fibre orientation can simply be described only through the angle φ for which different mean values ($\overline{\varphi} = 0°, 30°, 45°$) are assumed, whereas its variance is adopted to be very small ($\delta_\varphi = 1°$). The case of fibres randomly oriented is also analysed.

In order to study the effect of the fibre fracture bonding, quantified in the present model through the interface critical fracture energy $\mathcal{G}_{ic}$ or, equivalently, by the interface fracture toughness K_{ic}, different cases of such bonding-related parameters are taken into account. In particular, three values of the interface fracture toughness, K_{ic}, $K_{ic0.5} = K_{ic}/2$ and $K_{ic0.25} = K_{ic}/4$, are examined.

In Figures 6.21a and 6.21c, the dimensionless fibre detached length, $\xi = l/L_f = (L_f - L_{ad})/L_f$, is represented against the applied load by varying the fibre orientation, for the finite elements labelled e_1 and e_2 (Fig. 6.20b). In particular, the stress state in element e_2 can be supposed to be simply uniaxial, while the stress state in the element e_1 is much more complex due to the stress concentration in the notched zone. As can be noticed, the fibre detachment increases by increasing the load, especially for fibres nearly parallel to the maximum tensile principal stress direction ($\overline{\varphi} = 0°$ and $30°$), whereas the fibre debonding is lower - at the same load level - for fibres oriented in a random arrangement.

The sliding function is also represented in Figures 6.21b and 6.21d. Note that the effectiveness of the fibre in the FR beam decreases as the detachment proceeds. This occurs regardless of the fibre orientation, and such a decrease takes place, with different gradients, by increasing the load up to its final value for different orientations of the fibres.

In Figure 6.22, the same quantities such those in Figure 6.21 are represented for a reduced value of the interface fracture toughness ($K_{ic0.25} = K_{ic}/4$). In such a case, the fibre detachment takes place much more rapidly: for a given load level, the fibre debonding reaches values greater than those in the case of plain interface fracture toughness equal to K_{ic}, irrespective of the fibre orientation. As a matter of fact, also the sliding function value rapidly tends to zero even for low levels of the applied load.

In Figure 6.23, the load against the dimensionless debonded length is plotted by varying the fibre orientation, for different critical fracture energy values and for the two above-mentioned finite elements (e_1 and e_2 in Fig. 6.20b). All the curves are characterized by a rapid increase occurring at small values of the dimensionless debonded length ξ, followed by a plateau. Since $P(\xi)$ is an increasing function, it can be deduced that the fibre debonding is a stable phenomenon, which requires a continuous increment of the applied load to reach the final situation of completely detached fibre.

In Figure 6.24, the dimensionless debonded length distribution in the beam is represented in the case of horizontal (Fig. 6.24a and 6.24b) and randomly arranged fibres (Fig. 6.24c and 6.24d), for two different load levels. The detachment appears to be much more pronounced in the case of fibres nearly aligned with the tensile principal stress directions, whereas it is lower in the case of random fibre orientation. The effect of the stress concentration in the notched zone is remarkable since it

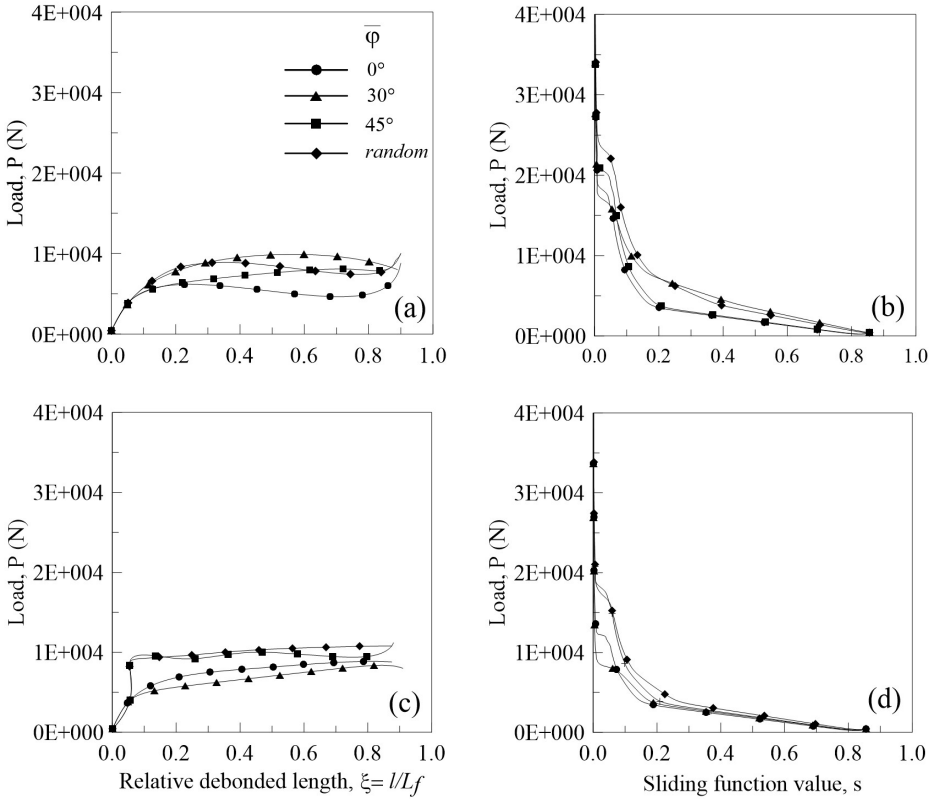

Figure 6.22: Relative fibre detachment for finite elements e_1 (a) and e_2 (c) (Fig. 6.20b) and sliding function value (el. e_1 (b); el. e_2 (d)) against the applied load P, for different fibre arrangements and for $K_{ic0.25} = K_{ic}/4$ of the concrete-like FR material.

produces a highly debonded area in the beam. As can be noted, nothing happens, in term of fibre detachment, in the unstressed and compressed zones of the beam for all the considered load levels.

In Figure 6.25, the sliding function distribution in the beam is represented for the same case previously described. As can be noted, the sliding function decreases in the zones subjected to traction, whereas its value tends to the unity in the compressed zones.

As far as the second material is concerned (polymer-like glass fibre-reinforced composite), the load against the detached length is displayed in Figure 6.26 for two significant finite elements of the discretization (e_1 and e_2 in Fig. 6.20b).

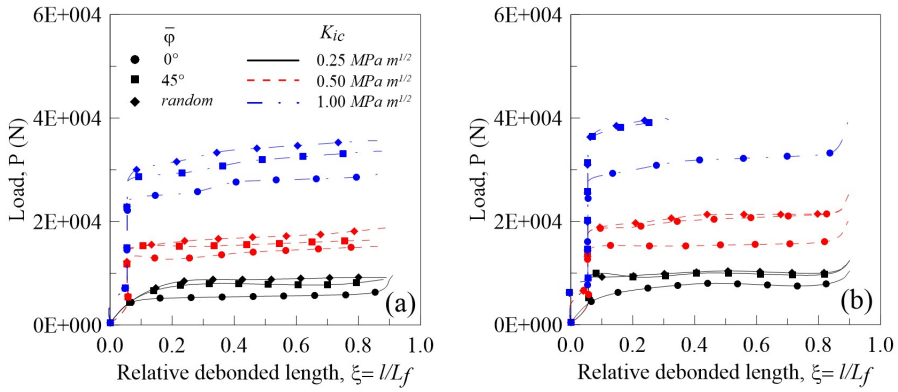

Figure 6.23: Relative debonded length for finite elements e_1 (a) and e_2 (b) (Fig. 6.20b) against the applied load P, for some fibre arrangements and for different values of K_{ic} of the concrete-like FR material.

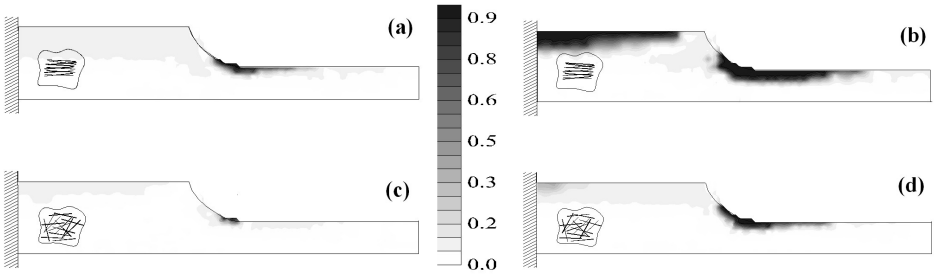

Figure 6.24: Dimensionless debonded length, ξ, in the notched beam for horizontal fibers ($\overline{\varphi} = 0°$) and load level equal to 0.5 (a) and 1.0 of its final value (b); distribution of ξ represented for the same load levels and for fibre randomly arranged (c), (d) ($K_{ic} = 1MPa\sqrt{m}$ for the concrete-like FR material).

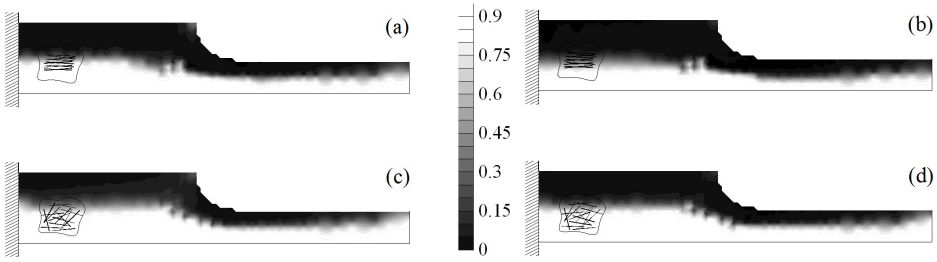

Figure 6.25: Sliding function, s, in the notched cantilever beam for horizontal fibers ($\overline{\varphi} = 0°$) and load level equal to 0.5 (a) and 1.0 of its final value (b); the distribution of ξ is represented for the same load levels and for fibre randomly arranged (c), (d) ($K_{ic} = 1MPa\sqrt{m}$ for the concrete-like FR material).

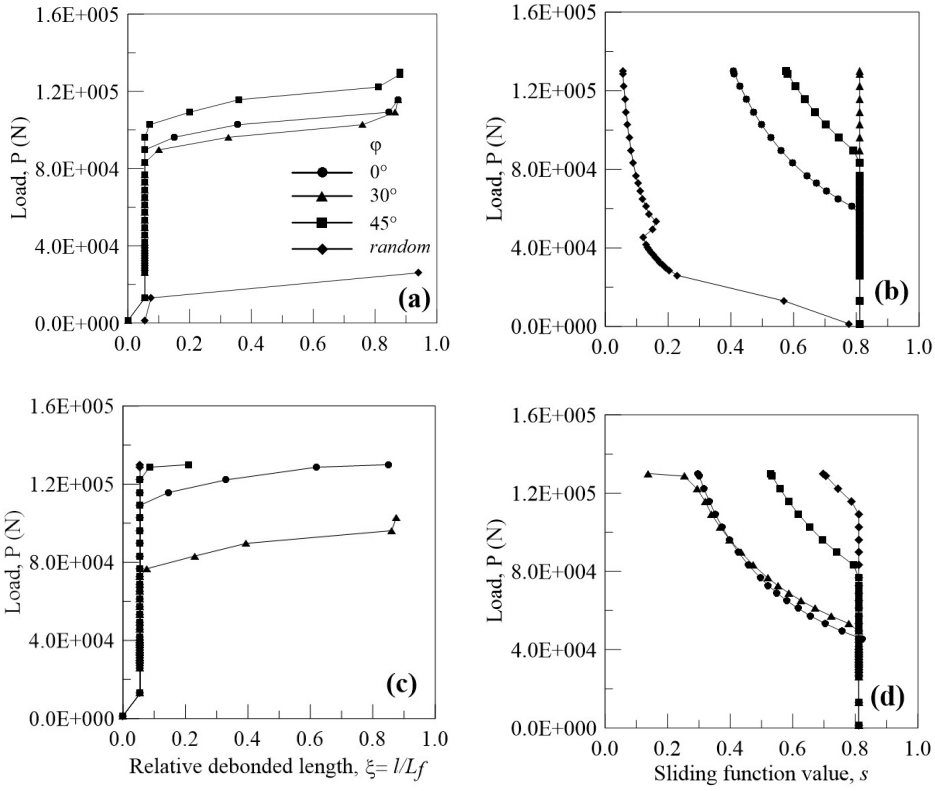

Figure 6.26: Relative fibre debonded length for finite elements e_1 (a) and e_2 (c) (Fig. 6.26b) and sliding function value (e_1 (b); e_2 (d)) against the applied load P, for different fibre arrangements and for $K_{ic} = 2.16MPa\sqrt{m}$ of polymer-like FR material.

In Figure 6.27, the same quantities such those in Figure 6.26 are represented for the interface fracture toughness equal to $K_{ic}/4$.

In Figure 6.28, the load against the dimensionless debonded length is plotted by varying the fibre orientation, for different critical fracture toughness values and, for the two above-mentioned finite elements (e_1 and e_2 in Fig. 6.20b). All the curves are characterized by a rapid increase occurring at small values of the dimensionless debonded length ξ, followed by a plateau. The curves show a pattern which is very similar to that of the concrete-like steel fibre-reinforced composite, previously examined.

In Figures 6.29 and 6.30, the dimensionless debonded length and the sliding function distributions are plotted in the case of horizontal and randomly arranged

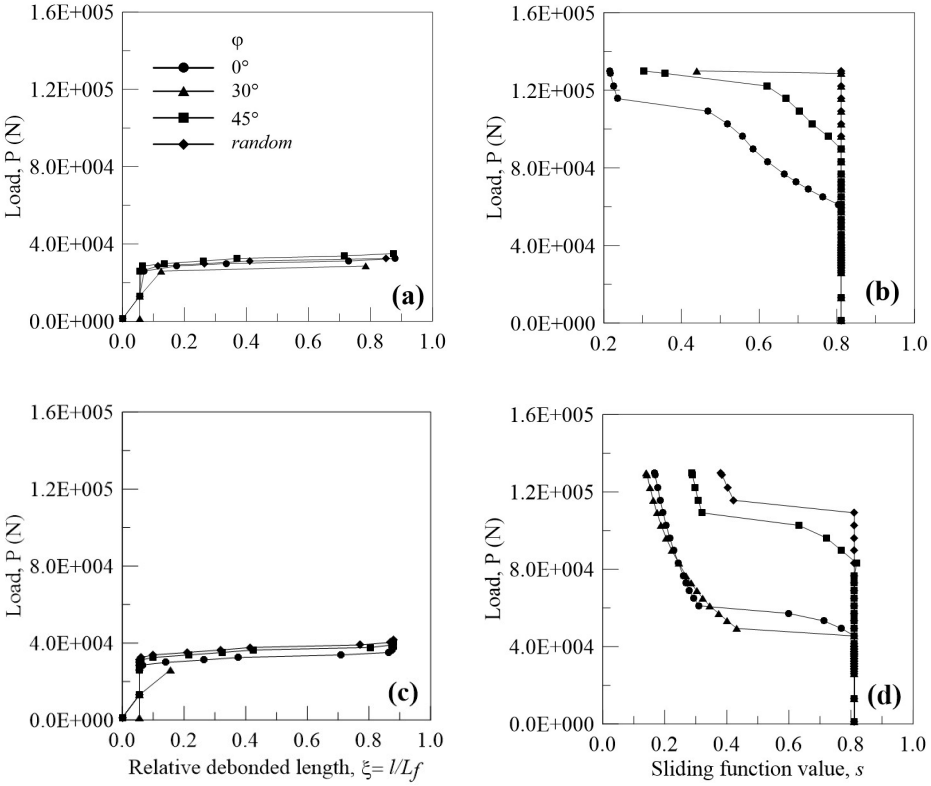

Figure 6.27: Dimensionless fibre detachment for finite elements e_1 (a) and e_2 (c) (Fig. 6.27b) and sliding function value (e_1 (b); e_2 (d)) against the applied load P, for different fibre arrangements and $K_{ic0.25} = K_{ic}/4$ of the polymer-like FR material.

fibres for two load levels. The same observations as those for Figure 6.24 and 6.25 can be made.

According to the analysed examples, the proposed fracture mechanics model for the fibre debonding can be used to quantify the fibre-matrix detachment and the sliding function value (that measures the fibre effectiveness in the composite). By changing the geometrical, mechanical and fracture parameters of the involved materials, the proposed model allow to quantitatively evaluate the micro-mechanisms taking place in the composites as well as their overall behaviour, as is usually desired from the design point of view.

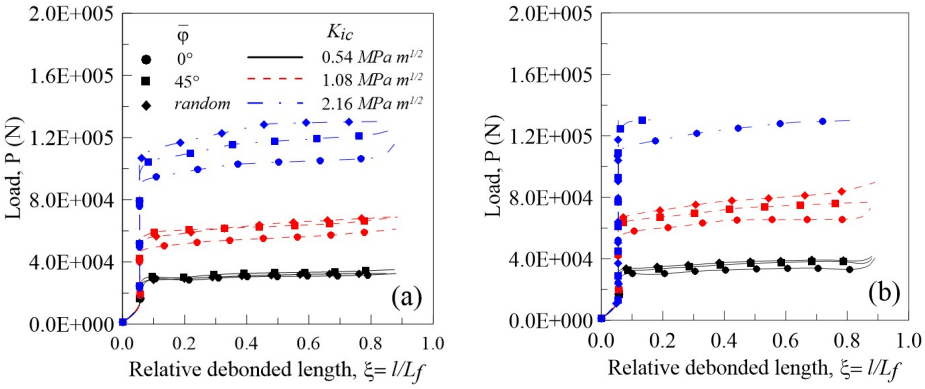

Figure 6.28: Dimensionless fibre detachment for finite elements e_1 (a) and e_2 (b) (Fig. 6.20b) against the applied load P, for some fibre arrangements and for different values of K_{ic} of the polymer-like FR material.

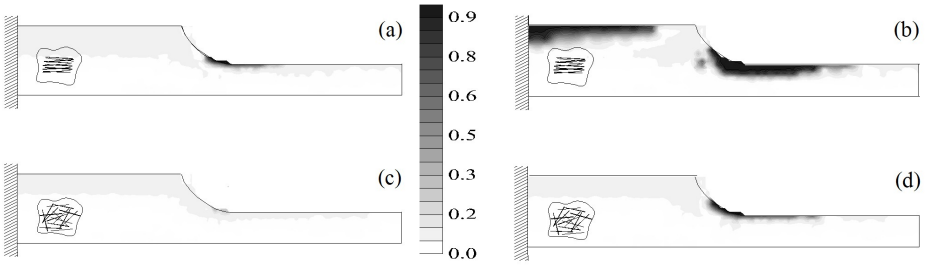

Figure 6.29: Dimensionless fibre detachment (ξ) in the notched cantilever beam for horizontal fibers ($\overline{\varphi} = 0^\circ$) and load level equal to 0.5 (a) and 1.0 of its final value (b); the distribution of ξ is represented for the same load levels and for fibers randomly arranged (c), (d) ($K_{ic} = 2.16MPa\sqrt{m}$ for the polymer-like FR material).

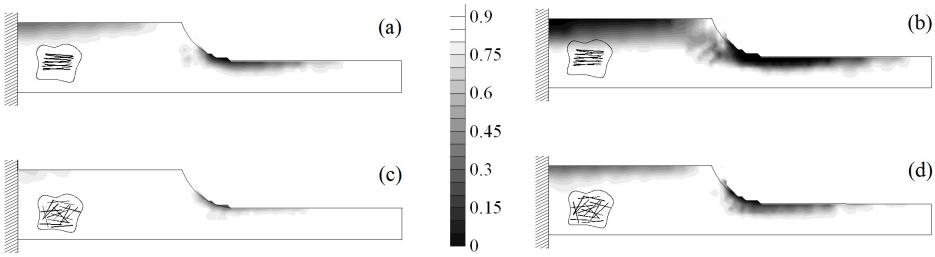

Figure 6.30: Sliding function (s) in the notched cantilever beam for horizontal fibers ($\overline{\varphi} = 0^\circ$) and load level equal to 0.5 (a) and 1.0 of its final value (b); the distribution of s is represented for the same load levels and for fibers randolmly arranged (c), (d) ($K_{ic} = 2.16MPa\sqrt{m}$ for the polymer-like FR material).

6.4 Cyclic loading simulations

6.4.1 Fatigue behaviour of a glass fibre-reinforced polyamide specimen

In the present example, the fatigue behaviour of a 13% glass fibre-reinforced polyamide specimen (with fibres oriented parallel or inclined by an angle $\overline{\varphi} = 30°$ with respect to the load direction) under constant amplitude uniaxial cyclic stress is examined [252].

The materials constituting the specimen have the following characteristics: matrix with Young modulus $E_m = 2.2GPa$, Poisson's ratio $\nu_m = 0.4$, fibres Young modulus $E_f = 72.45GPa$, Poisson's ratio $\nu_f = 0.23$, fibre diameter equal to $\phi_f = 10\mu m$ and fibre length equal to $2L_f = 5.5 \cdot 10^{-4}m$. The Paris constants of the interface are $C_i = 8.7 \cdot 10^{-9}$ and $m_i = 13.9$ (dl/dN in mm/cycle, ΔK_i in $MPa\sqrt{m}$), i.e. those of the matrix material, whereas the Wöhler's constants are $\sigma_0 = 10MPa$, $N_0 \cong 2 \cdot 10^6$, $B = 0.133$ (Fig. 6.31).

In Figure 6.31b, the experimental S-N curves for both fibre arrangements are reported. As can be noted, the effectiveness of the fibres aligned with the fatigue loading direction is evident and, for the same stress amplitude, a much greater number of loading cycles can be reached before material failure. The numerical simulations of the number of loading cycles to failure confirm such behaviour, providing results that are in acceptable agreement with the experimental data.

In Figure 6.32a, the damage parameter D_E, associated with the Young modulus of the matrix, is plotted together with the matrix strain against the number of loading cycles. In Figure 6.32b, the dimensionless fibre debonded length and the sliding function are plotted against the number of loading cycles: the function $s(\overline{\varepsilon}_f^m)$ decreases with the cyclic loading, indicating a decrease of the fibre capability to carry the applied load transferred from the matrix. As a consequence, the stress fraction sustained by the matrix increases with N (being constant the maximum applied stress during fatigue), and the damage in the bulk material increases. In the case of fibres aligned with the loading direction ($\overline{\varphi} = 0°$), the sliding parameter stabilises after a certain number of loading cycles, and the damage in the matrix appears to increase very slightly with N.

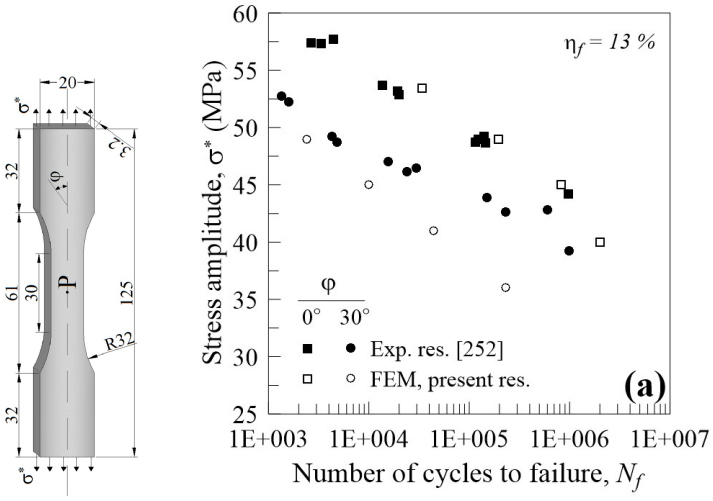

Figure 6.31: (a) Geometrical dimensions, expressed in (mm), and (b) Wöhler's curves of a glass fibre-reinforced polyamide specimen: experimental and present results [252].

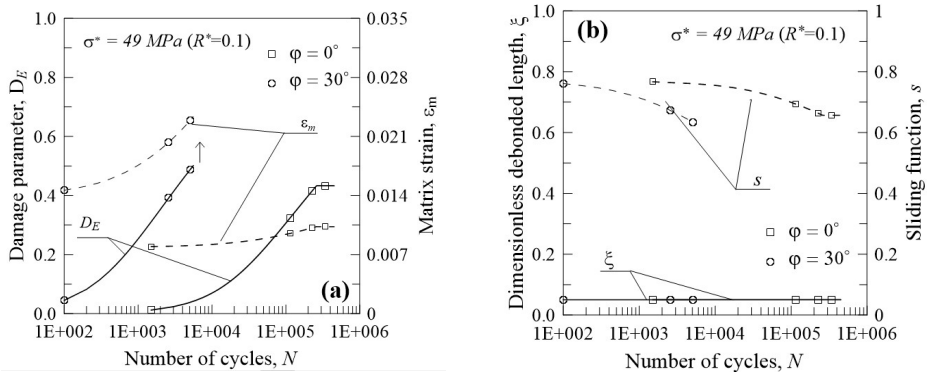

Figure 6.32: (a) Damage and strain evolution in the matrix (at point P) vs the number of stress cycles;(b) dimensionless fibre debonded length, ξ, and sliding parameter, s, (at point P) vs the number of stress cycles.

6.4.2 Fatigue behaviour of a glass fibre-reinforced polycarbonate specimen

The fatigue behaviour of a 20% glass (randomly arranged) fibre-reinforced polycarbonate specimen under constant amplitude uniaxial cyclic stress is herein examined [253].

The materials of the specimen have the following characteristics: matrix with

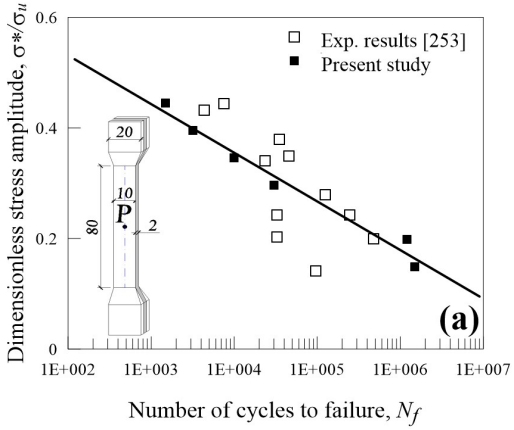

Figure 6.33: Wöhler's curves of a glass fibre-reinforced polycarbonate specimen (dimensions in mm): experimental and present results [253].

Young modulus $E_m = 2.2GPa$, Poisson's ratio $\nu_m = 0.2$, whereas the fibres have Young modulus $E_f = 72.45GPa$, Poisson's ratio $\nu_f = 0.3$, fibre diameter equal to $\phi_f = 10\mu m$ and fibre length equal to $2L_f = 4 \cdot 10^{-4}m$. The Paris constants of the interface are $C_i = 1.01 \cdot 10^{-4}$, $m_i = 3.1$ (dl/dN in mm/cycle, ΔK_i in $MPa\sqrt{m}$) corresponding to those of the matrix material, whereas the Wöhler's constants are $\sigma_0 = 5MPa$, $N_0 \cong 2 \cdot 10^6$, $B = 0.293$ (Fig. 6.33).

The attainment of the ultimate matrix strain value ($\varepsilon_u = 10\%$) during fatigue cycles identifies the failure condition under fatigue (Fig. 6.33). The dimensionless cyclic stress amplitude σ^*/σ_u (with $\sigma_u \cong 75MPa$ composite tensile strength) against the number of stress cycles is shown in Figure 6.33, where a satisfactory agreement with experimental results can be noted. Numerical S-N results appear to be approximately aligned along a straight line in the Wöhler diagram.

In Figure 6.34a, the damage values for a given value of σ^* in the matrix material and the matrix strain at point P are plotted against N, whereas in Figure 6.34b the dimensionless detached length and the sliding function at point P are represented against N.

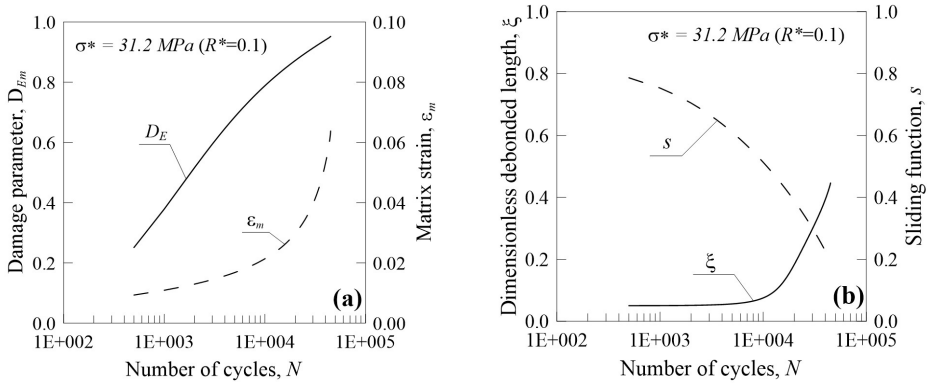

Figure 6.34: (a) Damage and strain evolution in the matrix (at point P) vs the number of stress cycles;(b) dimensionless fibre debonded length, ξ, and fibres sliding parameter, s, (at point P) vs the number of stress cycles.

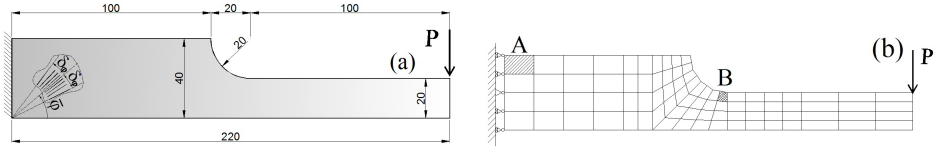

Figure 6.35: (a) Geometrical dimensions of the fibre-reinforced notched clamped beam expressed in (mm) and (b) Finite elements discratization.

6.4.3 Influence of the damage parameters on the fatigue behaviour of a composite notched beam

Finally, a parametric numerical test regarding a notched clamped beam under a repeated concentrated load applied to its extremity is examined (Fig. 6.35).

Different fibre contents ($\mu_f = 3\%, 5\%, 10\%$), two fibre arrangements ($\overline{\varphi} = 0°$ and random orientation), and stress amplitudes of the cyclic stress, measured through the stress amplitude at point A, (Fig. 6.36a) equal to $\Delta\sigma_a = 10MPa$, $15MPa$, $20MPa$ are assumed. For the sake of comparison, the case of a plain material is also examined.

The matrix material is characterized by Young modulus $E_m = 2.2GPa$ and Poisson's ratio $\nu_m = 0.15$, whereas Young modulus $E_f = 72.4$, Poisson's ratio $\nu_f = 0.3$ are adopted for the reinforcing fibres having semi-length and diameter $2L_f = 4 \cdot 10^{-4}$, $\phi_f = 10\mu m$ respectively. The interface fracture energy is assumed to be equal to $\mathcal{G}_{ic} = 100Nm$. The Paris constants of the interface are $C_i = 1.01 \cdot 10^{-4}$,

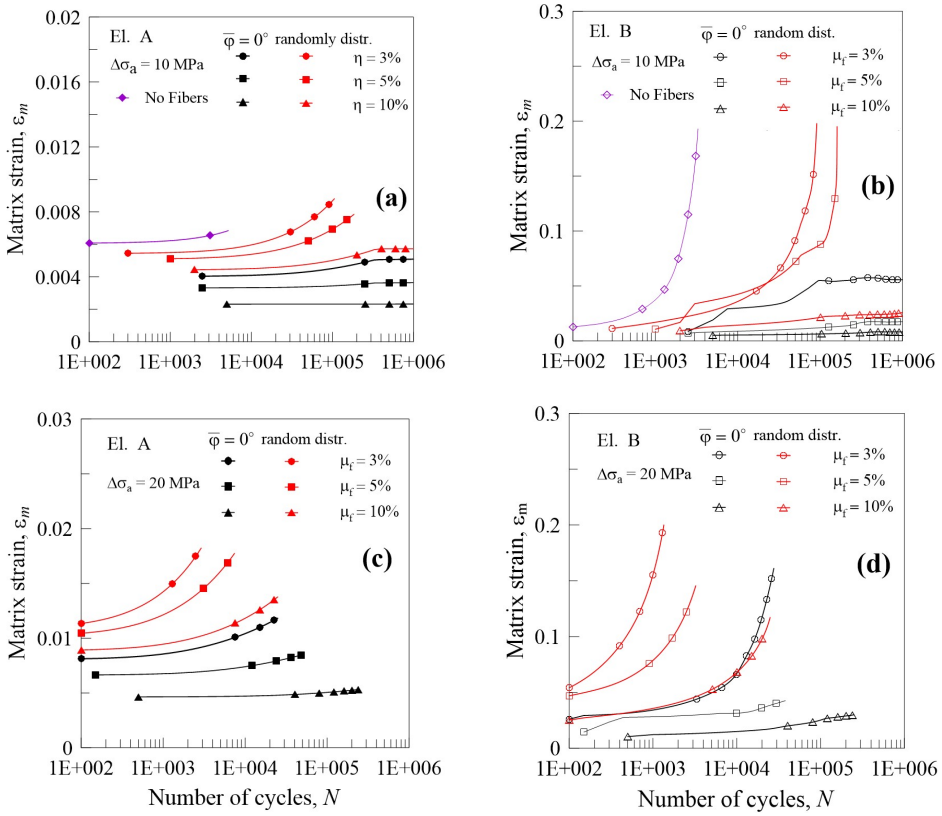

Figure 6.36: Matrix strain, ε_m, against number of cycles N, related two elements of the mesh: elem. A (a) and (c), and elem. B (b) and (d); for three different fibre volume fractions ($\mu_f = 3\%$, 5% and 10%), two fibre orientations ($\overline{\varphi} = 0°$ and random arrangement) and two values of applied load: $\Delta\sigma_a = 10MPa$ (a)and (b), and $\Delta\sigma_a = 20MPa$ (c) and (d). The case of no fibres is also plotted (a) and (b).

$m = 3.1$ (dl/dN in mm/cycle, ΔK_i in $MPa\sqrt{m}$; they are assumed to be equal to those of the matrix material) and the Wöhler's constants are $\sigma_0 = 5MPa$, $N_0 \cong 2 \cdot 10^6$, $B = 0.293$. Two small regions (identified by the finite elements A and B) of the beam are examined in order to study the cyclic load effects, i.e. an element close to the boundary constrain (element A) and an element placed close to the stress concentration region (element B).

In Figure 6.36, the matrix strain evolution is plotted against the number of loading cycles for different fibre arrangements, fibre contents and stress amplitude values. As can be observed, the effectiveness of the fibre phase decreases with N,

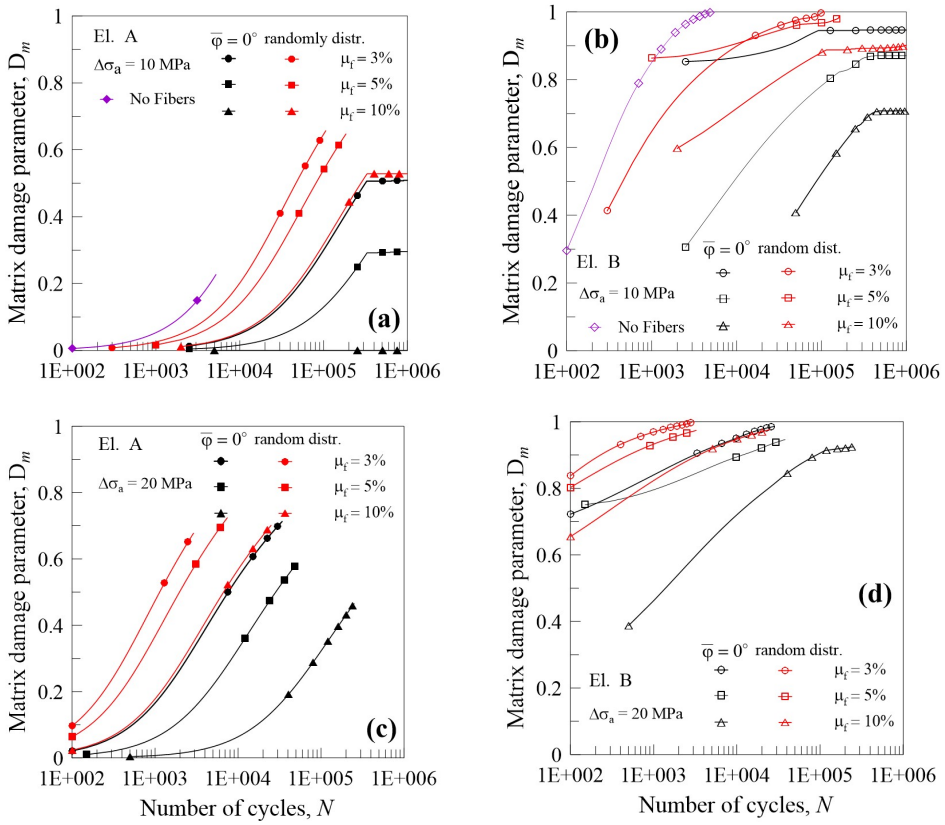

Figure 6.37: Matrix damage paramter, D_m, against number of cycles N, related two elements of the mesh: elem. A (a) and (c), and elem. B (b) and (d) for three different fibre volume fractions ($\mu_f = 3\%$, 5% and 10%), two fibre orientations ($\overline{\varphi} = 0°$ and random arrangement) and two values of applied load: $\Delta\sigma_a = 10MPa$ (a) and (b), and $\Delta\sigma_a = 20MPa$ (c) and (d). The case of no fibres is also plotted (a).

as is outlined by the increase of the strain in the matrix. An increase of the fibre volume content produces a reduction of the matrix strain; the case of fibres aligned with the horizontal direction seems to be more effective in limiting the matrix strain. The same qualitative behaviour can be recognised for both element A and element B of the beam; nevertheless, in the stress concentration zone (element B), the increase of the matrix strain is much more pronounced, especially for low fibre contents.

Figure 6.37 shows the damage evolution for the same cases reported in Figure 6.36. Since the matrix damage parameter, $D_m = D_E$, is strictly related to the

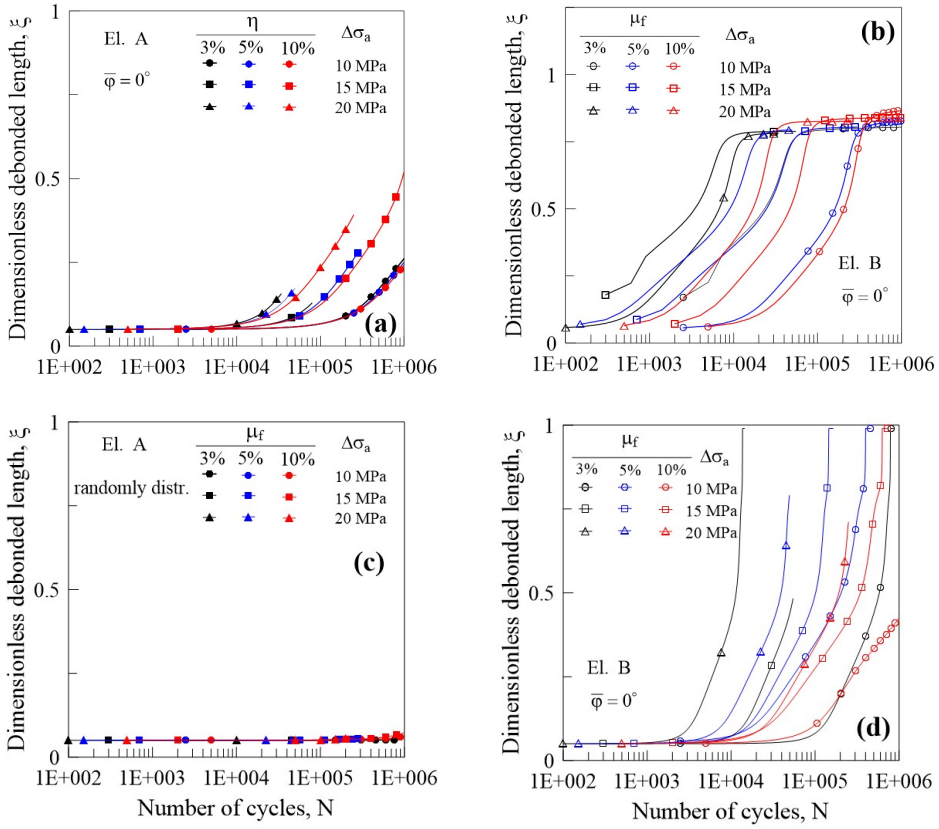

Figure 6.38: Dimensionless debonded length, ξ, against number of cycles N, for two elements of the mesh: elem. A (a) and (c), and elem. B (b) and (d) for three different fibre volume fractions ($\mu_f = 3\%$, 5% and 10%), three values of applied load: $\Delta\sigma_a = 10MPa$, $\Delta\sigma_a = 15MPa$ and $\Delta\sigma_a = 20MPa$, and two fibre orientations: $\overline{\varphi} = 0°$, (a) and (b), and randomly arranged (c) and (d).

matrix strain, a similar trend can be observed. It is worth noting that, in the case $\overline{\varphi} = 0°$, $\mu_f = 10\%$ and $\Delta\sigma_a = 10MPa$, the damage in the matrix remains equal to zero along the whole fatigue process, and the matrix strain is almost constant.

The fibre dimensionless debonded length, ξ, is plotted against the number of loading cycles N in Figure 6.38. As can be noted, the fibre detachment in the highly stressed element (B, Figure 6.38b, 6.38d) develops very quickly for both horizontal and randomly oriented fibres, whereas such a behaviour is much more mitigated in element A. At element B in the case of $\overline{\varphi} = 0°$, the fibre debonding stabilises around the value $\xi \cong 0.8$ for all the examined cases, while ξ rapidly tends

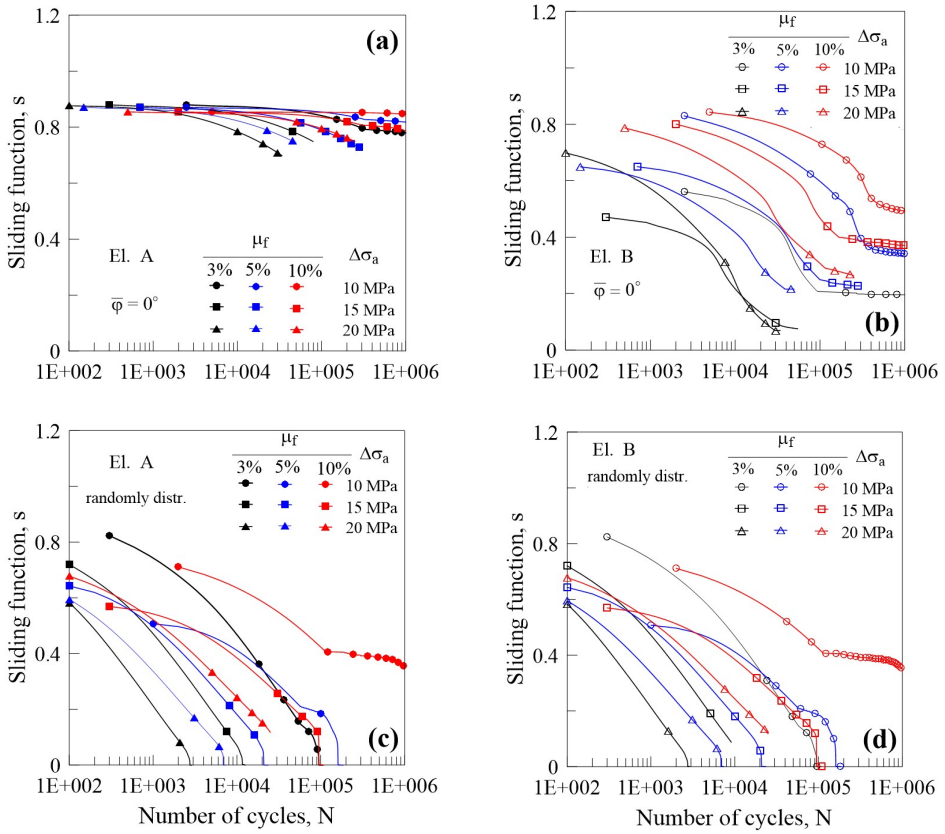

Figure 6.39: Sliding function, s, against number of cycles, N, for two elements of the mesh: elem. A (a) and (c), and elem. B (b) and (d) for three different fibre volume fractions ($\mu_f = 3\%$, 5% and 10%), three values of applied load: $\Delta\sigma_a = 10MPa$, $\Delta\sigma_a = 15MPa$ and $\Delta\sigma_a = 20MPa$, and two fibre orientations: $\overline{\varphi} = 0^\circ$, (a) and (b), and randomly arranged (c) and (d).

to 1.0 for random fibres arrangement.

The fibre effectiveness during fatigue is represented in Figure 6.39 through the sliding function, s which appears to be a decreasing function of N, with higher decreasing rate: (i) when the stress amplitude increases; (ii) when the fibre content decreases; (iii) for high value of the local stress (point B) (iv) when the random arrangement is examined instead of the case of $\overline{\varphi} = 0^\circ$.

The matrix material has been assumed to be representative also of the fibre-matrix interface material adopted in the numerical calculations. Note that the determination of the interface parameters is a difficult task [254], and some uncer-

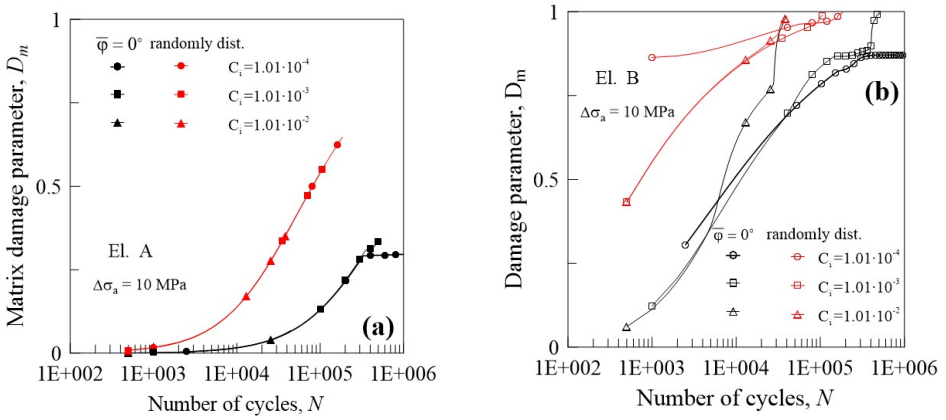

Figure 6.40: Matrix damage parameter, D_m, against number of cycles N, related to the elements A (a) and B (b), for $\mu_f = 5\%$, two fibre orientations ($\overline{\varphi} = 0°$ and random arrangement), $\Delta\sigma_a = 10MPa$ and for three values of interface fatigue constants, C_i.

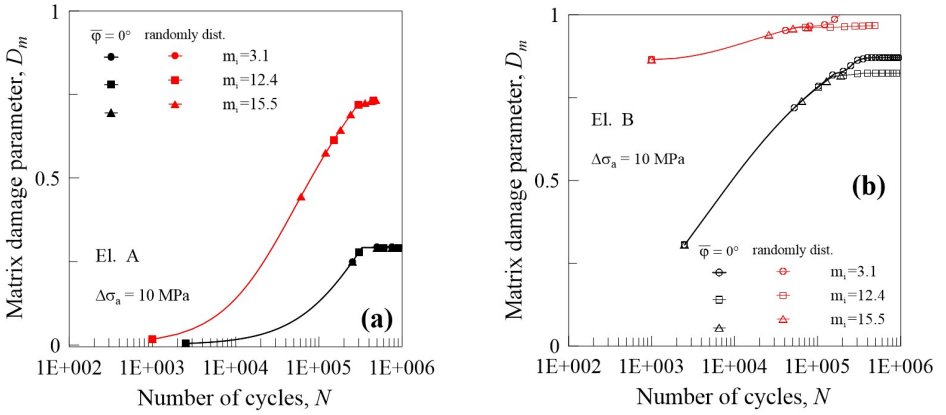

Figure 6.41: Matrix damage parameter, D_m, against number of cycles N, related to the elements A (a) and B (b), for $\mu_f = 5\%$, two fibre orientations ($\overline{\varphi} = 0°$ and random arrangement), $\Delta\sigma_a = 10MPa$ and for three values of interface fatigue constants, m_i.

tainties are unavoidable. For this reason, the influence of the Paris law constants of the interface, C_i and m_i, is herein taken into account by adopting different order of magnitude for C_i and different values of m_i.

In Figure 6.40, the damage taking place in the matrix is plotted against the number of loading cycles, N, for three values of C_i. As can be remarked, different values of the Paris constant are not very important for the damage evolution since, for a given N value, the damage is approximately independent of C_i.

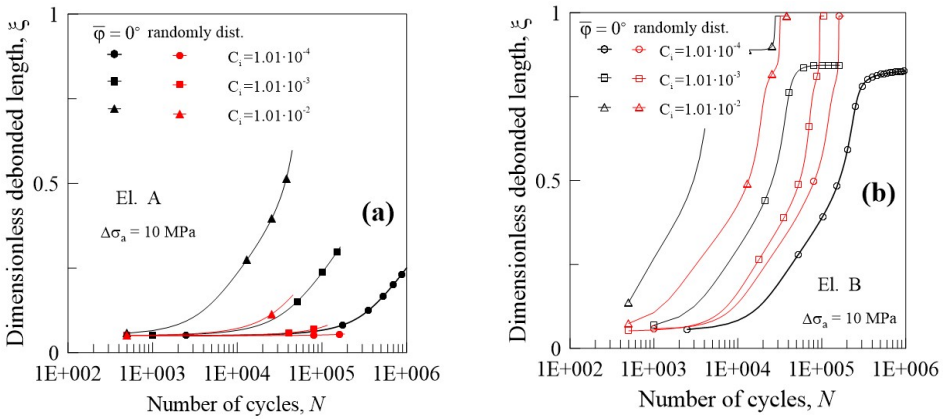

Figure 6.42: Dimensionless debonded length, ξ, against number of cycles N, related to the elements A (a), and B (b), for $\mu_f = 5\%$, two fibre orientations ($\overline{\varphi} = 0°$ and random arrangment), $\Delta\sigma_a = 10MPa$ and for three different values of interface fatigue constants, C_i.

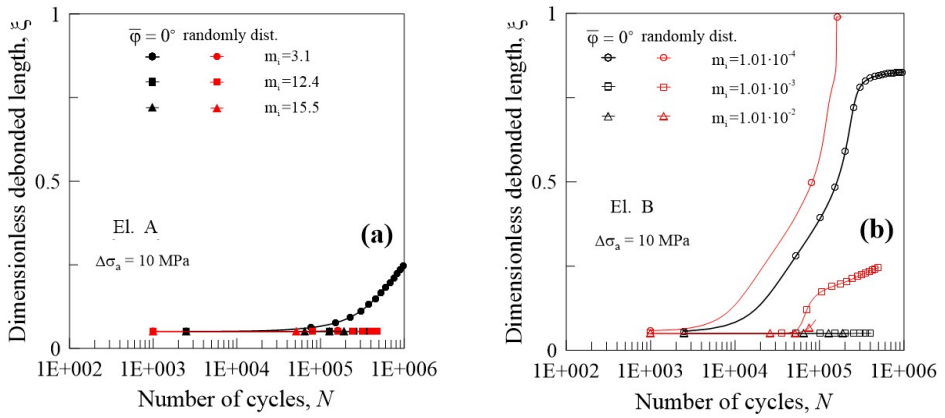

Figure 6.43: Dimensionless debonded length, ξ, against number of cycles N, related to the elements A (a), and B (b), for $\mu_f = 5\%$, two fibre orientations ($\overline{\varphi} = 0°$ and random arrangement), $\Delta\sigma_a = 10MPa$ and for three different values of interface fatigue constants, m_i.

In Figure 6.41, the damage occurring in the matrix is plotted against the number of loading cycles, N, for three values of m_i. Note that, the damage development is not influenced by such a parameter since, for a given number of loading cycles, the damage value is approximately independent of m_i. These results are interesting since allow to conclude that the uncertainty in the determination of the fatigue

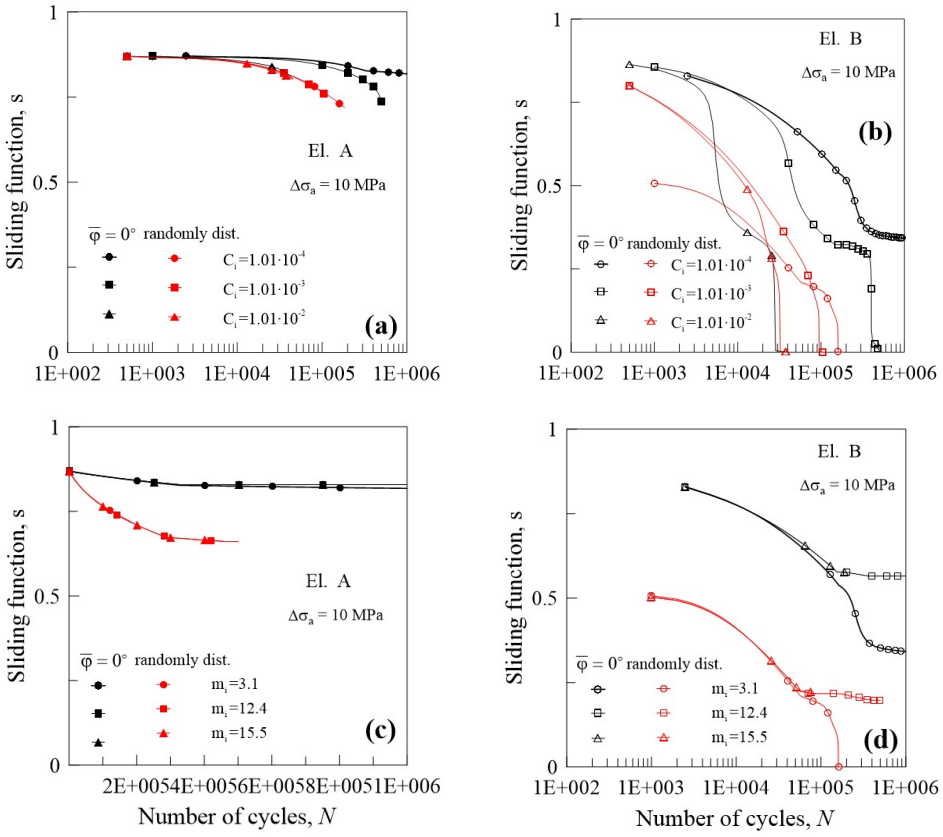

Figure 6.44: Sliding function, s, against the number of cycles N, related to the elements A (a), and B (b) for three values of interface fatigue constants, C_i, and related to the elements A (c), and B (d) for three values of interface fatigue constants, m_i, for $\mu_f = 5\%$, two fibre orientations ($\overline{\varphi} = 0^\circ$ and randomly distribution), $\Delta\sigma_a = 10MPa$.

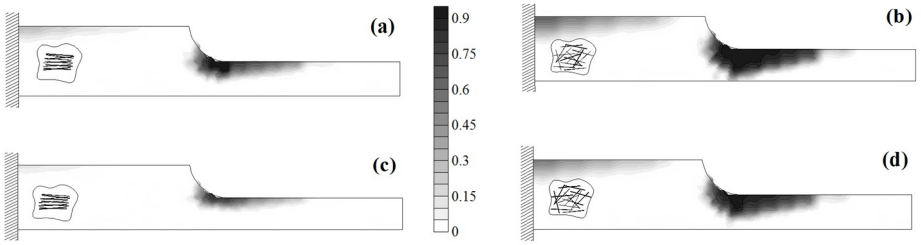

Figure 6.45: Distribution of the matrix damage parameter, D_m, for $\mu_f = 3\%$ (a) and (b), and for $\mu_f = 5\%$ (c) and (d), two fibre orientations $\overline{\varphi} = 0^\circ$ (a) and (c) and random arrangement (b) and (d) with $\Delta\sigma_a = 10MPa$ at $N = 91500$ cycles.

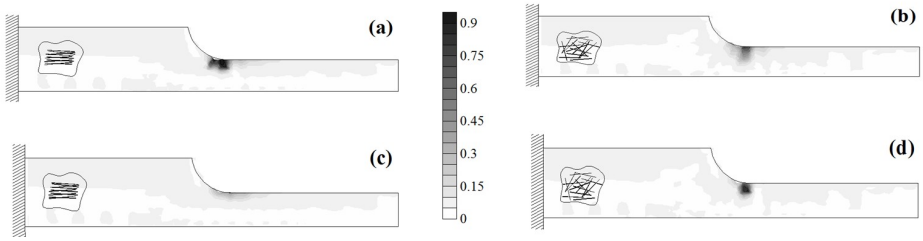

Figure 6.46: Distribution of the dimensionless debonded length, ξ, for $\mu_f = 3\%$ (a) and (b), and for $\mu_f = 5\%$ (c) and (d), two fibre orientations $\overline{\varphi} = 0°$ (a) and (c) and random arrangement (b) and (d) with $\Delta\sigma_a = 10MPa$ at $N = 91500$ cycles.

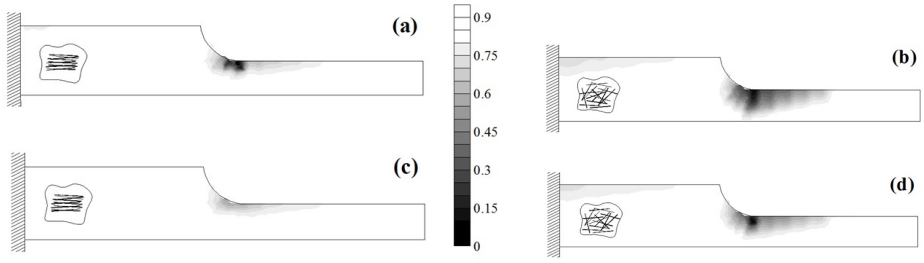

Figure 6.47: Distribution of the sliding function, s, for $\mu_f = 3\%$ (a) and (b), and for $\mu_f = 5\%$ (c) and (d), two fibre orientations $\overline{\varphi} = 0°$ (a) and (c) and random arrangement (b) and (d) with $\Delta\sigma_a = 10MPa$ at $N = 91500$ cycles.

interface parameters has low effects on the matrix damage.

In Figure 6.42, the dimensionless fibre detachment ξ is plotted against the number of loading cycles N for the three values of C_i examined above. The debonding appears to be heavily affected by the choice of C_i, especially in zones with low stress values and almost uniform stress distribution (element A).

In Figure 6.43, the dimensionless fibre detachment is plotted against the number of loading cycles N for the three values of m_i examined above; also in this case, the debonding appears to be heavily affected by the choice of m_i, especially in zones with high stress values and high stress gradient (element B), whereas this effect is less evident in the case of low stress values and almost uniform stress distribution (element A). However, such a microscopic quantity (ξ) must not be considered as a relevant parameter for the whole behaviour of the composite, for which the sliding function represents a more suitable parameter of the fibre effectiveness (Fig. 6.44).

Figures 6.45, 6.46 and 6.47 illustrate the distribution of the matrix damage, of

the fibre dimensionless debonded length and of the sliding function by using a grey scale contour map, for horizontal and randomly arranged fibres and for two fibre contents $\mu_f = 3\%$ and 5%, at a given number of loading cycles ($N = 91500$), for a stress amplitude equal to $\Delta\sigma_a = 10MPa$. The case of fibres randomly arranged corresponds to higher damage values in the matrix and lower sliding function values, denoting the more pronounced loss of efficiency of the reinforcing phase.

Concerning the fibre detached length, a unique trend cannot be easily recognised: the high amount of fibre content certainly is responsible for a reduction of the fibre debonding that appears to be practically not relevant for the case of $\overline{\varphi} = 0°$ and $\mu_f = 5\%$ (Fig. 6.46c).

6.5 Summary and Conclusions

In the present Ph.D. Thesis, a micro-mechanical model describing the behaviour of short fibre-reinforced composite materials has been developed and applied to some structural components in order to assess its capability to simulate fracture process and fatigue effects.

- A homogenisation approach, based on an energetic formulation, has been generalised in order to quantify the mechanical properties of short-fibre reinforced materials taking into account the spatial arrangement (fibre randomly or preferentially oriented) and distribution of the fibre reinforcing phase. The effectiveness of the composite is also considered by means of a proper parameter, the sliding function s, that quantifies the quality of the fibre-matrix interface bond.

- In order to examine all the micro-mechanical phenomena involved in static and fatigue problems, the mechanical behaviour of the single constituents of the composite and their reciprocal interaction are analysed.

- The matrix is assumed to be characterised by linear elastic, or elastic-plastic or brittle mechanical behaviour in case of monotonic loads, whereas an approach based on the experimental Wöhler diagrams (S-N curves) is adopted to simulate fatigue effects.

- The reinforcing phase is assumed to present a linear elastic behaviour until reaching a condition of failure at which the fibre breaks. The reciprocal interaction of fibre is also taken into account, whereas the effect of the cycle loading on the fibre material has been neglected.

- Particular attention is focused on the fibre-matrix interface debonding phenomenon which is responsible for the macro-mechanical properties of the whole composite material. A fracture mechanics based approach has been proposed, in alternative to the classical shear lag model, aimed to provide a suitable tool for the simulation of the mechanical behaviour of short-fibre reinforced materials subjected to both static and cyclic loads. A correlation between the present model and the shear lag model has been proposed in order to allow the quantification of the static critical interface parameters (such as fracture toughness and fracture energy), necessary to identify the

condition of incipient detachment propagation. The interface parameters, required by the fatigue propagation law, are assumed to be equal to those of the matrix. The assessment of such parameters is a hard task and still object of study.

- Finally, the formulation described in the previous Chapters, has been implemented in a non-linear 2-D FE code used for the simulation of simple structural components under static and cyclic loads. Some of the obtained results have been reported and discussed in the present Chapter.

- In conclusion, according to the presented results, the proposed micro-mechanical approach is able to model the macro-mechanical behaviour of short-fibre reinforced composite structural components subjected to static and cyclic loads, and is in good agreement with numerical and experimental literature data.

6.6 Future work

Further enhancing of the micro-mechanical model developed in the present Ph.D. Thesis and future research directions in this field are summarized below:

- Determination of a suitable method for estimating the interface parameters required by the fatigue propagation law.
- Capability to assess the fracture growth process in the matrix material due to the presence of cyclic loads.
- Finally, the damage effects due to multiaxial fatigue should be taken into account in order to make a comprehensive analysis of short fibre-reinforced composite materials.

Appendix A

SIFs Tables

In the present appendix the SIFs for a partially debonded fibre under remote radial (σ_r^∞) and longitudinal stress (σ_z^∞) are reported in dimensionless form in the following tables (Tables A.1- A.4):

Table A.1: Dimensionless Mode I SIFs under remote radial transversal stress σ_r^∞: $K_I^*(\sigma_r^\infty)$ for $\eta = 2L_f/\phi_f = 20$ (a), $\eta = 40$ (b) and $\eta = 80$ (c).

	$\xi = l/L_f$									
$\gamma = E_f/E_m$	0.05	0.1	0.2	0.3	0.4	0.5	0.6	0.7	0.8	0.9
(a) $\eta = 20$										
1	0.28732	0.20447	0.14813	0.12141	0.10514	0.09396	0.08570	0.07905	0.07418	0.07031
10	0.19001	0.08887	0.03658	0.01766	0.00802	0.00226	0.00000	0.00000	0.00000	0.00000
25	0.17988	0.08308	0.02446	0.01323	0.01126	0.00750	0.00555	0.00390	0.00246	0.00069
40	0.20589	0.09764	0.03274	0.01518	0.01438	0.01187	0.00813	0.00539	0.00349	0.00141
(b) $\eta = 40$										
1	0.20619	0.14219	0.10112	0.08212	0.07092	0.06324	0.05762	0.05324	0.04974	0.04706
10	0.12690	0.06483	0.02807	0.01452	0.00659	0.00307	0.00000	0.00000	0.00000	0.00000
25	0.10398	0.06277	0.02208	0.01080	0.00791	0.00671	0.00572	0.00468	0.00325	0.00167
40	0.14682	0.07641	0.02982	0.01733	0.01323	0.01060	0.00891	0.00713	0.00483	0.00237
(c) $\eta = 40$										
1	0.14495	0.09118	0.06416	0.05211	0.04495	0.04008	0.03673	0.03369	0.03145	0.02961
10	0.08570	0.04561	0.02062	0.01123	0.00629	0.00328	0.00127	0.00104	0.00016	0.00004
25	0.08651	0.01875	0.00884	0.01080	0.00636	0.00516	0.00458	0.00415	0.00362	0.00235
40	0.10190	0.05647	0.02512	0.01399	0.01050	0.00881	0.00753	0.00661	0.00562	0.00346

Table A.2: Dimensionless Mode II SIFs under remote radial transversal stress σ_r^{∞}: $K_{II}^{*}(\sigma_r^{\infty})$ for $\eta = 2L_f/\phi_f = 20$ (a), $\eta = 40$ (b) and for $\eta = 80$ (c).

	$\xi = l/L_f$									
$\gamma = E_f/E_m$	0.05	0.1	0.2	0.3	0.4	0.5	0.6	0.7	0.8	0.9
(a) $\eta = 20$										
1	0.08638	0.07076	0.05483	0.04655	0.04130	0.03760	0.03481	0.03255	0.03088	0.02964
10	0.45325	0.33513	0.24565	0.20223	0.17553	0.15685	0.14296	0.13181	0.12220	0.11367
25	0.52532	0.37890	0.27521	0.22508	0.19358	0.17217	0.15520	0.14098	0.12816	0.11612
40	0.55035	0.39785	0.28874	0.23795	0.20250	0.18217	0.15999	0.14406	0.12960	0.11615
(b) $\eta = 40$										
1	0.08039	0.05762	0.04223	0.03632	0.03205	0.02916	0.02684	0.02509	0.02368	0.022661
10	0.36031	0.25337	0.18335	0.15075	0.13130	0.11722	0.10686	0.09891	0.09223	0.08618
25	0.32112	0.28455	0.20516	0.16824	0.14567	0.13009	0.11827	0.10863	0.10003	0.09112
40	0.42015	0.29733	0.21504	0.17655	0.15298	0.13641	0.12364	0.11261	0.10291	0.09238
(c) $\eta = 40$										
1	0.06106	0.04158	0.03078	0.02575	0.02266	0.02052	0.01806	0.01765	0.01663	0.01580
10	0.24122	0.17074	0.12328	0.10138	0.08809	0.07892	0.07207	0.06912	0.06238	0.05865
25	0.26573	0.18656	0.13620	0.11188	0.09711	0.08692	0.07929	0.07331	0.06829	0.06335
40	0.27276	0.19489	0.14129	0.11633	0.10102	0.09062	0.08272	0.07644	0.07095	0.06502

Table A.3: Dimensionless Mode II SIFs under remote uniaxial longitudinal stress σ_z^∞: $K_{II}^*(\sigma_z^\infty)$ in a partially debonded fibre embedded in an infinite elastic domain, for $\xi = E_f/E_m = 1$ (a), $\xi = 10$ (b), $\xi = 25$ (c) and $\xi = 40$ (d).

	$\xi = l/L_f$									
$\eta = 2L_f/\phi_f$	0.05	0.1	0.2	0.3	0.4	0.5	0.6	0.7	0.8	0.9
$\gamma = 1$										
20	0.27412	0.18916	0.13175	0.10707	0.09250	0.08261	0.07531	0.06957	0.06468	0.05881
40	0.20367	0.14216	0.09980	0.08133	0.07038	0.06292	0.05742	0.05315	0.04966	0.04647
80	0.15634	0.10991	0.07750	0.06324	0.05476	0.04898	0.04471	0.04139	0.03872	0.03645
(b) $\gamma = 10$										
20	0.86035	0.59876	0.41909	0.34029	0.29273	0.25896	0.23161	0.20568	0.17506	0.12766
40	0.69903	0.49052	0.34508	0.28132	0.24339	0.21739	0.19596	0.18142	0.16449	0.13516
80	0.55294	0.38943	0.27478	0.22424	0.19415	0.17367	0.15853	0.14669	0.13664	0.12366
(c) $\gamma = 25$										
20	1.27836	0.89037	0.61994	0.49878	0.42285	0.36574	0.31616	0.26690	0.21128	0.14024
40	1.07722	0.75690	0.53264	0.43340	0.37388	0.33267	0.29914	0.26734	0.22877	0.16596
80	0.85914	0.60569	0.42752	0.34894	0.30209	0.27019	0.24651	0.22726	0.20804	0.17306
(d) $\gamma = 40$										
20	1.54414	1.07233	0.74173	0.59114	0.49466	0.42057	0.35563	0.29205	0.22402	0.14387
40	1.33482	0.93836	0.65983	0.53635	0.46108	0.40658	0.36069	0.31478	0.25882	0.18366
80	1.06853	0.75378	0.53213	0.43435	0.37598	0.33615	0.30618	0.28049	0.25140	0.19618

Table A.4: Interpolation coefficients of Eq. (5.38) for the dimensionless SIFs under radial transversal stress σ_r^∞ and longitudinal stress σ_z^∞ for different $\gamma = E_f/E_m$ ratios.

	a_0	a_1	a_2	a_3	b_1
$\gamma = 1$					
K_{Ir}^*	0.42489E0	-0.71183E-2	0.76727E-4	-0.34774E-6	-0.11489E1
K_{IIr}^*	0.11549E0	-0.10113E-2	0.95356E-5	-0.52086E-7	-0.30253E1
K_{IIz}^*	0.38544E0	-0.56249E-2	0.59626E-4	-0.25807E-6	-0.11367E1
$\gamma = 10$					
K_{Ir}^*	0.25737E0	-0.33317E-2	0.26451E-4	-0.92595E-7	-0.11528E1
K_{IIr}^*	0.63186E0	-0.80714E-2	0.74439E-4	-0.34428E-6	-0.17676E1
K_{IIz}^*	0.11354E1	-0.11633E-1	0.10131E-3	-0.38386E-6	-0.36168E1
$\gamma = 25$					
K_{Ir}^*	0.24584E0	-0.36507E-2	0.33933E-4	-0.11451E-6	-0.10954E1
K_{IIr}^*	0.75945E0	-0.13217E-1	0.13730E-3	-0.54980E-6	-0.18950E1
K_{IIz}^*	0.16213E1	-0.12268E-1	0.75024E-4	-0.20588E-6	-0.54516E1
$\gamma = 40$					
K_{Ir}^*	0.26752E0	-0.27182E-2	0.18083E-4	-0.56972E-7	-0.12860E1
K_{IIr}^*	0.76740E0	-0.10174E-1	0.89165E-4	-0.38477E-6	-0.21642E1
K_{IIz}^*	0.18987E1	-0.10358E-1	0.24708E-4	-0.48912E-7	-0.66635E1

	b_2	b_3	c_1	c_2	c_3
$\gamma = 1$					
K_{Ir}^*	0.16300E1	-0.81096E0	0.67404E-2	-0.21236E-4	-0.31940E-2
K_{IIr}^*	0.46316E0	-0.24229E0	0.44806E-3	0.11202E-5	-0.29993E-3
K_{IIz}^*	0.16424E1	-0.82658E0	0.63110E-2	-0.21659E-4	-0.29872E-2
$\gamma = 10$					
K_{Ir}^*	0.17253E1	-0.84446E0	0.71675E-2	-0.18886E-4	-0.42783E-2
K_{IIr}^*	0.25251E1	-0.12550E1	0.87866E-2	-0.17675E-4	-0.48112E-2
K_{IIz}^*	0.54188E1	-0.29052E1	0.15811E-1	-0.59947E-4	-0.57715E-2
$\gamma = 25$					
K_{Ir}^*	0.17074E1	-0.88436E0	0.68877E-2	-0.26041E-4	-0.34256E-2
K_{IIr}^*	0.24214E1	-0.11641E1	0.15110E-1	-0.68709E-4	-0.54715E-2
K_{IIz}^*	0.82259E1	-0.44946E1	0.21888E-1	-0.77623E-4	-0.76286E-2
$\gamma = 40$					
K_{Ir}^*	0.20650E1	-0.10766E1	0.65641E-2	-0.15595E-4	-0.40326E-2
K_{IIr}^*	0.30137E1	-0.14980E1	0.12654E-1	-0.32877E-4	-0.62314E-2
K_{IIz}^*	0.10060E2	-0.54857E1	0.25215E-1	-0.75036E-4	-0.98923E-2

Bibliography

[1] R.M.A. Jones. *Mechanics of Composite Materials.* Taylor and Francis Group, 1999.

[2] P.K. Mallick. *Mechanics of Composite Materials.* Taylor and Francis Group, 1999.

[3] Q.G. Cheng. *Fiber Reinforced Composites.* Nova Science Publishers, 2012.

[4] J.D. Eshelby. The determination of the elastic field of an ellipsoidal inclusion and related problems. *Proc. R. Soc.*, A241:376–396, 1957.

[5] Z. Hashin. The elastic moduli of heterogeneous materials. *J. Appl. Mech.*, 29:143–150, 1962.

[6] R. Hill. Elastic properties of reinforced solids: some theoretical principles. *J. Mech. Phys. Solids*, 11:357–372, 1963.

[7] Z. Hashin and B.W. Rosen. The elastic moduli of fiber-reinforced materials. *J. Appl. Mech.*, 31:223–232, 1964.

[8] R. Hill. Theory of mechanical properties of fibre-strengthened materials: I. elastic behaviour. *J. Mech. Phys. Sol.*, 12:199–212, 1964.

[9] Z. Hashin. On elastic behaviour of fibre reinforced materials of arbitrary transverse phase geometry. *J. Mech. Phys. Sol.*, 13:119–134, 1965.

[10] R.M. Christensen and K.H. Lo. Solutions for effective shear properties in 3 phase sphere and cylinder models. *J. Mech. Phys. Solids*, 27(4):315–330, 1979.

[11] V. Mantic. Solutions for effective shear properties in 3 phase sphere and cylinder models. *J. Mech. Phys. Solids*, 27(4):315–330, 1979.

[12] D. Notta-Cuvier, F. Lauro, B. Bennani, and R. Balieu. Damage of short-fibre reinforced materials with anisotropy induced by complex fibres orientations. *Mech. Mat.*, 68:193–206, 2014.

[13] P. Cornetti, V. Mantic, and A. Carpinteri. Finite fracture mechanics at elastic interfaces. *J. Sol. Struct.*, 49:1022–1032, 2012.

[14] A. Puck and H. Schürmann. Failure analysis of frp laminates by means of physically based phenomenological models. *Comp. Sci. and Tech.*, 58: 1045–1067, 1998.

[15] A.L. Kalamkarov and H.Q. Liu. A new model for a multiphase fibre-matrix composite materials. *J. Sol. Struct.*, 29:643–653, 1998.

[16] P. Raghavan and S. Ghosh. A continuum damage mechanics model for unidirectional composites undergoing interfacial debonding. *Mech. Mat.*, 37: 955–979, 2005.

[17] H. Berger, U. Gabbert, H. Köppe, R. Rodriguez-Ramos, J. Bravo-Castillero, R. Guinovart-Diaz, J.A. Otero, and G.A. Maugin. Finite element and asymptotic homogenization methods applied to smart composite materials. *Comput. Mech.*, 33:61–67, 2003.

[18] S. Kari, H. Berger, and U. Gabbert. Numerical evaluation of effective material properties of randomly distributed short cylindrical fibre composites. *Int. J. of Comp. Mat. Sci.*, 39:198–204, 2007.

[19] A.R. Maligno, N.A. Warrior, and A.C. Long. Finite element investigations on the microstructure of fibre-reinforced composites. *Express Polymer Letters*, 2:665–676, 2008.

[20] R. Brighenti. Numerical modelling of the fatigue behaviour of fiber reinforced composites. *Comp. Part B*, 35(3):197–210, 2004.

[21] A. Carpinteri, A. Spagnoli, and S. Vantadori. An elastic-plastic crack bridging model for brittle-matrix fibrous composite beams under cyclic loading. *Int. J. of Solids and Struct.*, 43:4917–4936, 2006.

[22] Y.X. Gan. Effect of interface structure on mechanical properties of advanced composite materials. *J. Mol. Sci.*, 10:5115–5134, 2009.

[23] J.K. Kim, C. Baillie, and Y.W. Mai. Interfacial debonding and fibre pull-out stresses. *J. Mat. Sci.*, 27:3143–3154, 1991.

[24] H.L. Cox. The elasticity and strength of paper and other fibrous materials. *Br. J. Appl. Phys.*, 3:73–79, 1952.

[25] S.A. Paipetis. *Science and Technology in Homeric Epics.* 2008.

[26] S.P. Rawal. Multifunctional composite materials and structures. *Comp. Compos. Mater.*, 6(6):67–86, 2003.

[27] M.J. Pindera and Y. Bansal. On the micromechanics-based simulation of metal matrix composite response. *J Eng Mater Technol*, 129(3):468–482, 2007.

[28] Z.. Hashin. *Theory of fiber reinforced materials.* 1972.

[29] J.D. Achenbach. *A theory of elasticity with microstructure for directionally reinforced composites.* 1975.

[30] A. Bensoussan, J.L. Lions, and G. Papanicolaou. *Asymptotic analysis for periodic structures.* 1978.

[31] R.M Christensen. *Mechanics of composite materials.* 1979.

[32] E. Sanchez-Palencia. *Non-inhomogeneous media and vibration theory.* 1980.

[33] P.M. Suquet. *Elements of homogenization for inelastic solid mechanics.* 1987.

[34] J Aboudi. *Mechanics of composite materials: a unified micromechanical approach.* 1991.

[35] A.L. Kalamkarov and A.G. Kolpakov. *Analysis, design and imization of composite structures.* 1997.

[36] S. Nemat-Nasser and M. Hori. *Micromechanics: overall properties of heterogeneous materials.* 1993.

[37] K. Markov and L. Preziosi. *Heterogeneous media: micromechanics modeling methods and simulations.* 2000.

[38] V.A. Buryachenko. *Micromechanics of heterogeneous materials.* 2007.

[39] M.J. Pindera, H. Khatam, A.S. Drago, and Y. Bansal. Micromechanics of spatially uniform heterogeneous media: A critical review and emerging approaches. *Composites Part B: Eng.*, 40:349–378, 2009.

[40] A.S. Drago and M.J. Pindera. Micro-macromechanical analysis of heterogeneous materials: macroscopically homogeneous vs periodic microstructures. *Compos. Sci. Technol.*, 67(6):1243–1263, 2007.

[41] M.J. Pindera and A.B. Bednarcyk. An efficient implementation of the gmc micromechanics model for multi-phased materials with complex microstructures. *Composites Part B: Eng.*, 30(1):87–105, 1999.

[42] C. Huet. Application of variational concepts to size effects in elastic heterogenous bodies. *J. Mech. Phys. Solids*, 38(6):813–841, 1990.

[43] S. Hazanov and C. Huet. Order relationships for boundary conditions effect in heterogenous bodies smaller than the representative volume. *J. Mech. Phys. Solids*, 42(12):1995–2011, 1994.

[44] S. Hazanov and M. Amieur. On overall properties of elastic heterogenous bodies smaller than the representative volume element. *Int. J. Eng. Sci.*, 33(9):1289–1301, 1995.

[45] S.J. Hollister and N. Kikuchi. A comparison of homogenization and standard mechanics analyses for periodic porous composites. *Comput. Mech.*, 10:73–95, 1992.

[46] S. Pecullan, L.V. Gibiansky, and S. Torquato. Scale effects on the elastic behavior of periodic and hierarchical two-dimensional composites. *J. Mech. Phys. Solids*, 47:1509–1542, 1999.

[47] G.L. Povirk. Incorporation of microstructural information into models of two-phase materials. *Acta Metall Mater.*, 43(8):3199–3206, 1995.

[48] M. Jiang, I. Jasiuk, and M. Ostoja-Starzewski. Apparent elastic and elastoplastic behavior of periodic composites. *Int. J. Solids Struct.*, 39:199–212, 2002.

[49] I. Saiki, K. Terada, K. Ikeda, and M. Hori. Appropriate number of unit cells in a representative volume element for micro-structural bifurcation encountered in a multi-scale modelling. *Comput. Methods Appl. Mech. Eng.*, 191:2561–2585, 2002.

[50] W. Voigt. Uber die beziehung zwischen den beiden elastizitatskonstanten isotroper korper. *Wied. Ann.*, 38:573–587, 1889.

[51] A. Reuss. Berechnung der fliessgrenze von mischkristallen auf grund der plastizitatbedingung fur einkristalle. *Z. Agnew. Math. Mech.*, 9:49–58, 1929.

[52] G.Z. Voyiadjis, Z.N. Taqieddin, and P.I. Kattan. Micromechanical approach to damage mechanics of composite materials with fabric tensors. *Composites Part B: Eng.*, 38:862–877, 2007.

[53] G.W. Postma. Wave propagation in a stratified medium. *J. Geophys.*, 20(4): 780–806, 1955.

[54] A.V. Hershey. The elasticity of an isotropic aggregate of anisotropic cubic crystals. *J. Appl. Mech.*, 21:236–, 1954.

[55] E. Kroner. Berechnung der elastischen konstanten der vielkristalls aus den konstanten des einkristalls. *Z. Phys.*, 151:504–, 1958.

[56] R. Hill. A self-consistent mechanics of composite materials. *Mech. Phys. Solids*, 13:2223–2227, 1965.

[57] T. Mori and K. Tanaka. Average stress in matrix and average elastic energy of materials with misfitting inclusions. *Acta Metall Mater.*, 21:571–574, 1973.

[58] M.J. Pindera and J. Aboudi. Micromechanical analysis of yielding of metal matrix composites. *Int. J. Plasticity*, 4(3):195–214, 1988.

[59] M. Ferrari. Composite homogenization via the equivalent poly-inclusion approach. *Compos. Eng.*, 4(1):37–45, 1994.

[60] S.K. Kanaun and D. Jeulin. Elastic properties of hybrid composites by the effective field approach. *J. Mech. Phys. Solids*, 49:2339–2367, 2001.

[61] G.P. Tandon and G.J. Weng. Average stress in the matrix and effective moduli of randomly oriented composites. *Compos. Sci. Technol.*, 27:111–132, 1986.

[62] G.P. Tandon and G.J. Weng. A theory of particle-reinforced plasticity. *J. Appl. Mech.*, 55(1):126–135, 1988.

[63] Y.P. Qiu and Weng G.J. The influence of inclusion shape on the overall elastoplastic behavior of a two-phase isotropic composite. *Int. J. Solids Struct.*, 27(12):1537–1550, 1991.

[64] Y.P. Qiu and Weng G.J. A theory of plasticity for porous materials and particlereinforced composites. *J. Appl. Mech.*, 59:261–268, 1992.

[65] Y.M. Wang and Weng G.J. The influence of inclusion shape on the overall viscoelastic behavior of composites. *J. Appl. Mech.*, 59(3):510–518, 1992.

[66] I. Doghri and L. Tinel. Micromechanical modeling and computation of elastic-plastic materials reinforced with distributed-orientation fibers. *Int. J. Plasticity*, 21(10):1919–1940, 2005.

[67] S. Mercier and A. Molinari. Homogenization of elastic-viscoplastic heterogeneous materials: a self-consistent and mori-tanaka schemes. *Int. J. Plasticity*, 25(6):1024–1048, 2009.

[68] X. Shu and B. Huang. Micromechanics-based dynamic modulus prediction of polymeric asphalt concrete mixture. *Composites Part B: Eng.*, 39:704–713, 2008.

[69] H.J. Bohm and Nogales S. Mori-tanaka models for the thermal conductivity of composites with interfacial resistance and particle size distribution. *Compos. Sci. Technol.*, 68:1181–1187, 2008.

[70] G.J. Dvorak. Transformation field analysis of inelastic composite materials. *Proc. R. Soc.*, A431:89–110, 1992.

[71] J.L. Chaboche, P. Kanoute, and A. Roos. On the capabilities of mean-field approaches for the description of plasticity in metal matrix composites. *Int. J. Plasticity*, 21(7):1409–1434, 2005.

[72] V.A. Buryachenko. Multiparticle effective field and related methods in micromechanics of composite materials. *Appl. Mech. Rev.*, 54:1–47, 2001.

[73] H.M. Yin, L.Z. Sun, and G.H. Paulino. Micromechanics-based elastic model for functionally graded materials with particle interactions. *Acta Mater.*, 52: 3535–3543, 2004.

[74] V.A. Buryachenko and A. Roy. Effective elastic moduli of nanocomposites with prescribed random orientation of nanofibers. *Composites Part B: Eng.*, 36:405–416, 2005.

[75] J.F. Mulhern, T.G. Rogers, and A.J.M. Spencer. Cyclic extension of an elastic fibre with an elastic-plastic coating. *J. Inst. Math. Appl.*, 3:21–40, 1967.

[76] T.Y. Chu and Z. Hashin. Plastic behavior of composites and porous media under isotropic stress. *Int. J. Eng. Sci.*, 9(10):971–994, 1971.

[77] M.J. Pindera, A.D. Freed, and S.M. Arnold. Effects of fiber and interfacial layer morphologies on the thermoplastic response of metal matrix composites. *Int. J. Solids Struct.*, 30(9):1213–1238, 1993.

[78] M.J. Pindera, R.S. Salzar, and T.O. Williams. An evaluation of a new approach for the thermoplastic response of metal matrix composites. *Compos. Eng.*, 3(12):1185–1201, 1993.

[79] W.B. Avery and C.T. Herakovich. Effect of fiber anisotropy on the thermal stresses in fibrous composites. *J. Appl. Mech.*, 53:751–756, 1986.

[80] T.O. Williams and M.J. Pindera. An analytical model for the inelastic axial shear response of unidirectional metal matrix composites. *Int. J. Plasticity*, 13(3):261–289, 1997.

[81] M. Paley and J. Aboudi. Micromechanical analysis of composites by the generalized method of cells. *Mech. Mater.*, 14:127–139, 1992.

[82] J. Aboudi, M.J. Pindera, and S.M. Arnold. Linear thermoelastic higher-order theory for periodic multiphase materials. *J. Appl. Mech.*, 68(5):697–707, 2001.

[83] M. Gattu. *Parametric finite volume theory for periodic heterogeneous materials.* 2007.

[84] H. Khatam and M.J. Pindera. Thermo-elastic moduli of lamellar composites with wavy architectures. *Composites Part B: Eng.*, 40(1):50–64, 2009.

[85] S. Nemat-Nasser and M. Hori. On two micro-mechanics theories for determining micro-macro relations in heterogeneous solids. *Mech. Mater.*, 31:667–682, 1999.

[86] B. Harris, J. Morley, and D.C. Phillips. On two micro-mechanics theories for determining micro-macro relations in heterogeneous solids. *J. Mater. Sci.*, 10:2050–, 1975.

[87] P.J. Lawrence. Some theoretical considerations of fibre pull-out from an elastic matrix. *J. Mater. Sci.*, 7:1–6, 1972.

[88] L.B. Greszczuk. 1969.

[89] A. Takaku and R.G.C. Arridge. The effect of interfacial radial and shear stress on fibre pull-out in composite materials. *J. Phys. D: Appl. Phys.*, 6: 2038, 1973.

[90] C. Gurney and J. Hunt. Quasi-static crack propagation. *Proc. Roy. Soc.*, A299:508–524, 1967.

[91] J.D. Outwater and M.C. Murphy. *On the fracture energy of unidirectional laminates.* 1969.

[92] J. Bowling and G.W. Groves. The debonding and pull-out of ductile wires from a brittle matrix. *J. Mater. Sci.*, 14:431–442, 1979.

[93] C. Atkinson, J. Avila, E. Betz, and R.E. Smelser. The rod pull out problem, theory and experiment,. *J. Mech. Phys. and Solids*, 30:97–120, 1982.

[94] H. Stang and S.P. Shah. Failure of fibre-reinforced composite by pull-out fracture. *J. Mater. Sci.*, 21:953–957, 1986.

[95] J. Harris. Shrinkage stresses in glass/resin composites. *J. Mater. Sci.*, 13: 173–177, 1978.

[96] H.E. Daniels. The statistical theory of the strength of bundles of threads. *Proc. Roy. Soc.*, A183:405–435, 1945.

[97] X.F. Zhou and H.D. Wagner. Fibre-matrix adhesion from the single-fibre composite test: nucleation of interfacial debonding. *Compos. Part A*, A30: 1387–1400, 1999.

[98] D.G. Harlow and S.L. Phoenix. The chain-of-bundles probability model for the strength of fibrous materials i: analysis and conjectures. *J. Compos. Mater.*, 12:195–214, 1978.

[99] J.M. Hedgepeth. *Stress Concentrations in Filamentary Structures.* 1961.

[100] J.M. Hedgepeth and P. van Dyke. Local stress concentrations in imperfect filamentary composite materials. *J. Compos. Mater.*, 1:294–309, 1967.

[101] H.D Wagner and A. Eitan. Stress concentration factors in two-dimensional composites: effects of material and geometrical parameters. *Compos. Sci. Technol.*, 46(4):353–362, 1993.

[102] W.A. Curtin. Theory of mechanical properties of ceramic matrix composites. *J. Am. Ceram. Soc.*, 74(11):2837–2845, 1991.

[103] C.M. Landis, M.A. McGlockton, and R.M. McMeeking. An improved shear lag model for broken fibers in composite materials. *J. Compos. Mater.*, 33: 667–680, 1999.

[104] C.M. Landis, I.J. Beyerlein, and R.M. McMeeking. Micromechanical simulation of the failure of fiber reinforced composites. *J. Mech. Phys. Solids*, 48(3):621–648, 2000.

[105] D.E. Gücer and J. Gurland. Comparison of the statistics of two fracture modes. *J. Mech. Phys. Solids*, 10:365–373, 1962.

[106] B.W. Rosen. *AIAA J.*, 2:1985–1991, 1964.

[107] B.W. Rosen. *Fibre Composite Materials.* 1965.

[108] C. Zweben. Tensile failure of fibre composites. *AIAA J.*, 6:2325–2331, 1964.

[109] D. Krajcinovic and M.A.G. Silva. Statistical aspects of the continues damage theory. *Int. J. Solids Struct.*, 18:551–562, 1982.

[110] D. Krajcinovic and A. Rinaldi. Thermodynamics and statistical physics of damage processes in quasi-ductile solids. *Mech. Mater*, 37:299–315, 2005.

[111] F. Li and Z. Li. Continuum damage mechanics based modeling of fiber-reinforced concrete in tension. *Int. J. Solids Struct.*, 38(5):777–793, 2001.

[112] F. Kun, S. Zapperi, and H.J. Herrmann. Damage in fiber bundle models. *Eur. Phys. J.*, B17:269–279, 2000.

[113] R.C. Hidalgo, Y. Moreno, F. Kun, and H.J. Herrmann. Fracture model with variable range of interaction. *Phys. Rev.*, E 65:46–148, 2002.

[114] F. Raischel, F. Kun, and H.J. Herrmann. Failure process of a bundle of plastic fibers. *Phys. Rev.*, E 73:66101–66112, 2006.

[115] L. Jr. Mishnaevsky and P. Brondsted. Micromechanical modelling of damage and fracture of unidirectional fibre reinforced composites: A review. *Comp. Mater. Sci.*, 44:1351–1359, 2009.

[116] J. Aveston, G.A. Cooper, and A. Kelly. *The Properties of Fibre Composites.*, pages 15–26. 1971.

[117] D.B. Marshall, B.N. Cox, and A.G. Evans. The mechanics of matrix cracking in brittle-matrix fiber composites. *Acta Metall.*, 33:2013–2021, 1985.

[118] D.B. Marshall and B.N. Cox. Tensile fracture of brittle matrix composites: influence of fibre strength. *Acta Metall.*, 35:2607–2619, 1987.

[119] B. Budiansky, J.W. Hutchinson, and A.G. Evans. Matrix fracture in fiber-reinforced ceramics. *J. Mech. Phys. Solids*, 34(2):167–189, 1986.

[120] J.W. Hutchinson and H.M. Jensen. Models of fiber debonding and pullout in brittle composites with friction. *Mech. Mater.*, 9(2):139–163, 1990.

[121] F.W. Zok. *Fracture and Fatigue of Continuous Fiber-Reinforced Metal Matrix Composites.*, pages 189–220. 2000.

[122] L.N. McCartney. Mechanics of matrix cracking in brittle-matrix fibre-reinforced composites. *Proc. Roy. Soc. London*, A 409:329–350, 1987.

[123] W.S. Slaughter. A self-consistent model for multi-fiber crack bridging. *Int. J. Solids Struct.*, 30(3):385–398, 1993.

[124] B. Budiansky and J.C. Amazigo. Toughening by aligned, frictionally constrained fibres. *J. Mech. Phys. Solids*, 37(1):93–109, 1989.

[125] W.S. Slaughter and J.L.Jr. Sanders. A model for load-transfer from an embedded fiber to an elastic matrix. *Int. J. Solids Struct.*, 28(8):1041–1052, 1991.

[126] B. Budiansky, A.G. Evans, and J.W. Hutchinson. Fiber-matrix debonding effects oncracking in aligned fiber ceramic composites. *Int. J. Solids Struct.*, 32(3):315–328, 1995.

[127] P.I. González-Chi and R.J. Young. Crack bridging and fibre pull-out in polyethylene fibre reinforced epoxy resins. *J. Mater. Sci.*, 33(24):5715–5729, 1995.

[128] M.R. Piggott. Debonding and friction at fibre-polymer interfaces. i: Criteria for failure and sliding. *Compos. Sci. Technol*, 30(4):295–306, 1987.

[129] F. Hild, A. Burr, and F.A. Leckie. Fibre breackage and fibre pull-out of fibre-reinforced ceramic-matrix composites. *Eur. J. Mech. A. Solids*, 13(6): 731–749, 1994.

[130] F. Hild, A. Burr, and F.A. Leckie. Matrix cracking and debonding of ceramic-matrix composites. *Int. J. Solids Struct.*, 33(8):1209–1220, 1996.

[131] A. Burr, F. Hild, and F.A. Leckie. Continuum description of damage in ceramic-matrix composites. *Eur. J. Mech. A. Solids.*, 16):53–78, 1997.

[132] A. Matzenmiller and R.L. Lublinear, J.and Taylor. A constitutive model for anisotropic damage in fiber-composites. *Mech. Mater.*, 20:125–152, 1995.

[133] G.Z. Voyiadjis and P.I. Kattan. Local approach to damage in elasto-plastic metal matrix composites. *Int. J. Damage Mech.*, 2(1):92–114, 1993.

[134] L.Jr. Mishnaevsky. *Computational Mesomechanics of Composites.* 2007.

[135] L.Jr. Mishnaevsky and S. Schmauder. Continuum mesomechanical finite element modelling in materials development: a state of art review. *Appl. Mech. Rev.*, 54(1):49–69, 2001.

[136] L.Jr. Mishnaevsky. Automatic voxel based generation of 3d microstructural fe models and itsapplication to the damage analysis of composites. *Mater. Sci. Eng.*, A407:11–23, 2005.

[137] J.R Brockenbrough, S. Suresh, and H.A. Wienecke. Deformation of metal-matrix composites with continuous fibers: geometrical effects of fiber distribution and shape. *Acta Metall. Mater.*, 39(5):735–752, 1991.

[138] X. Chen and T.D. Papathanasiou. Interface stress distributions in transversely loaded continuous fiber composites: parallel computation in multi-fiber rves using the boundary element method. *Compos. Sci. Technol.*, 64(9):1101–1114, 2004.

[139] D. Trias, J. Costa, J.A. Mayugo, and J.E. Hurtado. Random models versus periodic models for fibre reinforced composites. *Comput. Mater. Sci.*, 38(2): 316–324, 2006.

[140] D. Trias, J. Costa, A. Turon, and J.E. Hurtado. Determination of the critical size of a statistical representative volume element (srve) for carbon reinforced polymers. *Acta Mater.*, 54(13):3471–3484, 2006.

[141] N. Vejen and R. Pyrz. Transverse crack growth in glass/epoxy composites with exactly positioned long bibres part ii: Numerical. *Compos. Part B: Eng.*, 33(4):279–290, 2002.

[142] M.E. Walter. Response of fibre reinforced ceramic matrix composites through computational modeling of damage. *Mater. Sci. Eng.*, A249:14–21, 1998.

[143] X. Zhang, H.Y. Liu, and Y.W. Mai. Effects of fibre debonding and sliding on the fracture behaviour of fibre-reinforced composites. *Compos. Part A - Appl. Sci. Manufact.*, 35(11):1313–1323, 2004.

[144] X. Zhang, Z. Xia, and F. Ellyin. Nonlinear viscoelastic micromechanical analysis of fibre-reinforced polymer laminates with damage evolution. *Int. J. Solids Struct.*, 42(2):591–604, 2005.

[145] J.T. Fong. *What is fatigue damage?*, pages 243–266. 1982.

[146] G.P. Sendeckyj. *Life prediction for resin-matrix composite materials.*, pages 431–483. 1990.

[147] J. Degrieck and W.V. Paepegem. Fatigue damage modelling of fibre-reinforced composite materials: Review. *Appl. Mech. Rev.*, 54(4):279–300, 2001.

[148] G.P. Sendeckyj. *Fitting models to composite materials fatigue data.*, pages 245–260. 1981.

[149] B Harris. *Fatigue behaviour of polymer-based composites and life prediction methods.* 1985.

[150] J.R. Schaff and B.D. Davidson. Life prediction methodology for composite structures. part i-constant amplitude and two-stress level fatigue. *J. Compos. Mater.*, 31(2):128–157, 1997.

[151] H.T. Hahn and R.Y. Kim. Fatigue behaviour of composite laminates. *J. Compos. Mater.*, 10:55–70, 1976.

[152] T.K. O'Brien and K.L. Reifsnider. Fatigue damage evaluation through stiffness measurements in boron-epoxy laminates. *J. Compos. Mater.*, 15: 55–70, 1981.

[153] W. Hwang and K.S. Han. Cumulative damage models and multi-stress fatigue life prediction. *J. Compos. Mater.*, 20:125–153, 1986.

[154] Z. Hashin and A. Rotem. A fatigue criterionfor fibre reinforced composite materials. *J. Compos. Mater.*, 7:448–464, 1973.

[155] F. Ellyin and H. El-Kadi. A fatigue failure criterion for fiber reinforced composite laminae. *Composite Struct.*, 15:61–74, 1990.

[156] W. C.M. Lawrence. Thermal and mechanicalfatigue analysis of cfrp laminates. *Composite Struct.*, 25:339–344, 1993.

[157] T.P. Philippidis and A.P. Vassilopoulos. Fatigue strength prediction under multiaxial stress. *J. Composite Mater.*, 33(17):1578–1599, 1999.

[158] W. Hwang and K.S. Han. Fatigue of composites- fatigue modulus concept and life prediction. *J. Composite Mater.*, 20:154–165, 1986.

[159] F. Sidoroff and B. Subagio. *Fatigue damage modelling of composite materials from bending tests.*, pages 432–439. 1987.

[160] P.C. Chou and R. Croman. Residual strength in fatigue based on the strength-life equal rank assumption. *J. Composite Mater.*, 12:177–194, 1978.

[161] P.C. Chou and R. Croman. *Degradation and sudden-death models of fatigue of graphite/epoxy composites.*, pages 431–454. 1979.

[162] J.C. Halpin, K.L. Jerina, and T.A. Johnson. *Characterization of composites for the purpose of reliability evaluation.*, pages 5–64. 1973.

[163] H.W. Bergmann and R. Prinz. Fatigue life estimation of graphite/epoxy laminates under consideration of delamination growth. *Int. J. Numer. Methods Eng.*, 27:323–341, 1989.

[164] R. Prinz. *Damage rates for interlaminar failure of fatigue CFRP laminates.*, pages 189–193. 1990.

[165] X. Feng, A.J. Gilchrist, M.D.and Kinloch, and F.L. Matthews. *Development of a method for predicting the fatigue life of CFRP components.*, pages 407–414. 1997.

[166] C. Henaff-Gardin, M.C. Lafarie-Frenot, and I. Goupillaud. *Prediction of cracking evolution under uniaxial fatigue loading incross-ply composite laminates.*, pages 189–196. 1997.

[167] C. Henaff-Gardin, M.C. Lafarie-Frenot, and I. Goupillaud. *The use of a characteristic damagevariable in the study of transverse cracking development under fatigue loading in cross-ply laminates.*, pages 74–75. 2000.

[168] A.L. Highsmith and K.L. Reifsnider. *Stiffness-reduction mechanisms in composite laminates.*, pages 103–117. 1982.

[169] K.L. Reifsnider. The critical element model: a modeling philosophy. *Eng. Fracture Mech.*, 25:739–749, 1986.

[170] S.L. Ogin, P.A. Smith, and P.W.R. Beaumont. Matrix cracking and stiffness reduction during the fatigue of a (0/90)s gfrp laminate. *Composites Sci. Tech.*, 22:23–31, 1985.

[171] W.S. Carswell. Damage mechanics and composite behaviour. *Composite Struct.*, 10:335–342, 1985.

[172] N. Sato, S. Sato, and T. Kurauchi. *Fracture machanism of short glass fiber reinforced polyamide thermoplastics*, pages 1061–1066. 1982.

[173] M.R. Piggott. *Load Bearing Fibre Composites.* 1980.

[174] R.W. Lang, J.A. Manson, and R.W. Hertzberg. Mechanisms of fatigue in short glass fibre-reinforced polymers. *J. Mater. Sci.*, 22:4015–4030, 1987.

[175] J.C. Malzahn and K. Friedrich. Fracture resistence of short glass and carbon fibre/polyamide 6.6 composites. *J. Mater. Sci. Letters*, 3:861–866, 1984.

[176] J.J. Horst, N.V. Salienko, and J.L. Spoormaker. Fibre-matrix debonding stress analysis for short fibre-reinforced materials with matrix plasticity, finite element modelling and experimetal verification. *Composites Part A*, 29A: 525–531, 1998.

[177] A Dibenedetto and Salee. Fatigue crack propagation in graphite fibre reinforced nylon 66. *Pol. Eng. Sci.*, 19:512–518, 1979.

[178] Li V. C. and T. Matsumoto. Fatigue crack growth analysis of fibre reinforcedm concrete with effect of interfacial bond degradation. *Cem. Concr. Comp.*, 20: 339–351, 1998.

[179] D. Broek. *Elementary Engineering Fracture Mechanics.* 1991.

[180] S. Suresh. *Fatigue of Materials.* 1991.

[181] H. Kishimoto. Cyclic fatigue in ceramics. *JSME International Journal*, 34(4): 393–403, 1991.

[182] H. Stang and Z. Jun. *Experimental determination of fatigue crack growth in fiber reinforced concrete*, pages 1347–1352. 1994.

[183] T. Matsumoto and V.C. Li. *Uniaxial cyclic behavior of discontinuous fiber reinforced composites.*, pages 426–435. 1996.

[184] M.R. Kabir, W. Lutz, K. Zhu, and Schmauder S. Fatigue modeling of short fiber reinforced composites with ductile matrix under cyclic loading. *Comput. Mater. Sci.*, 36:361–366, 2006.

[185] M.L. Dunn and H. Ledbetter. Elastic-plastic behavior of textured short fiber composites. *Acta Mater.*, 45(8):3327–3340, 1997.

[186] J. Llorca. A numerical analysis of the damage mechanisms in metal-matrix composites under cyclic deformation. *Comput. Mater. Sci.*, 7:118–122, 1996.

[187] K. Zhu and S. Schmauder. Prediction of the failure properties of short fiber reinforced composites with metal and polymer matrix. *Comput. Mater. Sci.*, 28:743–748, 2003.

[188] A.L. Kalamkarov and A.G. Kolpakov. Design problems for the fibre-reinforced composite materials. *Compos. Part B*, 27B:485–492, 1996.

[189] A. Ngollé and J. Péra. Microstructural based modelling of the elastic modulus of fibre-reinforced cement composites. *Adv. Cem. Based Mat.*, 6:130–137, 1997.

[190] R. Brighenti. Fracture behaviour of brittle fibre-reinforced solids by anew fe formulation. *J. Compos. Struct.*, 91:324–336, 2009.

[191] G.N. Karam. Effect of fiber-fiber interaction on the strength properties of short fiber reinforced cements. *J. Compos. Technol. Res.*, 16:154–160, 1994.

[192] R. Brighenti, A. Carpinteri, and D. Scorza. A computational approach to evaluate the mechanical influence of fibres on brittle-matrix composite materials. *Comput. Mat. Sci.*, 64:212–215, 2012.

[193] G. Bolzon, G. Maier, and F. Tin-Loi. On multiplicity of solutions in quasi-brittle fracture computations. *Comput. Mech.*, 19:511–516, 1997.

[194] J. Oliver. On the discrete constitutive models induced by strong discontinuity kinematics and continuum constitutive equations. *Int. J. Sol. Struct.*, 37: 7207–7229, 2000.

[195] J. Alfaiate, A. Simone, and L.J. Sluys. Non-homogeneous displacement jumps in strong embedded discontinuities. *Int. J. Sol. Struct.*, 40:5799–5817, 2003.

[196] J.M. Sancho, J. Planas, D.A. Cendón, E. Reyes, and J.C. Gálvez. An embedded crack model for finite element analysis of concrete fracture. *Engng. Fract. Mech.*, 74:75–86, 2007.

[197] Y.R. Rashid. Analysis of reinforced concrete pressure vassels. *Nuclear Engng. Des.*, 7:334–344, 1968.

[198] A. Hillerborg, M. Modéer, and P.E. Peterson. Analysis of crack propagatin and crack growth in concrete by means of fracture mechanics and finite elements. *Cement Concr. Res.*, 7:773–782, 1976.

[199] J. Mosler and G. Meschke. Embedded crack vs. smeared crack models: a comparison of elementwise discontinuous crack path approaches with enphasis on mesh bias. *Comp. Mech. Appl. Mech. Engng.*, 193:807–814, 2004.

[200] R. de Borst, J.J.C Remmers, A. Needleman, and M.A. Abellan. Discrete vs smeared crack models for concrete fracture: bridging the gap. *Int. J. Numer. Anal. Meth. Geomech.*, 28:583–607, 2004.

[201] J. Alfaiate, E.B. Pires, and J.A.C. Martins. A finite element analysis of non-prescribed crack propagation in concrete. *Comput. Struct.*, 63:17–26, 1997.

[202] De Xie and A.M. Waas. Discrete cohesive zone model for mixed-mode fracture using finite element analysis. *Engng. Fract. Mech.*, 73:1783–1796, 2007.

[203] T. Belytschko, Y.Y. Lu, L. Gu, and M. Tabbara. Element-free galerkin methods for static and dynamic fracture. *Int. J. Solids Struct.*, 32:2547–2570, 1995.

[204] B. Nayrales, G. Touzot, and P. Villon. Generalizing the finite element method: diffuse approximation and diffuse elements. *Comput. Mech.*, 10:307–318, 1992.

[205] J. Dolbow, N. Möes, and T. Belytschko. An extended finite element method for modelling crack growth with frictional contact. *Comput. Meth. Appl. Mech. Engng.*, 190:6825–6846, 2001.

[206] X.H. Guo, F. Tin-Loi, and H. Li. Determination of quasibrittle fracture law for cohesive crack model. *Cement Concr. Res.*, 29:1055–1059, 1999.

[207] A. Carpinteri and R. Brighenti. A new continuum fe approach for fracture mechanics discontinuous problems. *Cement Concr. Res.*, 45:367–377, 2009.

[208] J. Alfaiate, G.N. Wells, and L.J. Sluys. On the use of embedded discontinuity elements with crack path continuity for mode-i and mixed-mode fracture. *Eng. Fract. Mech.*, 69:661–686, 2002.

[209] X.H. Guo and J. Degrieck. Experimental set-up for and numerical modelling of bending fatigueexperiments on plain woven glass/epoxy composites. *Compos. Struct.*, 51(1):1–8, 2001.

[210] W. Van Paepegemi and J. Degrieck. A new coupled approach of residual stiffness and strength for fatigue of the fibre-reinforced composites. *Int. J. Fatigue*, 24(7):747–762, 2002.

[211] M.R. Venkat, P. Mahajan, and R.K. Mittal. Effect of interfacial debonding and matrix cracking on mechanical properties of multidirectional composites. *Compos. Interfaces*, 15(4):379–409, 2008.

[212] R. Brighenti, A. Carpinteri, and D. Scorza. Stress-intensity factors at the interface edge of a partially detached fibre. *Theor. Appl. Fract. Mech.*, 67-68: 1–13, 2013.

[213] S. Kyriakides, R. Arseculeratne, E.J. Perry, and Liechti E.J. On the compressive failure of fiber-reinforced composites. *J. Sol. Struct.*, 32:689–738, 1995.

[214] T.J. Vogler, S.Y. Hsu, and S. Kyriakides. Composite failure under combined compression and shear. *J. Sol. Struct.*, 37:1765–1791, 2000.

[215] F. Greco and R. Luciano. A theoretical and numerical stability analysis for composite microstructures by using homogenization theory. *Compos. Part B*, 42(3):382–401, 2011.

[216] N.A. Noda, Q. Wang, and T. Morodomi. Analysis of intensity of singular stress at the end of a cylindrical inclusion. *Trans. Japan Soc. Mech. Engrs.*, 63:101–106, 1997.

[217] N.A. Noda, Y. Takase, and T. Iizuka. Generalized stress intensity factors at the fiber end in fiber reinforced plastics. *Trans. of the Japan Soc. Mech. Engineers, Part A*, 71(8):1132–1139, 2005.

[218] D.H. Chen and H. Nisitani. Singular stress fields near the corner of joined dissimilar materials. *J. Appl. Mech.*, 60:607–613, 1993.

[219] N.A. Noda, T. Genkai, and A. Wang. Intensity of singular stress fields at the end of a cylindrical inclusion. *J. Appl. Mech.*, 70:487–495, 2003.

[220] R.A. Chaudhuri. Three-dimensional singular stress field near a partially debonded cylindrical rigid fibre. *Compos. Struct.*, 72:141–150, 2006.

[221] M. Toya. A crack along the interface of a circular inclusion embedded in an infinite solid. *J. Mech. Phys. Solids*, 22:325–348, 1974.

[222] J. Varna, L.A. Berglund, and M.L. Ericson. Transverse single-fibre test for interfacial debonding in composites: 2. modelling. *Compos. Part A*, 28A: 317–326, 1997.

[223] G.P. Sendenckyj. Debonding of rigid curvilinear inclusions in longitudinal shear deformation. *Engng. Fract. Mech.*, 6:33–45, 1974.

[224] I. Demir, J. P. Hirth, and H.M. Zbib. The extended stress field around a cylindrical crack using the theory of dislocation pile-ups. *Int. J. Engng Sci.*, 30:829–845, 1992.

[225] H.M. Zbib, J.P. Hirth, and I. Demir. The stress intensity factor of cylindrical cracks. *Int. J. Engng Sci.*, 33:247–253, 1995.

[226] C. Wüthrich. Stress intensity factors for cylindrical cracks in long cylinders. *Engng Fract. Mech.*, 13:987–990, 1980.

[227] J. Dunders. Effect of elastic constants on stress in a composite under plane deformation. *J. Comp. Mater.*, 1:310–322, 1967.

[228] H. Nisitani, H. Saimoto, and D.H. Chen. Analysis of a symmetrical interface crack based on body force method. *Proceedings of the Annual meeting of JMSE/MMD*, pages 237–238, 1992.

[229] M.L. Williams. Stress singularities resulting from various boundary conditions in angular corners of plates in extension. *J. Appl. Mech.*, 19:526–528, 1952.

[230] D. Leguillon. Strength or toughness? a criterion for crack onset at a notch. *Eur. J Mech. A/Solids*, 21:61–72, 2002.

[231] Z. Yosibash, E. Priel, and D. Leguillon. A failure criterion for brittle elastic materials under mixed-mode loading. *Int. J Fract. Mech*, 141:291–312, 2006.

[232] J. Li and XB. Zhang. A failure criterion for brittle elastic materials under mixed-mode loading. *Int. J Fract. Mech*, 1(8):1385–1404, 2006.

[233] F. Greco, L. Leonetti, and P. Nevone Blasi. Non-linear macroscopic response of fiber-reinforced composite materials due to initiation and propagation of interface cracks. *Engng Fract. Mech.*, 80:92–113, 2012.

[234] J.C. Rice and G.C. Sih. Plane problems of crack in dissimilar media. *J. Appl. Mech.*, 32:418–423, 1965.

[235] A.H. England. A crack between dissimilar media. *J. Appl. Mech.*, 32:400–402, 1965.

[236] S.A. Hamoush and S.H. Ahmad. Mode i and mode ii stress intensity factors for cracks for interfacial cracks in a bi-material media. *Engng. Fract. Mech.*, 33(3):421–427, 1989.

[237] M.L. Williams. The stresses around a fault or crack in dissimilar media. *Bull. Seism. Soc. Amer.*, 49:199–204, 1959.

[238] F. Erdogan. Stress distribution in a nonhomogeneous elastic plane with cracks. *J. Appl. Mech.*, 30:232–236, 1963.

[239] F. Erdogan. Stress distribution in bonded dissimilar materials with cracks. *J. Appl. Mech.*, 32:403–410, 1965.

[240] Y. Murakami. *Stress Intensity Factor Handbook*. Pergamon Press Ltd, 2001.

[241] V. Tvergaard and J.W. Hutchinson. Mode iii effects on interface delamination. *J. Mech. Phys. Sol.*, 56:215–229, 2008.

[242] D. Broek. *Elementary engineering fracture mechanics*. Springer, 1982.

[243] L.J. Gibson, M.F. Ashby, G.N. Karam, U. Wegst, and H.R. Shercliff. The mechanical properties of natural materials. ii. microstructures for mechanical efficiency. *Proc. Math. Phys. Sci.*, 450:141–162, 1995.

[244] J.W.C. Dunlop and R. Weinkamer. Artful interfaces within biological materials. *Mat. Today*, 14:70–78, 2011.

[245] C. Wang. Fracture mechanics of single-fibre pull-out test. *J. Mat. Sci.*, 32: 483–490, 1997.

[246] R. Brighenti, A. Carpinteri, and D. Scorza. Fracture mechanics approach for a partially debonded cylindrical fibre. *Comp. Part B: Engng.*, 53:169–178, 2013.

[247] S. Li, A.M. Thouless, M.D.and Waas, J.A. Schroeder, and P.D. Zavattieri. Use of a cohesive-zone model to analyze the fracture of a fiber-reinforced polymer-matrix composite. *Comp. Sci. Tech.*, 65:537–549, 2005.

[248] O Bayard and O. Plé. Fracture mechanics of reactive powder concrete: material modelling and experimental investigations. *Eng. Fract. Mech.*, 70: 839–851, 2003.

[249] N. Buratti, C. Mazzotti, and Savoia M. Post-cracking behaviour of steel and macro-synthetic fibre-reinforced concretes. *Constr. Build. Mater.*, 25: 2713–2722, 2011.

[250] A. Bernasconi, D. Rossin, and C. Armanni. Analysis of the effect of mechanical recycling upon tensile strength of a short glass fibre reinforced polyamide 6,6. *Eng. Fract. Mech.*, 74:627–641, 2007.

[251] A. Bernasconi and F. Cosmi. Analysis of the dependence of the tensile behaviour of a short fibre reinforced polyamide upon fibre volume fraction, length and orientation. *Procedia Eng.*, 10:2129–2134, 2011.

[252] A. Bernasconi, P. Davoli, A. Basile, and A. Filippi. Effect of fibre orientation on the fatigue behaviour on a short glass fibre reinforced polyamide. *Int. J. Fat.*, 29:199–208, 2007.

[253] A. Zago. Constant amplitude fatigue of short glass and carbon fiber reinforced thermoplastics. *J. Reinfor. Plastics Compos.*, 20(7):564–595, 2001.

[254] M.J. Soapman, A. Nazari, J.A. Porter, and D. Arola. A comparison of fatigue crack growth in resin composite, dentin at the interface. *Dental. Mater.*, 23: 608–614, 2007.